Implications of nuclear interaction for nuclear structure and astrophysics within the relativistic mean-field model

By

Bharat Kumar

PHYS07201304004

Institute of Physics, Bhubaneswar
INDIA

A thesis submitted to the

Board of studies in Physical Sciences

In partial fulfillment of requirements

For the Degree of

DOCTOR OF PHILOSOPHY

of

HOMI BHABHA NATIONAL INSTITUTE

November, 2018

Certificate Will be Uploaded Soon

STATEMENT BY AUTHOR

This dissertation has been submitted in partial fulfillment of requirements for an advance degree at Homi Bhabha National Institute (HBNI) and deposited in the Library to be made available to borrowers under rules of the HBNI.

Brief quotations from this dissertation are allowed without special permission, provided that accurate acknowledgement of source is made. Requests for permission for extended quotation from or reproduction of this manuscript in whole or in part may be granted by the competent Authority of HBNI when in his or her judgment the proposed use of the meterial is in the interests of scholarship. In all other instances, however, permission must be obtained from the author.

(Bharat Kumar)

DECLARATION

I, **Bharat Kumar** , hereby declare that the investigations presented in the thesis have been carried out by me. The matter embodied in the thesis is original and has not been submitted earlier as a whole or in part for a degree/diploma at this or any other Institution/University.

(Bharat Kumar)

List of Publications arising from the thesis

Journal

Published

1. "Examining the stability of thermally fissile Th and U isotopes",
   Bharat Kumar, S. K. Biswal, S. K. Singh and S. K. Patra,
   Phys. Rev. C **2015**, 92, 054314-1−054314-10.

2. "Modes of decay in neutron-rich nuclei",
   Bharat Kumar, S. K. Biswal, S. K. Singh, Chirashree Lahiri, and S. K. Patra,
   Int. J. Mod. Phys. E **2016**, 25, 1650062-1−1650062-16.

3. "Tidal deformability of neutron and hyperon star with relativistic mean-field equations of state",
   Bharat Kumar, S. K. Biswal and S. K. Patra,
   Phys. Rev. C **2017**, 95, 015801-1−015801-10.

4. "Relative mass distributions of neutron-rich thermally fissile nuclei within statistical model",
   Bharat Kumar, M. T. Senthil Kannan, M. Balasubramaniam, B. K. Agrawal, S. K. Patra,
   Phys. Rev. C **2017**, 96, 034623-1−034623-10.

5. "New parameterization of the effective field theory motivated relativistic mean-field model",
   Bharat Kumar, S. K. Singh, B. K. Agrawal, S. K. Patra,
   Nucl. Phys. A **2017**, 966, 197-207.

6. "New relativistic effective interaction for finite nuclei, infinite nuclear matter and neutron stars",
   Bharat Kumar, S. K. Patra, and B. K. Agrawal
   Phys. Rev. C **2018**, 97, 045806-1−045806-16.

Communicated

1. "Structure effects on fission yields",
   Bharat Kumar, M. T. Senthil Kannan, M. Balasubramaniam, B. K. Agrawal, S. K. Patra, [Communicated to Int. J. Mod. Phys. E]*.

Conferences

1. **Talk:** "Analysis of parity doublet in medium mass nuclei",
   Bharat Kumar, S. K. Singh and S. K. Patra,
   Proceedings of the DAE Symp. on Nucl. Phys. **2014**, 59, 96-97.

2. **Poster:** "β-decay half-life of Th and U isotopes",
   Bharat Kumar, S. K. Biswal, S. K. Singh and S. K. Patra,
   Proceedings of the DAE Symp. on Nucl. Phys. **2015**, 60, 406-407.

3. **Poster:** "Evolution of N = 32,34 shell closure in relativistic mean field theory",
   Bharat Kumar, S. K. Biswal and S. K. Patra,
   Proceedings of the DAE-BRNS Symp. on Nucl. Phys. **2016**, 61, 196-197.

4. **Talk:** "Tidal effects in equal-mass binary neutron stars",
   Bharat Kumar,S. K. Biswal and S. K. Patra,
   Proceedings of the DAE-BRNS Symp. on Nucl. Phys. **2016**, 61, 868-869.

5. **Poster:** "Curvature of a neutron star",
   Bharat Kumar, S. K. Biswal and S. K. Patra,
   Proceedings of the DAE-BRNS Symp. on Nucl. Phys. **2016**, 61, 916-917.

6. **Poster:** "Search For Λ Shell Closures in Multi-Λ Hypernuclei",
   Asloob A. Rather, M. Ikram, M. Imran, **Bharat Kumar**, S. K. Biswal, S. K. Patra,
   Proceedings of the DAE-BRNS Symp. on Nucl. Phys. **2016**, 61, 178-179.

7. **Poster:** "Competition between α, β decay and Spontaneous Fission in Z=132 Superheavy Nuclei",
   Asloob A. Rather, M. Ikram, **Bharat Kumar**, S. K. Biswal,S. K. Patra
   Proceedings of the DAE-BRNS Symp. on Nucl. Phys. **2016**, 61, 202-203.

*A part of the paper will contribute to the thesis

8. **Poster:** "Effects of δ-meson on the maximum mass of the hyperon star",
   S. K. Biswal, **Bharat Kumar**, S. K. Patra,
   Proceedings of the DAE-BRNS Symp. on Nucl. Phys. **2016**, 61, 912-913.

9. **Poster:** "Effective relativistic mean field model for finite nuclei and neutron stars",
   Bharat Kumar, B. K. Agrawal and S. K. Patra,
   Proceedings of the DAE-BRNS Symp. on Nucl. Phys. **2017**, 62, 712-713.

10. **Invited talk:** "Tidal deformability of neutrons and hyperon star",
    Bharat Kumar and S. K. Patra,
    Proceedings of the DAE-BRNS Symp. on Nucl. Phys. **2017**, 62, 21-22.

(Bharat Kumar)

Dedicated To My Beloved My Mother, Uncle & Aunti Ji

ACKNOWLEDGMENTS

This thesis is no doubt the end of my journey in obtaining my Ph.D but it is the first dip in the holy ocean of intense knowledge which I wish to increase day by day through my work in nuclear physics as well as astrophysics. My thesis is proposed beautifully, shaped well, and put an end with the support and encouragement of numerous people including my supervisor, collaborators, friends, and family.

First of all, I would like to express my deep and sincere gratitude to my supervisor Prof. S. K. Patra for his guidance and all the useful discussions and continuous support over the past four years of my PhD research work at the Institute of Physics, Bhubaneswar. I greatly appreciate his patience to bear all my annoying behaviour and frequent arguments during our discussions. Through out my research work he taught me all the tit-bits by appreciating, encouraging and at times by his scoldings too which made me grow as an individual. He is solely responsible for all the positive outcomes of my papers as he fully supported me to have open discussions with researchers around the world. During the collaborative work, his faith in me and his open minded approach helped me in picking up new problems and approaching the right people. His rigorous and tight sessions at the preliminary days helped me in gaining the right momentum and his free and zero restrictions in the final year made me handle problems on my own. I feel very happy to have had the opportunity to work with such a wonderful advisor, and I look forward to our continued collaborations.

My special word of thanks should also go to Dr. Tanja Hinderer. She guided me very nicely the tidal deformability calculations via Skype while she was a postdoc in Max Plank Institute for Gravitational Physics, Germany. I thoroughly enjoyed the physics discussions with her and the learnings during the summer school at ICTS-TIFR, Bangalore. Her lecture has helped me a lot in understanding the basics and also in further calculations. Her help and friendly nature always made me feel at ease with her, and I feel privileged to be associated with a person like her during my PhD.

During my past years, I have collaborated with a fantastic group of people with whom I have discussed various aspects of the work presented here. I take this opportunity to express my deep sense of gratitude and respectful regards to Prof. B. K. Agrawal, for sharing knowledge and taking out his time to review, rectify and suggest on many of my papers. His ideas and concepts have a remarkable influence on my

entire work. It was my pleasure to work with him and I truly hope that I will be fortunate again to work with him in future. Also, I thank Dr. M. Balasubramaniam for his comments and suggestions on my paper.

I thank my senior Shailesh bhai for giving me the help I needed as a beginner. He is the person from whom I learnt the incorporation of ideas into a paper. I had really a good time with another senior of mine Subrat bhai, my best PhD mate, who never treated me as his junior. It was an enjoyable experience to work together in modifying the codes and working on problems. I thank Senthil for his active participations and for showing the enthusiasm to work together starting from the preliminary work to the end of our papers.

I would also like to extend a huge and warm thanks to Swagatika. She has been always beside me during the happy and hard moments to push me through her motivations, unconditional support and care for me. I thank her for the english corrections and suggestions in two manuscripts of mine. I thank Abdul for checking the derivations of the tidal deformability section and his valuable inputs in this thesis. It was indeed my pleasure to discuss physics with him. I would also like to take this opportunity to convey special thanks to Swagatika, Swati, Neha di, Shreyansh bhai, and Dr. P. Landry for carefully reading my thesis because of which I can see its present shape. Apart from this, I wish to thank my closest friends, Atul, Lakshmi, and Poonam for their moral support. Although, we devote less time together now a days as compared to the time spent in Jia Sarai Delhi but the sharing, bonding, affection and care is still intact in our hearts and will always be.

Last but not the least, this thesis would be meaningless if I do not mention the backbone of me, my mother. She is the most important person in my life. Facing all the hardships she single handedly managed my family and sacrificed everything for me and my siblings. She is the one whose strong will and determination towards life has given me the inspiration to work hard to the best of my capability. Also, my Uncle and Aunty need special attention as they are the ones who stood by me during my early struggling days and helped me financially, mentally and emotionally. They always treated me like their son and loved me immensely all these years. Without my Uncle's blessings and support I would not have dared to choose this field as my profession. After thanking my living gods; my mother, Uncle and Aunty, I thank the

almighty to have showered all the blessings and for providing me all the loving people around me whose support and love has made my world the most beautiful place to live in.

Contents

Synopsis

Nuclear physicists have been trying to understand systematically the nuclear systems ranging from finite nuclei to hot and dense nuclear matter within one theoretical framework. The nucleus is a many-body system constituting of strongly interacting and self-bound ensemble of protons and neutrons. Therefore, it becomes very difficult to describe the nucleus in a transparent way. One of the most successful and widely used methods is the relativistic field theory which takes into account the relativistic nucleons interacting with each other by exchanging mesons. The simplest approach of such a theory is the so-called relativistic mean field (RMF) approximation or quantum hadrodynamics that describes a nuclear system in the form of nucleonic Dirac field interacting with classical meson fields [1]. In this approach, a nuclear system is considered to be composed of relativistic nucleons whose self-energy is determined through meson fields which are generated by the nuclear density. It has also achieved great success in describing a variety of nuclear phenomena both in the low-density region and in the high-density region. At the high-density region, aLIGO/Virgo detectors and heavy ion colliders have significantly extended the window from which the nuclear matter and neutron star (NS) can be studied [2]. Such studies help in better understanding of the RMF model and also give new ideas to improve it further. Since it is a phenomenological model, its efficiency can be tested by comparing with the experiment. The purpose of this thesis is to study the implications of nuclear interaction for nuclear structure and astrophysics within the RMF model.

Since its discovery in 1896 by Becquerel, the α-decay has remained a powerful tool to study the nuclear structure. The α-decay theory was proposed by Gamow, Condon and Gurney in 1928. In simple quantum mechanical view α-decay is a quantum tunneling through the Coulomb barrier, which is forbidden by classical mechanics. The α-decay is not the only decay mode found in the heavy nuclei, we can also find other exotic decay modes like β-decay, spontaneous fission and *cluster*-decay. In *cluster*-decay, smaller nuclei like ^{16}O, ^{12}C, ^{20}Ne [3] and many other nuclei get emitted from a bigger nucleus. In the superheavy region of the nuclear chart, the prominent modes are the α-decay and spontaneous fission along the β-stability line. In fission, the nucleus splits, either through radioactive decay or bombardment of subatomic

particles like neutron. Moreover, the center of a heavy element spontaneously emits a charged particle as it breaks down into smaller nucleus. But it does not occur often, and happens only with the heavier elements like Uranium or Plutonium. Being thermally fissile nature, the two Uranium isotopes ^{233}U and ^{235}U, and one Plutonium isotope ^{239}Pu in the actinide region are suitable for energy production. Among these three radioactive isotopes, ^{235}U is the most important one for production of both nuclear power and nuclear bombs because ^{235}U is readily or more easily fissioned by the absorption of a neutron of low energy ($<$ 1 eV) which is also available on earth crust. In chapter 3, we examine if heavier neutron-rich isotopes of $^{216-250}$Th and $^{216-256}$U could exist having thermally fissile properties and if so what would be their stability and fission decay properties [4]. The potential energy surface (PES) calculation is employed which is based on the self-consistent Hartree approach. For this purpose, we use the so-called quadrupole constrained calculation. The solution without constraint will lead to one of the spherical or deformation minimum, but one can never get a potential curve. To calculate the complete PES curve, instead of minimizing the original Hamiltonian, one has to minimize the following constraint Hamiltonian H', defined as:

$$< H' >=< H - \lambda Q >, \tag{0.1}$$

where λ is the Lagrangian multiplier, which can be adjusted in such a way that the final deformation calculated from quadrupole $< Q >$ is β_2. Here, quadrupole deformation will always have the same angular dependence, *i e.*, spherical harmonics $Y_{20}(\theta, \phi)$. With the help of PES, we determine the fission barrier height which is the difference between the ground state and the highest saddle point. The higher the fission barrier, the longer is the fission lifetime. Further, the half-lives against the α decay of thermally fissile nuclei are obtained with a phenomenological formula of Viola and Seaborg, and also by using a quantum mechanical approach known as WKB method. A neutron-rich nucleus such as ^{254}U is stable against α decay and spontaneous fission, because the presence of a large number of neutrons makes the fission barrier broader. Thus, we can test the β decay lifetime to determine the stability of such types of nuclei.

Mass distribution of the fission fragments is one of the crucial characteristics in the

study of fission theory. Fong [5] has proposed a statistical theory to study asymmetric mass division of fission fragments. This theory says that the relative fission probability is equal to the product of densities of quantum states of the fissioning nuclei at the scission point. For the first time, we apply the temperature dependent relativistic mean-field model (TRMF) to study the binary mass distributions for recently predicted thermally fissile nuclei ^{250}U and ^{254}Th using level density approach [6]. The probability of yields of a particular fragment is obtained within the statistical theory with the inputs from TRMF like excitation energies and level density parameters for the fission fragments at a given temperature. The inclusion of temperature dependent BCS pairing is discussed in chapter 2, and the level density parameter and its relation with the relative mass yield is given in chapter 4.

After discussing the properties of neutron-rich thermally fissile nuclei, we shift our focus towards the NS properties, which is a highly neutron-rich system of the order of 10^{57} neutrons. Nuclear physicists have tried to derive an "equation of state" (EoS) that describes dense nuclear matter which is found inside a NS. Using the EoS of RMF model, the Tolman-Oppenheimer- Volkof (TOV) equation is solved to compute the structure of the NS. The study of Love numbers in Newtonian theory dates back 100 years by famous mathematician A. E. H. Love. In 2008, Flanagan and Hinderer proposed the gravitational wave phasing explicitly in terms of the tidal Love number in general relativity, which was recently confirmed by Earth-based gravitational waves (GWs) detectors such as Advanced LIGO, and Virgo [7]. The concept of the tides created between the NS is as follows: In NS-NS binary, the orbital motion causes the emission of GWs. As a result, there is removal of energy and angular momentum from the system, which make the orbits to decrease in radius and increase in frequency. Thus, there is the inspiraling motion of the compact bodies. After that, the GWs enter the frequency band in the inspiral and we get a clear picture of the shape and phasing of the waves. When the stars have larger orbital separation the tidal interaction between binary is negligible, and gravitational frequency is also low because NSs bodies behave as point masses at larger separation. When the star orbits get closer and closer, the orbital frequency increases sufficiently and the influence of the tidal interaction becomes significant. Finally, bodies get a tidal deformation thus influencing the shape of the bodies and phasing of the GWs. In chapter 5, we have calculated

various tidal Love numbers of the neutron and hyperon stars such as k_2, k_3, k_4, where the RMF EoSs have been imported from the hadronic and hyperonic nuclear matter under the β-equilibrium conditions [8]. Apart from these Love numbers, we have also reported the shape Love numbers and magnetic Love numbers of the stars.

In the literature near about 263 RMF force parameter sets are available, which determine the nuclear matter properties around the saturation density [9]. It is found that only 7-8% models satisfy all the experimental and empirical data. So, we need such type of models which can satisfy not only the nuclear matter experimental constraints but also the bulk properties of the finite nuclei. In addition, we can also test for EoS that comes from the observation of the NS mass. The Lagrangian of the G2 parameter set contains most of the self and cross-couplings which give better results not only for the finite nuclei but also for the nuclear matter systems. Still, the G2 model needs some corrections to get more reliable and better results. We have added the extra degrees of freedom *i.e.,* isovector scalar δ meson and the cross-coupling of ρ mesons to the σ and ω mesons to make the Lagrangian more proficient. The contribution of the δ meson is to take care of the large asymmetry of the system. Also, δ meson results in a stiff EoS at high densities due to the increased ρ meson nucleon coupling in order to reproduce the empirical symmetry energy at the nuclear saturation density. However, recent experimental results seem to suggest the need of an EoS softer even than those of most nonlinear RMF models without the inclusion of the δ meson. For finite nuclei, the inclusion of the δ meson can improve the description of bulk properties of finite nuclei, in particular at the drip lines where due to the large isospin asymmetry its contribution might be appreciable. The contribution of the δ meson might also be examined by analyzing the isovector part of the spin-orbit interaction. The $\omega - \rho$ cross-coupling plays a crucial role to modify the neutron-skin thickness of finite nuclei and the density-dependent symmetry energy of the nuclear matter at saturation density. Therefore, we have also tried to search for a suitable parameter set to reproduce all the experimental and empirical constraints. We have implemented the simulated annealing method to the problem of searching for global minimum in the hyperspace of the χ^2 function, which depends on the values of the parameters of a Lagrangian density of the extended RMF model. The set of experimental data used in our fitting procedure include the binding energy and

charge radii of the 8 spherical nuclei, ranging from lighter nuclei to heavy ones. While fitting, we have also included the binding energy per particle and symmetry energy at saturation density. Finally, we got new extended RMF parameter sets named as G3, and IOPB-I, which are applicable for finite nuclei, infinite nuclear matter, and neutron stars [9]. In chapter 6, we have discussed more about the G3 and IOPB-I parameter sets.

Bibliography

[1] J. D. Walecka, Ann. Phys. **83**, 491 (1974).

[2] P. B. Abbott *et al.*, Phys. Rev. Lett. **119**, 161101 (2017).

[3] B. K. Sharma, P. Arumugam, S. K. Patra, P. D. Stevenson, R. K. Gupta and W. Greiner, J. Phys. G. **32**, L1 (2006).

[4] Bharat Kumar, S. K. Biswal, S. K. Singh and S. K. Patra, Phys. Rev. C **92**, 054314 (2015).

[5] P. Fong, Phys. Rev. **102**, 434 (1956)

[6] Bharat Kumar, M. T. Senthil Kannan, M. Balasubramaniam, B. K. Agrawal, S. K. Patra, Phys. Rev. C **96**, 034623 (2017).

[7] *É.É.* Flanagan and T. Hinderer, Phys. Rev. D **77**, 021502 (2008).

[8] Bharat Kumar, S. K. Biswal and S. K. Patra, Phys. Rev. C **95**, 015801 (2017).

[9] M. Dutra *et al.*, Phys. Rev. C **90**, 055203 (2014)

[10] Bharat Kumar, S. K. Patra, and B. K. Agrawal, Phys. Rev. C **97**, 045806 (2018).

List of Figures

List of Tables

Chapter 1

Introduction

In 1911, Rutherford and his collaborators discovered nucleus from the famous gold-foil scattering experiment. This experiment suggested that mass of the atom is concentrated at the center of the atom known as nucleus. After that, it was known that the atomic mass number A of a nucleus is a bit more than twice the atomic number Z. Since then, many years have passed in pursuit of understanding the structure of the nucleus. Interestingly, Landau published a seminal paper in 1932 where he showed that the *"density of matter becomes so great that atomic nuclei come in contact, forming one gigantic nucleus" [1].* This paper of Landau marked the first theoretical speculation on the existence of neutron stars(NS). As proposed by Landau with his theory, a complete picture of the internal configuration of the nucleus in the form of experimental backing came up with the discovery of the neutron in 1932 when J. Chadwick used scattering data to calculate the mass of this neutral particle [2]. At that time, the nature of nucleon-nucleon interaction was not known because of its charge independent nuclear force. In 1935, Yukawa explained the nature of nuclear force and suggested that the massive bosons(mesons) mediate the interaction between nucleons [3]. He found theoretically that the $\pi-$meson mass is nearly 140 MeV, which provides an explanation for the residual strong force between nucleons. The muon has a mass of 105.7 MeV and does not participate in the strong nuclear interaction, which was found in 1937 experimentally in cosmic radiation and interpreted as a particle as suggested by Yukawa. But, Yukawa was not satisfied with this finding. Finally, a landmark progress was achieved in 1947 by a team led by the English physicist C. F.

Powell with the discovery of the $\pi-$meson in cosmic-ray particle interaction in Berkeley. Soon after, the heavier mesons ω, ρ and δ were found in different laboratories, which cover the nature of strong interaction [4]. Therefore, the concept of immensely strong nuclear force that binds nucleons came into picture, which is why the nuclear process is able to release a tremendous amount of energy—such as the thermonuclear fusion reaction that happen in the sun to produce virtually all elements in a process known as *nucleosynthesis*.

Later, a large number of phenomena and properties of nuclei came to be known, but many of them lacked in clarity. Nuclear fission is one of the most important discoveries in nuclear physics by Otto Hahn and Strassmann and subsequently, the chain reaction by E. Fermi led the foundation of energy production from the nucleus. The phenomenon of nuclear fission is a very complex process producing a huge amount of energy when heavy elements like uranium and thorium are irradiated with slow neutrons. The theory of fission process was first given by Meitner in 1939 [5]. In this process, a parent nucleus goes from the ground state to scission point through a deformation and then splits into two daughter nuclei. This decay process can be described as an interplay between the nuclear surface energy coming from the strong interaction and the Coulomb repulsion [6].

In this dissertation, we have addressed the answers related to the following questions as highlighted in the 2007 Nuclear Science Long Range Plan [7]:

1. *What is the nature of the nuclear force that binds protons and neutrons into stable nuclei and rare isotopes?*

2. *What is the next possibility of thermally fissile neutron-rich nuclei?*

3. *What is the nature of neutron stars and dense nuclear matter?*

Theoretically, the above raised questions can be answered with the help of various experimental work as follows:

(i) The study of very neutron-rich nuclei at and beyond the drip-line employing state-of-the art experimental techniques at leading facilities worldwide—such as new radioactive ion beam facilities HIFR at CSR [8, 9], FAIR at GSI [10, 11], Spiral at GANIL [12], RIBF at RIKEN [13] and FRIB at MSU [14], respectively. One of

the primary goals of the above mentioned research facilities on fission barrier and also in the production of neutron-rich heavy elements is to allow the study of their lifetimes and decays. To have a better understanding on the diversity of elements, the nuclear landscape is displayed in Fig. 1.1 [15]. The straight red dotted line shows the N=Z stable light nuclei. The red lines show the magic numbers. The black squares represent 255 stable nuclei existing in nature and their half-lives comparable to or longer than the age of the Earth. The stable nuclei are surrounded by the yellow area which represents a total of 3225 unstable nuclei, already synthesized in different laboratories in the world. The various theoretical models suggest that another 5000 isotopes depicting the green area comprises the unknown proton and neutron-rich regions that can be explored experimentally in the near future.

(ii) The equation of state (EoS) describes the complex behavior of the dense

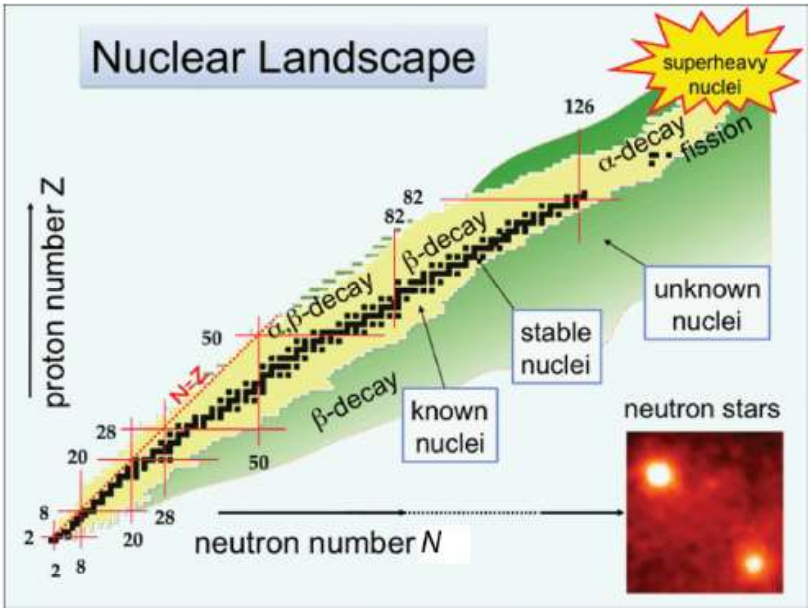

Figure 1.1: Nuclear landscape [15]: the black squares represent stable plus very long-lived nuclei that define the valley of stability. The yellow region assigns the range of unstable nuclei that have been explored by reactions employing stable nuclei by addition or removal of neutrons or protons. Many thousands of radioactive nuclei far from the valley of stability remain to be explored; this "terra incognito" is indicated in green.

nuclear matter that makes up neutron stars, which is difficult to extract from general X-ray astronomy. However, in August 2017, the Advanced Laser Interferometer Gravitational-Wave Observatory (aLIGO) and Virgo detectors made the first-ever observation of gravitational waves generated by the merger of two neutron stars [16]. This observation provides new insights on the properties of neutron stars, such as its mass and "tidal deformability"—the stiffness of a star in response to the forces caused by its companion's gravitational field. This observation has helped to decode many puzzling questions relating to the nature of dense matter, on the synthesis of the heavy elements, and to test gravity in the highly-relativistic or supranuclear-density regime [16].

1.1 Effective Mean-Field Theory

At present, nuclear physics and nuclear astrophysics are well described within the self-consistent effective mean-field models [17]. These effective theories are not only

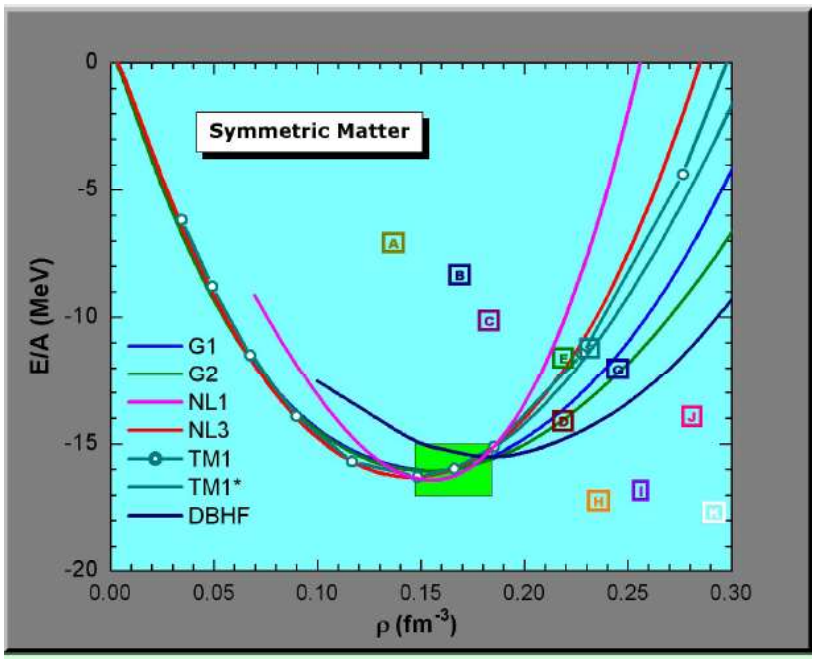

Figure 1.2: Binding energy (E/A) in MeV for symmetric nuclear matter as a function of density. The squares represent various non-relativistic models, solid lines represent the relativistic models, and the green box represents the empirical data.

successful to describe the properties of finite nuclei but also explain the nuclear matter at supranormal densities [18]. Recently, large number of nuclear phenomena are predicted near the nuclear drip lines within the relativistic and non-relativistic formalisms [19–21]. Consequently, several experiments are planned in various laboratories to probe the deeper side of the unknown nuclear territories, *i.e.*, the neutron and proton drip lines. Among the effective theories, the relativistic mean-field (RMF) model is one of the most successful self-consistent formalisms, that is currently drawing attention to the theoretical studies of such systems.

Although the construction of the energy density functional for the RMF model is different than those for the non-relativistic models, such as Skyrme [22, 23] and Gogny interactions [24], the obtained results for finite nuclei are in general very close to each other. The same accuracy in prediction is also valid for the properties of the neutron stars. At higher densities, the relativistic effects are accounted appropriately within the RMF model [25]. In the RMF model the interactions among nucleons are described through the exchange of mesons. These mesons are collectively taken as effective fields and denoted by classical numbers. In brief, the RMF formalism is the relativistic Hartree or Hartree-Fock approximation to the one-boson exchange (OBE) theory of nuclear interactions. In OBE theory, the nucleons interact with each other by exchange of isovector π, ρ, and δ mesons and isoscalars like η, and ω mesons. The π, and η mesons are pseudo-scalar in nature and do not obey the ground-state parity symmetry. At the mean-field level, they do not contribute to the ground-state properties of even nuclei.

The first and simplest successful relativistic Lagrangian is formed by taking only the contribution of the σ, ω and ρ mesons into account without any nonlinear term for the Lagrangian density [25]. This model predicts an unreasonably large incompressibility K of $\sim$ 550 MeV for the infinite nuclear matter at saturation [25]. To lower the value of K to an acceptable range, the self-coupling terms in the σ meson are included by Boguta and Bodmer [26]. Based on this Lagrangian density, a large number of parameter sets, such as NL1 [27], NL2 [27], NL-SH [28], NL3 [29] and NL3* [30] are calibrated. The addition of σ meson self-couplings improve the quality of finite nuclei properties and incompressibility remarkably. However, the equation of states at supranormal densities are quite stiff. Thus, the addition of vector meson

self-coupling is introduced into the Lagrangian density and different parameter sets are constructed [31–33]. These parameter sets are able to explain the finite nuclei and nuclear matter properties to a great extent, but the existence of the Coester band as well as the three-body effects need to be addressed. Fig. 1.2 depicts the binding energy per nucleon as a function of baryon density calculated by different relativistic and non-relativistic models for symmetric nuclear matter (SNM). It is noticed [34] that the EoS calculated by non-relativistic model do not reach to the Coester-band or empirical saturation point of SNM ($E/A \simeq -16.0$ MeV at $\rho_0 \simeq 0.16$ fm^{-3}). At higher density regime, all the models are showing different nature, which is used for the NS matter and hence questions the reliability of these models. Subsequently, nuclear physicists also changed their way of thinking and introduced different strategies to improve the result by designing the density-dependent coupling constants and effective-field-theory motivated relativistic mean field (ERMF) model [17, 35].

Further, motivated by the effective field theory, Furnstahl *et al.* [17] used all possible couplings up to fourth order of the expansion, exploiting the naive dimensional analysis (NDA) and naturalness, and obtained the G1 and G2 parameter sets. In the Lagrangian density, they considered only the contributions of the isoscalar-isovector cross-coupling, which has a greater implication for the neutron radius and EoS of asymmetric nuclear matter [36]. Later on it is realized that the contributions of δ mesons are also needed to explain certain properties of nuclear phenomena in extreme conditions [37, 38]. Though the contributions of the δ mesons to the bulk properties are nominal in the normal nuclear matter, the effects are significant for highly asymmetric dense nuclear matter. The δ meson splits the effective masses of proton and neutron, which influences the production of $K^{+,-}$ and π^+/π^- in the heavy-ion collision (HIC) [39]. Also, it increases the proton fraction in the β-stable matter and modifies the transport properties of the neutron star and heavy-ion reactions [40–42]. The source terms for both the ρ and δ mesons contain isospin density, but their origins are different. The ρ meson arises from the asymmetry in the number density and the evolution of the δ meson is from the mass asymmetry of the nucleons. The inclusion of δ mesons could influence the certain physical observables like neutron-skin thickness, isotopic shift, two neutron separation energy S_{2n}, symmetry energy $S(\rho)$, giant dipole resonance, and effective mass of the nucleons, which are correlated with the isovector

channel of the interaction. The density dependence of symmetry energy is strongly correlated with the neutron-skin thickness in heavy nuclei, but until now experiments have not fixed the accurate value of the neutron radius, which is under consideration for verification in parity-violating electron-nucleus scattering experiments [35, 43].

Inspired by all the previous parameter sets we too tried to search for a suitable one devoid of the shortcomings mentioned earlier and we finally developed new parameter sets G3 and IOPB-I for finite and infinite nuclear matter, and neutron stars system within the effective field theory motivated RMF theory. The Lagrangian of the G3 set includes all the necessary terms such as $\omega - \rho$, and $\sigma - \rho$ cross-couplings, and also δ meson. These cross-couplings modified the nature of the neutron skin-thickness for finite nuclei as well as the density-dependent symmetry energy and also constrains the equation of state of the pure neutron matter. The detailed analysis of the role of each term in the Lagrangian of the G3 and IOPB-I sets will be discussed in the next chapter 2. Till there is some discrepancy of the RMF models, which will discuss in the next subsection.

1.1.1 Limitations of the model

It is important to mention a few points about the limitations of the present approach which are as follows:

(1) In RMF formalism we work in the mean-field approximation of the meson field. In this approximation, we neglect the vacuum fluctuation, which is an indispensable part of the relativistic formalism. While calculating the nucleonic dynamics, we neglect the negative energy solution which means we work in the no sea approximation [44]. It has been discussed that the no-sea approximation and quantum fluctuation can improve the results upto a maximum of 20% for very light nuclei [45]. Therefore, the mean-field is not a preferable approach for the light region of the periodic table. However, for the heavy masses, this mean-field approach is quite good and can be used for any practical purpose.

(2) In order to solve the nuclear many-body system, here we use the Hartee formalism and neglect Fock term, which corresponds to the exchange correlation.

(3) To take care of the pairing correlation, we use a BCS-type pairing approach. This gives good results for the nuclei near the β-stability line, but it fails to incorporate properly the pairing correlation for the nuclei away from the β-stability line and superheavy nuclei [46]. Thus, a better approach like Hartree-Fock-Bogoliubov type pairing correlation is more suitable for the present region [47, 48].

(4) Parametrization plays an important role in improvising the results. The constants in RMF parametrizations are determined by fixing the experimental data for few spherical nuclei. We expect that the results may be improved by refitting the force parameters for more number of nuclei, including the deformed isotopes.

(5) The basic assumption in the RMF theory is that two nucleons interact with each other through the exchange of various mesons. There is no direct inclusion of three-body or higher effects. This effect is taken care of partially by including the self-coupling of mesons, and in recent relativistic approach various cross-couplings are added because of their importance.

(6) Although, there are various mesons observed experimentally, few of them are taken into consideration in the nucleon-nucleon interaction. The contribution of some of them are prohibited for symmetry reason and many are neglected due to their negligible contributions, because of their heavy mass. However, some of them has substantial contribution to the properties of nuclei, especially when the neutron-proton asymmetry is greater, such as δ meson [37, 49].

With this, we move on to the following section to introduce the applications related to RMF theory.

1.2 Nuclear fission

The process of nuclear fission gives rise to many puzzles and complexities, it has also proved to be successful in answering many questions of the nuclear phenomena. But a complete theoretical explanation is still not at hand. Initially, after the discovery of nuclear fission N. Bohr and J. Wheeler suggested a theoretical explanation by

liquid drop model (LDM) of atomic nuclei [6]. A fissile nucleus is treated as an incompressible liquid drop. These drops are uniformly distributed electric charge over the volume of a nucleus. The qualitative description of the dependence of the potential energy surface on the arbitrary deformation is shown in figure 1.3. The dashed line represents a potential energy surface due to the charged liquid drop. In this process, the fissioning nucleus goes through a number of intermediate states, and then liquid drops break up into two smaller droplets at scission point. Although, the LDM very well explain the general properties for the actinide nuclei, but it is found that all nuclei in the ground state show spherical shape. So, it is unable to explain the asymmetric mass division of the fission fragments which is described by Strutinsky in his method of "shell corrections" [50]. The solid line represents the inclusion of liquid drop energy with shell correction energy. The ground state (I), first barrier (E_f^A), second minimum (II), and the second barrier (E_f^B) are marked. The single-particle energy of the nucleons are affected by the shell correction as marked on the position I and II in figure 1.3. The gaps in the single-particle spectra have given additional binding to the nucleus which lower the ground state with respect to the liquid drop energy. Therefore, it create a barrier against fission. The height of the fission barrier (E_f^B) is calculated by taking the difference between the saddle and the ground state

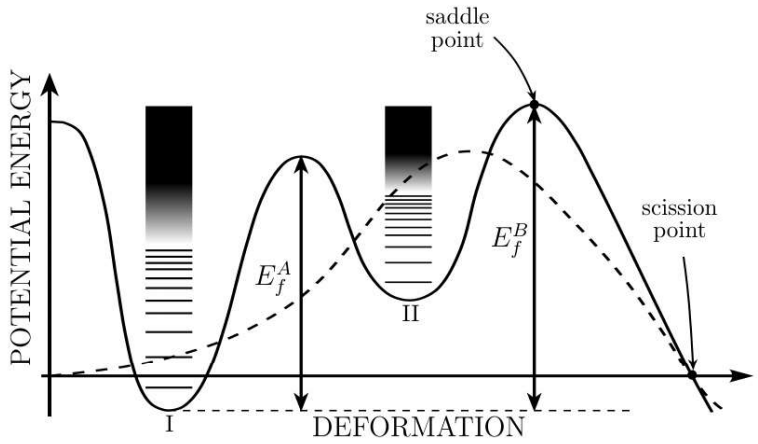

Figure 1.3: Potential energy surface as a function of deformation parameter. The solid line of the fission barrier with "shell correction". A dashed line represents the liquid drop fission barrier. The figure is taken from Ref. [51].

energies. The existence of the more massive nuclei is found on the saddle point, which makes it quite an exciting and valuable quantity to study. Nowadays, many modern approaches of using phenomenological nuclear-energy density functionals have come up to obtain nuclear ground-state properties in a self-consistent way. The construction of potential energy surface as a function of deformation parameter is calculated using the Lagrange multiplier to the Hamiltonin and minimize it.

The study of fission mass distribution is one of the major insights of the fission process. Conventionally, there are two different approaches, the statistical and the dynamical approaches for the study of fission process [52,53]. The latter is a collective calculations of the potential energy surface and the mass asymmetry. Further, the fission fragments are determined either as the minimum in the potential energy surface or by the maximum in the WKB penetration probability integral for the fission fragments. In statistical theory [53], the relative probability of the fission process depends on the density of the quantum states of the fragments at scission point. The mass and the charge distribution of the binary and the ternary fission is studied using the single particle energies of the finite range droplet model (FRDM) [54, 55]. In FRDM [56] formalism, the energy at a given temperature is calculated using the relation $E(T) = \sum_i n_i \epsilon_i$ with n_i and ϵ_i, the Fermi-distribution function and the single-particle energy corresponding to the ground state deformation [55]. The temperature dependence of the deformations of the fission fragments and the contributions of the pairing correlations are ignored. But the self-consistent temperature dependent RMF theory is taken care by the quantity as stated above.

1.3 GW170817:Tidal deformability of neutron stars

The neutron star is a tiny and compact object in the universe, which is formed after a core-collapse supernovae explosion. The mass of a NS is precisely measured from the observation of binary pulsar system, and its mass is observed to be as large as of $2M_\odot$ [57, 58]. The size of a $1.4M_\odot$ NS is about 10 km (or more), and has a central density ρ_c as high as 5 to 10 times larger than the density of normal nuclei $\rho_{nuc} = 2.8\times10^{14}$ g/cm^3 [59]. Therefore, the NS is one of the densest forms of matter in the universe. The nature and composition of such ultra-dense matter have remained

an essential question in the nuclear physics. At higher density ($2.0 \gtrsim \rho/\rho_0 \gtrsim 15.0$), various possibilities predict the emergence of new phases of matter, condensates of particles such as hyperons, kaons, etc.—which actively depend on the theoretical models. The structure of NS sensitively depends on the nuclear EoS. The star mass-radius plot is shown in Fig. 1.4, which is the solution of Tolman-Oppenheimer-Volkoff (TOV) equation, where energy density and pressure are the inputs [60]. A stiff (or hard) EoS tends to have larger pressure gradient for a given density. Such an EoS would be harder to compress and offers more support against gravity. Conversely, a soft EoS has smaller pressures gradient, and is more easily compressed. The figure shows that stars calculated with a stiffer EoS yield greater maximum masses and larger radii than stars derived from softer EoS. For example, the MS1 and MS1b EoSs suggest larger and massive NS [61].

In 1974, Russell Hulse and Joseph Taylor discovered the first binary neutron star system (BNS) called as PSR 1913+16. The most exciting measurement in this system is the observation which revealed that BNS orbiting towards each other and were also shrinking at a rate of 10 mm per year. This shrinkage is caused by the loss of orbital energy due to gravitational radiation [62]. The measurements provided the first proof that such waves exist. Fig. 1.5 is the graphical representation of the gravitational

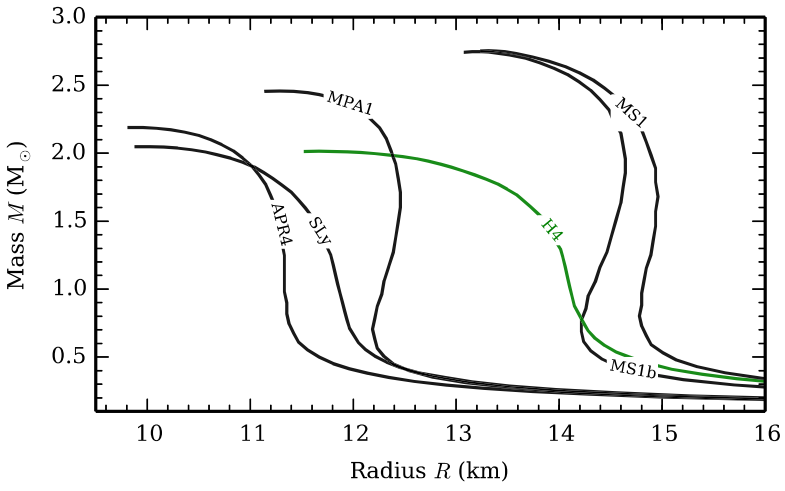

Figure 1.4: The mass-radius plot for the neutron (black curve) and hyperon (green curve) stars [61].

waves produced by the BNS [63]. In this process, two stars rotate about a common center of mass. As they rotate, they send gravitational waves and in the process, the orbits lose energy and get closer and closer, which is called inspiralling. As they get closer they send off more gravitational waves and gets even closer, eventually colliding with each other. Just before the merger, the star get tidally disturbed by external tidal field because of the other companion star—which produces a small correction in the phase of the gravitational waves. The inspiral phase of a NS-NS merger creates an extremely strong tidal gravitational field that deform the multipolar structure of the stars. This effect can be specified in terms of the so-called tidal deformability λ of the stars (or tidal Love number, which gives the information about the internal structure of the NS) [64–66].

The Love numbers directly affect the size of tidal bulging on bodies which occur due to the non-uniform external gravitational field. To explain this we take the case of Sun and Earth where Sun is considered as a point mass. It has been observed that the gravitational field of the Sun is strongest on that side of the Earth which is much close to the Sun than the other side. As a result of which there is relative acceleration leading to the quadrupole deformation as viewed in the Earth's center-of-mass frame. Thus the overall result is the formation of the two high tides per day at a given point on Earth.

Placing a spherical star in a static external quadrupolar tidal field $\mathcal{E}_{ij}$ results in deformation of the star along with quadrupole deformation, which is the leading order

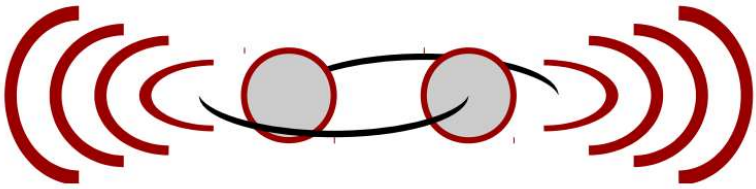

Figure 1.5: The schematic representation of the gravitational waves produced by the inspiral of compact bodies in a binary neutron stars system. The figure is taken from Ref. [63].

perturbation. Such a deformation is measured by [64, 66]

$$\lambda = -\frac{Q_{ij}}{\mathcal{E}_{ij}} = \frac{2}{3} k_2 R^5 \ , \tag{1.1}$$

$$\Lambda = \frac{2k_2}{3C^5}, \tag{1.2}$$

where Q_{ij} is the induced quadrupole moment of a star in binary, and $\mathcal{E}_{ij}$ is the static external quadrupole tidal field of the companion star. λ is the tidal deformability parameter depending on the EoS via both the NS radius and a dimensionless quantity k_2, called the second Love number [65, 66]. Λ is the dimensionless version of λ, and C is the compactness parameter ($C = M/R$). However, in general relativity we have to distinguish k_2 between gravitational fields generated by masses (electric type), and those generated by the motion of masses, i.e., mass currents (magnetic type) that has no analogue in Newtonian gravity [67, 68]. Equation (1.1) indicates that λ

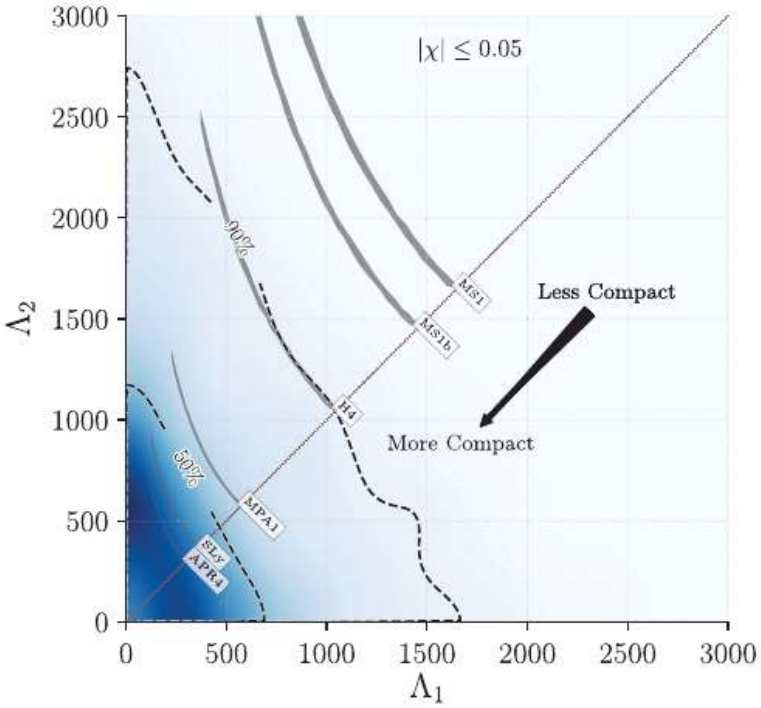

Figure 1.6: The plot for the tidal deformability of binary neutron stars for the low-spin prior as given in Fig. 5 of GW170817 [16]. The dashed line represents the 90% and 50% confidence limit. The diagonal dashed line marked the $\Lambda_1 = \Lambda_2$ boundary.

strongly depends on the radius of the NS as well as on the value of k_2. Moreover, k_2 depends on the internal structure of the constituent body and directly enters into the gravitational wave phase of inspiraling BNS which in turn conveys information about the EoS. As the radii of the NS increases, the deformation by the external field becomes large as there will be an increase in gravitational gradient with the simultaneous increase in radius. In other words, stiff (soft) EoS yields large (small) deformation in the BNS system. Since the force of attraction between stars becomes more and more important in the course of time, because of the reduction of the orbital distance between them. The orbital distance between the binary decreases as the companion star emits gravitational radiation. As a result, the binary accelerates and finally merges with each other and possibly turns to a black hole. Before the merger, the estimation of the leading order quadrupole electric tidal Love number k_2 along with other higher order Love numbers k_3 and k_4 are very important for the detection of gravitational wave.

Recently, advanced LIGO and Virgo detectors informed first time the direct detection of gravitational waves from inspiralling NS-NS binary, which is referred as GW170817 [16]. The chirp mass of binary is found to be $1.188^{+0.004}_{-0.002} M_{\odot}$ for the 90% credible intervals, which is precisely measured from data analysis of GW170817. The dimensionless tidal deformabilities Λ_1 and Λ_2 with 90% and 50% confidence limit are shown in Fig. 1.6, that obtained for two stars in the BNS merger observed by GW170817. The measurement is reported in the form of a limit given for the average dimensionless tidal deformability[1] $\tilde{\Lambda} \leq 800$ for low-spin prior 1.6. According to GW170817, the stiffer EoSs are ruled out such as MS1, and MS1b, respectively.

1.4 Plan of the thesis

The main aim of this thesis is to study the implications of nuclear interaction for nuclear structure and astrophysics within the RMF model. Also, we extend the version of RMF models which is successful in the finite and infinite nuclear matter regime.

The thesis is organized as follows. After the introduction, we outline the ERMF

[*]The definition of the dimensionless tidal deformability $\tilde{\Lambda}$ is given by Eq. (6.7).

Lagrangian including $\omega - \rho$ cross-coupling and δ meson in chapter 2. The equation of motion of the fields are derived for different fields $\phi, \sigma, \omega, \rho, \delta$, and electromagnetic field. The temperature dependent BCS and Quasi-BCS pairing correlation for the open shell nuclei are also discussed in this chapter. I would outline briefly the EoS for infinite nuclear matter and its properties. These derivations are the building blocks of different calculations presented in the forthcoming chapters.

In chapter 3, we use the axially deformed RMF formalism to calculate the bulk properties of the thermally fissile nuclei including the potential energy surface and single-particle energy levels. For this purpose, we describe the selection of the basis space for exotic nuclei which require a large model space to get a proper convergence solution of the system. Finally, various decay modes are calculated using either empirical formula or by using the well-known double folding formalism with M3Y nucleon-nucleon potential.

In chapter 4, we use the temperature-dependent axially deformed RMF formalism. To calculate the total binding energy of the system, we use the axially symmetric harmonic oscillator basis space for Fermion and Boson. The excitation energy, the level density parameter, and inverse level density parameters are calculated within the TRMF formalism. The relative mass distributions of neutron-rich thermally fissile nuclei ^{254}Th and ^{250}U are studied using a statistical model. The calculated results are compared with the finite range droplet models (FRDM) predictions.

The Newtonian and relativistic tidal Love number mathematical derivations are given in the chapter 5. In particular,we will derive the important expression for the various tidal Love numbers, average tidal deformability, orbital frequency, gravitational energy flux, orbital decay and gravitational wave phase of the binary neutron star. Next, we discuss the state of matter in neutron and hyperon star by using the condition of hydrostatic beta equilibrium. Then we present the mass-radius results with the help of famous TOV equation. The various tidal Love numbers and tidal deformability of neutron and hyperon stars are calculated. The cut-off frequency of the neutron and hyperon stars are also discuss in this chapter. Throughout the thesis, we have taken the value of $G = c = 1$.

In chapter 6, following the derivation in chapter 2 of binding energy, charge radius, and analytical expression for the symmetry energy and incompressibility coefficient of

the symmetric nuclear matter at saturation we discuss the strategy of the parameter fitting using the simulated annealing method in chapter 6. After getting the new parameter sets G3, and IOPB-I, the results on binding energy, two-neutron separation energy, isotopic shift, and neutron-skin thickness of finite nuclei are discussed thoroughly. The mass-radius and tidal deformability of neutron star obtained by new parameter sets are also discussed in chapter 6.

Finally,the summary and concluding remarks are given in chapter 7.

Chapter 2

Relativistic mean-field theory

Quantum hadrodynamics is a quantum field theory where nucleons and mesons are treated as elementary degrees of freedom. The credit for origin of relativistic nuclear model goes to the work of Düerr [69] who revised the non-relativistic field theoretical nuclear model of Johnson and Teller [70], and was re-introduced by Green and Miller in [71]. Finally, the simple $\sigma - \omega$ model was introduced by J. D. Walecka in 1974, who mentioned the main features of the nucleon-nucleon interaction [25]. This model has been renormalizable. Unfortunately, renormalizable has encountered difficulties due to substantial effects from loop integrals that incorporate the dynamics of the quantum vacuum. The effective theory is an alternative. In this chapter, we first added the isovector part into the effective Lagrangian in which the coupling of nucleons to the δ and ρ mesons and the cross-coupling of the ρ mesons to the σ and ω mesons along with their interactions to σ, ω, and ρ mesons are included. Then, we have explained how to use it to compute ground-state properties of finite nuclei. Next, we will discuss the pairing correlations for open-shell nuclei. Finally, we move to the discussion related to the equation of states for an infinite nuclear matter, which is very important nowadays after the detection of gravitational waves from binary neutron stars.

2.1 Energy density functional and equations of motion

The beauty of an effective Lagrangian is that one can ignore the basic difficulties of the formalism, like renormalization and divergence of the system [17]. The model can be used directly by fitting the coupling constants and some masses of the mesons. The ERMF Lagrangian has an infinite number of terms with all types of self- and cross-couplings. It is necessary to develop a truncation procedure for practical use. Generally, the meson fields constructed in the Lagrangian are smaller than the mass of the nucleon. Their ratio could be used as a truncation scheme as is done in Refs. [17, 19, 72, 73] along with the NDA and naturalness properties. The basic nucleon-meson ERMF Lagrangian (with δ meson, WR) up to fourth order with exchange mesons like σ, ω, ρ mesons and photon A is given as [17, 49]:

$$
\begin{aligned}
\mathcal{E}(r) \;=\; & \sum_{\alpha}\varphi_{\alpha}^{\dagger}(r)\Bigg\{-i\boldsymbol{\alpha}\cdot\boldsymbol{\nabla}+\beta\left[M-\Phi(r)-\tau_3 D(r)\right]+W(r)+\frac{1}{2}\tau_3 R(r)+\frac{1+\tau_3}{2}A(r) \\
& -\frac{i\beta\boldsymbol{\alpha}}{2M}\cdot\left(f_{\omega}\boldsymbol{\nabla}W(r)+\frac{1}{2}f_{\rho}\tau_3\boldsymbol{\nabla}R(r)\right)\Bigg\}\varphi_{\alpha}(r)+\left(\frac{1}{2}+\frac{\kappa_3}{3!}\frac{\Phi(r)}{M}+\frac{\kappa_4}{4!}\frac{\Phi^2(r)}{M^2}\right)\frac{m_s^2}{g_s^2}\Phi^2(r) \\
& -\frac{\zeta_0}{4!}\frac{1}{g_{\omega}^2}W^4(r)+\frac{1}{2g_s^2}\left(1+\alpha_1\frac{\Phi(r)}{M}\right)\left(\boldsymbol{\nabla}\Phi(r)\right)^2-\frac{1}{2g_{\omega}^2}\left(1+\alpha_2\frac{\Phi(r)}{M}\right) \\
& \left(\boldsymbol{\nabla}W(r)\right)^2-\frac{1}{2}\left(1+\eta_1\frac{\Phi(r)}{M}+\frac{\eta_2}{2}\frac{\Phi^2(r)}{M^2}\right)\frac{m_{\omega}^2}{g_{\omega}^2}W^2(r)-\frac{1}{2e^2}\left(\boldsymbol{\nabla}A(r)\right)^2 \\
& -\frac{1}{2g_{\rho}^2}\left(\boldsymbol{\nabla}R(r)\right)^2-\frac{1}{2}\left(1+\eta_{\rho}\frac{\Phi(r)}{M}\right)\frac{m_{\rho}^2}{g_{\rho}^2}R^2(r)-\Lambda_{\omega}\left(R^2(r)W^2(r)\right) \\
& +\frac{1}{2g_{\delta}^2}\left(\boldsymbol{\nabla}D(r)\right)^2+\frac{1}{2}\frac{{m_{\delta}}^2}{g_{\delta}^2}\left(D^2(r)\right)\;, \qquad (2.1)
\end{aligned}
$$

where Φ, W, R, D, and A are the fields[†]; g_{σ}, g_{ω}, g_{ρ}, g_{δ}, and $\frac{e^2}{4\pi}$ are the coupling constants; and m_{σ}, m_{ω}, m_{ρ}, and m_{δ} are the masses for σ, ω, ρ, and δ mesons and photon, respectively. The parameters, such as $\eta_1, \eta_2, \Lambda_{\omega}, \alpha_1, \alpha_2, f_{\omega}$ have their own importance to explain various properties of finite nuclei and nuclear matter. For instance, the

[†] $W(r)=g_{\omega}V_0(r), \Phi(r)=g_{\sigma}\Phi_0(r), R(r)=g_{\rho}b_0(r)$, and $D(r)=g_{\delta}D_0(r)$ are the scaled mean-fields with different coupling constants.

surface properties of finite nuclei is analyzed through non-linear interactions of η_1 and η_2 as discussed in Ref. [19].

Now, our aim is to solve the field equations for the baryons and mesons (nucleon, σ, ω, ρ, and δ) using the variational principle. We obtained the meson equation of motion using the equation $\left(\frac{\partial \mathcal{E}}{\partial \phi_i}\right)_{\rho=const} = 0$. The single-particle energy for the nucleons is obtained by using the Lagrange multiplier ε_i, which is the energy eigenvalue of the Dirac equation constraining the normalization condition $\sum_i \varphi_i^\dagger(r)\varphi_i(r) = 1$ [74]. The Dirac equation for the wave function $\varphi_i(r)$ becomes

$$\frac{\partial}{\partial \varphi_i^\dagger(r)}\left[\mathcal{E}(r) - \sum_i \varphi_i^\dagger(r)\varphi_i(r)\right] = 0, \tag{2.2}$$

i.e.

$$\begin{aligned}\Big\{ -i\boldsymbol{\alpha}\cdot\boldsymbol{\nabla} \;\; + \;\; & \beta[M - \Phi(r) - \tau_3 D(r)] + W(r) + \frac{1}{2}\tau_3 R(r) + \frac{1+\tau_3}{2}A(r) \\ & -\frac{i\beta\boldsymbol{\alpha}}{2M}\cdot\left[f_\omega \boldsymbol{\nabla} W(r) + \frac{1}{2} f_\rho \tau_3 \boldsymbol{\nabla} R(r)\right]\Big\}\, \varphi_\alpha(r) = \varepsilon_\alpha\, \varphi_\alpha(r)\,. \end{aligned} \tag{2.3}$$

The mean-field equations for Φ, W, R, D, and A are given by

$$\begin{aligned} -\Delta\Phi(r) + m_s^2\Phi(r) &= g_s^2\rho_s(r) - \frac{m_s^2}{M}\Phi^2(r)\left(\frac{\kappa_3}{2} + \frac{\kappa_4}{3!}\frac{\Phi(r)}{M}\right) \\ &\quad + \frac{g_s^2}{2M}\left(\eta_1 + \eta_2\frac{\Phi(r)}{M}\right)\frac{m_\omega^2}{g_\omega^2}W^2(r) + \frac{\eta_\rho}{2M}\frac{g_s^2}{{g_\rho}^2}m_\rho^2 R^2(r) \\ &\quad + \frac{\alpha_1}{2M}[(\boldsymbol{\nabla}\Phi(r))^2 + 2\Phi(r)\Delta\Phi(r)] + \frac{\alpha_2}{2M}\frac{g_s^2}{g_\omega^2}(\boldsymbol{\nabla}W(r))^2, \end{aligned} \tag{2.4}$$

$$\begin{aligned} -\Delta W(r) + m_\omega^2 W(r) &= g_\omega^2\left(\rho(r) + \frac{f_\omega}{2}\rho_{\rm T}(r)\right) - \left(\eta_1 + \frac{\eta_2}{2}\frac{\Phi(r)}{M}\right)\frac{\Phi(r)}{M}m_\omega^2 W(r) \\ &\quad - \frac{1}{3!}\zeta_0 W^3(r) + \frac{\alpha_2}{M}[\boldsymbol{\nabla}\Phi(r)\cdot\boldsymbol{\nabla}W(r) + \Phi(r)\Delta W(r)] \\ &\quad -2\,\Lambda_\omega {g_\omega}^2 R^2(r) W(r)\,, \end{aligned} \tag{2.5}$$

$$\begin{aligned} -\Delta R(r) + m_\rho^2 R(r) &= \frac{1}{2}g_\rho^2\left(\rho_3(r) + \frac{1}{2}f_\rho\rho_{{\rm T},3}(r)\right) - \eta_\rho\frac{\Phi(r)}{M}m_\rho^2 R(r) \\ &\quad -2\,\Lambda_\omega {g_\rho}^2 R(r) W^2(r)\,, \end{aligned} \tag{2.6}$$

$$-\Delta A(r) = e^2\rho_{\rm p}(r)\,, \tag{2.7}$$

$$-\Delta D(r) + {m_\delta}^2 D(r) = g_\delta^2\rho_{s3}\,, \tag{2.8}$$

where the baryon, scalar, isovector, proton, and tensor densities are

$$\begin{aligned}\rho(r) &= \sum_i n_i \varphi_i^\dagger(r)\varphi_i(r) \\ &= \rho_p(r) + \rho_n(r) \\ &= \frac{2}{(2\pi)^3}\int_0^{k_p} d^3k + \frac{2}{(2\pi)^3}\int_0^{k_n} d^3k, \end{aligned} \tag{2.9}$$

$$\begin{aligned}\rho_s(r) &= \sum_i n_i \varphi_i^\dagger(r)\beta\varphi_i(r) \\ &= \rho_{sp}(r) + \rho_{sn}(r) \\ &= \sum_i \frac{2}{(2\pi)^3}\int_0^{k_i} d^3k \frac{M_i^*}{(k_i^2 + M_i^{*2})^{\frac{1}{2}}}, \end{aligned} \tag{2.10}$$

$$\begin{aligned}\rho_3(r) &= \sum_i n_i \varphi_i^\dagger(r)\tau_3\varphi_i(r) \\ &= \rho_p(r) - \rho_n(r), \end{aligned} \tag{2.11}$$

$$\begin{aligned}\rho_{s3}(r) &= \sum_i n_i \varphi_i^\dagger(r)\tau_3\beta\varphi_i(r) \\ &= \rho_{ps}(r) - \rho_{ns}(r) \end{aligned} \tag{2.12}$$

$$\rho_{\rm p}(r) = \sum_i n_i \varphi_i^\dagger(r)\left(\frac{1+\tau_3}{2}\right)\varphi_i(r), \tag{2.13}$$

$$\rho_{\rm T}(r) = \sum_i n_i \frac{i}{M}\boldsymbol{\nabla}\cdot\left[\varphi_i^\dagger(r)\beta\boldsymbol{\alpha}\varphi_i(r)\right], \tag{2.14}$$

and

$$\rho_{\rm T,3}(r) = \sum_i n_i \frac{i}{M}\boldsymbol{\nabla}\cdot\left[\varphi_i^\dagger(r)\beta\boldsymbol{\alpha}\tau_3\varphi_i(r)\right]. \tag{2.15}$$

Here k_i is the nucleon's Fermi momentum and the summation is over all the occupied states. The qualitative structure of the fields (such as V and S) for the finite nucleus are shown in Fig. 2.1. The nucleons and mesons are composite particles and their vacuum polarization effects have been neglected. Hence, the negative-energy states do not contribute to the densities and current [27]. In the fitting process, the coupling

constants of the effective Lagrangian are determined from a set of experimental data which takes into account the large part of the vacuum polarization effects in the *no-sea approximation*. It is clear that the *no-sea approximation* is essential to determine the stationary solutions of the relativistic mean-field equations which describe the ground-state properties of the nucleus. The Dirac sea holds the negative-energy eigenvectors of the Dirac Hamiltonian, which is different for different nuclei. Thus, it depends on the specific solution of the set of nonlinear RMF equations. The Dirac spinors can be expanded in terms of vacuum solutions which form a complete set of plane wave functions in spinor space. This set will be complete when the states with negative energies are the part of the positive energy states and create the Dirac sea of the vacuum.

The effective masses of proton, M_p^*, and neutron, M_n^* are written as

$$M_p^* = M - \Phi(r) - D(r), \tag{2.16}$$

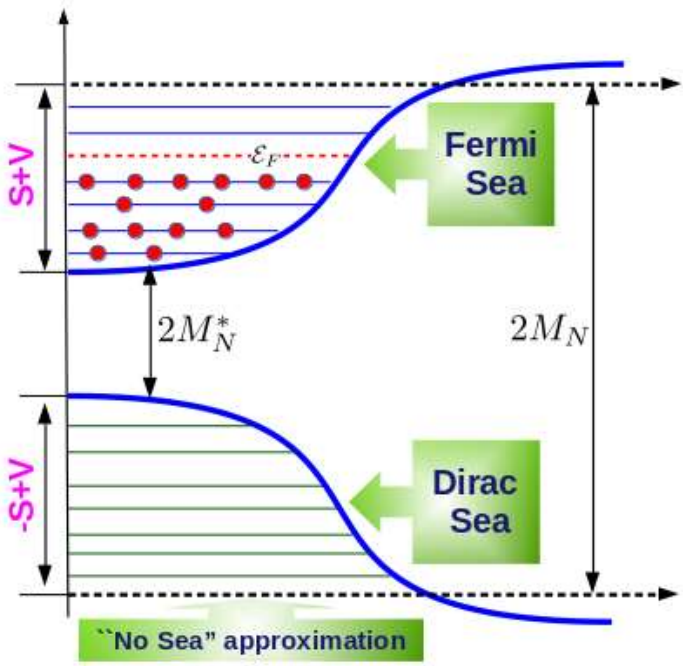

Figure 2.1: The qualitative structure of the Lorentz scalar field S and vector field V in finite nuclei. M_N, and M_N^* are the mass of the nucleons and effective mass of the nucleons, respectively. Dirac positive energy S+V and negative energy -S+V states are shown.

$$M_n^* = M - \Phi(r) + D(r). \tag{2.17}$$

The vector potential is

$$V(r) = g_\omega V_0(r) + \frac{1}{2} g_\rho \tau_3 b_0(r) + e\frac{(1-\tau_3)}{2} A_0(r). \tag{2.18}$$

and the scalar potential is

$$S(r) = g_\sigma \Phi_0(r) + g_\delta \tau_3 \delta_0(r) \tag{2.19}$$

where, $\Phi_0(r)$, $\delta_0(r)$ are scalar fields by σ and δ mesons, respectively. The set of coupled differential equations is solved self-consistently to describe the ground-state properties of finite nuclei. In the fitting procedure, we used the experimental data of binding energy (BE) and charge radius r_{ch} for a set of spherical nuclei (^{16}O, ^{40}Ca, ^{48}Ca, ^{68}Ni, ^{90}Zr, ^{100,132}Sn, and ^{208}Pb). The total binding energy is obtained by

$$\begin{aligned} E_{total} &= E_{part} + E_\sigma + E_\omega + E_\rho \\ &\quad + E_\delta + E_{\omega\rho} + E_c + E_{pair} + E_{c.m.}, \end{aligned} \tag{2.20}$$

where E_{part} is the sum of the single-particle energies of the nucleons and E_σ, E_ω, E_ρ, E_δ, and E_c are the contributions of the respective mesons and Coulomb fields. The pairing E_{pair} and the center of mass motion $E_{c.m.} = \frac{3}{4} \times 41 A^{-1/3}$ MeV energies are also taken into account [19, 75, 76].

2.2 Temperature dependent BCS pairing

The pairing correlation plays a distinct role in open-shell nuclei. The effect of pairing correlation is markedly seen with increase in mass number A. Moreover it helps in understanding the deformation of medium and heavy nuclei. It has a lean effect on both bulk and single particles properties of lighter mass nuclei because of the availability of limited pairs near the Fermi surface. We take the case of T=1 channel of pairing correlation i.e, pairing between proton- proton and neutron-neutron. In this case, a nucleon of quantum states $|jm_z\rangle$ pairs with another nucleons having same I_z value with quantum states $|j - m_z\rangle$, since it is the time reversal partner of the

other. In both nuclear and atomic domain the ideology of BCS pairing is the same. The even-odd mass staggering of isotopes was the first evidence of its kind for the pairing energy. Considering the mean-field formalism, the violation of the particle number is seen only due to the pairing correlation. We find terms like $\varphi^{\dagger}\varphi$ (density) in the RMF Lagrangian density but we put an embargo on terms of the form $\varphi^{\dagger}\varphi^{\dagger}$ or $\varphi\varphi$ since it violates the particle number conservation. We apply externally the BCS pairing approximation for our calculation to take the pairing correlation into account. The pairing interaction energy in terms of occupation probabilities v_i^2 and $u_i^2 = 1 - v_i^2$ is written as [77, 78]:

$$E_{pair} = -G\left[\sum_{i>0} u_i v_i\right]^2, \tag{2.21}$$

with G is the pairing force constant. The variational approach with respect to the occupation number v_i^2 gives the BCS equation [77]:

$$2\epsilon_i u_i v_i - \triangle(u_i^2 - v_i^2) = 0, \tag{2.22}$$

with the pairing gap $\triangle = G\sum_{i>0} u_i v_i$. The pairing gap ($\triangle$) of proton and neutron is taken from the empirical formula [79, 80]:

$$\triangle = 12 \times A^{-1/2}. \tag{2.23}$$

To calculate the properties of nuclei at finite temperature one has to include the temperature in the set of coupled equations. For this, the temperature is introduced in the partial occupancies in the BCS approximation is given by,

$$n_i = v_i^2 = \frac{1}{2}\left[1 - \frac{\epsilon_i - \lambda}{\tilde{\epsilon_i}}[1 - 2f(\tilde{\epsilon_i}, T)]\right], \tag{2.24}$$

with

$$f(\tilde{\epsilon_i}, T) = \frac{1}{(1 + exp[\tilde{\epsilon_i}/T])} \quad and$$

$$\tilde{\epsilon_i} = \sqrt{(\epsilon_i - \lambda)^2 + \triangle^2}. \tag{2.25}$$

The function $f(\tilde{\epsilon_i}, T)$ represents the Fermi Dirac distribution for quasi particle energy $\tilde{\epsilon_i}$. The chemical potential $\lambda_p(\lambda_n)$ for protons (neutrons) is obtained from the constraints of particle number equations

$$\sum_i n_i^Z = Z,$$
$$\sum_i n_i^N = N. \tag{2.26}$$

The sum is taken over all proton and neutron states. The entropy is obtained by,

$$S = -\sum_i \left[n_i \, ln(n_i) + (1 - n_i) \, ln(1 - n_i) \right]. \tag{2.27}$$

The total energy and the gap parameter are obtained by minimizing the free energy,

$$F = E - TS. \tag{2.28}$$

In constant pairing gap calculations, for a particular value of pairing gap $\triangle$ and force constant G, the pairing energy E_{pair} diverges, if it is extended to an infinite configuration space. In fact, in all realistic calculations with finite range forces, $\triangle$ is not constant, but decreases with large angular momenta states above the Fermi surface. Therefore, a pairing window in all the equations are extended up-to the level $|\epsilon_i - \lambda| \leq 2(41A^{-1/3})$ as a function of the single particle energy. The factor 2 has been determined so as to reproduce the pairing correlation energy for neutrons in ^{118}Sn using Gogny force [24, 78, 79].

2.3 Quasi-BCS pairing

For fitting, we consider a seniority-type interaction as a tool by taking a constant value of G for the active pair shell. The BCS approach does not go well for nuclei away from the stability line because, in the present case, with the increase in the number of neutrons or protons the corresponding Fermi level goes to zero and the number of available levels above it minimizes. To complement this situation we see that the particle-hole and pair excitation's reach the continuum. In Ref. [22] we notice that if we make the BCS calculation using the quasi-particle state as in Hartree-Fock-Bogoliubov (HFB) calculation, then the BCS binding energies are coming out to be very close to the HFB, but rms radii (i.e the single-particle wave functions) greatly depend on the size of the box where the calculation is done. This is because

of the unphysical neutron (proton) gas in the continuum where wave-functions are not confined in a region. The above shortcomings of the BCS approach can be improved by means of the so-called quasi-bound states, i.e, states bound because of their own centrifugal barrier (centrifugal-plus-Coulomb barrier for protons) [19–21]. Our calculations are done by confining the available space to one harmonic oscillator shell each above and below the Fermi level to exclude the unrealistic pairing of highly excited states in the continuum [19].

2.3.1 The Nuclear Equation of State

The nuclear equation of state plays vital role in explaining many properties of nuclear matter and neutron star etc. Most importantly, the EoS very well explains the complex behaviour of the dense matter that makes up neutron star. In static, infinite, uniform, and isotropic nuclear matter, all the gradients of the fields in Eqs. (2.4)–(2.8) vanish. By the definition of infinite nuclear matter, the electromagnetic interaction is also neglected. The expressions for energy density and pressure for such a system are obtained from the energy-momentum tensor [81]:

$$T_{\mu\nu} = \sum_i \partial_\nu \phi_i \frac{\partial \mathcal{L}}{\partial\left(\partial^\mu \phi_i\right)} - g_{\mu\nu}\mathcal{L}. \tag{2.29}$$

The zeroth component of the energy-momentum tensor $< T_{00} >$ gives the energy density and the third component $< T_{ii} >$ determine the pressure of the system [49]:

$$\begin{aligned}
\mathcal{E} &= \frac{2}{(2\pi)^3}\int d^3k E_i^*(k) + \rho W + \frac{m_s^2\Phi^2}{g_s^2}\left(\frac{1}{2} + \frac{\kappa_3}{3!}\frac{\Phi}{M} + \frac{\kappa_4}{4!}\frac{\Phi^2}{M^2}\right) \\
&\quad -\frac{1}{2}m_\omega^2\frac{W^2}{g_\omega^2}\left(1 + \eta_1\frac{\Phi}{M} + \frac{\eta_2}{2}\frac{\Phi^2}{M^2}\right) - \frac{1}{4!}\frac{\zeta_0 W^4}{g_\omega^2} + \frac{1}{2}\rho_3 R \\
&\quad -\frac{1}{2}\left(1 + \frac{\eta_\rho\Phi}{M}\right)\frac{m_\rho^2}{g_\rho^2}R^2 - \Lambda_\omega(R^2W^2) + \frac{1}{2}\frac{m_\delta^2}{g_\delta^2}\left(D^2\right),
\end{aligned} \tag{2.30}$$

$$\begin{aligned}
P &= \frac{2}{3(2\pi)^3}\int d^3k \frac{k^2}{E_i^*(k)} - \frac{m_s^2\Phi^2}{g_s^2}\left(\frac{1}{2} + \frac{\kappa_3}{3!}\frac{\Phi}{M} + \frac{\kappa_4}{4!}\frac{\Phi^2}{M^2}\right) \\
&\quad +\frac{1}{2}m_\omega^2\frac{W^2}{g_\omega^2}\left(1 + \eta_1\frac{\Phi}{M} + \frac{\eta_2}{2}\frac{\Phi^2}{M^2}\right) + \frac{1}{4!}\frac{\zeta_0 W^4}{g_\omega^2} \\
&\quad +\frac{1}{2}\left(1 + \frac{\eta_\rho\Phi}{M}\right)\frac{m_\rho^2}{g_\rho^2}R^2 + \Lambda_\omega(R^2W^2) - \frac{1}{2}\frac{m_\delta^2}{g_\delta^2}\left(D^2\right),
\end{aligned} \tag{2.31}$$

where $E_i^*(k)=\sqrt{k^2+M_i^{*2}}$ $(i=p,n)$ is the energy and k is the momentum of the nucleon. In the context of density functional theory, it is possible to parametrize the exchange and correlation effects through local potentials (Kohn–Sham potentials), as long as those contributions are small enough [82]. The Hartree values control the dynamics in the relativistic Dirac-Brückner-Hartree-Fock calculations. Therefore, the local meson fields in the RMF formalism can be interpreted as Kohn-Sham potentials and in this sense Eqs. (2.3–2.8) include effects beyond the Hartree approach through the nonlinear couplings [17].

2.3.2 Nuclear Matter Properties

In 1936, the semi-empirical mass formula was developed by Bethe-Weizsacker based on the liquid drop model. This mass model is quite successful in describing some bulk properties of finite nuclei. In the liquid drop model, the binding energy per particle of a nucleus can be constructed as follows:

$$\frac{E(Z,N)}{A} = M - a_v + a_s A^{-1/3} + a_c \frac{Z^2}{A^{2/3}} + a_{asym}\frac{(N-Z)^2}{A^2} + \dots \tag{2.32}$$

where M is the nucleon mass, and $A = Z + N$ is the total number of nucleons. a_v, a_s, a_c, and a_{asym} are the volume, surface, Coulomb, and asymmetry term, respectively. The liquid drop model can be extended to introduce the infinite nuclear matter (means Z, N, and V go to infinity) by switching off the Coulomb term *i.e* $a_c = 0$, and neglecting the surface contribution. Therefore, the binding energy per nucleon of the system is given by

$$\begin{aligned} \frac{E(Z,N)}{A} - M &= -a_v + a_{asym}\frac{(N-Z)^2}{A^2} \\ e(\rho,\alpha) &= \frac{\mathcal{E}}{\rho_B} - M \equiv -a_v + a_{asym}\alpha^2, \end{aligned} \tag{2.33}$$

where $\alpha = (N-Z)/A = \frac{\rho_n-\rho_p}{\rho_n+\rho_p}$ is known as the neutron excess of the infinite nuclear matter. As suggested above the infinite nuclear matter is incompressible. Conventionally, we can expand binding energy per particle for compressible nuclear matter around $\alpha = 0$:

$$\begin{aligned} e(\rho,\alpha) &= e(\rho,\alpha=0) + \Big(\frac{\partial e(\rho,\alpha)}{\partial\alpha}\Big)_{\alpha=0}\alpha + \frac{1}{2}\Big(\frac{\partial^2 e(\rho,\alpha)}{\partial\alpha^2}\Big)_{\alpha=0}\alpha^2 + \dots \\ &= e(\rho) + S(\rho)\alpha^2 + \mathcal{O}(\alpha^4), \end{aligned} \tag{2.34}$$

where the linear term in α vanishes due to the charge symmetry of nuclear force, $e(\rho)$ is energy density of the symmetric nuclear matter (SNM) ($\alpha = 0$), and $\alpha = 1$ corresponds to pure neutron matter. The symmetry energy $S(\rho)$ of the system defined as:

$$S(\rho) = \frac{1}{2}\left[\frac{\partial^2 e(\rho,\alpha)}{\partial\alpha^2}\right]_{\alpha=0}. \tag{2.35}$$

The isospin asymmetry arises due to the difference in densities and masses of the neutron and proton. The density-type isospin asymmetry is taken care by ρ meson (isovector-vector meson) and mass asymmetry by the δ meson (isovector - scalar meson). The general expression for symmetry energy $S(\rho)$ is a combined expression of ρ and δ mesons, which is defined as [19, 37, 83, 84]

$$S(\rho) = S^{kin}(\rho) + S^{\rho}(\rho) + S^{\delta}(\rho), \tag{2.36}$$

with

$$S^{kin}(\rho) = \frac{k_F^2}{6E_F^*},\ S^{\rho}(\rho) = \frac{g_\rho^2\rho}{8m_\rho^{*2}} \tag{2.37}$$

and

$$S^{\delta}(\rho) = -\frac{1}{2}\rho\frac{g_\delta^2}{m_\delta^2}\left(\frac{M^*}{E_F}\right)^2 u_\delta\left(\rho, M^*\right). \tag{2.38}$$

The last function u_δ is from the discreteness of the Fermi momentum. This momentum is quite large in nuclear matter and can be treated as a continuum and continuous system. The function u_δ is defined as

$$u_\delta\left(\rho, M^*\right) = \frac{1}{1 + 3\frac{g_\delta^2}{m_\delta^2}\left(\frac{\rho^s}{M^*} - \frac{\rho}{E_F}\right)}. \tag{2.39}$$

In the limit of continuum, the function $u_\delta \approx 1$. The whole symmetry energy ($S^{kin} + S^{pot}$) arises from ρ and δ mesons and is given as

$$S(\rho) = \frac{k_F^2}{6E_F^*} + \frac{g_\rho^2\rho}{8m_\rho^{*2}} - \frac{1}{2}\rho\frac{g_\delta^2}{m_\delta^2}\left(\frac{M^*}{E_F}\right)^2, \tag{2.40}$$

where E_F^* is the Fermi energy and k_F is the Fermi momentum. The mass of the ρ meson modified, because of the cross-coupling of ρ-ω fields and is given by

$$m_\rho^{*2} = \left(1 + \eta_\rho\frac{\Phi}{M}\right)m_\rho^2 + 2g_\rho^2(\Lambda_\omega W^2). \tag{2.41}$$

The cross-coupling of isoscalar-isovector mesons (Λ_ω) modifies the density dependence of $S(\rho)$ without affecting the saturation properties of the SNM [43, 85, 86]. In the numerical calculation, the coefficient of symmetry energy $S(\rho)$ is obtained by the energy difference of symmetric and pure neutron matter at saturation. In our calculation, we have taken the isovector channel into account to make the new parameters, which incorporate the currently existing experimental observations, and predictions are made keeping in mind some future aspects of the model. The symmetry energy can be expanded as a Taylor series around the saturation density ρ_0 as

$$S(\rho) = J + L\mathcal{Y} + \frac{1}{2}K_{sym}\mathcal{Y}^2 + \frac{1}{6}Q_{sym}\mathcal{Y}^3 + \mathcal{O}[\mathcal{Y}^4], \tag{2.42}$$

where $J = S(\rho_0)$ is the symmetry energy at saturation and $\mathcal{Y} = \frac{\rho-\rho_0}{3\rho_0}$. The coefficients $L(\rho_0)$, $K_{sym}(\rho_0)$, and Q_{sym} are defined as:

$$L = 3\rho\frac{\partial S(\rho)}{\partial\rho}\bigg|_{\rho=\rho_0}, \tag{2.43}$$

$$K_{sym} = 9\rho^2\frac{\partial^2 S(\rho)}{\partial\rho^2}\bigg|_{\rho=\rho_0}, \tag{2.44}$$

$$Q_{sym} = 27\rho^3\frac{\partial^3 S(\rho)}{\partial\rho^3}\bigg|_{\rho=\rho_0}. \tag{2.45}$$

Similarly, we obtain the asymmetric nuclear matter incompressibility as $K(\alpha) = K + K_\tau\alpha^2 + \mathcal{O}(\alpha^4)$ and K_τ is given by [87]

$$K_\tau = K_{sym} - 6L - \frac{Q_0 L}{K}, \tag{2.46}$$

where $Q_0 = 27\rho^3\frac{\partial^3(\mathcal{E}/\rho)}{\partial\rho^3}$ in SNM.

Here, L is the slope and K_{sym} represents the curvature of $S(\rho)$ at saturation density. A large number of investigations have been made to fix the values of J, L, and K_{sym} [85,88–93]. The density dependence of symmetry energy is a key quantity to control the properties of both finite nuclei and infinite nuclear matter [94]. Currently, the available information on symmetry energy $J = 31.6 \pm 2.66$ MeV and its slope $L = 58.9 \pm 16$ MeV at saturation density are obtained by various astrophysical observations [95]. To date, the precise values of J, L, and the neutron radii for finite nuclei are not known experimentally; it is essential to discuss the behavior of the symmetry energy as a function of density in our new parameter sets G3 and IOPB-I (see chapter 6).

Chapter 3

Decay modes of Th and U isotopes

The properties of recently predicted thermally fissile Th and U isotopes are studied within the framework of relativistic mean-field approach using axially deformed harmonic oscillator basis. We calculated the ground, first intrinsic excited state for highly neutron-rich thorium and uranium isotopes. The possible modes of decay such as α decay and β decay are analyzed. We found that the neutron-rich isotopes are stable against α decay, however they are very unstable against β-decay. The life time of these nuclei is predicted to be tens of seconds against β decay. If these nuclei utilized before their decay time, a lot of energy can be produced with the help of multifragmentation fission [96]. Also, these nuclei have great implications from the astrophysical point of view. In specific case of $^{228-230}$Th and $^{228-234}$U isotopes, we found isomeric states having energy range of 2 to 3 MeV and three maxima in the potential energy surface.

3.1 Introduction

Nowadays uranium and thorium isotopes have attracted great attention in nuclear physics due to the thermally fissile nature of some of them [96]. These thermally fissile materials have tremendous importance in energy production. To date, the known thermally fissile nuclei are ^{233}U, ^{235}U and ^{239}Pu; of these, only ^{235}U has a long lifetime, and it is the only thermally fissile isotope available in nature [96]. Thus, presently an important area of research is the search for any other thermally fissile

nuclei apart from ^{233}U, ^{235}U and ^{239}Pu. Recently, Satpathy *et al.* [96] showed that uranium and thorium isotopes with neutron number N=154-172 have a thermally fissile property. They performed a calculation with a typical example of ^{250}U as this nucleus has a low fission barrier with a significantly large barrier width, which makes it stable against spontaneous fission. Apart from the thermally fissile nature, these nuclei also play an important role in nucleosynthesis in stellar evolution. As these nuclei are stable against spontaneous fission, the prominent decay modes may be the emission of α, β, and *cluster* particles from the neutron-rich thermally fissile (uranium and thorium) isotopes.

To measure the stability of these neutron-rich U and Th isotopes, we investigate the α and β decay properties of these nuclei. Also, we extend our calculations to estimate the binding energy, root mean square radii, quadrupole moments and other structural properties.

From the last three decades, the relativistic mean field (RMF) formalism has been a formidable theory in describing finite nuclear properties throughout the periodic chart and infinite nuclear matter properties concerned with the dense cosmic objects such as neutron star. Along the same line RMF theory is also good enough for study the clusterization [97], α decay [98], and β decay of nuclei. The presence of cluster in heavy nuclei like ^{222}Ra, ^{232}U, ^{239}Pu, and ^{242}Cm has been studied using RMF formalism [99, 100]. It gives a clear prediction of α like (N=Z) matter in the central part for heavy nuclei and a *cluster*-like structure (N=Z and $N \neq Z$) for light-mass nuclei [97]. The proton emission as well as cluster decay phenomena is well studied using RMF formalism with M3Y [101], LR3Y [102], and NLR3Y [103] nucleon-nucleon potentials in the framework of single- and double-folding models, respectively. Here, we used the RMF formalism with the well known NL3 parameter set [29] for all our calculations.

3.2 RMF Formalism

In the present chapter, we use the axially deformed RMF formalism to calculate various nuclear phenomena. The meson-nucleon interaction is given by the Lagrangian

density [25, 81, 104–107]

$$\begin{aligned}\mathcal{L} &= \overline{\psi_i}\{i\gamma^\mu\partial_\mu - M\}\psi_i + \frac{1}{2}\partial^\mu\sigma\partial_\mu\sigma - \frac{1}{2}m_\sigma^2\sigma^2 \\ &-\frac{1}{3}g_2\sigma^3 - \frac{1}{4}g_3\sigma^4 - g_s\overline{\psi_i}\psi_i\sigma - \frac{1}{4}\Omega^{\mu\nu}\Omega_{\mu\nu} \\ &+\frac{1}{2}m_w^2V^\mu V_\mu + \frac{1}{4}c_3(V_\mu V^\mu)^2 - g_w\overline{\psi}_i\gamma^\mu\psi_iV_\mu \\ &-\frac{1}{4}\vec{B}^{\mu\nu}.\vec{B}_{\mu\nu} + \frac{1}{2}m_\rho^2\vec{R}^\mu.\vec{R}_\mu - g_\rho\overline{\psi}_i\gamma^\mu\vec{\tau}\psi_i.\vec{R}^\mu \\ &-\frac{1}{4}F^{\mu\nu}F_{\mu\nu} - e\overline{\psi}_i\gamma^\mu\frac{(1-\tau_{3i})}{2}\psi_iA_\mu, \end{aligned} \tag{3.1}$$

where, ψ is the single-particle Dirac spinor and meson fields are denoted as σ, V^μ, and R^μ for σ, ω, and ρ mesons, respectively. The electromagnetic interaction between protons is denoted by photon field A^μ. g_s, g_ω, g_ρ, and $\frac{e^2}{4\pi}$ are the coupling constants for the σ,ω, and ρ meson and photon fields, respectively. The strengths of the self-coupling σ meson (σ^3 and σ^4) are denoted by g_2 and g_3, with c_3 as the non-linear coupling constant for ω meson. The nucleon mass is denoted M, where the σ, ω, and $\rho-$ meson masses are m_s, m_ω, and m_ρ, respectively. The field tensors of the isovector mesons and the photon are given by,

$$\Omega^{\mu\nu} = \partial^\mu V^\nu - \partial^\nu V^\mu, \tag{3.2}$$

$$\vec{B}^{\mu\nu} = \partial^\mu\vec{R}^\nu - \partial^\nu\vec{R}^\mu, \tag{3.3}$$

$$F^{\mu\nu} = \partial^\mu A^\nu - \partial^\nu A^\mu. \tag{3.4}$$

From the classical Euler-Lagrangian equation, we get the Dirac equation and Klein- Gordan equation for the nucleon and meson fields, respectively. The Dirac equation for the nucleon is solved by expanding the Dirac spinor into lower and upper components, while the mean-field equation for bosons is solved in the deformed harmonic oscillator basis with β_0 as the deformation parameter. The nucleon equation along with different meson equations form a set of coupled equations, which can be solved by iterative method.

The calculations are simplified under the shadow of various symmetries like conservation of parity, no-sea approximation and time reversal symmetry, which kills all spatial components of the meson fields and the antiparticle-state contribution to the nuclear observable.

The quadrupole deformation parameter β_2 is calculated from the resulting quadropole moments Q of the proton Q_p and neutron Q_n through the following relation:

$$Q = Q_n + Q_p = \sqrt{\frac{16\pi}{5}}(\frac{3}{4\pi}AR^2\beta_2), \tag{3.5}$$

where $R = 1.2A^{1/3}$. The root-mean-square charge radius (r_{ch}), proton radius (r_p), neutron radius (r_n), and matter radius (r_m) are given as [104]:

$$< r_p^2 >= \frac{1}{Z}\int \rho_p(r_\perp, z)r_p^2 d\tau_p, \tag{3.6}$$

$$< r_n^2 >= \frac{1}{N}\int \rho_n(r_\perp, z)r_n^2 d\tau_n, \tag{3.7}$$

$$r_{ch} = \sqrt{r_p^2 + 0.64}, \tag{3.8}$$

$$< r_m^2 >= \frac{1}{A}\int \rho(r_\perp, z)r^2 d\tau, \tag{3.9}$$

here all symbols have their own usual meaning. The total energy of the system is calculated by Eq. (2.20).

3.2.1 Pauli blocking approximation

It is a tough task to compute the BE and quadrupole moment of odd-N or odd-Z or both odd-N and odd-Z numbers (odd-even, even-odd, or odd-odd) nuclei. To do this, one needs to include the additional time-odd term, as done in the SHF Hamiltonian [108], or empirically the pairing force in order to take care the effect of an odd neutron or odd-proton [109]. In an odd-even or odd-odd nucleus, the time reversal symmetry is violated in mean-field models. In our RMF calculations, we neglect the space components of the vector fields, which are odd under time reversal and parity. These are important in the determination of magnetic moments [110] but have a very small effect on bulk properties such as BEs or quadrupole deformations, and they can be neglected [111] in the present context. Here, for the odd-Z or odd-N calculations, we employ the Pauli blocking approximation, which restores the time-reversal symmetry. In this approach, one pair of conjugate states, $\pm m$, is taken out of the pairing scheme. The odd particle stays in one of these states, and its

corresponding conjugate state remains empty. In principle, one has to block different states around the Fermi level in turn to find the one that gives the lowest energy configuration of the odd nucleus. For odd-odd nuclei, one needs to block both the odd neutron and odd proton.

3.3 Calculations and results

In this section, we evaluate our results for the BE, rms radius, quadrupole deformation parameter for recently predicted thermally fissile isotopes of Th and U. These nuclei are quite heavy and require a large number of oscillator bases, which takes considerable time for computation. In the first subsection here we describe how to select the basis space, and the results and discussion follow.

3.3.1 Selection of basis space

The Dirac equation for fermions (proton and neutron) and the equation of motion for bosons ($\sigma-$, $\omega-$, $\rho-$ and A_0) obtained from the RMF Lagrangian are solved self-consistently using an iterative method. These equations are solved in an axially deformed harmonic oscillator expansion basis, N_F and N_B for fermionic and bosonic wave functions, respectively.

For heavy nuclei, a large number of basis space N_F and N_B are needed to get a converged solution. To reduce the computational time without compromising the convergence of the solution, we have to choose an optimal number of model spaces for both fermion and boson fields. To choose optimal values for N_F and N_B, we select ^{240}Th as a test case and increase the basis quanta from 8 to 20 step by step. The obtained results for BE, charge radius and quadrupole deformation parameter are shown in Fig. 3.1. In our calculations, we notice an increment of 200 MeV in BE upon going from $N_F = N_B$ =8 to 10. This increment in energy decreases upon going to a higher oscillator basis. For example, change in energy is $\sim$ 0.2 MeV with a change in $N_F = N_B$ from 14 to 20, and the increment in r_c values is 0.12 fm, respectively. Keeping in mind the increase in convergence time for larger quanta as well as the size of the nuclei considered, we finally use $N_F = N_B = 20$ in our calculations to get suitable convergence results, which is the current accuracy of the present RMF

models.

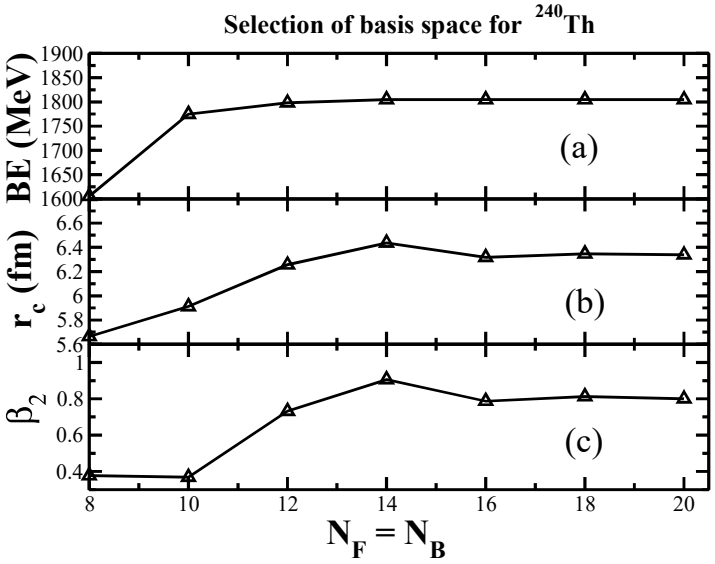

Figure 3.1: Variation of the (a) calculated binding energy (BE), (b) charge radii (r_c), and quadrupole deformation parameter (β_2) are given with the bosonic and fermionic basis.

3.3.2 Binding energies, charge radii and quadrupole deformation parameters

To be sure about the predictivity of our model, first we calculate the BE, charge radii r_c, and quadrupole deformation parameter β_2 for some of the known cases. We have compared our results with the experimental data wherever available or with the Finite Range Droplet Model (FRDM) of Möller *et al.* [15,56,112,113]. The results are listed in Tables 3.1 and 3.2. From the tables, it is obvious that the calculated BEs are comparable with the FRDM as well as experimental values. Further inspection of the tables reveals that the FRDM results are closer to the data. This may be due to the fitting of the FRDM parameters for almost all known data. However, in the case of most RMF parametrizations, the constants are determined by using a few spherical nuclei data along with certain nuclear matter properties. Thus the prediction of the RMF results are considered to be reasonable, but not excellent.

Ren *et al.* [114, 115] have reported that the ground states of several superheavy nuclei are highly deformed states. Since, these are very heavy isotopes, the general assumption is that the ground state probably remains in deformed configuration (liquid drop picture). When these nuclei are excited either by a thermal neutron or by any other means, its intrinsic excited state becomes extraordinarily deformed and attains the scission point before it goes to fission. This can also be easily realized from the PES curve. Our calculations agree with the prediction of Ren *et al.* for other superheavy regions of the mass table. However, this conclusion is contradicted in [116], according to which the ground state of superheavy nuclei is either spherical or normally deformed.

In some cases of U and Th isotopes, we get more than one solution. The solution corresponding to the maximum BE is the ground state configuration and all other solutions are the intrinsic excited states. In some cases, the ground state BE does not match the experimental data. However, the BE, whose quadrupole deformation parameter β_2 is closer to the experimental data or to the FRDM value match well with each other. For example, the BEs of ^{236}U are 1791.7, 1790.0, and 1790.4 MeV with RMF, FRDM, and experimental data, respectively, and the corresponding β_2 are 0.276, 0.215, and 0.272. Similar to the BE, we get β_2 and charge radius r_c RMF results comparable with the FRDM and experimental values.

3.3.3 Potential energy surface

In late 1960's, the structure of PES found renewed interest for its role in the nuclear fission process. In the majority of PESs for actinide nuclei, there exist a second maximum, which splits the fission barrier into inner and outer segments [117]. It also has a crucial role for the characterization of ground state, intrinsic excited state, occurrence of shape coexistence, radioactivity, and spontaneous and induced fission. The structure of the PES is defined mainly from the shell structure, which is strongly related to the distance between the mass centers of the nascent fragments. The macroscopic-microscopic liquid drop theory has been given a key concept of fission, where the surface energy is in the form of collective deformation of the nucleus.

In Figs. 3.2 and 3.3 we have plotted the PES for some selected isotopes of Th and U nuclei. The constraint binding energy BE$_c$ versus the quadrupole deformation

Table 3.1: The calculated binding energies BE, quadrupole deformation parameter β_2, rms radii for the ground states and few selective intrinsic excited state of U isotopes, using RMF formalism with NL3 parameter set. The experimental and FRDM data [15, 56, 112, 113] are also included in the table. See the text for more details.

	RMF (NL3)						FRDM		Experiment		
Nucleus	r_n	r_p	r_{rms}	r_{ch}	β_2	BE (MeV)	BE(MeV)	β_2	r_{ch}	β_2	BE (MeV)
^{216}U	5.762	5.616	5.700	5.673	0	1660.5	1649.0	-0.052			
	6.054	5.946	6.008	5.999	0.608	1650.8					
^{218}U	5.789	5.625	5.721	5.682	0	1678.0	1666.7	0.008			1665.6
	6.081	5.957	6.029	6.011	0.606	1666.9					
^{220}U	5.819	5.641	5.745	5.698	0	1692.2	1681.2	0.008			1680.8
	6.109	5.971	6.052	6.025	0.605	1682.6					
^{222}U	5.849	5.661	5.772	5.717	0	1705.1	1695.7	0.048			1695.6
	6.142	5.990	6.079	6.043	0.611	1697.9					
^{224}U	5.878	5.681	5.798	5.737	0	1717.9	1710.8	0.146			1710.3
	6.198	6.032	6.131	6.085	0.645	1712.8					
^{226}U	5.907	5.701	5.824	5.757	0	1730.8	1724.7	0.172			1724.8
	6.232	6.053	6.160	6.106	0.652	1727.4					
	5.935	5.721	5.850	5.776	0	1743.6					
^{228}U	5.966	5.743	5.877	5.798	0.210	1741.7	1739.0	0.191			1739
	6.259	6.068	6.182	6.120	0.651	1741.3					
^{230}U	5.964	5.739	5.875	5.795	0	1756.0	1752.6	0.199		0.260	1752.8
	6.000	5.765	5.907	5.821	0.234	1755.4					
	6.293	6.091	6.213	6.143	0.658	1753.7					
^{232}U	5.994	5.755	5.900	5.810	0	1766.8	1765.7	0.207		0.267	1765.9
	6.033	5.785	5.935	5.840	0.251	1768.2					
	6.364	6.167	6.286	6.218	0.712	1766.8					
^{234}U	6.021	5.767	5.923	5.823	0	1776.4	1778.2	0.215	5.829	0.265	1778.6
	6.065	5.803	5.963	5.858	0.267	1780.3					
	6.415	6.209	6.334	6.260	0.738	1778.2					
^{236}U	6.092	5.819	5.987	5.874	0.276	1791.7	1790.0	0.215	5.843	0.272	1790.4
	6.446	6.230	6.363	6.281	0.744	1789.4					
^{238}U	6.124	5.838	6.015	5.892	0.283	1802.5	1801.2	0.215	5.857	0.272	1801.7
	6.488	6.263	6.402	6.314	0.763	1800.4					

Table 3.2: Same as Table I, but for Th isotopes.

	RMF (NL3)						FRDM		Experiment		
Nucleus	r_n	r_p	r_{rms}	r_{ch}	β_2	BE (MeV)	BE (MeV)	β_2	r_{ch}	β_2	BE(MeV)
^{216}Th	5.781	5.594	5.704	5.651	0	1673.5	1663.6	0.008			1662.7
	6.034	5.897	5.977	5.951	0.567	1663.8					
^{218}Th	5.812	5.611	5.730	5.667	0	1686.5	1677.2	0.008			1676.7
	6.105	5.959	6.045	6.013	0.616	1678.2					
^{220}Th	5.842	5.631	5.757	5.687	0	1698.1	1690.2	0.030			1690.6
	6.140	5.983	6.076	6.036	0.624	1692.8					
^{222}Th	5.873	5.651	5.784	5.707	0	1709.7	1704.6	0.111		0.151	1704.2
	6.174	6.007	6.107	6.060	0.631	1706.1					
^{224}Th	5.902	5.672	5.81	5.728	0	1721.4	1717.4	0.164		0.173	1717.6
	6.222	6.021	6.142	6.074	0.640	1718.9					
^{226}Th	5.931	5.692	5.837	5.748	0	1733.0	1729.9	0.173		0.225	1730.5
	6.25	6.036	6.166	6.089	0.642	1731.9					
^{228}Th	5.955	5.710	5.859	5.766	0	1743.9	1742.5	0.182	5.748	0.229	1743.0
	5.989	5.729	5.888	5.785	0.227	1744.5					
	6.292	6.065	6.203	6.118	0.661	1743.4					
^{230}Th	5.990	5.727	5.888	5.783	0	1754.2	1754.6	0.198	5.767	0.246	1755.1
	6.026	5.751	5.920	5.807	0.232	1756.0					
	6.315	6.111	6.236	6.163	0.671	1753.1					
^{232}Th	6.060	5.773	5.950	5.828	0.251	1767.0	1766.2	0.207	5.784	0.248	1766.7
	6.240	6.010	6.151	6.063	0.681	1765.0					
^{234}Th	6.093	5.793	5.979	5.848	0.269	1777.5	1777.2	0.215		0.238	1777.6
^{236}Th	6.122	5.812	6.006	5.866	0.272	1787.6	1787.6	0.215			1788.1
^{238}Th	6.152	5.832	6.033	5.887	0.281	1797.5	1797.7	0.224			1797.8
^{240}Th	6.180	5.846	6.057	5.901	0.292	1806.6	1807.2	0.224			

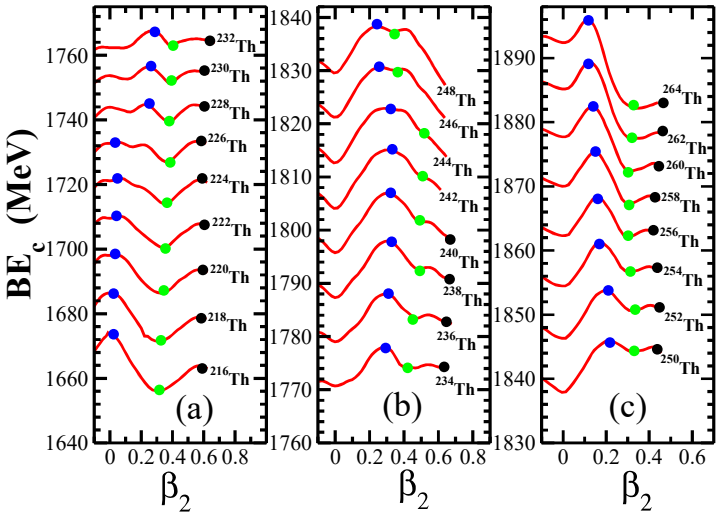

Figure 3.2: The potential energy surface is a function of the quadrupole deformation parameter (β_2) for Th isotopes. The difference between the leftmost (blue) and the middle (green) circles represents the first fission barrier heights B_f (in MeV). See text for details.

parameter β_2 are shown. A nucleus undergoes fission process when the nucleus becomes highly elongated along an axis. This can be done most simply by modifying the single-particle potential with the help of a constraint, i.e., the Lagrangian multiplier λ. Then, the system becomes more or less compressed depending on the Lagrangian multiplier λ. In other words, in a constraint calculation, we minimize the expectation value of the Hamiltonian $< H' >$ instead of $< H >$, which are related to each other by the relation [118–122]:

$$H^{'} = H - \lambda Q, \qquad with \qquad Q = r^2 Y_{20}(\theta, \phi), \tag{3.10}$$

where λ is fixed by the condition $< Q >_\lambda = Q_0$.

Usually, in an axially deformed constraint calculation for a nucleus, we see two maxima in the PES diagram: (i) prolate and (ii) oblate or spherical. However, in some cases, more than two maxima are seen. If the ground state energy is distinctly more than other maxima, then the nucleus has a well-defined ground-state configuration. On the other hand, if the difference in BEs between two or three maxima is negligible,

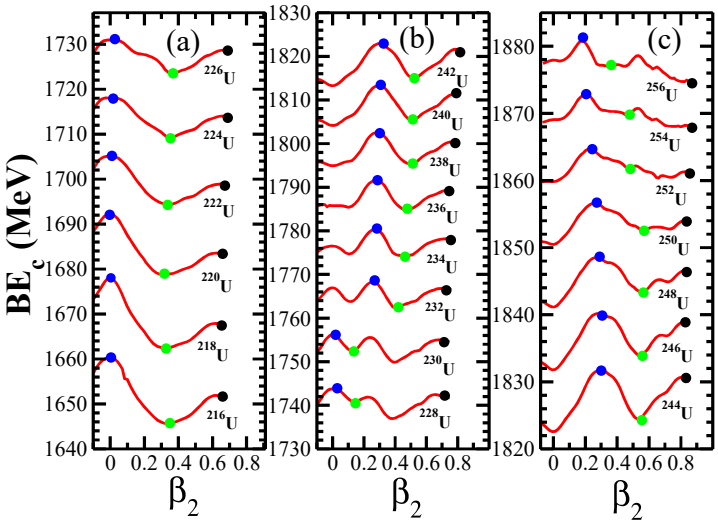

Figure 3.3: Same as Fig. 3.2, but for U isotopes.

then the nucleus is in the shape coexistence configuration. In this case, a configuration mixing calculation is needed to determine the ground-state solution of the nucleus, which is beyond the scope of the present calculation. It is to be noted here that in a constraint calculation, the maximum BE (major peak in the PES diagram) corresponds to the ground-state configuration and all other solutions (minor peaks in the PES curve) are the intrinsic excited states.

The fission barrier B_f is an important quantity for study the properties of fission reaction. We calculate the fission barrier from the PES curve for some selected even-even nuclei, which are listed in Table 3.3. From the table, it can be seen that the fission barrier for ^{228}Th turns out to be 5.69 MeV, comparable to the FRDM and experimental values of $B_f = 7.43$ and 6.50 MeV, respectively. Similarly, the calculated B_f of ^{232}U is 5.65 MeV, which also agrees well with the experimental data, 5.40 MeV. In some cases, the fission barrier height is 1−2 MeV lower or higher than the experimental data. The double-humped fission barrier is reproduced in all these cases. Similar types of calculations are done in Refs. [123–126].

In nuclei like $^{228-230}$Th and $^{228-234}$U, we find three maxima. Among these maxima, two are found at normal deformation (spherical and normal prolate), but the third

Table 3.3: First fission barrier heights B_f (in MeV) of some even-even actinide nuclei from RMF(NL3) calculations compared with FRDM and experimental data [56].

Nucleus	$B_f^{cal.}$	B_f^{FRDM} [56]	$B_f^{exp.}$ [56]
^{228}Th	5.69	7.43	6.50
^{230}Th	5.25	7.57	7.0
^{232}Th	4.85	7.63	6.30
^{234}Th	4.34	7.44	6.65
^{232}U	5.65	6.61	5.40
^{234}U	6.30	6.79	5.80
^{236}U	6.64	6.65	5.75
^{238}U	7.15	4.89	5.90
^{240}U	7.66	5.59	5.80

one is situated far away, i.e., at a relatively large quadrupole deformation. Upon careful inspection, one can also see that one of them (mostly the peak nearer to the spherical region) is not strongly pronounced and can be ignored in certain cases. This third maximum separates the second barrier by a depth of $1-2$ MeV, responsible for the formation of resonance state, which has been observed experimentally [127]. For some of the uranium isotopes $^{216-230}$U, the ground states are predicted to be spherical in the RMF formalism, agreeing with the FRDM results. The other isotopes in the series $^{232-256}$U are found to be in the prolate ground state, matching the experimental data. Similarly, the thorium nuclei $^{216-226}$Th are spherical in shape and $^{228-264}$Th are in the prolate ground configuration. In addition to these shapes, we also note sallow regions in the PES curves of both Th and U isotopes. These fluctuation in the PES curves could be due to the limitation of mean field approximation and one needs a theory beyond mean-field to overcome such fluctuations. For example, the Generator Coordinate Method or Random Phase Approximation could be an improved formalism to take care of such effects [128]. Beyond the second hump, we

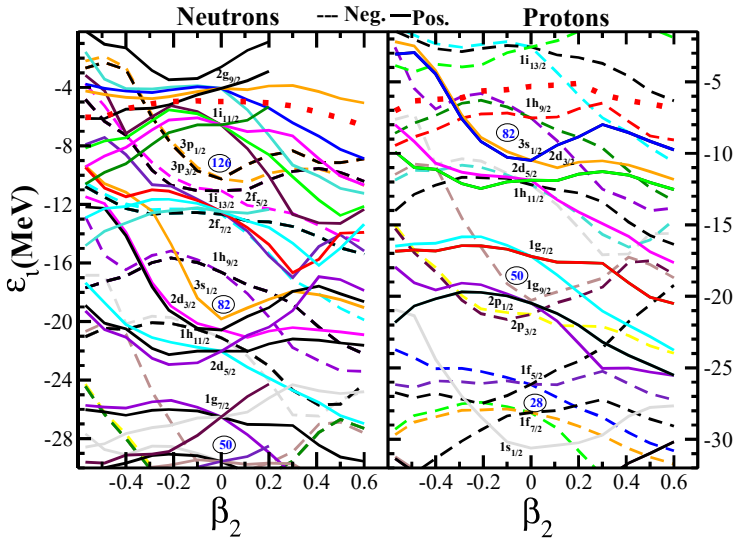

Figure 3.4: Single-particle energy levels for ^{232}Th as a function of the quadrupole deformation parameter β_2. The Fermi levels are denoted by the dotted(red) curve.

find the PES curve goes down and down, and never up again. This is the process wherein the liquid drop gets more and more elongated and reaches the fission stage. The PES curve from which it starts to go down is marked by the scission points, which are shown by the rightmost, black dot on the PES curves of Figs. 3.2 and 3.3.

3.3.4 Evolution of single-particle energy with deformation

In this subsection, we evaluate the neutron and proton single-particle energy levels for some selected Nilssion orbits with different values of deformation parameter β_2 using the constraint calculations. The results are shown in Figs. 3.4 and 3.5, which explain the origin of the shape change along the α decay chains of the thorium and uranium isotopes. The positive-parity orbit is shown by solid line, negative-parity orbit by dashed lines and the dotted (red) line indicates the Fermi energy for ^{232}Th and ^{236}U.

For small-Z nuclei, the electrostatic repulsion is very weak, but at a higher value of Z (superheavy nuclei), the electrostatic repulsion is much stronger so that the nuclear liquid drop becomes unstable to surface distortion [129] and fission. In such

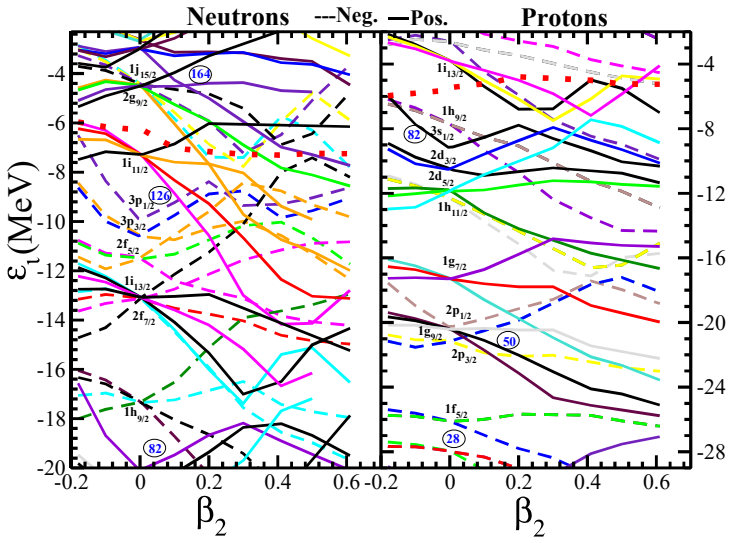

Figure 3.5: Same as Fig. 3.4 but for the ^{236}U nucleus.

a nucleus, the single-particle density is very high and the energy separation is small, which determines that the shell stabilizes the unstable Coulomb repulsion. This effect is clear for heavy elements approaching N=126, with a gap between $3p_{1/2}$ and $1i_{11/2}$ of about 2−3 MeV, in a neutron single-particle of ^{236}U and ^{232}Th. In both Figs.3.4 and 3.5, the neutron single-particle energy level $1i_{13/2}$ lies between $2f_{7/2}$ and $2f_{5/2}$, creating a distinct shell gap at N=114. In ^{232}Th and ^{236}U, with increasing deformation the opposite-parity levels of $2g_{9/2}$ and $1j_{15/2}$,which are far apart in the spherical solution, come close to each other. This gives rise to the parity doublet phenomena [49,130,131].

3.4 Mode of decays

In this section, we will discuss various mode of decays encounter by these thermally fissile nuclei both in the β-stability line and away from it. This is important, because the utility of heavy, and mostly, nuclei which are away from stability lines depends very much on their lifetime. For example, we do not get ^{233}U and ^{239}Pu in nature, because of their short lifetimes, although these two nuclei are extremely useful for energy production. That is why ^{235}U is the most needed isotope in the uranium

series, for its thermally fissile nature in energy production in the fission process, both for civilian and for military use. The common mode of instability for such heavy nuclei are spontaneous fission, α, β, and *cluster* decays. All these decays depend on the neutron-to-proton ratio as well as the number of nucleons present in the nucleus.

3.4.1 α- and β-decays half-lives

In some previous work [99,100], it has been analyzed the densities of nuclei in a more detailed manner. From that analysis, we concluded that there is no visible cluster either in the ground or in the excited intrinsic states. The possible clusterizations are the α-like matter in the interior and neutron-rich matter in the exterior region of normal and neutron-rich superheavy nuclei, respectively. Thus, the possible mode of decays are α decay for β-stable nuclei and β^- decay for neutron-rich isotopes. To estimate the stability of such nuclei, we have to calculate the α-decay $T_{1/2}(\alpha)$ and the β-decay $T_{1/2}(\beta)$ half-lives times.

The Q_α energy and α-decay half-life $T^\alpha_{1/2}$

To calculate the α decay half-life $T^\alpha_{1/2}$, one has to know the Q_α energies of the nucleus. This can be estimated by knowing the BEs of the parents and daughter and the BE of the α particle, i.e., the BE of ^{4}He. The BEs are obtained from experimental data wherever available and from other mass formulas as well as the RMF Lagrangian as have been discussed earlier in Ref. [132]. The Q_α energy is evaluated by using the relation:

$$\begin{aligned} Q_\alpha(N,Z) &= BE(N,Z) - BE(N-2,Z-2) \\ &- BE(2,2). \end{aligned} \tag{3.11}$$

Here, $BE(N,Z)$, $BE(N-2,Z-2)$ and $BE(2,2)$ are the BEs of the parent, daughter, and ^{4}He nuclei (BE= 28.296 MeV) with neutron number N and proton number Z.

Knowing the Q_α values of nuclei, we roughly estimate the α decay half-lives $log_{10}T^\alpha_{1/2}(s)$ of various isotopes using the phenomenological formula of Viola and Seaborg [134]:

$$log_{10}T^\alpha_{1/2}(s) = \frac{(aZ-b)}{\sqrt{Q_\alpha}} - (cZ+d) + h_{log}. \tag{3.12}$$

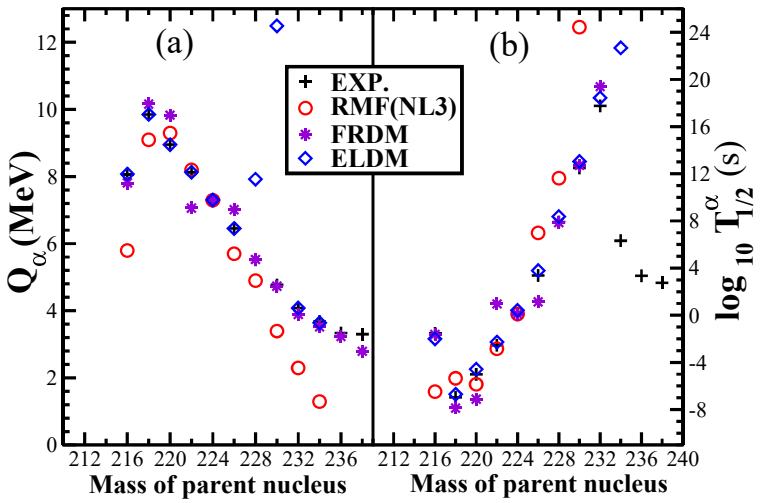

Figure 3.6: The Q_α and half-life time $T^\alpha_{1/2}$ of the α decay chain for Th isotopes are calculated using RMF, FRMD [56, 113], and ELDM [133] and compared with the experiment (EXP.) [15].

The value of the parameters a, b, c, and d are taken from the recent modified parametrizations of Sobiczewski *et al.* [135], which are $a = 1.66175$, $b = 8.5166$, $c = 0.20228$, $d = 33.9069$. The quantity h_{log} accounts for the hindrances associated with the odd proton and neutron numbers as given by Viola and Seaborg [134], namely

$$h_{log} = \begin{cases} 0, & \text{Z and N even} \\ 0.772, & \text{Z odd and N even} \\ 1.066, & \text{Z even and N odd} \\ 1.114, & \text{Z and N odd.} \end{cases}$$

The $Q_\alpha-$values obtained from RMF calculations for Th and U isotopes are shown in Figs. 3.6 and 3.7. Our results also compared with other theoretical predictions [113, 133] and experimental data [112]. The agreement of RMF results with others as well as with experiment is pretty well. Although the agreement in Q_α value is quite good, one must note that the $T^\alpha_{1/2}(s)$ values may vary a lot, because of the exponential factor in the equation. That is why it is better to compare $log_{10}T^\alpha_{1/2}(s)$ instead of $T^\alpha_{1/2}(s)$ values. These are compared in the right panel in Figs. 3.6 and 3.7. We note

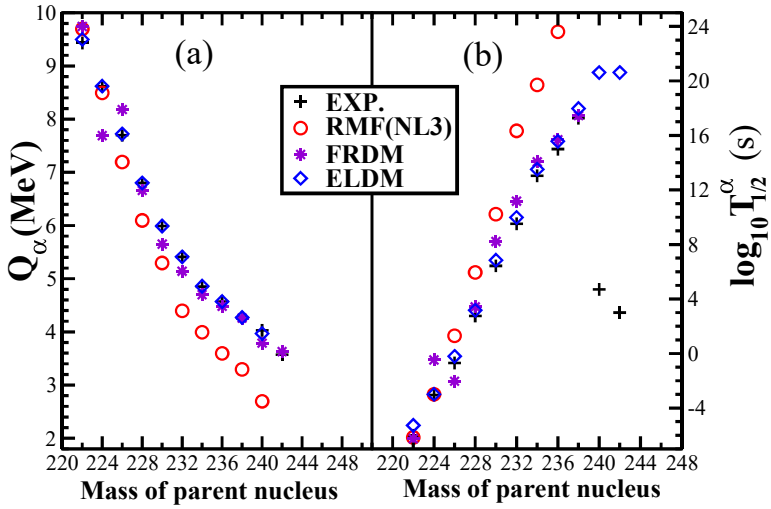

Figure 3.7: Same as Fig. 3.6, but for U.

that our prediction matches well with other calculations as well as experimental data.

Further, a careful analysis of $log_{10}T^{\alpha}_{1/2}$ (in seconds) for even-even thorium reveals that the Q_α value decreases with an increase in the mass number A of the parent nucleus. The Q_α energy of Th isotopes given by Duarte *et al.* [133] deviates a lot when mass of the parent nucleus reaches A=230. The corresponding $log_{10}T^{\alpha}_{1/2}$ increases almost monotonically linearly with an increase in mass number of the same nucleus. The experimental values of $log_{10}T^{\alpha}_{1/2}$ deviate a lot in the heavy mass region (with parent nuclei 234-238). A similar situation is found in the case of uranium isotopes also, which are shown in Fig. 3.7. It is noteworthy that the origin of α decay or *cluster* decay phenomena are purely quantum mechanical process. Thus the quantum tunneling plays an important role in such decay processes. The deviation of experimental α decay lifetime from the calculated results obtained by the empirical formula may not be suitable for such heavy nuclei, which are away from the stability line, and more involved quantum mechanical treatment is needed for such cases.

3.4.2 Quantum mechanical calculation of α-decay half-life $T_{1/2}^{WKB}$

In this subsection, we do an approximate evaluation of the α decay half-life using a quantum mechanical approach. This approach is used recently [98] for the evaluation of proton-emission as well as cluster decay. The obtained results satisfactorily match with known experimental data. Since these nuclei are prone to α decay or spontaneous fission, we need to calculate these decays to examine the stability. It is shown by Satpathy *et al.* [96] that by addition of neutrons to Th and U isotopes, the neutron-rich nuclei become surprisingly stable against spontaneous fission. Thus, the possible modes of decay may be α and β emission. To estimate the α decay, one needs the optical potential of the α and daughter nuclei, where a bare nucleon-nucleon potential, such as M3Y [101], LR3Y [102], NLR3Y [103] or DD-M3Y [136] interaction is essential. In our calculations, we have taken the widely used M3Y interaction for this purpose. For simplicity, we use spherical densities of the cluster and daughter. Here, ρ_c is the cluster density of the α particle and the daughter nucleus ρ_d are obtained from RMF(NL3) formalism [29]. Then, the nucleus-nucleus optical potential is calculated by using the well-known double-folding procedure to the M3Y [101] nucleon-nucleon interaction, supplemented by a zero-range pseudopotential representing the single-nucleon exchange effects (EX). The Coulomb potential V_c is added to obtain the total interaction potential $V(R) = V_n(R) + V_c(R)$. When the α particle tunnels through the potential barrier between two turning points, the probability of emission of the α particle is obtained by the WKB approximation. Using this approximation, we have made an attempt to investigate the α decay of the neutron-rich thorium and uranium isotopes. The double folded [101, 137] interaction potential V_n(M3Y+EX) between the alpha cluster and daughter nucleus having densities ρ_c and ρ_d is

$$V_n(\vec{R}) = \int \rho_c(\vec{r_c})\rho_d(\vec{r_d})v|\vec{r_c} - \vec{r_d} + \vec{R} = s|d^3r_c d^3r_d, \tag{3.13}$$

where $v(s)$ is the zero-range pseudopotential representing the single-nucleon exchange effects,

$$v(s) = 7999\frac{e^{-4s}}{4s} - 2134\frac{e^{-2.5s}}{2.5s} + J_{00}(E)\delta(s), \tag{3.14}$$

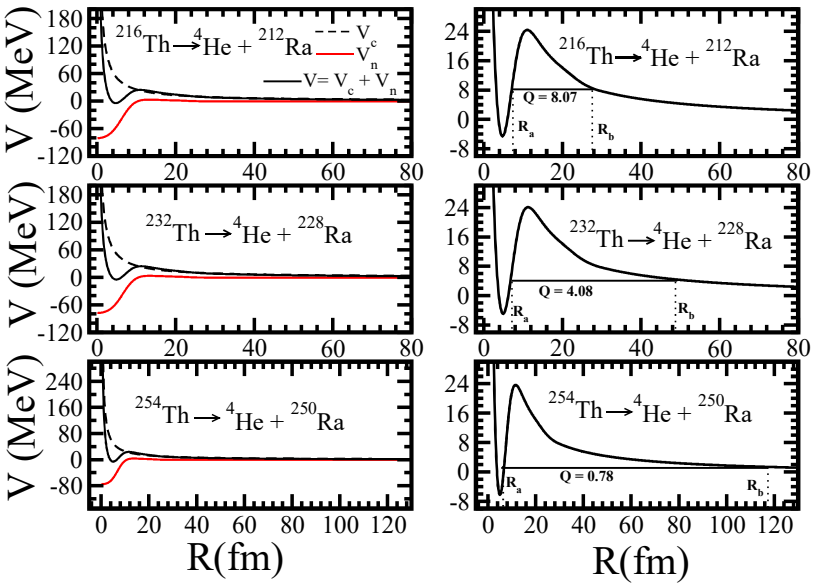

Figure 3.8: In the left panel of the plot Coulomb potential $V_c(R)$, total interaction potential V(R) and folded potential $V_n(R)$(M3Y+EX) for Th isotopes are given. In the right panel of the figure the penetration path with an energy equal to the Q(MeV) value of the α-decay shown by horizontal line.

with the exchange term [138]

$$J_{00}(E) = -276(1 - 0.005E/A_\alpha(c))MeVfm^3. \tag{3.15}$$

Here, $A_\alpha(c)$ is the mass of the cluster, i.e., the α particle mass and E is energy measured in the center of mass of the α particle or the cluster-daughter nucleus system, equal to the released $Q-$value. The Coulomb potential between the α and daughter nucleus is

$$V_c(R) = Z_c Z_d e^2/R, \tag{3.16}$$

and total interaction potential is

$$V(R) = V_n(R) + V_c(R). \tag{3.17}$$

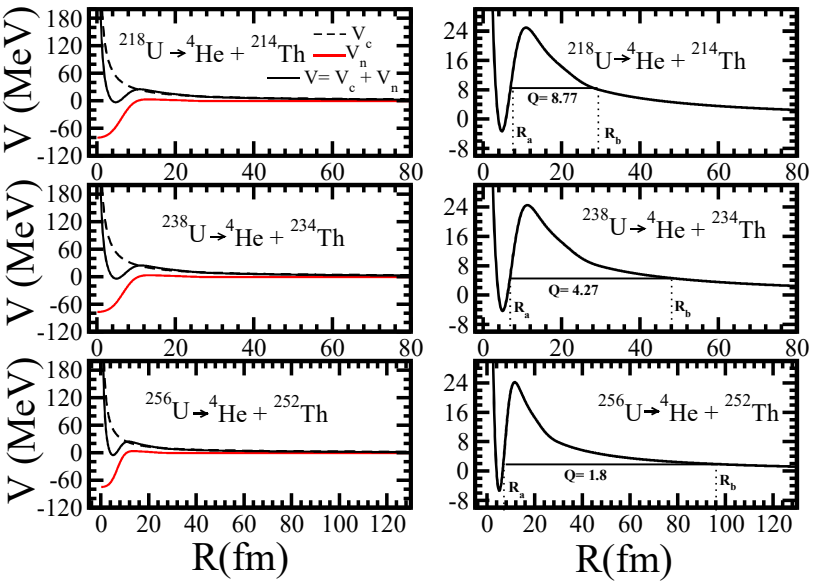

Figure 3.9: Same as Fig. 3.8, but for U.

When the α particle tunnels through a potential barrier of two turning points R_a and R_b, then the probability of the α decay is given by

$$P = exp\left[-\frac{2}{\hbar}\int_{R_a}^{R_b} 2\mu[V(R) - Q]^{1/2} dR \right]. \tag{3.18}$$

The decay rate is defined as

$$\lambda = \nu P, \tag{3.19}$$

with the assault frequency $\nu = 10^{21}$ s^{-1}. The half-life is calculated as:

$$T_{1/2}^{WKB} = \frac{0.693}{\lambda}. \tag{3.20}$$

The total interaction potential (black curve) of the daughter and α nuclei are shown in Figs. 3.8 and 3.9. The central well is due to the average nuclear attraction of all the nucleons and the hill-like structure is due to the electric repulsion of the protons. The α particle with Q-value trapped inside the two turning points R_a and R_b of the barrier. The penetration probability P is given in the third column of Table 3.4 for

Table 3.4: The penetrability P is evaluated using WKB approximation. The half-lives $T_{1/2}^{WKB}$ and $T_{1/2}^{\alpha}$ are calculated by quantum mechanical tunneling processes and Viola - Seaborg formula [134]. Experimental Q_α values are used for known masses and for unknown nuclei, Q_α obtained from RMF.

Parent	Q_α(MeV)	P	$T_{1/2}^{WKB.}$(s.)	$T_{1/2}^{\alpha}$(s.)
^{216}Th	8.072 [15]	2.109×10^{-21}	3.28×10^{-1}	3.0×10^{-3}
^{232}Th	4.081 [15]	6.17×10^{-37}	1.12×10^{17}	5.07×10^{17}
^{254}Th	0.78 [RMF]	1.90×10^{-55}	3.6×10^{35}	1×10^{107}
^{218}U	8.773 [15]	1.26×10^{-20}	5.5×10^{-2}	1.0×10^{-4}
^{238}U	4.27 [15]	1.163×10^{-37}	5.95×10^{15}	2.219×10^{17}
^{256}U	1.8 [RMF]	3.783×10^{-44}	1.83×10^{22}	1.218×10^{55}

some selected cases of thorium and uranium isotopes. The probabilities for ^{216}Th and ^{218}U are relatively high, because of the small width as compared to its barrier height. So, it is easier for the α particle to escape from these two turning points.

As we increase the number of neutron in a nucleus, the Coulomb force becomes weak due to the hindrance of repulsion among the protons. In such cases, the width of the two turning points is very large and the barrier height is small. Thus, the probability of α decay for ^{254}Th and ^{256}U is almost infinity and this type of nuclei are stable against α or *cluster* decays. These neutron-rich thermally fissile Th and U isotopes are also stable against spontaneous fission. Since these are thermally fissile nuclei, a feather touch deposition of energy with thermal neutron, it undergoes fission. Thus, half-life of the spontaneous fission is nearly infinity. We have compared our quantum mechanical tunneling results with the empirical formula of Viola and Seaborg [134] in Table 3.4. For known nuclei, like ^{232}Th and ^{238}U both the results match well, however, it deviates enormously from each other for unknown nuclei both in neutron-rich and neutron-deficient region. In general, independent of the formula or model used, the α decay mode is rare for ultra-asymmetric nuclei. In such isotopes, the possible decay mode is the β decay.

3.4.3 β-decay

As we have discussed, the prominent mode of instability of neutron-rich Th and U nuclei is the β decay, we have given an estimation of such decay in this subsection. Actually, the β-decay lifetime should be evaluated on the microscopic level, but that is beyond the present thesis. Here we have used the empirical formula of Fiset and Nix [139], which is defined as:

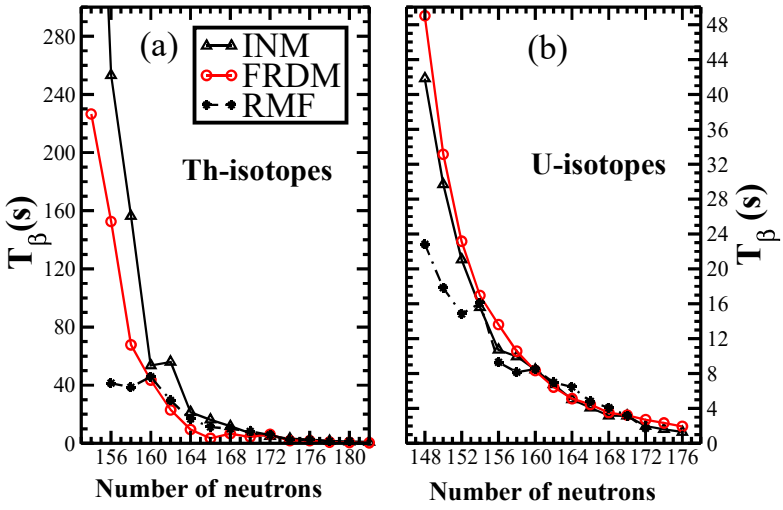

Figure 3.10: The β-decay half-lives for Th and U isotopes are calculated using the formula of Fiset and Nix [139] [eq. (24)]. Ground-state binding energies are taken from FRDM [113], INM [140], and RMF models.

$$T_\beta = (540 \times 10^{5.0}) \frac{{m_e}^5}{\rho_{d.s.}({W_\beta}^6 - {m_e}^6)} s. \tag{3.21}$$

Similar to the α decay, we evaluate the Q_β value for Th and U series using the relation $Q_\beta = BE(Z+1, A) - B(Z, A)$ and $W_\beta = Q_\beta + {m_e}^2$. Here, $\rho_{d.s.}$ is the average density of states in the daughter nucleus ($e^{-A/290}$ $\times$ number of states within 1 MeV of the ground state). To evaluate the bulk properties, such as BE of odd-Z nuclei, we used the Pauli blocking prescription as discussed in Sec. 3.2.1. The obtained results are displayed in Fig. 3.10 for both Th and U isotopes. From the figure, it is clear that for neutron-rich Th and U nuclei, the prominent mode of decay is β decay. This means

that once a neutron-rich thermally fissile isotope is formed by some artificial means in the laboratory or naturally in supernovae explosion, it immediately undergoes β decay. In our rough estimation, the lifetime of ^{254}Th and ^{256}U, which are the nuclei of interest, is tens of seconds. If this prediction of time period is acceptable, then on the nuclear physics scale, it is reasonably a good time for further use of the nuclei. It is worth to mention here that thermally fissile isotopes in the Th and U series have neutron number N=154-172 keeping N=164 in the middle of the island. So, in the case of the short lifetime of ^{254}Th and ^{256}U, one can choose a lighter isotope of the series for practical utility.

3.5 Conclusions

In summary, we have done a thorough structural study of recently predicted thermally fissile isotopes in the Th and U series in the framework of RMF theory. Although there are certain limitations of the present approach, the qualitative results will remain unchanged even when the drawbacks of the model taken into account. The heavier isotopes of these two nuclei show various shapes including very large prolate deformations in highly excited configurations. The change in single-particle orbits along the line of quadrupole deformation are analyzed and parity doublet states found in some cases. Using an empirical estimation, we find that the neutron-rich isotopes of these thermally fissile nuclei are predicted to be stable against α and *cluster* decays. Spontaneous fission also does not occur, because the presence of a large number of neutrons makes the fission barrier broader. However, these nuclei are highly β unstable. Our calculation predicts that the β lifetime is tens of seconds for ^{254}Th and ^{256}U and this time increases for nuclei that have lower neutron number but thermally fissile. This finite lifetime of these thermally fissile isotopes could be very useful for energy production with nuclear reactor technology. If these neutron-rich nuclei are used as nuclear fuel, the reactor will achieve critical conditions much more rapidly than with normal nuclear fuel, because of the release of a large number of neutrons during the fission process.

Chapter 4

Relative mass distributions of neutron-rich thermally fissile nuclei

In this chapter, we study the binary mass distribution for the recently predicted thermally fissile neutron-rich uranium and thorium nuclei using statistical model. The level density parameters needed for the study are evaluated from the excitation energies of the temperature dependent relativistic mean field formalism. The excitation energy and the level density parameter for a given temperature are employed in the convolution integral method to obtain the probability of the particular fragmentation. As representative cases, we present the results for the binary yields of ^{250}U and ^{254}Th. The relative yields are presented for three different temperatures: T = 1, 2 and 3 MeV.

4.1 Introduction

The fission phenomenon is one of the most interesting subjects in the field of nuclear physics. To study fission properties, a large number of models have been proposed. The fissioning of a nucleus is successfully explained by the liquid drop model, and the semi-empirical mass formula is the best and simple oldest tool to get a rough estimation of the energy released in a fission process. The pioneering work of Vautherin and Brink [141], who applied the Skyrme interaction in a self-consistent method for the calculation of ground-state properties of finite nuclei, opened a new dimension

in the quantitative estimation of nuclear properties. Subsequently, the Hartree-Fock and time dependent Hartree-Fock formalisms [142] were also implemented to study the properties of fission. Most recently, the microscopic relativistic mean field approximation, which is another successful theory in nuclear physics, is also used for the study of nuclear fission [143].

In the last few decades, the availability of neutron-rich nuclei in various laboratories across the globe opened up new research in the field of nuclear physics, because of their exotic decay properties. The effort towards the synthesis of superheavy nuclei in laboratories such as Dubna (Russia), GSI (Germany), RIKEN (Japan) and BNL (USA) is also quite remarkable. Due to all these, the periodic table has been extended, to date, upto atomic number $Z = 118$ [144]. The decay modes of these superheavy nuclei are very different than the usual modes. Mostly, we understand that a neutron-rich nucleus has a large number of neutron than nuclei in the light or medium mass region of the periodic table. The study of these neutron-rich superheavy nuclei is very interesting because of their ground-state structures and various mode of decays, including multifragment fission (more than two fragments) [143]. Another interesting feature of some neutron-rich uranium and thorium nuclei is that, similar to ^{233}U, ^{235}U and ^{239}Pu, the nuclei $^{246-264}$U and $^{244-262}$Th are also thermally fissile, which is extremely important for energy production in the fission process. If the neutron-rich uranium and thorium nuclei are viable sources, then these nuclei will be more effective for achieving the critical condition in a controlled fission reaction.

Now the question arises, how we can get a reasonable estimation of the mass yield in the spallation reaction of these neutron-rich thermally fissile nuclei? As mentioned earlier in this section, there are many formalisms available in the literature to study these cases. Here, we adopt the statistical model developed by Fong [53]. The calculation is further extended by Rajasekaran and Devanathan [54] to study the binary mass distributions using the single-particle energies of the Nilsson model. The obtained results are in good agreement with the experimental data. In the present study, we would like to replace the single-particle energies with the excitation energies of a successful microscopic approach: the relativistic mean field (RMF) formalism.

For last few decades, the RMF formalism [25, 79, 79, 104] with various parameter sets has successfully reproduced the bulk properties, such as binding energies,

root-mean-square radii, quadrupole deformation, etc., not only for nuclei near the $\beta-$stability line but also for nuclei away from it. Further, the RMF formalism has been successfully applied to the study of clusterization of known cluster emitting heavy nucleus [97,145,146] and the fission of hyper-hyper deformed ^{56}Ni nucleus [147]. Rutz *et al.* [148] reproduced the double, and triple humped fission barrier of ^{240}Pu, ^{232}Th and the asymmetric ground-states of ^{226}Ra using the RMF formalism. Moreover, the symmetric and asymmetric fission modes are also successfully reproduced. Patra *et al.* [143] studied the neck configuration in the fission decay of neutron-rich U and Th isotopes. The main goal of this present chapter is to understand the binary fragmentation yields of such neutron-rich thermally fissile superheavy nuclei. ^{250}U and ^{254}Th are taken for further calculations as the representative cases. We have used the temperature dependent relativistic mean field (TRMF) as described in chapter 2, which modifies the BCS pairing (in Sec. 2.2).

4.2 Formalism

The possible binary fragments of the considered nucleus are obtained by equating the charge-to-mass ratio of the parent nucleus to the fission fragments as [55]:

$$\frac{Z_P}{A_P} \approx \frac{Z_i}{A_i}, \tag{4.1}$$

with A_P, Z_P and A_i, Z_i ($i = 1$ and 2) correspond to mass and charge numbers of the parent nucleus and the fission fragments [54]. The constraints, $A_1+A_2 = A$, $Z_1+Z_2 = Z$ and $A_1 \geq A_2$ are imposed to satisfy the conservation of charge and mass number in a nuclear fission process and to avoid the repetition of fission fragments. Another constraint i.e., the binary charge numbers from $Z_2 \geq 26$ to $Z_1 \leq 66$, is also taken into consideration from the experimental yield [149] to generate the combinations, assuming that the fission fragments lie within these charge range.

4.2.1 Statistical theory

The statistical theory [53, 150] assumes that the probability of the particular fragmentation is directly proportional to the folded level density ρ_{12} of that fragments

with the total excitation energy E^*, i.e., $P(A_j, Z_j) \propto \rho_{12}(E^*)$. Here,

$$\rho_{12}(E^*) = \int_0^{E^*} \rho_1(E_1^*)\, \rho_2(E^* - E_1^*)\, dE_1^*, \tag{4.2}$$

and ρ_i is the level density of two fragments ($i = 1,\ 2$). The nuclear level density [151, 152] is expressed as a function of fragment excitation energy E_i^* and the single-particle level density parameter a_i:

$$\rho_i\left(E_i^*\right) = \frac{1}{12}\left(\frac{\pi^2}{a_i}\right)^{1/4} E_i^{*(-5/4)} \exp\left(2\sqrt{a_i E_i^*}\right). \tag{4.3}$$

In Refs. [55,153], the excitation energies of the fragments using the ground state single-particle energies of finite range droplet model (FRDM) [113] at a given temperature T keeping the total number of proton and neutron fixed is calculated. In the present study, we apply the self-consistent TRMF theory to calculate the E^* of the fragments. The excitation energy is calculated as,

$$E_i^*(T) = E_i(T) - E_i(T = 0). \tag{4.4}$$

The level density parameter a_i is given as,

$$a_i = \frac{E_i^*}{T^2}. \tag{4.5}$$

The relative yield is calculated as the ratio of the probability of a given binary fragmentation to the sum of the probabilities of all the possible binary fragmentations:

$$Y(A_j, Z_j) = \frac{P(A_j, Z_j)}{\sum_j P(A_j, Z_j)}, \tag{4.6}$$

where A_j and Z_j refer to the binary fragmentations involving two fragments with mass and charge numbers A_1, A_2 and Z_1, Z_2 obtained from Eq. (4.1). The competing basic decay modes such as neutron/proton emission, α decay, and ternary fragmentation are not considered. In addition to these approximations, we have also not included the dynamics of the fission reaction, which are really important to get a quantitative comparison with the experimental measurements. The presented results are the prompt disintegration of a parent nucleus into two fragments (democratic breakup). The resulting excitation energy would be liberated as prompt particle emission or delayed emission, but such secondary emissions are also ignored.

4.3 Results and discussions

In our very recent work [154], we have calculated the ternary mass distributions for ^{252}Cf, ^{242}Pu and ^{236}U with the fixed third fragments $A_3 =$ ^{48}Ca, ^{20}O and ^{16}O respectively for the three different temperatures $T = 1$, 2 and 3 MeV within the TRMF formalism. The structure effects of binary fragments are also reported in Ref. [155]. In this article, we study the mass distribution of ^{250}U and ^{254}Th as representative cases from the range of neutron-rich thermally fissile nuclei $^{246-264}$U and $^{244-262}$Th. Because of the neutron-rich nature of these nuclei, a large number of neutrons are emitted during the fission process. These nucleons help to achieve the critical condition much sooner than the normal fissile nuclei.

To assure the predictability of the statistical model, we also study the binary fragmentation of naturally occurring ^{236}U and ^{232}Th nuclei. The possible binary fragments are obtained using Eq. (4.1). To calculate the total binding energy at a given temperature, we use the axially symmetric harmonic oscillator basis expansion N_F and N_B for the Fermion and Boson wave-functions to solve the Dirac and the Klein Gordon Eqs. (as described in chapter 2, Sec. 2.1) iteratively. It is reported [156] that the effect of basis space on the calculated binding energy, quadrupole deformation parameter (β_2) and the rms radii of nucleus are almost equal for the basis set $N_F = N_B = 12$ to 20 in the mass region A $\sim$ 200 . Thus, we use the basis space $N_F = 12$ and $N_B = 20$ to study the binary fragments up to mass number A $\sim$ 182. The binding energy is obtained by minimizing the free energy, which gives the most probable quadrupole deformation parameter β_2 and the proton (neutron) pairing gaps $\triangle_p$ ($\triangle_n$) for the given temperature. At finite temperature, the continuum corrections due to the excitation of nucleons need to be considered. The level density in the continuum depends on the basis space N_F and N_B [157]. It is shown that the continuum corrections need not be included in the calculations of level densities up to the temperature T $\sim$ 3 MeV [158, 159].

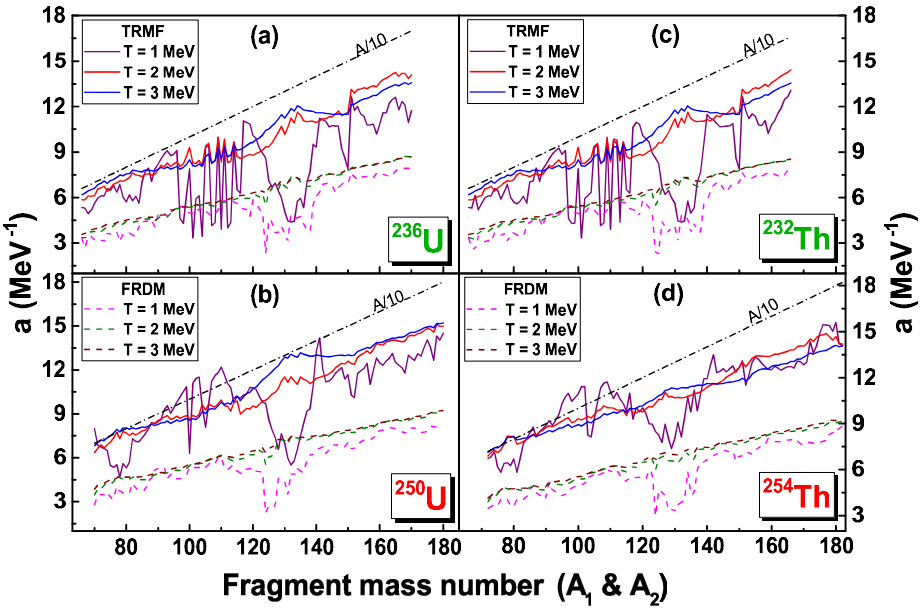

Figure 4.1: The level density parameter a for the binary fragmentation of ^{236}U, ^{250}U, ^{232}Th, and ^{254}Th at temperature $T = 1$, 2 and 3 MeV within the TRMF (solid lines) and FRDM (dashed lines) formalisms.

4.3.1 Level density parameter and level density within TRMF and FRDM formalisms

In TRMF, the excitation energies E^* and the level density parameters a_i of the fragments are obtained self consistently from Eqns. (4.4) to (4.5). The FRDM calculations are also done for comparison. In this case, level density of the fragments are evaluated from the ground-state single-particle energies of the FRDM of Möller *et al.* [56] which are retrieved from the Reference Input Parameter Library (RIPL-3) [160]. The total energy at a given temperature is calculated as $E(T) = \sum n_i \epsilon_i$; ϵ_i are the ground-state single-particle energies and n_i are the Fermi-Dirac distribution function. The T-dependent energies are obtained by varying the occupation numbers at a fixed particle number for a given temperature and given fragment. The level density parameter a is a crucial quantity in the statistical theory for the estimation of yields. These values of a for the binary fragments of ^{236}U, ^{250}U, ^{232}Th and ^{254}Th obtained from TRMF and FRDM are depicted in Fig. 4.1. The empirical estimations

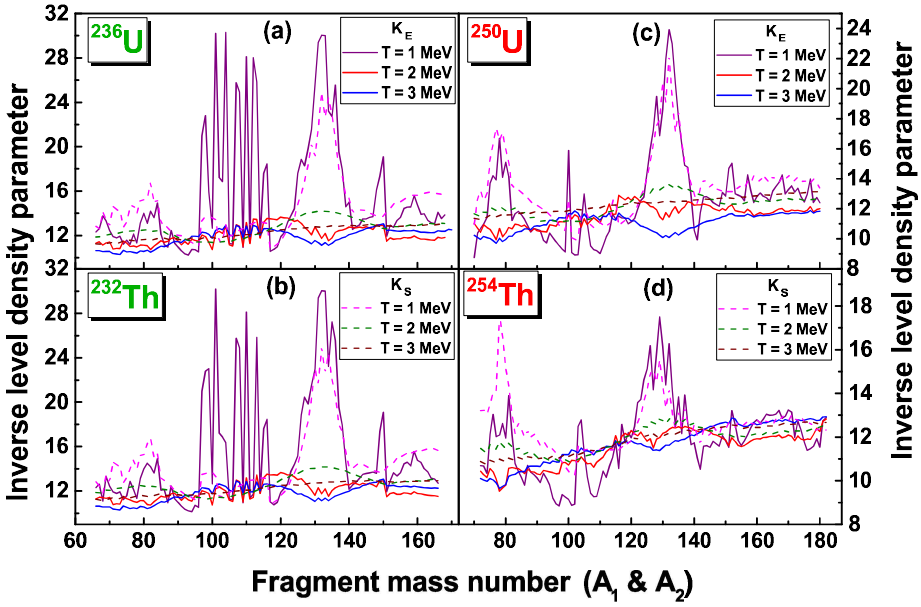

Figure 4.2: The inverse level density parameters K_E (solid lines) and K_S (dashed lines) are obtained for ^{236}U, ^{250}U, ^{232}Th, and ^{254}Th at temperatures T = 1, 2 and 3 MeV.

$a = A/K$ are also given for comparison, with K being the inverse level density parameter. In general, the K value varies from 8 to 13 with the increasing temperature. However, the level density parameter is considered to be constant up to $T \approx$4 MeV. Hence, we take the practical value of $K = 10$ as mentioned in Ref. [161]. The a values of TRMF are close to the empirical level density parameter. The FRDM level density parameters are appreciably lower than the referenced a. Further, in both models at $T = 1$ MeV, there are more fluctuations in the level density parameter due to the shell effects of the fragments. At $T = 2$ and 3 MeV, the variations are small. This may be due to the fact that the shell become degenerate at the higher temperatures. All fragments becomes spherical at temperature $T \approx$3 MeV as shown in Ref. [155].

The level density parameter a is evaluated in two different ways using excitation energy and the entropy of the system as:

$$a_E = \frac{E^*}{T^2}, \qquad a_S = \frac{S}{2T}. \tag{4.7}$$

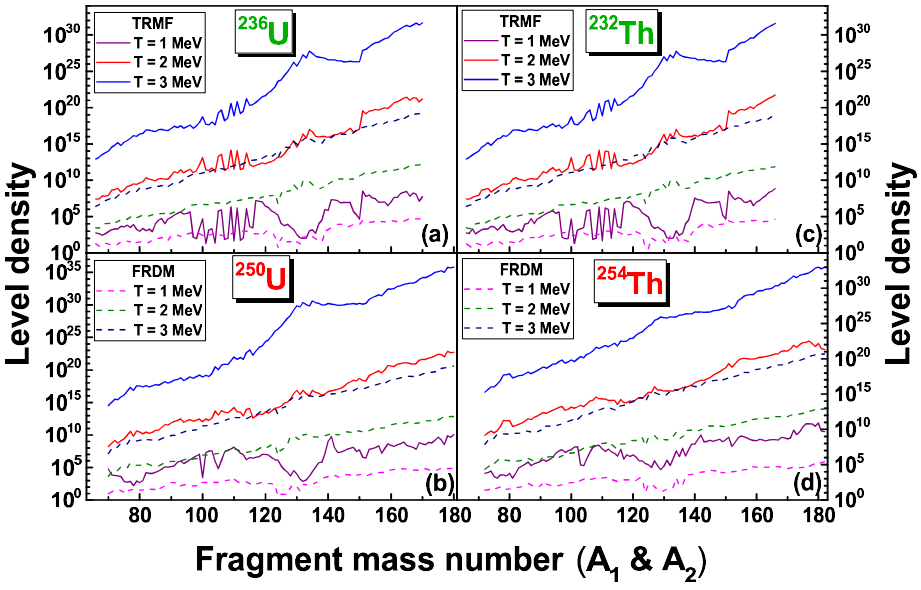

Figure 4.3: The level density of the binary fragmentations of ^{236}U, ^{250}U, ^{232}Th, and ^{254}Th at temperature $T = 1$, 2 and 3 MeV within the TRMF (solid lines) and FRDM (dashed lines) formalisms.

For instance, the inverse level density parameters K_E and K_S of ^{236}U, ^{250}U, ^{232}Th, and ^{254}Th within TRMF formalism are depicted in Fig. 4.2. Both K_S and K_E have maximum fluctuation upto 30 MeV at T =1 MeV. These values reduce to $10-13$ MeV at temperature $T = 2$ MeV or above. It is to be noted that at $T = 3$ MeV, the inverse level density parameter substantially lower around the mass number $A \sim$130 in all cases. This may be due to the neutron closed shell ($N = 82$) in the fission fragments of ^{236}U and ^{232}Th and the neutron-rich nuclei ^{250}U and ^{254}Th. The level density for the fission fragments of ^{236}U, ^{250}U, ^{232}Th and ^{254}Th are plotted as a function of mass number in Fig. 4.3 within the TRMF and FRDM formalisms at three different temperatures, $T = 1$, 2 and 3 MeV.

The level density ρ has maximum fluctuations at $T = 1$ MeV for all considered nuclei in TRMF model, similar to the level density parameter a. The ρ values are substantially lower at mass number $A \sim 130$ for all nuclei. In Fig. 4.3, one can notice that the level density has small kinks in the mass region $A \sim 71 - 81$ of ^{236}U and $A \sim 77 - 91$ of ^{250}U, compared with the neighboring nuclei at temperature $T = 2$ MeV. Consequently, the corresponding partner fragments have also higher ρ

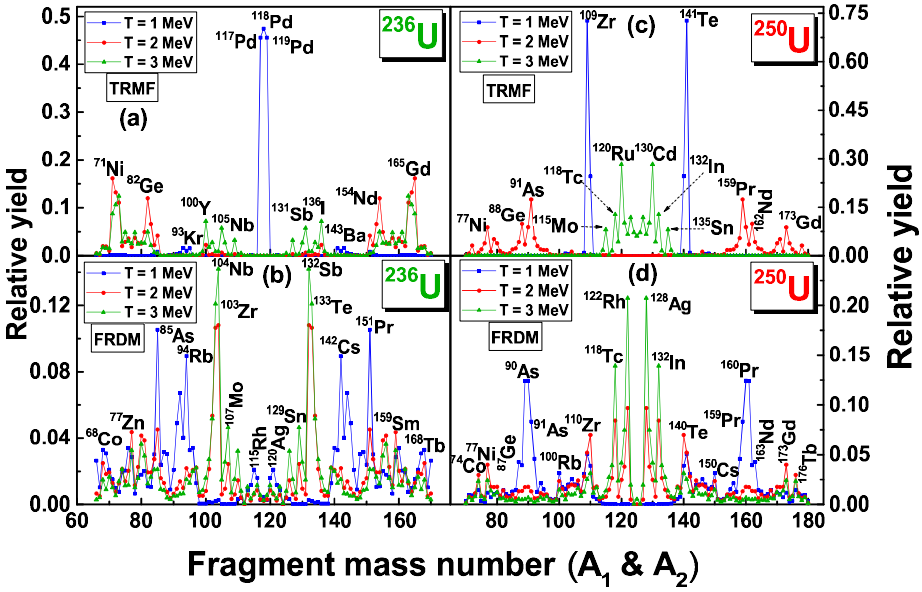

Figure 4.4: Mass distribution of ^{236}U and ^{250}U at temperatures $T = 1$, 2 and 3 MeV. The total yield values are normalized to the scale 2.

values. A further inspection reveals that the level density of the closed shell nucleus around $A \sim 130$ has higher value than the neighboring nuclei for both ^{236,250}U, but it has lower yield due to the smaller level density of the corresponding partners. At $T = 3$ MeV, the level density of the fragments around mass number $A \sim$72 and 130 have larger values compared to other fragments of ^{236}U. On the other hand, the level density in the vicinity of neutron number $N = 82$ and proton number $Z = 50$ for the fragments of the neutron-rich ^{250}U nucleus is quite high, because of the close shell of the fragments. This is evident from the small kink in the level density of ^{130}Cd ($N = 82$), ^{132}In ($N \sim 82$) and ^{135}Sn ($Z = 50$). Again, for ^{232}Th, the level densities are found to be maximum at around mass number $A \sim$81 and 100 for $T = 2$ MeV. In case of ^{254}Th, the ρ values are found to be large for the fragments around $A \sim 78$ and 97 at $T = 2$ MeV. Their corresponding partners have also similar behavior. For higher temperature $T = 3$ MeV, the higher ρ values of ^{232}Th fragments are notable around mass number $A \sim 130$. Similarly, for ^{254}Th, the fission fragments around $A \sim 78$ have higher level density at $T = 3$ MeV. In general, the level density increases towards the neutron closed shell ($N = 82$) nucleus.

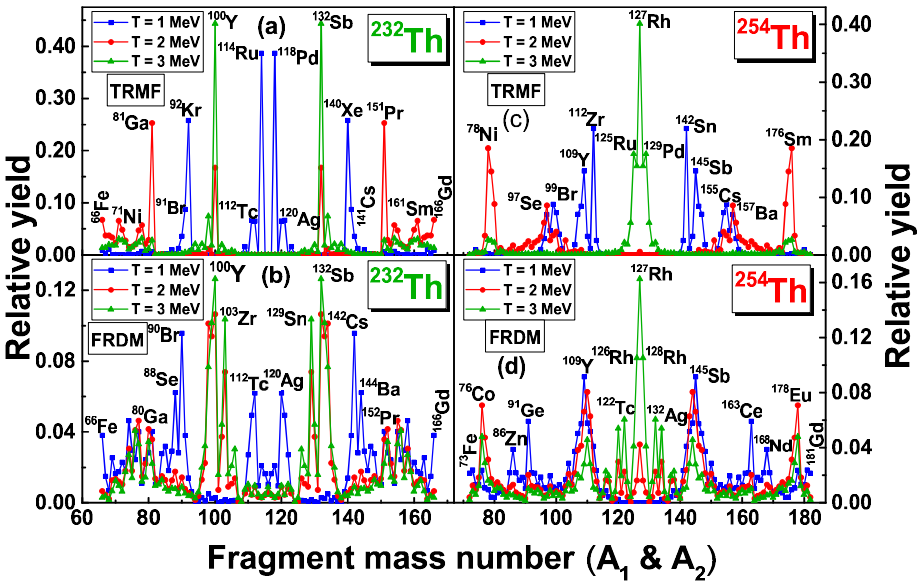

Figure 4.5: Mass distribution of ^{232}Th and ^{254}Th at temperatures T = 1, 2 and 3 MeV. The total yield values are normalized to the scale 2.

4.3.2 Relative fragmentation distribution in binary systems

In this section, the mass distributions of ^{236}U, ^{232}Th and the neutron-rich nuclei ^{250}U and ^{254}Th are calculated at temperatures T = 1, 2 and 3 MeV using TRMF and FRDM excitation energies and the level density parameters a as explained in Sec. 4.2. The binary mass distributions of ^{236,250}U and ^{232,254}Th are plotted in Figs. 4.4 and 4.5. The total energy at finite temperature and ground-state energy are calculated using the TRMF formalism as discussed in Sec. 4.3.1. From the excitation energy E* and the temperature T, the level density parameter a and the level density ρ of the fragments are calculated using Eq. (4.3). From the fragment level densities ρ_i, the folding density ρ_{12} is calculated using the convolution integral as in Eq. (4.2) and the relative yields are calculated using Eq. (4.6). The total yields are normalized to the scale 2.

The mass yield of normal nuclei ^{236}U and ^{232}Th are briefly explained first, followed by a detailed description of the neutron-rich nuclei. The results of most favorable fragment yields of ^{236,250}U and ^{232,254}Th are listed in Table 4.1 at three different temperatures T = 1, 2 and 3 MeV, for both TRMF and FRDM formalisms. From Figs. 4.4 and 4.5, it is shown that the mass distributions for ^{236}U and ^{232}Th are quite

different from those of the neutron-rich ^{250}U and ^{254}Th isotopes.

The symmetric binary fragmentation ^{118}Pd $+^{118}$Pd for ^{236}U is the most favorable combination. In TRMF, the fragments with close shell ($N = 100$ and $Z = 28$) combinations are more probable at the temperature $T = 2$ MeV. The blend region of neutron and proton close shell ($N \approx 82$ and $Z \approx 50$) has the considerable yield values at $T = 3$ MeV. The fragmentations ^{151}Pr $+^{85}$As, ^{142}Cs $+^{94}$Rb and ^{144}Ba $+^{92}$Kr are the favorable combinations at temperature $T = 1$ MeV in FRDM formalism. For higher temperatures $T = 2$ and 3 MeV, the closed shell or near closed shell fragments ($N = 82$, 50 and $Z = 28$) have larger yields. From Fig. 4.5 in TRMF formalism, the combinations ^{118}Pd $+^{114}$Ru and ^{140}Xe $+^{92}$Kr are the possible fragments at $T = 1$ MeV for the nucleus ^{232}Th. At $T = 2$ MeV, we find maximum yields for the fragments with the close shell or near close shell combinations ($N = 82$, 50). For higher temperature $T = 3$ MeV, near the neutron close shell ($N \sim 82$), ^{132}Sb $+^{100}$Y is the most favorable fragmentation pair compared with all other yields. Similar fragmentations are found in the FRDM formalism at $T = 2$ and 3 MeV. In addition, the probability of the evaluation of ^{129}Sn $+^{103}$Zr is also quite substantial in the fission process. For $T = 1$ MeV, the yield is more or less similar with the TRMF model.

From Fig. 4.4, for ^{250}U the fragment combinations ^{140,141}Te $+^{110,109}$Zr have the maximum yields at $T = 1$ MeV in TRMF. This is also consistent with the evolution of the subclosed proton shell $Z = 40$ in Zr isotopes [162]. Contrary to this almost symmetric binary yield, the mass distribution of this nucleus in FRDM formalism an asymmetric evolution of fragment combinations such as ^{160,159}Pr $+^{90,91}$As, ^{163,162}Nd$+^{87,88}$Ge and ^{150}Cs $+^{100}$Rb. Interestingly, at $T = 2$ and 3 MeV, the more favorable fragment combinations have one of the closed shell nuclei. At $T = 2$ MeV, ^{159}Pr $+^{91}$As, ^{162}Nd $+^{88}$Ge and ^{173}Gd $+^{77}$Ni are the more probable fragmentations (see Fig. 4.4(c)). It is reported by Satpathy *et al.* [163] and experimentally verified by Patel *et al.* [164] that $N = 100$ is a neutron close shell for the deformed region, where $Z = 62$ acts like a magic number. In FRDM, ^{128}Ag $+^{122}$Rh, ^{132}In $+^{118}$Tc, ^{140}Te $+^{110}$Zr and ^{173}Gd $+^{77}$Ni have larger yield at temperature $T = 2$ MeV. With the TRMF method, the most favorable fragments are confined in the single region ($A \approx 114 - 136$) which is a blend of vicinity of neutron ($N = 82$) and proton ($Z = 50$) closed shell nuclei at $T = 3$ MeV. The fragment combinations ^{130}Cd $+^{120}$Ru, ^{132}In

$+^{118}$Tc and ^{135}Sn $+^{115}$Mo are the major yields for ^{250}U at $T = 3$ MeV in TRMF calculations. With the FRDM method, at $T = 3$ MeV, more probable fragments are similar those at $T = 2$ MeV. A comparison between Fig. 4.4(c) and 4.4(d) clarifies that, although the prediction of FRDM and TRMF at $T = 3$ MeV are qualitatively similar, they are quantitatively very different at $T = 2$ MeV in both the predictions. Also, from Fig. 4.4, it is inferred that the yields of the fragment combinations in blend region increases and in other regions decreases at $T = 2$ MeV.

In the present study, the total energy of the parent nucleus A is more than the sum of the energies of the daughters A_1 and A_2. Here, the dynamics of entire process starting from the initial stage up to the scission are ignored. As a result, the energy conservation in the spallation reaction is not taken into account. The fragment yield can be regarded as the relative fragmentation probability, which is obtained from Eq. (4.6). Now we analyze the fragmentation yields for Th isotopes and the results are depicted in Fig. 4.5 and Table 4.1. In this case, one can see that the mass distribution broadly spreads through out the region $A_i = 66 - 166$. Again, the most concentrated yields can be divided into two regions I (A_1 = 141-148 and A_2 = 106-113) and II (A_1 = 152-158 and A_2 = 102-96) for ^{254}Th in TRMF formalism at the temperature $T = 1$ MeV. The most favorable fragmentation ^{142}Sn $+^{112}$Zr is obtained from region I. The other combinations in that region have also considerable yields. In region II, the isotopes of Ba and Cs appears, curiously, along with their corresponding partners. Categorically, in FRDM predictions, region I has larger yields at $T = 1$ MeV. The other possible fragmentations are ^{163}Ce $+^{91}$Ge, ^{168}Nd $+^{86}$Zn and ^{181}Gd $+^{73}$Fe (See Fig. 4.5 (b,d)). The mass distribution is different with different temperature, and the maximum yields at $T = 2$ MeV in TRMF formalism are ^{174,175,176}Sm $+^{80,79,78}$Ni. Apart from these combinations, there are other considerable yields can be seen in Fig. 4.5 for region II. The prediction of maximum probability of the fragments production in FRDM method are ^{144}Sb $+^{110}$Y, ^{178}Eu $+^{76}$Co and ^{127}Rh $+^{127}$Rh at $T = 2$ MeV. Besides these yields, one can find other notable evolution of masses in region I due to the vicinity of the proton close shell. Interestingly, at $T = 3$ MeV, the symmetric binary combination ^{127}Rh $+^{127}$Rh has the largest yield due to the neutron close shell ($N = 82$) of the fragment ^{127}Rh. The other yield fragments have exactly or nearly a magic nucleon combination, mostly neutron ($N = 82$) as one of the fragment. A

considerable yield is also seen for the proton close shell ($Z = 28$) Ni or/and (Z =62) Sm isotopes supporting our earlier prediction [155]. This confirms the prediction of Sm as a deformed magic nucleus [163, 164]. Another observation of the present calculations show that the yields of the neutron-rich nuclei agree with the symmetric mass distribution of Chaudhuri *et al.* [165] at large excitation energy, which contradicts the recent prediction of large asymmetric mass distribution of neutron-deficient Th isotopes [166]. These two results [165, 166] along with our present calculations confirm that the symmetric or asymmetric mass distribution at different temperature depends on the proton and neutron combination of the parent nucleus. In general, both TRMF and FRDM predict maximum yields for both symmetric and asymmetric binary fragmentations followed by other secondary fragmentations emissions, depending on the temperature as well as the mass number of the parent nucleus. Thus, the binary fragments have larger level density ρ comparing with other nuclei because of neutron/proton close shell fragment combinations at $T = 2$ and 3 MeV. This results consistent with the fact that most favorable fragments have larger phase space than the neighboring nuclei as reported earlier [154, 155].

To this end, it may be mentioned that the differences in the mass distributions or the relative yields calculated using TRMF and FRDM approaches mainly arise due to the differences in the level densities associated with these approaches. The mean values and the fluctuations in the level density parameter and the corresponding level density are even qualitatively different in both the approaches considered. This possibly stems from the fact that the single-particle energies in the FRDM are temperature independent. The temperature dependence of the excitation energy, required to calculate the level density parameter, comes only from the modification of the single-particle occupancy due to the Fermi distribution. In the TRMF approach, the excitation energy for each fragment at a given temperature is calculated self-consistently. Therefore, the deformation and the single-particle energies changes with temperature.

For the neutron-rich nuclei, the fragments having neutron/proton close shell $N =$ 50, 82 and 100 have maximum possibility of emission at $T = 2$ and 3 MeV (for both nuclei ^{250}U and ^{254}Th). This is a general trend we could expect for all neutron-rich nuclei. It is worthwhile to mention some of the recent reports and predictions

Table 4.1: The relative fragmentation yield (R.Y.) = $Y(A_j, Z_j) = \dfrac{P(A_j, Z_j)}{\sum P(A_j, Z_j)}$ for ^{236}U, ^{250}U, ^{232}Th and ^{254}Th, obtained with TRMF at the temperatures T = 1, 2 and 3 MeV are compared with the FRDM prediction (The yield values are normalized to 2).

Parent	T (MeV)	TRMF		FRDM		Parent	T (MeV)	TRMF		FRDM	
		Fragment	R.Y.	Fragment	R.Y.			Fragment	R.Y.	Fragment	R.Y.
^{236}U	1	^{118}Pd + ^{118}Pd	0.949	^{151}Pr + ^{85}As	0.210	^{250}U	1	^{141}Te + ^{109}Zr	1.454	^{160}Pr + ^{90}As	0.248
		^{119}Pd + ^{117}Pd	0.910	^{142}Cs + ^{94}Rb	0.178			^{140}Te + ^{110}Zr	0.491	^{161}Pr + ^{89}As	0.247
		^{143}Ba + ^{93}Kr	0.032	^{144}Ba + ^{92}Kr	0.134			^{148}Xe + ^{102}Sr	0.014	^{159}Pr + ^{91}As	0.166
	2	^{165}Gd + ^{71}Ni	0.323	^{132}Sb + ^{104}Nb	0.216		2	^{159}Pr + ^{91}As	0.348	^{128}Ag + ^{122}Rh	0.193
		^{164}Gd + ^{72}Ni	0.264	^{133}Te + ^{103}Zr	0.213			^{162}Nd + ^{88}Ge	0.197	^{132}In + ^{118}Tc	0.168
		^{163}Gd + ^{73}Ni	0.0.221	^{151}Pr + ^{85}As	0.210			^{160}Pr + ^{90}As	0.176	^{140}Te + ^{110}Zn	0.140
		^{154}Nd + ^{82}Ge	0.240	^{159}Sb + ^{77}Zn	0.087			^{173}Gd + ^{77}Ni	0.175	^{141}Te + ^{109}Zn	0.100
	3	^{163}Gd + ^{73}Ni	0.249	^{132}Sb + ^{104}Nb	0.283		3	^{130}Cd + ^{120}Ru	0.565	^{128}Ag + ^{122}Rh	0.414
		^{164}Gd + ^{72}Ni	0.214	^{133}Te + ^{103}Zr	0.242			^{132}In + ^{118}Tc	0.255	^{132}In + ^{118}Tc	0.278
		^{136}I + ^{100}Y	0.143	^{134}Te + ^{102}Zr	0.102			^{127}Ag + ^{123}Rh	0.236	^{129}Ag + ^{121}Rh	0.149
		^{131}Sb + ^{105}Nb	0.114	^{129}Sn + ^{107}Mo	0.092			^{135}Sn + ^{115}Mo	0.161	^{130}Cd + ^{120}Ru	0.083
^{232}Th	1	^{118}Pd + ^{114}Ru	0.773	^{142}Cs + ^{90}Br	0.190	^{254}Th	1	^{142}Sn + ^{112}Zr	0.439	^{145}Sb + ^{109}Y	0.183
		^{140}Xe + ^{92}Kr	0.515	^{144}Ba + ^{88}Se	0.124			^{145}Sb + ^{109}Y	0.291	^{163}Ce + ^{91}Ge	0.118
		^{141}Cs + ^{91}Br	0.174	^{120}Ag + ^{112}Tc	0.123			^{155}Cs + ^{99}Br	0.176	^{144}Sb + ^{110}Y	0.115
		^{120}Ag + ^{112}Tc	0.129	^{158}Pm + ^{74}Cu	0.092			^{157}Ba + ^{97}Se	0.139	^{168}Nd + ^{86}Zn	0.077
	2	^{151}Pr + ^{81}Ga	0.505	^{132}Sb + ^{100}Y	0.213		2	^{176}Sm + ^{78}Ni	0.370	^{144}Sb + ^{110}Y	0.161
		^{132}Sb + ^{100}Y	0.334	^{134}Te + ^{98}Sr	0.202			^{175}Sm + ^{79}Ni	0.290	^{178}Eu + ^{76}Co	0.141
		^{166}Gd + ^{66}Fe	0.134	^{129}Sn + ^{103}Zr	0.146			^{157}Ba + ^{97}Se	0.172	^{144}Sb + ^{110}Y	0.132
	3	^{132}Sb + ^{100}Y	0.886	^{132}Sb + ^{100}Y	0.252		3	^{127}Rh + ^{127}Rh	0.803	^{127}Rh + ^{127}Rh	0.325
		^{134}Te + ^{98}Sr	0.148	^{129}Sn + ^{103}Zr	0.207			^{129}Pd + ^{125}Ru	0.350	^{127}Rh + ^{127}Rh	0.210
		^{155}Nd + ^{77}Zn	0.063	^{134}Te + ^{98}Sr	0.153			^{128}Rh + ^{126}Rh	0.307	^{132}Ag + ^{122}Tc	0.120

of multifragment fission for neutron-rich uranium and thorium nuclei. When such a neutron-rich nucleus breaks into nearly two fragments, the products exceed the drip-line, leaving few nucleons (or light nuclei) free. As a result, these free particles along with the scission neutrons enhance the chain reaction in a thermonuclear device. These additional particles (nucleons or light nuclei) responsible for reaching the critical condition much faster than in the usual fission for normal thermally fissile nucleus. Thus, the neutron-rich thermally fissile nuclei, such as $^{246-264}$U and $^{244-262}$Th, will be very useful for energy production.

4.4 Summary and conclusions

The fission mass distributions of $\beta-$stable nuclei ^{236}U and ^{232}Th and the neutron-rich thermally fissile nuclei ^{250}U and ^{254}Th are studied within a statistical model. The possible combinations are obtained by equating the charge-to-mass ratio of the parents to that of the fragments. The excitation energies of fragments are evaluated from the temperature dependent self-consistent binding energies at the given T and the ground-state binding energies which are calculated from the RMF model. The level densities and the yields combinations are manipulated using the convolution integral approach. The fission mass distributions of the aforementioned nuclei are also evaluated from the FRDM formalism for comparison. The level density parameter a and inverse level density parameter K are also studied to see the difference between results with these two methods. Besides fission fragments, the level densities are also discussed in the present chapter. For ^{236}U and ^{232}Th, the symmetric and nearly symmetric fragmentations are more favorable at temperature $T = 1$ MeV. Interestingly, in most of the cases we find one of the favorable fragment has a close shell or near close shell configuration (N = 82,50 and $Z = 28$) at temperature $T = 2$ and 3 MeV. Further, Zr isotopes has larger yield values for ^{250}U and ^{254}Th with their accompanying possible fragments at $T = 1$ MeV. The Ba and Cs isotopes with their partners are also more possible for ^{254}Th. This could be due to the deformed close shell in the region $Z = 52 - 66$ of the periodic table [167]. The Ni isotopes and the neutron close shell ($N \sim 100$) nuclei are some of the prominent yields for both ^{250}U and ^{254}Th at temperature $T = 2$ MeV. At $T = 3$ MeV, the neutron close shell ($N = 82$) is one of

the largest yield fragments. The symmetric fragmentation ^{127}Rh $+^{127}$Rh is possible for ^{254}Th due to the N =82 close shell occurs in binary fragmentation. For ^{250}U, the larger yield values are confined to the junction of neutron and proton closed shell nuclei.

Chapter 5

Tidal deformability

In this chapter[3], we systematically study the tidal deformability for neutron and hyperon stars using relativistic mean field equations of state (EoSs). The tidal effect plays an important role during the early part of the evolution of compact binaries. Although, the deformability associated with the EoSs has a small correction, it gives a clean gravitational wave signature in binary inspiral. These are characterized by various Love numbers k_l (l=2, 3, 4), that depend on the EoS of a star for a given mass and radius. The tidal effect of star could be efficiently measured through advanced LIGO detector from the final stages of inspiraling binary neutron star merger.

5.1 Introduction

When two neutron stars approach, they come under the influence of each other via gravity and then get distorted. As an after effect is that tides are raised exactly the same way as tides are created on Earth due to Moon. The newly formed tides pick the energy out of the orbit resulting in the speedy motion of the inspiral. This can be detected and measured in the form of gravitational waves. Larger are the size of the neutron stars, bigger are the tides formed. From the equation of state we can determine the size of neutron stars alongwith its tidal deformation. Moreover, in the experimental front, from the measurements of the neutron star masses and extent of tidal deformation their size and equation of state can be calculated.

[‡]This paper was published before the detection of gravitational waves from binary neutron star merger.

Consider two bodies A, and B as shown in the Fig 5.1, which are separated by a distance r and both the bodies are having a typical size of radius R [168, 169]. We assume that $R < r$, which indicates that the binaries are entirely isolated. Also, each body is surrounded by a vacuum region which we call as the buffer zone. When the objects are very close to each other, they will share their outer envelopes. As the bodies are isolated from one another neither any ejection of matter has taken place nor accreted. The orbital motion of each body will get affected when the binaries start interacting and transfer their masses.

The dynamics of the external and internal body is governed by the mutual gravitational interaction, which yields the orbital timescale given by $T_{orb} \sim (r^3/m)^{1/2}$, where m is the mass of the typical body. Similarly, the internal dynamics of the inner body is controlled by the hydrodynamical process, that gives the internal times scale $T_{int} \sim (R^3/m)^{1/2}$. Subsequently, the internal and external dynamics take place over the widely separated time scale ($T_{int} << T_{orb}$), which means that both the dynamics have decoupled mostly from one another. Notice that the star's dynamics are not fully decoupled. For example, Moon is responsible for formation of tides on Earth and it is because of the orbital position of the Moon. Then the tidal deformation of the Earth modifies its gravitational potential. As a result, it affects the orbit of the

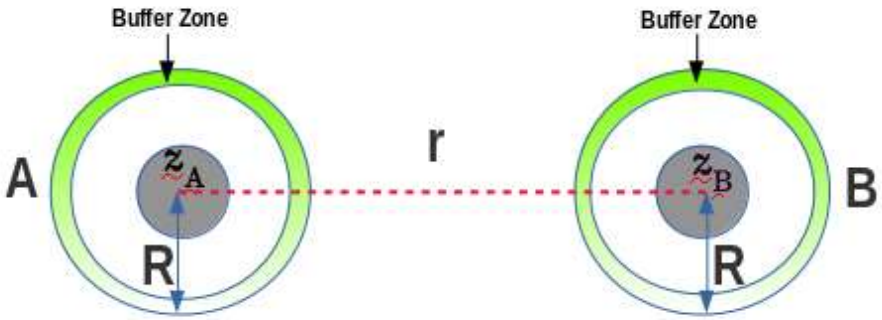

Figure 5.1: Plot for the two body system . The light green shaded region represents the weak-field buffer zone. The center-of-mass of each body is z_A, and z_B, respectively. The space-time is decomposed into a weak-field region and a strong-field region surrounding each compact object (gray).

Moon.

5.1.1 Newtonian tidal interactions

Newton's law of universal gravitation predicts that the gravitational force between two objects is proportional to the objects masses and inversely proportional to the square of the distance between them. The law, which applies to weakly interacting objects traveling at speed much slower than that of light. As we know that the Newtonian gravity is used as a limit of weak-field relativistic gravity, based on this Einstien developed the concept of curvature space-time and general relativity. Newtonian gravity is conveniently formulated in a fixed rectilinear coordinate system in terms of an absolute time coordinate.

We consider each body is constituted of N number of arbitrary points as shown in Fig. 5.1. Then, the total potential u is a linear superposition of the individual potentials created by each body. Hence we can write the gravitational potential at position $\vec{x}$ due to the point mass [170–172]

$$u = -\sum_A \frac{M}{|\vec{x} - \vec{x'}|}, \tag{5.1}$$

and also due to a system of the extended object with density ρ

$$u = -\int d^3x' \frac{\rho(\vec{x'})}{|\vec{x} - \vec{x'}|} \quad . \tag{5.2}$$

To calculate the dynamics of the extended objects, we determine the external and internal potentials of each body. The total potential is represented as $u = u_A^{int} + u_A^{ext}$.

Using Taylor's series expansion, we expand a field $\phi(\vec{x})$ around $\vec{z_A}$ as

$$\begin{aligned}
\phi(\vec{x}) &= \phi(\vec{z_A}) + (\vec{x} - \vec{z_A}) \frac{\partial \phi(\vec{x})}{\partial \vec{x}}\Big|_{\vec{z_A}} + \frac{(\vec{x} - \vec{z_A})^2}{2} \frac{\partial^2 \phi(\vec{x})}{\partial^2 \vec{x}}\Big|_{\vec{z_A}} + \dots \\
&= \phi(\vec{z_A}) + (x - z_A)^i \partial_i \phi(\vec{x})\Big|_{\vec{z_A}} + (x - z_A)^i (x - z_A)^j \partial_i \partial_j \phi(\vec{x})\Big|_{\vec{z_A}} + \dots \\
&= \sum_{l=0} \frac{1}{l!} (x - z_A)^L \partial_L \phi(\vec{x})\Big|_{\vec{z_A}}.
\end{aligned} \tag{5.3}$$

where L is a multi-index representing the l indices such as $(x-z_A)^L = (x-z_A)^i(x-z_A)^j \ldots (x-z_A)^l$ and $\partial_L = \partial/\partial x^i\ \partial/\partial x^j \ldots \partial/\partial x^l$. Now, we write the internal potential at a point $\vec{z_A}$ using Eq. (5.2)

$$\begin{aligned} u_A^{int}(\tilde{x}) &= -\sum_{l=0}^{\infty} \frac{(-1)^l}{l!} \int d^3\vec{x'} \rho_A(\vec{x'})(x'-z_A)^L \partial_L \Big(\frac{1}{|\vec{x}-\vec{x'}|} \Big) \Big|_{\vec{x'}=\vec{z_A}} \\ &= -\sum_{l=0}^{\infty} \frac{(-1)^l}{l!} \int d^3\vec{x'} \rho_A(\vec{x'})(x'-z_A)^L \partial_L \Big(\frac{1}{r} \Big) \Big|_{\vec{x'}=\vec{z_A}}, \end{aligned} \tag{5.4}$$

where $r = |\vec{x}-\vec{x'}| = \sqrt{\delta_{ij}x^i x^j}$, and $n^i = \frac{x^i}{r}$. We note that $\partial_L \frac{1}{|\vec{x}-\vec{x'}|}$ is a symmetric trace free(STF) tensor for $\vec{x} \neq \vec{x'}$ because the trace of any pair of indices $\partial_i \partial_i \frac{1}{|\vec{x}-\vec{x'}|} = \Delta^2 \frac{1}{|\vec{x}-\vec{x'}|} = -4\pi\delta^{(3)}(\vec{x}-\vec{x'})$ is zero unless $\vec{x}$ coincides with the center-of-mass [173]. Now, we use the following identities [168]:

$$\begin{aligned} (i)\ \partial_j r &= \partial_j \sqrt{\delta_{ik}x^i x^k} = \frac{1}{2r}\delta_{ik}\Big[\delta_{ij}x^k + \delta_{jk}x^i\Big] \\ &= \frac{1}{2r}\Big[\delta_{jk}x^k + \delta_{ij}x^i\Big] = \frac{1}{2r}\Big[2x^j\Big] = n^j \end{aligned} \tag{5.5}$$

$$\begin{aligned} (ii)\ \partial_j n_k &= \partial_j\Big(\frac{x^k}{r}\Big) = \frac{\delta_{jk}}{r} - \frac{1}{r^2}x^k\partial_j r \\ &= \frac{\delta_{jk}}{r} - \frac{1}{r^2}x^k n^j = \frac{1}{r}(\delta_{jk} - n_j n_k) \end{aligned} \tag{5.6}$$

$$(iii)\ \partial_j\Big(\frac{1}{r}\Big) = -\frac{1}{r^2}\partial_j r = -\frac{1}{r^2}n_j \tag{5.7}$$

$$(iv)\ \partial_L\Big(\frac{1}{r}\Big) = \sum_{l=0}^{\infty}(-1)^l(2l-1)!!\frac{n^{<L>}}{r^{l+1}} \tag{5.8}$$

The internal potential at a point $\vec{x}$ can now be written as

$$\begin{aligned} u_A^{int} &= -\sum_{l=0}^{\infty}\frac{(-1)^l}{l!}\partial_L\Big(\frac{1}{r}\Big)\Big|_{\vec{x'}=\vec{z_A}} \int d^3\vec{x'}\rho_A(\vec{x'})(x'-z_A)^L \\ &= -\sum_{l=0}^{\infty}\frac{(-1)^l}{l!}\partial_L\Big(\frac{1}{r}\Big)\Big|_{\vec{x'}=\vec{z_A}} M_A^L \\ &= -\sum_{l=0}^{\infty}\frac{(-1)^l}{l!}(-1)^l(2l-1)!!\frac{n^{<L>}}{r^{l+1}}M_A^L \\ &= -\sum_{l=0}^{\infty}\frac{(2l-1)!!}{l!}\frac{n^{<L>}}{r^{l+1}}M_A^L, \end{aligned} \tag{5.9}$$

where M_A^L is the l^{th} multipole moment of the body defined by

$$M_A^L = \int d^3\vec{x'}\rho_A(\vec{x'})(x' - z_A)^L \tag{5.10}$$

$M_A = \int d^3x\ \rho\ , \quad l = 0$ for monopole
$M_A^i = \int d^3x\ \rho(x - z_A)^i = 0\ , \quad l = 1$ for dipole
$M_A^{ij} = \int d^3x\ \rho(x - z_A)^{<ij>} = Q_A^{ij}\ , \quad l = 2$ for quadrupole
where $(x - z_A)^{<ij>} = (x - z_A)^i(x - z_A)^j - \frac{1}{3}\delta_{ij}|\vec{x} - \vec{z_A}|^2$

$$n^{<ij>} = n^i n^j - \frac{1}{3}\delta^{ij}, \tag{5.11}$$

Similarly, we can expand the external potential about the center-of-mass of body A

$$\begin{aligned} u_A^{ext}(\vec{x}) &= \sum_{l=0} \frac{1}{l!}(x - z_A)^L \partial_L \phi_A^{ext}(\tilde{x})\Big|_{\tilde{x}=\tilde{z_A}} \\ &= \sum_{l=0} \frac{1}{l!}(x - z_A)^L \mathcal{E}_A^L. \end{aligned} \tag{5.12}$$

Where $\mathcal{E}_A^L$ is the external tidal field due to the potential from object B

$$\begin{aligned} \mathcal{E}_A^L &= -\partial_L u_A^{ext}(\vec{x})\Big|_{\vec{x}=\vec{z_A}} \\ &= -\partial_L u_B^{int}(\vec{x})\Big|_{\vec{x}=\vec{z_A}} \\ &= -\partial_L\Big(-\sum_{l=0}^{\infty}\frac{(-1)^l}{l!}M_B^L\partial_L\frac{1}{|\vec{x} - \vec{z_B}|}\Big)_{\vec{x}=\vec{z_A}} \\ &= \sum_{l=0}^{\infty}\frac{(-1)^l}{l!}M_B^L\partial_L\frac{1}{|\vec{z_A} - \vec{z_B}|} = \sum_{l=0}^{\infty}\frac{(-1)^l}{l!}M_B^L\partial_L\frac{1}{r_{AB}}. \end{aligned} \tag{5.13}$$

Here, $r_{AB} = |\vec{z_A} - \vec{z_B}|$ is the separation between two body. Some useful identities are:

$$\mathcal{E}^L = -\partial_L\Big(\frac{M_B}{r_{AB}}\Big). \tag{5.14}$$

for $L = 2$

$$\begin{aligned} \mathcal{E}^{ij} &= -\partial_i\partial_j\Big(\frac{M_B}{r_{AB}}\Big) \\ &= -\frac{M_B}{r_{AB}^3}(3n_in_j - \delta_{ij})_{AB} \\ &= -\frac{3M_B}{r_{AB}^3}(n_in_j - \frac{1}{3}\delta_{ij})_{AB} \\ &= -\frac{3M_B}{r_{AB}^3}n_{AB}^{<ij>}. \end{aligned} \tag{5.15}$$

5.1.2 Constructing the Lagrangian and energy describing a binary system of extended objects

The Lagrangian is constructed from the kinetic and potential energies of the system as $L = T - V$. Using the Lagrangian we can determine the equation of motion via the Euler-Lagrange equations.

First we consider the bodies to be inside their respective "buffer" zones as shown in Fig. 5.1, i.e. when the distances are large compared to the size of the body but small compared to the distance of the companion. The total kinetic energy for each object can be decomposed into the contributions from the center-of-mass of each body as well as from the internal kinetic energy about the center-of-mass of each body [172]:

$$\begin{aligned}
T &= T_A + T_B; \\
T &= \frac{1}{2}\int_A d^3x\ \rho\ \dot{\vec{z}}_A^2 + \frac{1}{2} M_B\ \dot{\vec{z}}_B^2 + T^{int} \\
&= \frac{1}{2} v^2 \Big[\frac{M_A M_B^2}{M^2} + \frac{M_B(-M_A^2)}{M^2} \Big] + T^{int} \\
&= \frac{1}{2} v^2 M_A M_B \Big[\frac{M_A + M_B}{M^2} \Big] + T^{int} \\
&= \frac{1}{2} v^2 \frac{M_A M_B}{M} + T^{int} \\
&= \frac{1}{2}\mu v^2 + T^{int}, \qquad (5.16)
\end{aligned}$$

where $\mu = \frac{M_A M_B}{M}$ is the reduced mass of the body.

Similarly, For the extended object A, the point-mass companion's potential is $M_B/|\vec{x} - \vec{z_B}|$. When this potential is expanded about A's center of mass it becomes

$$u_A^{companion} = \sum_{l=0}^{\infty} \frac{1}{l!} (x - z_A)^L \mathcal{E}_L. \qquad (5.17)$$

The potential energy V_A due to the center of mass motion $\vec{z_A}$ is

$$\begin{aligned}
V_A &= -\frac{1}{2}\int_A d^3x\ \rho_A\ u_A^{companion} \\
&= -\frac{1}{2}\int_A d^3x \Big(-\sum_{l=0}^{\infty} \frac{1}{l!} (\vec{x} - \vec{z_A})^L \mathcal{E}_L \Big) \rho_A \\
&= -\frac{M_A M_B}{2\, r_{AB}} + \frac{1}{2}\sum_{l=1}^{\infty} \frac{1}{l!} \mathcal{E}_L \int_A d^3x\ (\vec{x} - \vec{z_A})^L \rho_A \\
&= -\frac{M_A M_B}{2\, r_{AB}} + \frac{1}{4}\mathcal{E}_{ij} Q^{ij}. \qquad (5.18)
\end{aligned}$$

Similarly, the potential energy V_B of the point mass influenced by the field of the extended body is

$$\begin{aligned} V_B &= -\frac{1}{2} M_B u_B^{companion} \\ &= -\frac{1}{2} M_B \sum_{l=0}^{\infty} \frac{(2l-1)!!}{l!} \frac{n_B^{<L>}}{r_{BA}^{l+1}} M_L \\ &= -\frac{M_A M_B}{2\, r_{BA}} + \sum_{l=1}^{\infty} \frac{(2l-1)!!}{l!} \frac{n_B^{<L>}}{r_{BA}^{l+1}} M_L \\ &= -\frac{M_A M_B}{2\, r} - \frac{1}{2}\frac{3}{2} Q_{ij} M_B \frac{n_B^{<ij>}}{r^3} \\ &= -\frac{M_A M_B}{2\, r_{BA}} + \frac{1}{4} \mathcal{E}_{ij} Q^{ij}. \end{aligned} \tag{5.19}$$

Now, we want to calculate the total potential energy upto $l = 2$ and put $r_{AB} = r_{BA} = r$. Thus,

$$\begin{aligned} V &= V_A + V_B + V^{int}, \\ &= -\frac{M_A M_B}{r} + \frac{1}{2} \mathcal{E}_{ij} Q^{ij} + V^{int}. \end{aligned} \tag{5.20}$$

Hence, the total Lagrangian of the system can be written as

$$\begin{aligned} L &= \frac{1}{2}\mu v^2 + T^{int} - (-\frac{M_A M_B}{r} + \frac{1}{2} \mathcal{E}_{ij} Q^{ij} + V^{int}) \\ &= \frac{1}{2}\mu v^2 + \frac{M_A M_B}{r} - \frac{1}{2} \mathcal{E}_{ij} Q^{ij} + T^{int} - V^{int} \\ &= \frac{1}{2}\mu v^2 + \frac{M_A M_B}{r} - \frac{1}{2} \mathcal{E}_{ij} Q^{ij} + L_{int}(Q, \dot{Q}, ...)\ . \end{aligned} \tag{5.21}$$

The internal Lagrangian describes only the elastic potential energy associated with the tidal deformation [65]:

$$L_{int} = -\frac{1}{4\lambda} Q_{ij} Q^{ij}. \tag{5.22}$$

Where λ is the tidal deformability parameter. We will assume that the tidal effects are small and can be treated as a linear perturbation. The tidally induced adiabatic quadrupole moment is given by

$$Q_{ij} = -\lambda \mathcal{E}_{ij}. \tag{5.23}$$

Noted that Eq.(5.23) can be translated to a relativistic result within the same approximation and interpreting $\mathcal{E}$ regarding the curvature tensor, i.e. $\mathcal{E}_{ij} = R_{0i0j}$ call as Riemann tensor.

Eq. (5.21) can be written as

$$\begin{aligned} L &= \frac{1}{2}\mu v^2 + \frac{M_A M_B}{r} - \frac{1}{2}\mathcal{E}_{ij}Q^{ij} - \frac{1}{4\lambda}Q_{ij}Q^{ij} \\ &= \frac{1}{2}\mu v^2 + \frac{M_A M_B}{r} - \frac{1}{2}\mathcal{E}_{ij}(-\lambda\mathcal{E}^{ij}) - \frac{1}{4}(-\lambda\mathcal{E}_{ij})(-\lambda\mathcal{E}^{ij}) \\ &= \frac{1}{2}\mu v^2 + \frac{M_A M_B}{r} + \frac{1}{2}(\lambda\mathcal{E}_{ij})(\mathcal{E}^{ij}) - \frac{1}{4}(\lambda\mathcal{E}_{ij})(\mathcal{E}^{ij}) \\ &= \frac{1}{2}\mu v^2 + \frac{M_A M_B}{r} + \frac{1}{4}\lambda\, \mathcal{E}_{ij}\mathcal{E}^{ij} \\ &= \frac{1}{2}\mu v^2 + \frac{M_A M_B}{r} + \frac{\lambda}{4}6\frac{M_B^2}{r^6} \\ &= \frac{1}{2}\mu v^2 + \frac{M_A M_B}{r} + \frac{3}{2}\lambda\frac{M_B^2}{r^6}. \end{aligned} \tag{5.24}$$

For the Lagrangian above, we can calculate the energy associated with the system by

$$E = \frac{1}{2}\mu v^2 - \frac{M_A M_B}{r} - \frac{3}{2}\lambda\frac{M_B^2}{r^6}. \tag{5.25}$$

Now, we need to transform Cartesian to spherical polar coordinates, and the motion takes place in a fixed orbital plane with $\theta = \pi/2$, and $\dot{\theta} = 0$. We can define finally energy of the two body system comes out to be [170]:

$$E = \frac{1}{2}\mu(\dot{r}^2 + r^2\dot{\phi}^2) - \frac{\mu M}{r} - \frac{3M_B^2\lambda}{2\, r^6}. \tag{5.26}$$

For the linear tidal correction $r = r_0(1 + \delta r)$, where $\delta r = dr/r_0 << 1$ is the dimensionless quantity. Consider a circular orbit, $\dot{r} = 0 = \ddot{r}$,$\dot{\phi} = \Omega$ is the orbital angular frequency, and $r_0 = M^{1/3}\Omega^{-2/3}$ is the orbital radius, respectively. At linear order tidal effects we obtain $\delta r = \frac{3M_B^2\lambda\Omega^{10/3}}{\mu M^{8/3}}$. Hence, the Eq. (5.26) can be written as

$$\begin{aligned} E(\Omega) &= \frac{1}{2}\mu r_0^2(1 + 2\delta r)\Omega^2 - \frac{\mu M}{r_0(1 + \delta r)} - \frac{3M_B^2\lambda}{2\, r_0^6(1 + \delta r)^6} \\ &= -\frac{1}{2}\mu(M\Omega)^{2/3}\Big[1 - \frac{9M_B^2\lambda\Omega^{10/3}}{\mu M^{8/3}} + \dots\Big]. \end{aligned} \tag{5.27}$$

Tidal contribution to the energy E of the binary stars in terms of the post-Newtonian dimensionless parameter x is given by

$$E(x) = -\frac{1}{2}M\eta x\Big[1 + (PN - PP\ \ corr.) - 9\frac{M_B}{M_A}\frac{\lambda_A}{M^5}x^5 + A \leftrightarrow B\Big]. \tag{5.28}$$

where, $x = (\Omega M)^{2/3}$, and $\eta = M_A M_B/M^2$ is the symmetric mass relation. Second term represents the leading order terms to the post-Newtonian point-particle corrections.

5.1.3 Gravitational wave energy flux

The rate of energy loss due to gravitational radiation can be found from the quadrupole formula $\dot{E}_{GW} = -\frac{1}{5}\left\langle \dddot{Q}^T_{ij}\, \dddot{Q}^T_{ij} \right\rangle$. The quantity Q^T_{ij} is the total quadrupole of the system, and can be written as

$$\begin{aligned} Q^T_{ij} &= \mu r^2 n^{<ij>} + \frac{3\lambda M_B}{r^3} n^{<ij>} \\ &= n^{<ij>}\left[\mu r^2 + \frac{3\lambda M_B}{r^3}\right] \\ &= n^{<ij>}\zeta, \end{aligned} \tag{5.29}$$

where $\zeta = \mu r^2 + \frac{3\lambda M_B}{r^3}$, and $n^{<ij>} = n_i n_j - \frac{1}{3}\delta_{ij}$. For circular orbit $\dot{r} = 0$, $n_i = (cos\phi, sin\phi, 0), \phi_i = (-sin\phi, cos\phi, 0), \dot{n_i} = \Omega\phi_i, \dot{\phi} = -\Omega n_i, n_i\phi^i = 1, n^i n_i = 1$, and $\phi_i\phi^i = 1$, respectively.

$$\begin{aligned} \frac{dn^{<ij>}}{dt} &= \dot{n_i}n_j + n_i\dot{n_j} \\ &= \Omega\phi_i n_j + n_i\Omega\phi_j \\ &= \Omega(\phi_i n_j + n_i\phi_j), \\ \frac{d^2n^{<ij>}}{dt^2} &= \Omega\frac{d}{dt}(\phi_i n_j + n_i\phi_j) \\ &= \Omega(\dot{\phi_i}n_j + \phi_i\dot{n_j} + \dot{n_i}\phi_j + n_i\dot{\phi_j}) \\ &= \Omega(-\Omega n_i n_j + \phi_i\Omega\phi_j + \Omega\phi_i\phi_j - n_i\Omega n_j) \\ &= \Omega^2(-2n_i n_j + 2\phi_i\phi_j) \\ &= 2\Omega^2(-n_i n_j + \phi_i\phi_j), \\ \frac{d^3n^{<ij>}}{dt^3} &= 2\Omega^2\frac{d}{dt}(-n_i n_j + \phi_i\phi_j) \\ &= 2\Omega^2(-\dot{n_i}n_j - n_i\dot{n_j} + \dot{\phi_i}\phi_j + \phi_i\dot{\phi_j}) \\ &= 2\Omega^2(-\Omega\phi_i n_j - n_i\Omega\phi_j - \Omega n_i\phi_j - \phi_i\Omega n_j) \\ &= -2\Omega^3(2\phi_i n_j + 2n_i\phi_j) \\ &= -4\Omega^3(\phi_i n_j + n_i\phi_j), \end{aligned} \tag{5.30}$$

So, the flux can be written as

$$\begin{aligned}
\dot{E}_{GW} &= -\frac{1}{5}\left\langle \dddot{Q}^T_{ij}\ \dddot{Q}^T_{ij}\right\rangle \\
&= -\frac{1}{5}4\zeta^2\Omega^3(\phi_i n_j + n_i\phi_j)4\Omega^3(\phi_i n_j + n_i\phi_j) \\
&= -\frac{1}{5}16\zeta^2\Omega^6(\phi_i n_j\phi_i n_j + \phi_i n_j n_i\phi_j + n_i\phi_j\phi_i n_j + n_i\phi_j n_i\phi_j) \\
&= -\frac{1}{5}16\zeta^2\Omega^6(1+0+0+1) = -\frac{32}{5}\zeta^2\Omega^6 \\
&= -\frac{32}{5}\Omega^6\left[\mu r^2 + \frac{3\lambda M_B}{r^3}\right]^2 \\
&= -\frac{32}{5}\Omega^6\left[\mu^2 r^4 + \frac{6\mu r^2\lambda M_B}{r^3} + \frac{9\lambda^2 M_B^2}{r^6}\right] \\
&= -\frac{32}{5}\Omega^6\left[\mu^2 r^4 + \frac{6\mu\lambda M_B}{r} + \dots\right] \\
&= -\frac{32}{5}\Omega^6\left[\mu^2 r_0^4(1+\delta r)^4 + \frac{6\mu\lambda M_B}{r_0(1+\delta r)}\right] \\
&= -\frac{32}{5}\Omega^6\left[\mu^2 r_0^4(1+4\delta r) + \frac{6\mu\lambda M_B}{r_0}\right] \\
&= -\frac{32}{5}\Omega^6\mu^2 r_0^4\left[1 + 4\delta r + \frac{6\lambda M_B}{\mu r_0^5}\right] \\
&= -\frac{32}{5}\Omega^6\mu^2(M^{1/3}\Omega^{-2/3})^4\left[1 + 4\frac{3\lambda M_B^2\Omega^{10/3}}{\mu M^{8/3}} + \frac{6\lambda M_B}{\mu(M^{1/3}\Omega^{-2/3})^5}\right] \\
&= -\frac{32}{5}\Omega^{10/3}\mu^2 M^{4/3}\left[1 + \frac{6\lambda M_B\Omega^{10/3}}{\mu M^{5/3}}\left(1 + \frac{2M_B}{M}\right)\right] \\
&= -\frac{32}{5}\Omega^{10/3}\mu^2 M^{4/3}\left[1 + \delta\dot{E}\right], \qquad (5.31)
\end{aligned}$$

where $\dot{E}$ is the tidal correction on the gravitational waves.

$$\delta\dot{E} = \frac{6\lambda M_B\Omega^{10/3}}{\mu M^{5/3}}\left(1 + \frac{2M_B}{M}\right), \qquad (5.32)$$

The energy flux for a quasicircular inspiral for binary stars is given by [170]:

$$\dot{E}_{GW} = -\frac{32}{5}\eta^2 x^5\left[1 + (PN - PP\ \ corr.) + 6\frac{M_A + 3M_B}{M_A}\frac{\lambda_A}{M^5}x^5 + A \leftrightarrow B\right]. \qquad (5.33)$$

5.1.4 Orbital decay due to gravitational waves

To estimate the orbital decay, we consider the tidal contribution to the energy E and energy flux $\dot{E}_{GW}$ for quasicircular inspiral [170, 172]. Therefore, one can write

$$\frac{d\Omega}{dt} = \frac{d\Omega}{dE}\frac{dE}{dt} = \frac{\dot{E}_{GW}}{(\frac{dE}{d\Omega})}\ . \qquad (5.34)$$

Differentiating Eq. (5.27) with respect to Ω, we get

$$\begin{aligned}\frac{dE}{d\Omega} &= -\frac{1}{3}\mu M^{2/3}\Omega^{-1/3}\Big[1-\frac{54\lambda M_B^2\Omega^{10/3}}{\mu M^{8/3}}\Big] \\ &= -\frac{1}{3}\mu M^{2/3}\Omega^{-1/3}[1+\Delta], \end{aligned} \tag{5.35}$$

where, $\Delta = -\frac{54\lambda M_B^2\Omega^{10/3}}{\mu M^{8/3}}$, and Eq. (5.34) can be written for an extended object with a point mass. Now,

$$\begin{aligned}\frac{d\Omega}{dt} &= \frac{-\frac{32}{5}\Omega^{10/3}\mu^2M^{4/3}[1+\delta\dot{E}]}{-\frac{1}{3}\mu M^{2/3}\Omega^{-1/3}[1+\Delta]} \\ &= \frac{96}{5}\mu M^{2/3}\Omega^{11/3}[1+\delta\dot{E}-\Delta] \\ &= \frac{96}{5}\mu M^{2/3}\Omega^{11/3}\Big[1+\frac{6\lambda M_B\Omega^{10/3}}{\mu M^{5/3}}\Big(1+\frac{2M_B}{M}\Big)+\frac{54\lambda M_B^2\Omega^{10/3}}{\mu M^{8/3}}\Big] \\ &= \frac{96}{5}\mu M^{2/3}\Omega^{11/3}\Big[1+\frac{6\lambda M_B\Omega^{10/3}}{\mu M^{8/3}}\Big(9M_B+M+2M_B\Big)\Big] \\ &= \frac{96}{5}\mu M^{2/3}\Omega^{11/3}\Big[1+\frac{6\lambda M_B\Omega^{10/3}}{\mu M^{8/3}}\Big(M+11M_B\Big)\Big] \\ &= \frac{96}{5}\mathcal{M}_{ch}^{5/3}\Omega^{11/3}\Big[1+\frac{6\lambda M_B\Omega^{10/3}}{\mu M^{8/3}}\Big(M+11M_B\Big)\Big], \end{aligned} \tag{5.36}$$

where, $\mathcal{M}_{ch} = \mu^{3/5}M^{2/5}$ is the chirp mass of the binary system, and similarly, we can write orbital decay for two extended objects

$$\begin{aligned}\frac{d\Omega}{dt} &= \frac{96}{5}\mathcal{M}_{ch}^{5/3}\Omega^{11/3}\Big[1+\frac{6\lambda_A M_B\Omega^{10/3}}{\mu M^{8/3}}\Big(M+11M_B\Big)\Big]+(A\leftrightarrow B) \\ &= \frac{96}{5}\mathcal{M}_{ch}^{5/3}\Omega^{11/3}\Big[1+\frac{6\Omega^{10/3}}{\mu M^{8/3}}\Big(\lambda_A M_B(M+11M_B)+\lambda_B M_A(M+11M_A)\Big)\Big] \\ &= \frac{96}{5}\mathcal{M}_{ch}^{5/3}\Omega^{11/3}\Big[1+\frac{156\Omega^{10/3}}{M^{5/3}}\frac{1}{26}\Big(\frac{M_A+12M_B}{M_A}\lambda_A+\frac{M_B+12M_A}{M_B}\lambda_B\Big)\Big] \\ &= \frac{96}{5}\mathcal{M}_{ch}^{5/3}\Omega^{11/3}\Big[1+\frac{156\Omega^{10/3}}{M^{5/3}}\tilde{\lambda}\Big], \end{aligned} \tag{5.37}$$

where, $\tilde{\lambda}$ is the average tidal deformability of the binary stars [64].

$$\tilde{\lambda} = \frac{1}{26}\Big(\frac{M_A+12M_B}{M_A}\lambda_A+\frac{M_B+12M_A}{M_B}\lambda_B\Big). \tag{5.38}$$

When the masses of the stars are equal $M_A = M_B$ then $\tilde{\lambda} = \lambda_A = \lambda_B$. The evolution of the gravitational-wave frequency is determined by [65]

$$\begin{aligned}
\frac{dx}{dt} &= \frac{d}{dt}(\Omega M)^{2/3} = \frac{2}{3}M^{2/3}\Omega^{-1/3}\frac{d\Omega}{dt} \\
&= \frac{2}{3}M^{2/3}\Omega^{-1/3}\frac{96}{5}\mu M^{2/3}\Omega^{11/3}\Big[1 + \frac{6\lambda_A M_B \Omega^{10/3}}{\mu M^{8/3}}\Big(11M_B + M\Big) + A \leftrightarrow B\Big] \\
&= \frac{64}{5}\mu M^{4/3}\Omega^{10/3}\Big[1 + (PN - PP\ \ corr.) + \frac{156\Omega^{10/3}}{M^{5/3}}\tilde{\lambda}\Big] \\
&= \frac{64}{5}\frac{\eta x^5}{M}\Big[1 + (PN - PP\ \ corr.) + 156\frac{\tilde{\lambda}}{M^5}x^5\Big] \\
&= \frac{64}{5}\frac{\eta x^5}{M}\Big[1 + (PN - PP\ \ corr.) + 156\tilde{\Lambda}\ x^5\Big]. \qquad (5.39)
\end{aligned}$$

Where $\tilde{\Lambda}$ is the dimensionless tidal deformability, and the quadrupole gravitational wave phase Φ can be calculated by

$$\frac{d\Phi}{dt} = 2\Omega = 2x^{3/2}/M\ . \qquad (5.40)$$

5.1.5 Relativistic tidal interactions

We will now derive the $l = 2, 3, 4$ tidal love numbers of a star which depend on the equation of state. The star's quadrupole moment Q_{ij}, and the external tidal field $\mathcal{E}_{ij}$ come in the asymptotic expansion coefficients of the total metric at a large distance r from the star. This expansion includes the metric component g_{tt} in asymptotically Cartesian, mass-centered coordinates [174], and we have

$$\begin{aligned}
-\frac{(1 + g_{tt})}{2} &= \phi^{int} + \phi^{ext} \qquad (5.41) \\
&= -\frac{M}{r} - \frac{3Q_{ij}}{2r^3}\Big(n_i n_j - \frac{1}{3}\delta_{ij}\Big) + \cdots + \frac{\mathcal{E}_{ij}}{2}r^2 n_i n_j\ . \qquad (5.42)
\end{aligned}$$

where $n^i = x^i/r$, and both Q_{ij} and $\mathcal{E}_{ij}$ are symmetric and traceless. The first term represents the monopole piece of the standard gravitational potential, which depends on the object's mass M. The second term is the body's response decaying with r^{-3} that measured regarding the tidal Love number k_2. The last term is describing an external tidal field growing with r^2. Now, our aim is to derive the relativistic Love numbers within the context of the linear perturbation theory. To this, the initially spherical object is perturbed slightly by an applied tidal field. Therefore, we start

with the equilibrium of a static, spherically symmetric, and the relativistic star which is described by a space-time metric $g^{(0)}_{\alpha\beta}$ given by [175]:

$$g^{(0)}_{\alpha\beta} = diag\Big[- e^{\nu(r)}, e^{\lambda(r)}, r^2, r^2 sin^2\theta\Big]. \tag{5.43}$$

Static perturbations of the system is considered to study the tidal deformation of the star. Also, we focus on the even-parity perturbations in the Regge-Wheeler gauge which is the angular dependence of the components of a linearized metric perturbation into spherical harmonics [176]. The perturbed metric can be written as

$$h_{\alpha\beta} = diag\Big[- e^{\nu(r)} H(r), -e^{\lambda(r)} H(r), r^2 K(r), r^2 sin^2\theta \; K(r)\Big] Y_{20}(\theta, \phi), \tag{5.44}$$

where $Y_{20}(\theta,\phi) = \frac{1}{4}\sqrt{(\frac{5}{\pi}}(-1 + 3 \; cos^2\theta)$,$Y_{20}(\theta,\phi) = \frac{1}{4}\sqrt{(\frac{5}{\pi}}(-1 + 3 \; x^2)$. Here, $x = cos\theta$, $sin^2\theta = 1 - cos^2\theta = 1 - x^2$.

$$h_{\alpha\beta} = diag\Big[- e^{\nu(r)} H(r), -e^{\lambda(r)} H(r), r^2 K(r), r^2 (1 - x^2) \; K(r)\Big] \frac{1}{4}\sqrt{\frac{5}{\pi}}(-1 + 3 \; x^2) \; . \tag{5.45}$$

The full metric of the space-time is given by

$$g_{\alpha\beta} = g^0_{\alpha\beta} + h_{\alpha\beta} \; . \tag{5.46}$$

Eq. (5.46) can be solved with the following conditions:
(i) First, the perturbed Einstein equations (for $l \geq 2$) for the perfect fluid is to be determined. Then, the derivative of the stress-energy-momentum tensor is to be found out by taking

$$\delta T^\nu_\mu = (\delta\mathcal{E} + \delta P) u_\mu u^\nu + (P + \mathcal{E})(u_\mu \delta u^\nu + u_\nu \delta u^\mu) + \delta P \delta^\nu_\mu \; . \tag{5.47}$$

The nonvanishing components of the stress-energy moments tensor are $\delta T^0_0 = -\delta\mathcal{E} = -(dP/d\mathcal{E})^{-1}\delta P$ and $\delta T^i_i = \delta P$. However, all off-diagonal components vanish identically, since $\delta u^i = 0$.
(ii) T^ν_μ of the Einstein equations (A.36) can be expressed concerning the perturbed metric and inserting previous result (i). Therefore, the linearized Einstein equation with all the combined components is given by

$$\delta G^\nu_\mu = 8\pi \delta T^\nu_\mu. \tag{5.48}$$

Now, we need to write different components of the Einstein tensors δG^{ν}_{μ}.

For $tt-$component:

$$\begin{aligned}\delta G^{t}_{t} &= \frac{e^{-\lambda(r)}}{8r^2}\sqrt{\frac{5}{\pi}}(-1+3x^2)(-4e^{\lambda(r)}K(r)+H(r)(2+6e^{\lambda(r)} \\ &- 2r\lambda'(r))+r(2H'(r)+K'(r)(6-r\lambda'(r))+2rK''(r))). \end{aligned} \tag{5.49}$$

For $rr-$component:

$$\begin{aligned}\delta G^{r}_{r} &= \frac{e^{-\lambda(r)}}{8r^2}\sqrt{\frac{5}{\pi}}(-1+3x^2)(4e^{\lambda(r)}K(r)+H(r)(-2+6e^{\lambda(r)} \\ &- 2r\nu'(r))-r(2H'(r)+K'(r)(2+r\nu'(r)))). \end{aligned} \tag{5.50}$$

For $\theta\theta-$component:

$$\begin{aligned}\delta G^{\theta}_{\theta} &= -\frac{1}{16r}e^{-\lambda(r)}\sqrt{\frac{5}{\pi}}(-1+3x^2)(2H(r)\lambda'(r)-2H(r)\nu'(r)+rH(r)\lambda'(r)\nu'(r) \\ &- rH(r)\nu'(r)^2+H'(r)(-4+r\lambda'(r)-3r\nu'(r))+K'(r)(-4+r\lambda'(r) \\ &- r\nu'(r))-2rH''(r)-2rK''(r)-2rH(r)\nu''(r)). \end{aligned} \tag{5.51}$$

For $\phi\phi-$component is same as the $\theta\theta-$component. Hence, $\delta G^{\theta}_{\theta}-\delta G^{\phi}_{\phi}=0$.

For $r\theta-$component:

$$\begin{aligned}\delta G^{r}_{\theta} &= -\frac{3}{4}e^{-\lambda(r)}\sqrt{\frac{5}{\pi}}\;x(H'(r)+K'(r)+H(r)\nu'(r))=0, \\ K'(r) &= -H'(r)-H(r)\nu'(r), \\ K''(r) &= -H''(r)-H'(r)\nu'(r)-H'(r)\nu''(r). \end{aligned} \tag{5.52}$$

$$\begin{aligned}\delta P &= (\delta G^{\theta}_{\theta}+\delta G^{\phi}_{\phi})/16\pi \\ &= -\frac{1}{128\pi^{3/2}r}e^{-\lambda(r)}\sqrt{5}(-1+3x^2)(2H(r)\lambda'(r)-2H(r)\nu'(r)+rH(r)\lambda'(r)\nu'(r) \\ &- rH(r)\nu'(r)^2+H'(r)(-4+r\lambda'(r)-3r\nu'(r))+K'(r)(-4+r\lambda'(r) \\ &- r\nu'(r))-2rH''(r)-2rK''(r)-2rH(r)\nu''(r)). \end{aligned} \tag{5.53}$$

To obtain the differential equation for H, we need to subtract the rr-component

of the Einstein equation from the tt-component.

$$\delta G^{\beta}_{\alpha} = 8\pi\delta T^{\beta}_{\alpha},$$
$$\delta G^{t}_{t} - \delta G^{r}_{r} = 8\pi(T^{0}_{0} + T^{i}_{i})$$
$$\delta G^{t}_{t} - \delta G^{r}_{r} + 8\pi(\frac{d\mathcal{E}}{dP}\delta P + \delta P) = 0$$
$$-\frac{1}{4r^2}\Big(H(r)(24e^{\lambda(r)} + r(2(-1+\frac{d\mathcal{E}}{dP})\nu'(r) + (1+\frac{d\mathcal{E}}{dP})r\nu'(r)^2 - \lambda'(r)(2(3+\frac{d\mathcal{E}}{dP})$$
$$+(1+\frac{d\mathcal{E}}{dP})r\nu'(r)) + 2(1+\frac{d\mathcal{E}}{dP})r\nu''(r))) + r(-(1+\frac{d\mathcal{E}}{dP})H'(r)(-4 + r\lambda'(r) - 3r\nu'(r))$$
$$+(-(3+\frac{d\mathcal{E}}{dP})(-4+r\lambda'(r)) + (-1+\frac{d\mathcal{E}}{dP})r\nu'(r))(-H'(r) - H(r)\nu'(r))$$
$$+2r((1+\frac{d\mathcal{E}}{dP})H''(r) + (3+\frac{d\mathcal{E}}{dP})(-H'(r)\nu'(r) - H''(r) - H(r)\nu''(r))))\Big) = 0. \quad (5.54)$$

We can write the second-order radial differential equation for the metric variable H in the form

$$H''(r) + C_1 H'(r) + C_0 H = 0, \quad (5.55)$$

where C_1, and C_0 are the coefficients of the $H'(r)$, and $H(r)$, which are extracted from the Eq. (5.54).

$$C_1 = \frac{2}{r} + \frac{1}{2}(\nu'(r) - \lambda'(r)) = \frac{2}{r} + e^{\lambda(r)}\Big[\frac{2m(r)}{r^2} + 4\pi r(P - \mathcal{E})\Big], \quad (5.56)$$

and

$$\begin{aligned} C_0 &= e^{\lambda(r)}\Big[-\frac{l(l+1)}{r^2} + 4\pi(\mathcal{E}+P)\frac{d\mathcal{E}}{dP} + 4\pi(\mathcal{E}+P)\Big] \\ &+ \nu''(r) + (\nu'(r))^2 + \frac{1}{2r}(2 - r\nu')(3\nu' + \lambda') \\ &= e^{\lambda(r)}\Big[-\frac{l(l+1)}{r^2} + 4\pi(\mathcal{E}+P)\frac{d\mathcal{E}}{dP} + 4\pi(5\mathcal{E}+9P)\Big] - (\nu'(r))^2, \quad (5.57) \end{aligned}$$

where the TOV (as derived in appendix A) equations are used to rewrite C_1 and C_0. We also consider the multipolar order l, which taken the leading quadrupolar even-parity tide [64]. Therefore, the second-order differential equation for H can be rewritten as

$$H''(r) + \Big[\frac{2}{r} + e^{\lambda(r)}\Big(\frac{2m(r)}{r^2} + 4\pi r(P-\mathcal{E})\Big)\Big]H'(r) + \Big[e^{\lambda(r)}\Big(-\frac{l(l+1)}{r^2}$$
$$+ \quad 4\pi(\mathcal{E}+P)\frac{d\mathcal{E}}{dP} + 4\pi(5\mathcal{E}+9P)\Big) - (\nu'(r))^2\Big]H(r) = 0. \quad (5.58)$$

The second-order differential equation for H is converted into two first order differential equation for β as

$$\frac{dH(r)}{dr} = \beta(r), \tag{5.59}$$

and

$$\begin{aligned}
\frac{d\beta(r)}{dr} &= e^{\lambda(r)}H(r)\Big[-4\pi\Big(5\mathcal{E}+9P+\frac{(\mathcal{E}+P)}{dP/d\mathcal{E}}\Big)+\frac{l(l+1)}{r^2}+4e^{\lambda(r)}\Big(\frac{m(r)}{r^2}+4\pi rP\Big)^2\Big] \\
&+ \frac{2\beta(r)}{r}e^{\lambda(r)}\Big[-1+\frac{m(r)}{r}+2\pi r^2(\mathcal{E}-P)\Big] \\
&= \Big(1-\frac{2m(r)}{r}\Big)^{-1}H(r)\Big[-4\pi(5\mathcal{E}+9P+\frac{(\mathcal{E}+P)}{dP/d\mathcal{E}})+\frac{l(l+1)}{r^2}+2\Big(1-\frac{2m(r)}{r}\Big)^{-1} \\
&\Big(\frac{m(r)}{r^2}+4\pi rP\Big)^2\Big]+\frac{2\beta(r)}{r}\Big(1-\frac{2m(r)}{r}\Big)^{-1}\Big[-1+\frac{m(r)}{r}+2\pi r^2(\mathcal{E}-P)\Big],
\end{aligned} \tag{5.60}$$

Defining the quantity $y(r) = r\beta(r)/H(r)$ for the internal solution, we can differentiate $y(r)$ with respect to r. The equations are

$$\begin{aligned}
y'(r)H(r)+yH'(r)-\beta(r)-r\beta'(r) &= 0 \\
y'(r)H(r)+(y-1)\beta(r)-r\beta'(r) &= 0 \\
\beta(r)(y(r)-1)+\frac{2H(r)y(r)\Big(r-m(r)+2\pi r^3(P-\mathcal{E})\Big)}{r(r-2m(r))}-\frac{r^2H(r)}{r-2m(r)}\Big(\frac{l(l+1)}{r^2} & \\
+\frac{4(m(r)+4\pi r^3P)^2}{r^3(r-2m)}-\frac{4\pi(P+\mathcal{E}+(9P+5\mathcal{E})/dP/d\mathcal{E}}{dP/d\mathcal{E}}\Big)+H(r)y'(r) &= 0 \\
\frac{y(r)H(r)}{r}(y(r)-1)+\frac{2H(r)y(r)\Big(r-m(r)+2\pi r^3(P-\mathcal{E})\Big)}{r(r-2m(r))}-\frac{r^2H(r)}{r-2m(r)}\Big(\frac{l(l+1)}{r^2} & \\
+\frac{4(m(r)+4\pi r^3P)^2}{r^3(r-2m)}-\frac{4\pi(P+\mathcal{E}+(9P+5\mathcal{E})/dP/d\mathcal{E}}{dP/d\mathcal{E}}\Big)+H(r)y'(r) &= 0,
\end{aligned} \tag{5.61}$$

Multiplying $r/H(r)$ in both sides, we can get

$$\begin{aligned}
y(r)(y(r)-1)+\frac{2y(r)\Big(r-m(r)+2\pi r^3(P-\mathcal{E})\Big)}{(r-2m(r))}-\frac{r^3}{r-2m(r)}\Big(\frac{l(l+1)}{r^2}\\
+\frac{4(m(r)+4\pi r^3P)^2}{r^3(r-2m)}-\frac{4\pi(P+\mathcal{E}+(9P+5\mathcal{E})/dP/d\mathcal{E}}{dP/d\mathcal{E}}\Big)+ry'(r) &= 0\\
ry'(r)+y(r)^2+y(r)\Big(-1+\frac{2(r-m(r)+2\pi r^3(P-\mathcal{E}))}{(r-2m(r))}\Big)-\frac{r^3}{r-2m(r)}\Big(\frac{l(l+1)}{r^2}\\
+\frac{4(m(r)+4\pi r^3P)^2}{r^3(r-2m)}-\frac{4\pi(P+\mathcal{E}+(9P+5\mathcal{E})/(dP/d\mathcal{E})}{dP/d\mathcal{E}}\Big) &= 0\\
ry'(r)+y(r)^2+y(r)\Big(\frac{r-4\pi r^3(\mathcal{E}-P)}{(r-2m(r))}\Big)+r^2\Big\{\frac{4\pi r\Big(\frac{P+\mathcal{E}}{dP/d\mathcal{E}}+9P+5\mathcal{E}-\frac{l(l+1)}{r^2}\Big)}{r-2m(r)}\\
-4\Big[\frac{m(r)+4\pi r^3P}{r^2(1-2m(r)/r}\Big]^2\Big\} &= 0\\
ry'(r)+y(r)^2+y(r)F(r)+r^2Q(r) &= 0.
\end{aligned} \tag{5.62}$$

Here, $F(r)=\frac{r-4\pi r^3(\mathcal{E}-P)}{(r-2m(r))}$, and $Q(r)=\frac{4\pi r\Big(\frac{P+\mathcal{E}}{dP/d\mathcal{E}}+9P+5\mathcal{E}-\frac{l(l+1)}{r^2}\Big)}{r-2m(r)}-4\Big[\frac{m(r)+4\pi r^3P}{r^2(1-2m(r)/r}\Big]^2$.

Again, we can write the second-order differential equation (5.55) for outside the star $r=R$ regarding associated Legendre Legendre equation with m=2 [67, 177]:

$$(x^2-1)H''(x)+2xH'(x)-\Big(l(l+1)+\frac{4}{x^2-1}\Big)H(x)=0, \tag{5.63}$$

where the prime stands for d/dx, $m(r=R)=M$, and $x=R/M-1$ is the independent variable. Therefore, the general solution of the Eq. (5.63) can be written as

$$H(x)=a_P\hat{P}_{l2}(x)+a_Q\hat{Q}_{l2}(x). \tag{5.64}$$

Where a_P, and a_Q are the integration constants which determines through matching to the internal solution. Substituting the value of $y(r)$ into Eq. (5.64), we get

$$y(x)=(1+x)\frac{\hat{P}'_{l2}(x)+a_l\hat{Q}'_{l2}(x)}{\hat{P}_{l2}(x)+a_l\hat{Q}_{l2}(x)}, \tag{5.65}$$

where $a_l=a_Q/a_P$ determines by matching to the internal solution concerning the compactness $C=M/R$ of the star

$$a_l=-\frac{\hat{P}'_{l2}(x)-Cy_l\ \hat{P}_{l2}(x)}{\hat{Q}'_{l2}(x)-Cy_l\ \hat{Q}_{l2}(x)}\Big|_{x=R/M-1}. \tag{5.66}$$

On the other hand, a_l can be related to dimensionless tidal Love number k_l [67]. One can define as

$$k_l = \frac{1}{2}C^{2l+1}a_l, \tag{5.67}$$

with $l = 2, 3, 4, \ldots$ are the quadrupole, octupole, and hexadecapole numbers. For quadrupole Love number k_2, we have

$$\begin{aligned} k_2 &= \frac{1}{2}C^5 a_2 \\ &= \frac{8}{5}(1-2C)^2C^5[2C(y_2-1)-y_2+2]\Big\{2C(4(y_2+1)C^4+(6y_2-4)C^3 \\ &+ (26-22y_2)C^2+3(5y_2-8)C-3y_2+6)-3(1-2C)^2 \\ &\quad (2C(y_2-1)-y_2+2)log\Big(\frac{1}{1-2C}\Big)\Big\}^{-1}, \end{aligned} \tag{5.68}$$

for octupole Love number k_3

$$\begin{aligned} k_3 &= \frac{8}{7}(1-2C)^2C^7[2(y_3-1)C^2-3(y_3-2)C+y_3-3]\Big\{2C[4(y_3+1)C^5+2(9y_3-2)C^4 \\ &- 20(7y_3-9)C^3+5(37y_3-72)C^2-45(2y_3-5)C+15(y_3-3)]-15(1-2C)^2 \\ &\quad (2(y_3-1)C^2-3(y_3-2)C+y_3-3)log\Big(\frac{1}{1-2C}\Big)\Big\}^{-1}, \end{aligned} \tag{5.69}$$

and for hexadecapole Love number k_4 can be written as

$$\begin{aligned} k_4 &= \frac{32}{147}(1-2C)^2C^9[12(y_4-1)C^3-34(y_4-2)C^2+28(y_4-3)C-7(y_4-4)] \\ &\quad \Big\{2C[8(y_4+1)C^6+(68y_4-8)C^5+(1284-996y_4)C^4+40(55y_4-116)C^3 \\ &+ (5360-1910y_4)C^2+105(7y_4-24)C-105(y_4-4)]-15(1-2C)^2[12(y_4-1)C^3 \\ &- 34(y_4-2)C^2+28(y_4-3)C-7(y_4-4)]log\Big(\frac{1}{1-2C}\Big)\Big\}^{-1}. \end{aligned} \tag{5.70}$$

Tidal deformability of neutron and hyperon star

The detection of gravitational wave is a major breakthrough in astrophysics/cosmology which is detected for the first time by advanced Laser Interferometer Gravitational-wave Observatory (aLIGO) detector [178]. Inspiraling and coalescing of binary black-hole results in the emission of gravitational waves. We may expect that in a few years the forthcoming aLIGO [178], VIRGO [179], and KAGRA [180] detectors will also detect gravitational waves emitted by binary neutron star (NSs). This detection is certainly posed to be a valuable guide and will help in a better understanding of a

highly compressed baryonic system. Flanagan and Hinderer [64–66] have recently pointed out that tidal effects are also potentially measurable during the early part of the evolution when the waveform is relatively clean. It is understood that the late inspiral signal may be influenced by tidal interaction between binary stars (NS-NS), which gives the important information about the equation-of-state (EoS). The study of Refs. [170, 171, 181–188] inferred that the tidal effects could be measured using the recent generation of gravitational wave (GW) detectors.

In 1911, the mathematician A. E. H. Love [189] introduced the dimensionless parameter in Newtonian theory that is related to the tidal deformation of the Earth is due to the gravitational attraction between the Moon and the Sun on it. This Newtonian theory of tides has been imported to the general relativity [185, 190], where it shows that the electric and magnetic type dimensionless gravitational Love number is a part of the tidal field associated with the gravitoelectric and gravitomagnetic interactions. The tidal interaction in a compact binary system has been encoded in the Love number and is associated with the induced deformation responded by changing shapes of the massive body. We are particularly interested for a NS in a close binary system, focusing on the various Love numbers k_l (l=2, 3, 4) due to the shape changes (like quadrupole, octupole and hexadecapole in the presence of an external gravitational field). Although higher Love numbers (l=3, 4) give negligible effect, still these Love numbers (k_l) can have vital importance in future gravitational wave astronomy. However, geophysicists are interested to calculate the surficial Love number h_l, which describes the deformation of the body's surface in a multipole expansion [68,185,190].

We have used the EoS from the relativistic mean field (RMF) [25, 27, 47] and the newly developed effective field theory motivated RMF (E-RMF) [191,192] approximation in our present calculations. Here, the degrees of freedoms are nucleon, $\sigma-$, $\omega-$, $\rho-$, $\pi-$mesons and photon. This theory fairly explains the observed massive neutron star, like PSR J1614-2230 with mass $M = 1.97 \pm 0.04 M_{\odot}$ [57] and PSR J0348+0432 ($M = 2.01 \pm 0.04 M_{\odot}$) [58].

The baryon octets are also introduced as the stellar system is in extraordinary condition such as highly asymmetric or extremely high density medium [196]. The

Table 5.1: Parameters and saturation properties for NL3 [29], G2 [192], FSUGold [193], and FSUGold2 [194]. The parameters g_σ, g_ω, g_ρ, k_3, and k_4 are calculated from nuclear matter the given saturation properties using the relations suggested by the authors of Ref. [195].

Parameters	NL3	G2	FSUGold	FSUGold2
m_n(MeV)	939	939	939	939
m_σ(MeV)	508.194	520.206	491.5	497.479
m_ω(MeV)	782.501	782	783	782.5
m_ρ(MeV)	763	770	763	763
g_σ	10.1756	10.5088	10.5924	10.3968
g_ω	12.7885	12.7864	14.3020	13.5568
g_ρ	8.9849	9.5108	11.7673	8.970
k_3(MeV)	1.4841	3.2376	0.6194	1.2315
k_4	-5.6596	0.6939	9.7466	-0.2052
η_1	0	0.65	0	0
η_2	0	0.11	0	0
η_ρ	0	0.390	0	0
ζ_0	0	2.642	12.273	4.705
Λ_ω	0	0	0.03	0.000823
Nuclear matter properties				
ρ_0(fm^{-3})	0.148	0.153	0.148	0.1505±0.00078
E/A(MeV)	-16.299	-16.07	-16.3	-16.28±0.02
K$_\infty$(MeV)	271.76	215	230	238.0± 2.8
J(MeV)	37.4	36.4	32.59	37.62±1.11
L(MeV)	118.2	101.2	60.5	112.8± 16.1
m_n^*/m_n	0.6	0.664	0.610	0.593±0.004

coupling constants for nucleon-mesons are fitted to reproduce the properties of a finite number of nuclei, which then predict not only the observables of $\beta-$stable nuclei, but also of drip-lines and superheavy regions [25, 26, 28, 29, 79, 197, 198]. The hyperon-meson couplings are obtained from the quark model [199–201]. Recently, however, the couplings are improved by taking into consideration some other properties of strange nuclear matter [202].

5.2 Results and Discussions:

In this section, we present the results of our calculations in Figs. 1-9 and Table 5.2. Our calculated results of the EoS and related outcomes are discussed in the

subsequent subsections.

5.2.1 EoSs of neutron and hyperon star

For a given Lagrangian density Eq. (2.1), one can solve the equations of motion in the mean-field level, *i.e.* the exchange of mesons create a uniform meson field, where the nucleons moves in a simple harmonic motion. Then we calculate the energy-momentum tensor within the mean field approximation (i.e. the meson fields are replaced by their classical number) and get the EoS as a function of baryon density (Eqns. (2.30), and (2.31) are derived in chapter 2). The EoS remains uncertain at density larger than the saturation density of nuclear matter, $\rho_n \sim 3 \times 10^{14}$ g cm^{-3}. At these densities, neutrons can no longer be considered, which may consists mainly of heavy baryons (mass greater than nucleon) and several other species of particles expected to appear due to the rapid rise of the baryon chemical potentials [203]. The β-equilibrium and charge neutrality are two important conditions for the neutron/hyperon rich-matter. Both these conditions force the stars to have $\sim$90% of neutrons and $\sim$10% protons. With the inclusion of baryons, the $\beta-$equilibrium conditions between chemical potentials for different particles are

$$\begin{aligned} \mu_p = \mu_{\Sigma^+} &= \mu_n - \mu_e, \\ \mu_n = \mu_{\Sigma^0} = \mu_{\Xi^0} &= \mu_n, \\ \mu_{\Sigma^-} = \mu_{\Xi^-} &= \mu_n + \mu_e, \\ \mu_\mu &= \mu_e, \end{aligned} \tag{5.71}$$

and the charge neutrality condition is satisfied by

$$n_p + n_{\Sigma^+} = n_e + n_{\mu^-} + n_{\Sigma^-} + n_{\Xi^-}. \tag{5.72}$$

The EoS then gives the corresponding pressure and energy density (as discussed in chapter 2) of the charge-neutral β-equilibrated NS matter (which includes the lowest lying octet of baryons).

Fig.5.2 displays the EoSs for G2 [192], FSUGold2 [194], FSUGold [193] and NL3 [29] parameter sets. From Fig. 5.2(a), it is obvious that all the EoSs follow

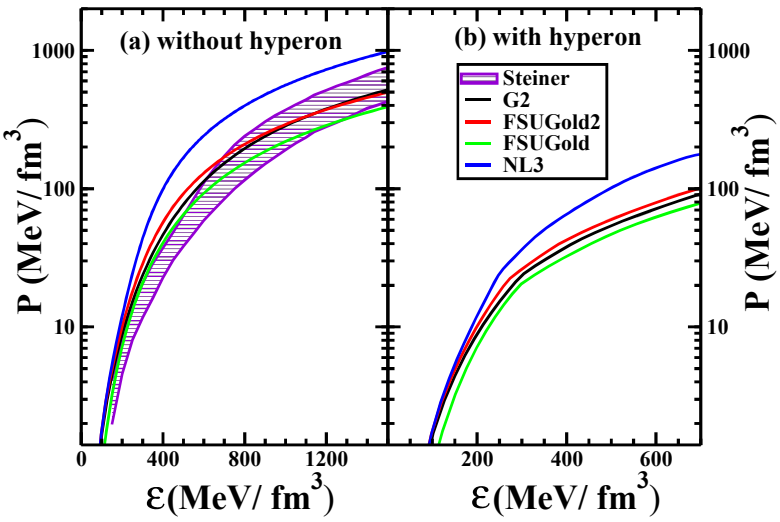

Figure 5.2: The equations of state obtained for nuclear and hyper-nuclear matter under charge neutrality as well as the $\beta-$equilibrium condition for G2 [192], FSUGold2 [194], FSUGold [193], and NL3 [29] force parameters are compared with the empirical data [59] (shaded area in the graph) for $r_{ph} = R$ with the uncertainty of 2σ. Here, R and r_{ph} are the neutron radius and the photospheric radius, respectively.

a similar trend. Among these four, the celebrity NL3 set gives the stiffest EoS and the relatively new FSUGold represents the softer character. This is because of the large and positive k_4 value as well as the introduction of isoscalar-isovector coupling (Λ_ω) in the FSUGold set [193]. To have an understanding on the softer and stiffer EoSs by various parametrizations, we compared their coupling constants and other parameters of the sets in Table 5.1. We notice a large variation in their effective masses, incompressibilities and other nuclear matter properties at saturation. For higher energy density $\mathcal{E} \sim 500 - 1400$ MeV fm^{-3}, except NL3 set, which has the lowest nucleon effective mass, all other sets are found in the region of empirical data with the uncertainty of 2σ [59].

Fig. 5.2(b) shows a hump type structure on the nucleon-hyperon EoS at $\mathcal{E}$ around 400-500 MeV fm^{-3}. This kink ($\mathcal{E} \sim$ 200-300 MeV) shows the presence of hyperons in the dense system. Here, the repulsive component of the vector potential becomes

more important than the attractive part of the scalar interaction. As a result the coupling of the hyperon-nucleon strength gets weak. At a given baryon density, the inclusion of hyperons lower significantly the pressure compared to the EoS without hyperons. This is possible due to the higher energy of the hyperons, as the neutrons are replaced by the low-energy hyperons. The hyperon couplings are expressed as the ratio of the meson-hyperon and meson-nucleon couplings:

$$\chi_\sigma = \frac{g_{Y\sigma}}{g_{N\sigma}}, \chi_\omega = \frac{g_{Y\omega}}{g_{N\omega}}, \chi_\rho = \frac{g_{Y\rho}}{g_{N\rho}}. \tag{5.73}$$

In the present calculations, we have taken $\chi_\sigma = 0.7$ and $\chi_\omega = \chi_\rho = 0.783$. One can find similar calculations for stellar mass in Refs. [195, 204–206].

5.2.2 Mass and radius of neutron and hyperon star

Once the equations of state for various relativistic forces are fixed, then we extend our study for the evaluation of the mass and radius of the isolated neutron star. The Tolmann-Oppenheimer-Volkov (TOV) equations (as derived in Appendix A) have to be solved for this purpose, where EoSs are the inputs.

For a given EoS, the TOV equations must be integrated from the boundary conditions $P(0) = P_c$, and $M(0) = 0$, where P_c and $M(0)$ are the pressure and mass of the star at $r = 0$ and the value of $r(= R)$, where the pressure vanish defines the surface of the star. Thus, at each central density we can uniquely determine a mass M and a radius R of the static neutron and hyperon stars using the four chosen EoSs. The estimated result for the maximum mass as a function of radius compared with the highly precise measurements of two massive ($\sim 2M_\odot$) neutron stars [57, 58] and extraction of stellar radii from x-ray observation [59], are shown in Figs. 5.3(a) and 5.3 (b) . From recent observations [57, 58], it is clearly illustrated that the maximum mass predicted by any theoretical model should reach the limit $\sim 2.0M_\odot$, which is consistent with our present prediction from the G2 EoS of nucleonic matter compact star with mass $1.99M_\odot$ and radius 11.25 km. From x-ray observation, Steiner *et al.* [59] predicted that the most-probable neutron star radii lie in the range 11-12 km with neutron star masses$\sim 1.4M_\odot$ and predicted that the EoS is relatively soft in the density range 1-3 times the nuclear saturation density. As explained earlier, stiff EoS like NL3 predicts a larger stellar radius 13.23 km and a maximum mass 2.81 $M_\odot$.

Though FSUGold and FSUGold2 are from the same RMF model with similar terms in the Lagrangian, their results for NS are quite different with FSUGold2 suggesting a larger and heavier NS with mass $2.12M_{\odot}$ and radius 12.12 km compare to mass and radius ($1.75M_{\odot}$ and 10.76 km) of the FSUGold. Because in FSUGold2 EoS at high densities, the impact comes from the quartic vector coupling constant ζ_0 and also the large value of the slope parameter $L = 112.8 \pm 16.1$ MeV (see Table 5.1) tend to predict the NS with large radius [86]. From the observational point of view, there are large uncertainties in the determination of the radius of the star [207–209], which is a hindrance to get a precise knowledge on the composition of the star atmosphere. One can see that G2 parameter is able to reproduce the recent observation of $2.0M_{\odot}$ NS. But the presence of hyperon matter under β-equilibrium soften the EoS, because they are more massive than nucleons and when they start to fill their Fermi sea slowly replacing the highest energy nucleons. Hence, the maximum mass of NS is reduced by $\sim$0.5 unit solar mass due to the high baryon density. For example, the stiffer NL3 EoS gives the maximum NS mass $\sim 2.81M_{\odot}$ and the presence of hyperon matter reduces the mass to $\sim 2.25M_{\odot}$ as shown in Fig. 5.3(b).

These results give us warning that most of the present sets of hyperon couplings are unable to reproduce the recently observed mass of NS like PSR J1614-2230 with mass $M = 1.97 \pm 0.04M_{\odot}$ [57] and the PSR J0348+0432 with $M = 2.01 \pm 0.04M_{\odot}$ [58]. Probably, this suggest us to modify the coupling constants and get the EoS properly, so that one can explain all the mass-radius observations to date. Further, one can see that in Fig. 5.3(b) mass-radius curve of G2, FSUGold, FSUGold2 with hyperon lies in the range of the predicted EoS between the r_{ph}=R and $r_{ph} \gg$R cases is the high density behavior [59].

5.2.3 Various tidal Love number of compact star

To estimate the Love numbers k_l (l=2, 3, 4), along with the evaluation of the TOV equations, we have to compute $y = y_l(R)$ with initial boundary condition $y(0) = l$ from the following first order differential equation (5.62) iteratively [64, 66, 67, 190]: Once, we know the value of $y = y_l(R)$, the electric tidal Love numbers k_l are found from the Eq. (5.67).

As we have emphasized earlier, the dimensionless Love number k_l ($l = 2, 3, 4$)

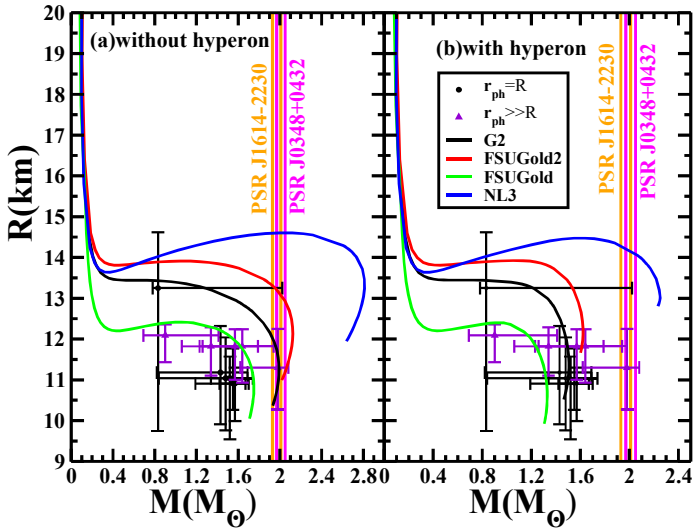

Figure 5.3: The mass-radius profile for the force parameters like G2 [192], FSUGold2 [194], FSUGold [193] and NL3 [29] used. The solid circles($r_{ph} = R$) and triangles($r \gg R$) are represent the observational constraints [59], where r_{ph} is the photospheric radius. The verticle sheded region corresponds to the recent observation [57, 58].

is an important quantity to measure the internal structure of the constituent body. These quantities directly enter into the gravitational wave phase of inspiralling binary neutron stars (BNS) and extract the information of the EoS. Notice that Eqns. (5.68)-(5.70) contain an overall factor $(1-2C)^2$, which tends to zero when the compactness approaches the compactness of the black hole, *i.e.* C^{BH}=1/2 [210]. Also, it is to be pointed out that with the presence of multiplication order factor C with $(1-2C)^2$ in the expression of k_l that the value of the Love number of a black hole simply becomes zero, *i.e.*, k_l^{BH}=0.

Fig. 5.4 shows the tidal Love numbers k_l (l=2, 3, 4) as a function of compactness parameter C for the NS with four selected EoSs. The result of k_l suddenly deceases with increasing compactness ($C = 0.06-0.25$). For each EoS, the value of k_2 appears to be maximum between $C = 0.06 - 0.07$. However, we are mainly interested in the NS masses at $\sim 1.4 M_\odot$. Because of the tidal interactions in the NS binary, the shape of the star acquires quadrupole, octupole, hexadecapole and other higher order

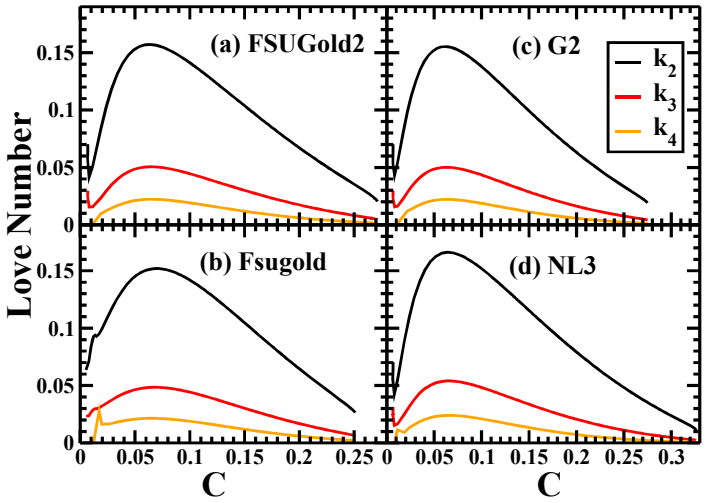

Figure 5.4: The tidal Love numbers k_2, k_3, k_4 as a function of the mass of the four selected EoSs of the neutron star.

deformations. The value of the Love numbers for corresponding shapes are shown in Table 5.2. The values of k_l decreases gradually with increase of multipole moments. Thus, the quadrupole deformibility has maximum effects on the binary star merger. Similarly, in Fig. 5.5, the dimensionless Love number k_l is shown as a function of compactness for the hyperon star. With the inclusion of hyperons, the effect of the core is negligible due to the softness of the EoSs. The values of k_l is different for a typical neutron-hyperon star with mass 1.4 $M_\odot$ for various sets are listed in the lower portion of Table 5.2. The radius and respective mass-radius ratio is also given in the Table 5.2. The table also reflects that the Love numbers decrease slightly or remains unchanged with the addition of hyperon in the NS. The NS surface or solid crust is not responsible for any tidal effects, but instead it is the matter mainly in the outer core that gives the largest contribution to the tidal Love numbers. It is relatively unaffected by changing the composition of the core. Thus instigate the calculation for the surficial Love number h_l for both neutron and hyperon star binary.

Next, we calculate the surficial Love number h_l which describes the deformation of the body's surface in a multipole expansion. Recently, Damour and Nagar [210]

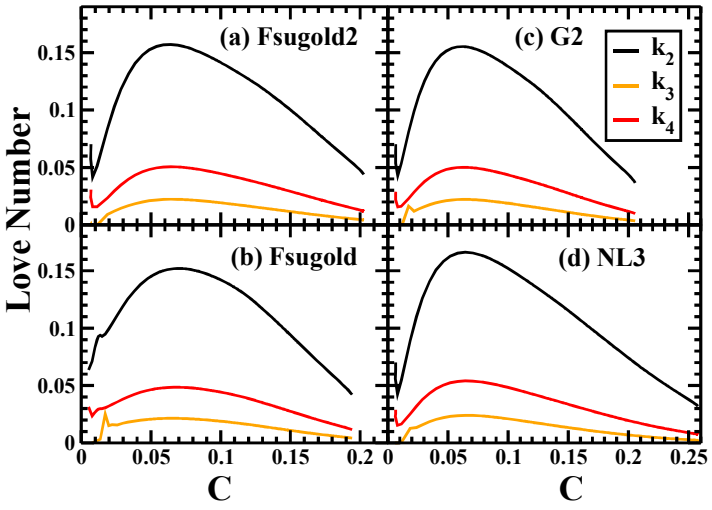

Figure 5.5: Same as Fig. 5.4 but for hyperon star.

have given the surficial Love number (also known as shape Love number) h_l for the coordinate displacement δR of the body's surface under the external tidal force. Alternatively, Landry and Poisson [68] have proposed the definition of Newtonian Love number in terms of a curvature perturbation $\delta\mathcal{R}$ instead of a surface displacement δR. For a perfect fluid, the relation between the surficial Love number h_l and tidal Love number k_l is given as

$$h_l = \Gamma_1 + 2\Gamma_2 k_l, \tag{5.74}$$

where

$$\Gamma_1 = \frac{l+1}{l-1}(1-C)F(-l,-l,-2l;2C) - \frac{2}{l-1}F(-l,-l-1,-2l;2C),$$

and

$$\Gamma_2 = \frac{l}{l+2}(1-C)F(l+1,l+1,2l+2;2C) + \frac{2}{l+2}F(l+1,l,2l+2;2C).$$

where F(a,b,c;z) is the hypergeometric function. Figure 5.6 shows the results of surficial Love number h_l of a NS as a function of compactness parameter C. Unlike the initially increasing and then decreasing trend of the tidal Love number k_l, the surficial

Table 5.2: Properties of a $1.4M_{\odot}$ neutron and hyperon star for different classes of the EoS. The quadrupolar tidal deformability λ and uncertainty error $\Delta\tilde{\lambda}$ in (10^{36}g cm^2 s^2).

EoS	$R(km)$	C	f_c(Hz)	k_2	k_3	k_4	h_2	h_3	h_4	λ	$\Delta\tilde{\lambda}$	Λ
Neutron Star												
NL3	14.422	0.144	1256.7	0.1197	0.0353	0.0142	0.9775	0.6519	0.5074	7.466	2.027	1288.81
G2	13.148	0.157	1440.9	0.0934	0.0265	0.0103	0.8879	0.5951	0.4596	3.668	1.486	652.76
FSUGold2	13.850	0.149	1332.4	0.1040	0.0301	0.0119	0.9275	0.6237	0.4854	5.299	1.763	944.08
FSUGold	12.236	0.170	1608.0	0.0882	0.0244	0.0071	0.8589	0.5634	0.4268	2.418	1.178	414.13
Hyperon Star												
NL3	14.430	0.143	1252.9	0.1203	0.0355	0.0143	0.9800	0.6541	0.5096	7.527	2.018	1341.20
G2	12.686	0.163	1520.6	0.0804	0.0229	0.0088	0.8434	0.5707	0.4399	2.641	1.321	465.83
FSUGold2	13.690	0.151	1355.9	0.0988	0.0287	0.0113	0.9108	0.6154	0.4789	4.750	1.696	839.04
$(\text{FSUGold})_{1.3M_{\odot}}$	9.922	0.194	2119.0	0.0421	0.0116	0.0042	0.6884	0.4683	0.3518	0.4048	0.530	102.14

Love number h_l decreases almost exponentially with the compactness parameter. At the minimum value of the compactness parameter, the maximum value of the shape Love number of each multipole moment approaches 1. Thus, we zero in on to the Newtonian relation i.e., $h_l = 1 + 2k_l$. Again one can compute from Table 5.2 that the surficial Love number h_l decreases $\sim 20\%$ from one moment to another. For example, $h_2 = 0.9775$ and $h_3 = 0.6519$ and $h_4 = 0.5074$ for NL3 parameter sets.

Furthermore, we also calculate the "magnetic" tidal Love number j_l. Here, we give only the quadrupolar case ($l = 2$), which is expressed as:

$$\begin{aligned} j_2 = \Big\{96C^5(2C-1)(y_2-3)\Big\}\Big\{5(2C(12(y_2+1)C^4 \\ +2(y_2-3)C^3 + 2(y_2-3)C^2 + 3(y_2-3)C - 3y_2 + 9) \\ +3(2C-1)(y_2-3)log(1-2C))\Big\}^{-1}. \end{aligned} \tag{5.75}$$

After inserting the value of y_2 in eq. (5.68), we compute the magnetic tidal Love number j_2 in a hydrostatic equilibrium condition for a nonrotating NS. This gives important information about the internal structure [190] without changing the tidal Love number k_2. At C=0.01, the magnetic Love number j_2 is nearly 0.4. In both cases (with and without hyperons), j_2 is maximum within the compactness 0.06 to 0.07 for all the four EoSs (See Fig. 5.7). Then the value of j_2 decreases sharply with an increase of compactness. The NL3 parameter set gives a maximum j_2 in both the systems, while the rest of the three sets predict comparable j_2.

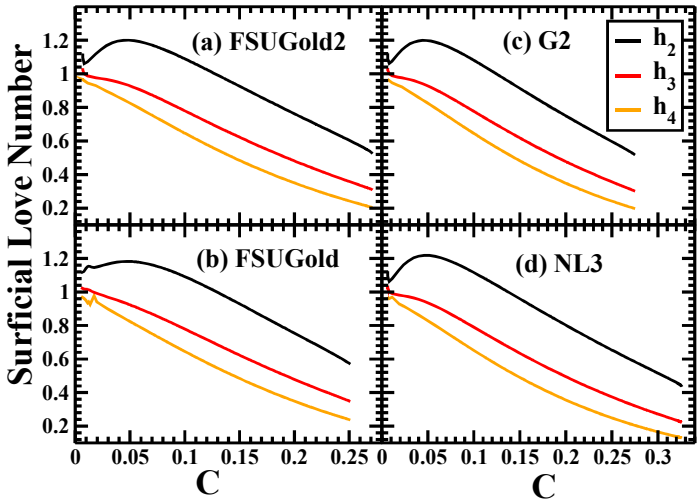

Figure 5.6: Surficial Love number h_l as a function of compactness C of a neutron star, for selected values of l.

5.2.4 Tidal deformability and cut-off frequency of compact star

To examine the results of tidal deformability with and without hyperons, we have shown the tidal deformability λ as a function of C in Fig. 5.8, where we have considered a single NS under the influence of an external tidal field with adiabatic approximation using the four EoSs. In this case, the orbital evolution time scale is much larger than the time scale needed to assume the star as a stationary configuration. From the very beginning, we mark an infinitely large λ corresponding to a small compactness i.e., C ~0.02. Further, the λ value falls to a minimum that rises again resulting in a hump like pattern for each EoS. It is noteworthy that in Fig. 5.8(b) by introducing the NL3 case with hyperon, there is remarkable but mere deviation in λ value i.e 7.527 g cm^2 s^2 (without hyperon λ= 7.466 g cm^2 s^2). Since, the tidal deformability λ is a surface phenomenon, it is very much affected by the radius of the star in both neutron star and hyperon star. Thus, the tidal deformability λ becomes highly sensitive on the radius R even though k_2 is small. We estimate the radii to be within 12.236−14.422 km for a NS of mass $1.4M_\odot$ and the range is 13.690−14.430

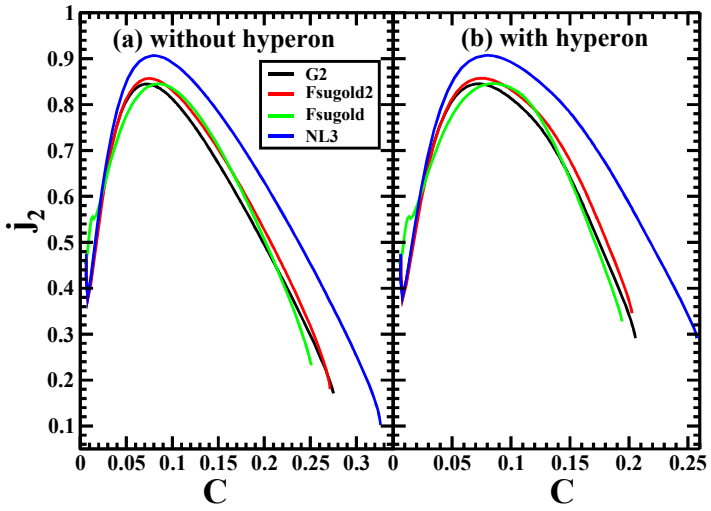

Figure 5.7: The magnetic tidal Love number for selected EoSs.

km for neutron-hyperon star for all the four stiff or soft EoS (see Table 5.2).

Figure 5.9, shows the tidal deformability for both neutron and hyperon stars. We have a large radius for a smaller stellar mass of $\sim 0.1 M_{\odot}$ in both cases. At this value of mass and radius, the tidal deformability λ becomes maximum, because for a large radius with smaller mass, the force of attraction within the star is weak and when another star comes closure, the gravitational pull over ride maximum at the surface part of the star. This phenomenon is true for both neutron as well as hyperon stars [64, 66]. Then, suddenly the tidal deformibility decreases and again increases as shown in the figure making a broad peak at around $M = 0.7 - 0.8 M_{\odot}$ and then decreases smoothly with increase in the mass of the star. Since, the tidal deformibility depends a lot on both mass and radius of a NS, it is imperative to measure the radius of the star precisely, as the mass is already measured with very good precession. Recently, Steiner *et al.*, predicted the most extreme limit for the tidal deformabilities between $0.6\times\ 10^{36}$ and $6\times\ 10^{36}$ g cm^2 s^2 for $1.4 M_{\odot}$ with 95% confidence. This range can be constrained on high dense matter of any measurements [211]. Mostly, the binaries masses are about $1.4 M_{\odot}$, so in particular we are interested in studying the phenomena within this mass range and the results are summarize in Table 5.2.

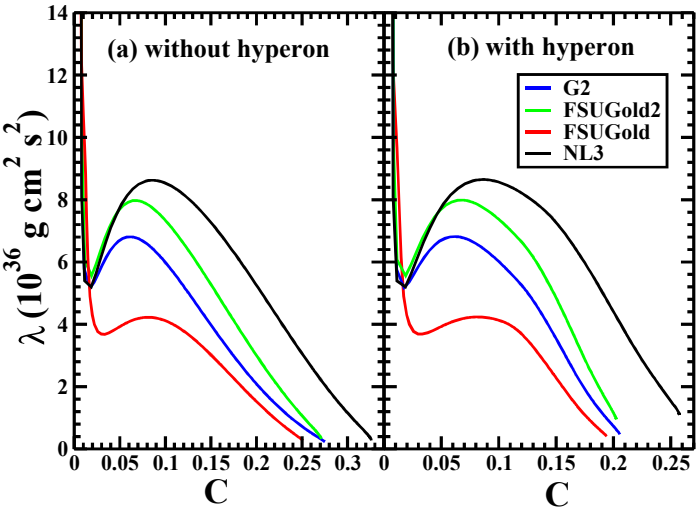

Figure 5.8: The tidal deformability λ as a function of the compactness C for the four EoS with and without hyperon.

Comparing the results, we notice that the tidal deformability λ is quite sensitive to the EoS. It is more for stiffer EoS, because of the high-density behavior of the symmetry energy [212].

Finally, we calculate the weighted tidal deformability (Eq. (5.38)) of the binary neutron star of mass m_1 and m_2 and the root mean square (rms) measurement uncertainty $\Delta\tilde{\lambda}$ can be calculated following approximate formula [64, 66]:

$$\Delta\tilde{\lambda} \approx \alpha \left(\frac{M}{M_\odot}\right)^{2.5} \left(\frac{m_2}{m_1}\right)^{0.1} \left(\frac{f_{cut}}{Hz}\right)^{-2.2} \left(\frac{D}{100Mpc}\right), \tag{5.76}$$

where $\alpha = 1.0 \times 10^{42}$ g cm^2 s^2 is the tidal deformability for a single Advanced LIGO detector and f_{cut} (f_{end}) cutoff frequency [185] for the end stage of the inspiral binary neutron stars. D denotes the luminosity distance from the source to observer.

The weighted tidal deformibility for neutron and hyperon stars and their corresponding masses as cut-off frequency f_{cut} is shown in Fig. 5.10. The cut-off frequency is a stopping criterion to estimate when the tidal model no longer describes the binary. Here, we take the cut-off to be approximately when the two neutron stars come into contact, estimated as in Eq.36 of Ref. [185]. Specifically, we use $f_{cut} = 2f_{orb.}^{N(R_1+R_2)}$,

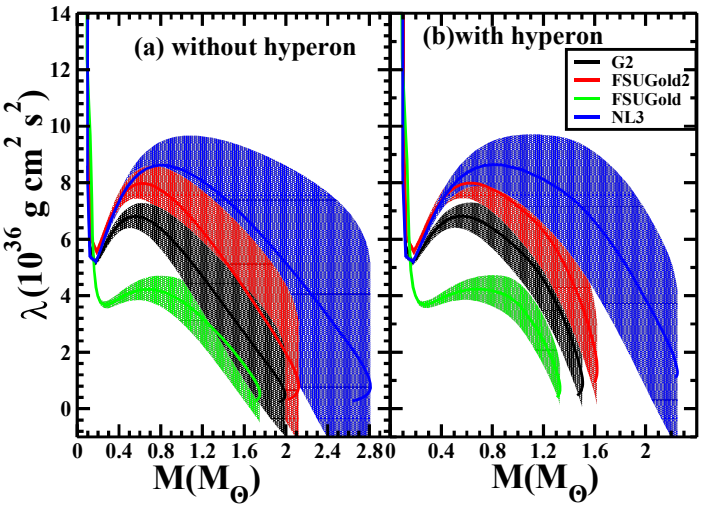

Figure 5.9: Tidal deformability λ of a single NS as a function of the neutron-star mass for a range of EoSs. The estimate of uncertainties in measuring λ for equal mass binaries at a distance of $D = 100$ Mpc is shown for the aLIGO detector in shaded area. (b) Same as (a), but for hyperon star.

where $f_{orb.}^{N(R_1+R_2)}$ is the Newtonian orbital frequency corresponding to the orbital separation where two unperturbed neutron stars with radii R_1 and R_2 would touch. In the upper panel Fig. 5.10(a), 5.10(c), it shows the variation of mass of the binary as a function of cut-off frequency f_{cut}. Here, we considered $m_1 = m_2$, i.e., both the masses of the binary are equal. Initially, the masses of the stars $0.2M_\odot$ remain almost constant up to $f_{cut} \approx 400$ Hz. Then the mass increases nearly exponentially up to a maximum mass of $\approx 1.75-2.81M_\odot$ (for NS) and $\approx 1.33-2.25M_\odot$ (for hyperon star) and then decreases. By this time, the cut-off frequency f_{cut} attains quite large value. When the individual mass of the binary is $1.4M_\odot$, the NL3 set weighted tidal deformibility achieves the cut-off frequency $f_{cut} \approx 1256.7$ Hz as the minimum contrary to the $f_{cut} \approx 1608.0$ Hz of FSUGold at the same mass of the single NS. It is also clear from the figure that the weighted tidal deformability of the NS for the four models are 7.466, 3.668, 5.229 and 2.418 for NL3, G2, FSUGold2 and FSUGold, respectively, with the corresponding frequencies 1256.7, 1440.9, 1332.4 and 1608.0 Hz.

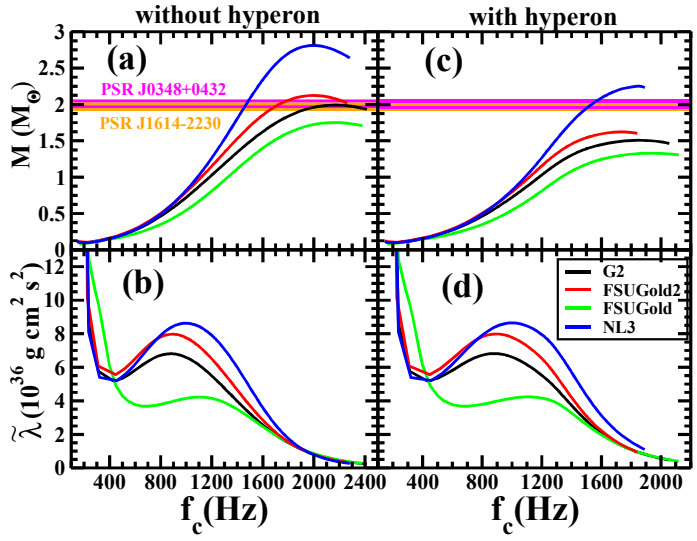

Figure 5.10: (a),(c) The mass-cut-off frequency f_c profile of normal and hyperon stars using four EoSs. (b) The tidal deformabilty with cut-off frequency plot of the neutron star. (d) Same as (b), but for hyperon star.

Using the cut-off frequency, we calculate the uncertainty in the measurement of the tidal deformability ($\Delta\tilde{\lambda}$) obtained from these four EoSs for an equal-mass binary star inspiral at 100 Mpc from aLIGO detector (shaded region in Fig. 5.9). The uncertainty in the lower mass region ($0.4-1.0M_\odot$) of the NS $\Delta\tilde{\lambda}$ is smaller. Similar results are found in the case of hyperon star also. Interestingly, the error ($\Delta\tilde{\lambda}$) increases with increase the mass of the binary for all the EoSs. From Table 5.2, by comparing the $\Delta\tilde{\lambda}$ obtained from all the EoSs, we find that predicted errors are greater than the measured value for a star of mass $1.4M_\odot$.

5.3 Summary and Conclusions

In summary, four different models have been extensively applied which are obtained from effective field theory motivated relativistic mean field formalism. This effective interaction model satisfies the nuclear saturation properties and reproduce the bulk properties of finite nuclei with a very good accuracy. We used these four forces

of interaction and calculate the EoS for neutron and hyperon stars matter. It is noteworthy that each term of the interaction has its own meaning and has specific character. The inclusion of extra terms (nucleons replaced by baryons octet) in the Lagrangian contribute to soften the EoS and the matter becomes less compressible. Hence, there is a decrease in the maximum mass by $\sim 0.5 M_{\odot}$ than the pure neutron star.

We have extended our calculations to various tidal responses both for electric-type (even-parity) and magnetic-type (odd-parity) of neutron and hyperon stars in the influence of an external gravitational tidal field. The Love numbers are directly connected with surficial Love number h_l associated with the surface properties of the stars. Subsequently, we study the quadrupolar tidal deformability λ of normal neutron star and hyperon star using different set of equations of state. These tidal deformabilities particularly depend on the quadrupole Love number k_2 and radius (R) of the isolated star. Although the maximum value of k_2 is not very sensitive to the EoS for neutron and hyperon stars lying in the range $k_2 \approx 0.144 - 0.170$ and $0.143 - 0.194$ for neutron and hyperon stars, respectively, but it is very much sensitive to the radius of the star.

We find that aLIGO can constrain on the existence of hyperon star, i.e., the inner core of the NS has hyperons, but detecting them can be much harder. However, it should be able to constraint the neutron star deformability to $\lambda \leq 10 \times 10^{36}$ g cm^2 s^2 for a binary of $1.4 M_{\odot}$ neutron stars at a distance 100 Mpc from the detector. In future, we expect that aLIGO should be able to measure λ even for neutron stars masses up to $2.0 M_{\odot}$ and consequently constrain the stiffness of the equations of state. It is worth mentioning that the present calculations are based on the extrapolation of the formula $\Delta\tilde{\lambda}$ given in Ref. [64, 213, 214]. Here, the systematic uncertainties in the model that was used to obtain the measurability estimates are neglected.

Chapter 6

New parameter sets G3, and IOPB-I

In this chapter, we have discussed the newly developed relativistic forces, G3, and the Institute of Physics Bhubaneswar-I (IOPB-I), which are broadly applicable for the study of finite nuclei, infinite nuclear matter, and neutron star. Using these forces, we calculate the binding energies, charge radii, isotopic shift, and neutron-skin thickness for some selected nuclei. From the ground-state properties of superheavy nuclei (Z=120), it is noticed that considerable shell gaps appear at neutron numbers N=172, 184, and 198, manifesting the magicity at these numbers. The low-density behavior of the equation of state for pure neutron matter is compatible with other microscopic models. Along with the nuclear symmetry energy, its slope and curvature parameters at the saturation density are consistent with those extracted from various experimental data. We calculate the neutron star properties such as mass-radius, and tidal deformability using the equation of state composed of nucleons and leptons in β-equilibrium condition.

6.1 Introduction

The nuclear physics inputs are essential in understanding the properties of dense objects like neutron stars. The relativistic mean field models based on the effective field theory (ERMF) motivated Lagrangian density have been instrumental in describing

the neutron star properties, since, the ERMF models enables one to readily include the contributions from various degrees of freedoms such as hyperons, kaons and Bose condensates. The model parameters are obtained by adjusting them to reproduce the experimental data on the bulk properties for a selected set of finite nuclei. However, these parameterizations give remarkable results for bulk properties such as binding energy, quadrupole moment, root mean square radius not only for beta stable nuclei, but also for nuclei away from the stability line [19, 79]. However, the same model, sometimes does not appropriately reproduce the behavior of the symmetric nuclear matter and pure neutron matter at supranormal densities as well as those for the pure neutron matter at the subsaturation densities.

The ERMF model usually includes the contributions from the self and cross-couplings of isoscalar-scalar σ, isoscalar-vector ω and isovector-vector ρ mesons. The inclusion of various self and cross-couplings makes the model flexible to accommodate various phenomena associated with the finite nuclei and neutron stars adequately without compromising the quality of the fit to those data considered a priory. For example, the self-coupling of σ mesons remarkably reduces the nuclear matter incompressibility to the desired values [26]. The cross-coupling of ρ mesons with σ or ω allows one to vary the neutron-skin thickness in a heavy nucleus like ^{208}Pb over a wide range [36, 215]. These cross-couplings are also essential to produce desired behavior for the equation of state of pure neutron matter. Though, the effects are marginal, but, the quantitative agreement with the available empirical informations call for them [215,216]. Noticed that ERMF Lagrangian density in Eq. (2.1) contains various coupling constants corresponding to different mesons. Thus, we can say that each term has its own physical significance alongwith some limitations and if we omit any one of them then it will be very difficult to describe the Hamiltonian as a whole. So, to overcome the limitations all possible terms are to be included and the model needs to be extended. For this, we strive for new parameter sets.

One may also consider the contributions due to the couplings of the meson field gradients to the nucleons as well as the tensor coupling of the mesons to the nucleons within the ERMF model [19]. These additional couplings are required from the naturalness view point, but very often they are neglected. Only the parameterizations of the ERMF model in which the contributions from gradient and tensor couplings

of mesons to the nucleons considered are the TM1*, G1 and G2 [17, 19]. However, these parameterizations display some disconcerting features. For instance, the nuclear matter incompressibility and/or the neutron-skin thickness associated with the TM1*, G1 and G2 parameter sets are little too large in view of their current estimates based on the measured values for the isoscalar giant monopole and the isovector giant dipole resonances in the ^{208}Pb nucleus [217, 218]. The equation of state (EoS) for the pure neutron matter at sub-saturation densities show noticeable deviations with those calculated using realistic approaches.

Recently, the detection of gravitational waves from the binary neutron star GW170817 is a major breakthrough in astrophysics and was detected for the first time by the advanced Laser Interferometer Gravitational- wave Observatory (aLIGO) and advanced VIRGO detectors [16]. This detection has certainly proved to be a valuable guidance to study matter under the most extreme conditions. In-spiraling and coalescing objects of a binary neutron star result in gravitational waves. Due to the merger, a compact remnant remains whose nature is decided by two factors: (i) the masses of the inspiraling objects and (ii) the equation of state of the neutron star matter. For final state, the formation of either a neutron star or a black hole depends on the masses and stability of the objects. The chirp mass is measured very precisely from data analysis of GW170817 and it is found to be $1.188^{+0.004}_{-0.002}M_{\odot}$ for the 90% credible intervals. It is suggested that the total mass should be $2.74^{+0.04}_{-0.01}M_{\odot}$ for low-spin priors and $2.82^{+0.47}_{-0.09}M_{\odot}$ for high-spin priors [16]. Moreover, the maximum mass of nonspinning neutron stars(NSs) as a function of radius is observed with the highly precise measurements of $M \approx 2.0M_{\odot}$. From the observations of gravitational waves, we can extract information regarding the radii or tidal deformability of the nonspinning and spinning NSs [64–66]. Once we succeed in getting this information, it is easy to get the neutron star matter equation of state [219, 220].

In this chapter, we constructed two set of new parameters G3, and the Institute of Physics Bhubaneswar-I (IOPB-I), using the simulated annealing method (SAM) [221–223] and explored the generic prediction of properties of finite nuclei, nuclear matter, and neutron stars within the ERMF formalism. Our new parameter set yields the considerable shell gap appearing at neutron numbers N=172, 184 and 198 showing the magicity of these numbers. The behavior of the density-dependent symmetry

energy of nuclear matter at low and high densities is examined in detail. The effects of the core EoS on the mass, radius, and tidal deformability of an NS are evaluated using the static $l = 2$ perturbation of a Tolman-Oppenheimer-Volkoff solution.

6.2 Parameter Fitting

Having developed in chapter 2 most of the required formalism related to the properties of finite nuclei, infinite nuclear matter, and the neutron star. We are now in a position to implement the calibration of a new energy density functional by extending the model Lagrangian with addition of relevant terms and determine the two new sets of force parameters using the SAM. The SAM is used to determine the parameters used in the Lagrangian density [224, 225]. The SAM is useful in the global minimization technique; i.e., it gives accurate results when there exists a global minimum within several local minima. Usually, this procedure is used in a system in which the number of parameters is more than the number of observables [226–228]. In this simulation method, the system stabilizes when the temperature T (a variable which controls the energy of the system) goes down [221–223]. Initially, the nuclear system is put at a high temperature (highly unstable) and then allowed to cool down slowly so that it is stabilized in a very smooth way and finally reaches the frozen temperature (stable or systematic system). The variation of T should be very small near the stable state. The $\chi^2 = \chi^2(p_1, \ldots, p_N)$ values of the considered systems are minimized (least-squares fit), which is governed by the model parameters p_i. The general expression of the χ^2 can be given as:

$$\chi^2 = \frac{1}{N_d - N_p} \sum_{i=1}^{N_d} \left(\frac{M_i^{exp} - M_i^{th}}{\sigma_i} \right)^2 . \tag{6.1}$$

Here, N_d and N_p are the numbers of experimental data points and fitting parameters, respectively. The experimental and theoretical values of the observables are denoted by M_i^{expt} and M_i^{th}, respectively. The σ_i's are the adopted errors [229]. The adopted errors are composed of three components, namely, the experimental, numerical, and theoretical errors [229]. As the name suggests, the experimental errors are associated with the measurements; numerical and theoretical errors are associated with the numerics and the shortcomings of the nuclear model employed, respectively. In

Table 6.1: The vector v_0 and v_1 contains the lower and upper limits of each of the components of the vector v which used for implementing the SAM-based algorithm for searching the global minimum of χ^2. The vector d represents the maximum displacement allowed in a single step for the components of the vector v.

Parameter	v	v_0	v_1	d
$\mathcal{E}_0$	-16.02	-16.30	-15.70	0.025
K_∞	230.0	210.0	245.0	1.0
ρ_0	0.148	0.140	0.165	0.001
M^*/M	0.525	0.5	0.9	0.002
J	32.1	28.0	35.0	0.08
g_δ	2.0	0.0	15.0	0.2
η_1	0.410	0.4	0.8	0.002
η_2	0.10	0.09	0.12	0.002
η_ρ	0.590	0.1	0.7	0.003
Λ_ω	0.03	0.02	0.09	0.002
α_1	1.73	1.0	2.0	0.005
α_2	-1.51	-1.65	-1.40	0.005
β_σ	-0.083	-0.09	-0.08	0.00001
β_ω	-0.55	-0.6	-0.4	0.001
ζ_0	1.01	1.01	1.01	0.0
$f_\rho/4$	3.0	0.0	6.0	0.03
$f_\omega/4$	0.4	0.0	1.0	0.005
m_s	510.0	480.0	570.0	0.450

principle, there exists some arbitrariness in choosing the values of σ_i, which is partially responsible for the proliferation of the mean-field models. The only guidance available from the statistical analysis is that the χ^2 per degree of freedom [Eq. (6.1)] should be close to unity. In the present calculation, we used some selected fit data for binding energy and the root mean square radius of the charge distribution for some selected nuclei and the associated adopted errors on them [230].

In our calculations, we have built two new parameter sets G3, and IOPB-I and analyzed its effects for finite and infinite nuclear systems. Thus, we performed an overall fit with 13 parameters for G3, and 8 for IOPB-I, where the nucleons as well as the masses of the two vector mesons in free space are fixed at their experimental values, i.e., $M = 939$ MeV, $m_\omega = 782.5$ MeV, $m_\rho = 763.0$ MeV, and $m_\delta = 980.0$ MeV. The effective nucleon mass can be used as a nuclear matter constraint at the saturation density ρ_0 along with other empirical values like incompressibility, binding energy per nucleon, and asymmetric parameter J. While fitting the parameter, the values of effective nucleon mass M^*/M, nuclear matter incompressibility K, and symmetry energy coefficient J are constrained within 0.50–0.90, 210–245 MeV, and 28–35 MeV, respectively.

We use SAM algorithm and follow the steps which are:

1. We initiate the steps by taking a suitable guess value for the vector v and then calculate χ^2 (say, χ^2_{old}) by the help of Eq. (6.1) for particular set of experimental data and the corresponding ERMF results together with the theoretical errors.

2. By using the following steps we create a new set of ERMF parameters. We choose a uniform random number for assigning a new value for the component v_r as $v_r \rightarrow v_r + \eta d_r$, where η is a uniform random number that lies within the range -1 to +1. The above step is repeated again and again. We stop when the new value of v_r comes out to be within its allowed limits defined as v_0 and v_1. This modified v is then used to generate new ERMF parameters. Thus, even a small change in the value of component of the vector v will lead to changes in the values of several ERMF parameters. For example, a change in the value of K_∞ will alter the values of the ERMF parameters k_2, k_3, and M^*.

3. We take the newly generated ERMF parameters and use in the Metropolis

algorithm. We calculate the quantity $P(\chi^2)$ where

$$P(\chi^2) = e^{(\chi^2_{old} - \chi^2_{new})/T}. \tag{6.2}$$

We obtain the χ^2_{new} by taking the newly generated set of the ERMF parameters. Also, the T is a control parameter which we get from the Cauchy annealing schedule given by

$$T(k) = T_i/(k+1); \qquad k = 1, 2, 3, ... \tag{6.3}$$

The newly generated ERMF parameter set is confirmed only when $P(\chi^2) > \beta$, where β is an uniform random number that lies between 0 and 1.

The newly developed G3, and IOPB-I sets along with NL3 [29], FSUGold2 [194], FSUGarnet [231], and G2 [17] are given for comparison in Table 6.2. The calculated results of the binding energy and charge radius are compared with the known experimental data [112, 144]. It is to be noted that in the original ERMF parametrization, only five spherical nuclei were taken into consideration while fitting the parameters with the binding energy, charge radius and single particle energy [17]. However, here, eight spherical nuclei are used for the fitting as listed in Table 6.3.

6.3 Results and Discussions

In this section we discuss our calculated results for finite nuclei, infinite nuclear matter and neutron stars. For finite nuclei, binding energy, rms radii for neutron and proton distributions, isotopic shift, two-neutron separation energy, and neutron-skin thickness are analyzed. Similarly, for infinite nuclear matter systems, the binding energies per particle for symmetric and asymmetric nuclear matter including pure neutron matter at both subsaturation and suprasaturation densities are compared with other theoretical results and experimental data. The parameter sets G3, and IOPB-I is also applied to study the structure of neutron stars using $\beta-$equilibrium and charge neutrality conditions.

6.3.1 Finite Nuclei

(i) Binding energies, charge radii, isotopic shift and neutron-skin thickness

We used eight spherical nuclei to fit the experimental ground-state binding energies and charge radii using the SAM. The calculated results are listed in Table 6.3 and compared with other theoretical models as well as experimental data [112, 144]. It can be seen that the NL3 [29], FSUGold2 [194], FSUGarnet [231], and G2 [17] models successfully reproduce the energies and charge radii as well. Even though the *"mean-field models are not expected to work well for the light nuclei," the results deviate only marginally for the ground-state properties for light nuclei* [232]. We noticed that both the binding energy and charge radius of ^{16}O are well produced by IOPB-I. However, the calculated charge radii of ^{40,48}Ca slightly underestimate the data. We would like to emphasize that it is an open problem to mean-field models to predict the evolution of charge radii of $^{38-52}$Ca (see Fig. 3 in Ref. [233]).

In Fig. 6.1 we plot the differences between the calculated and experimental binding energies for 70 spherical nuclei [230] obtained using different parameter sets. The

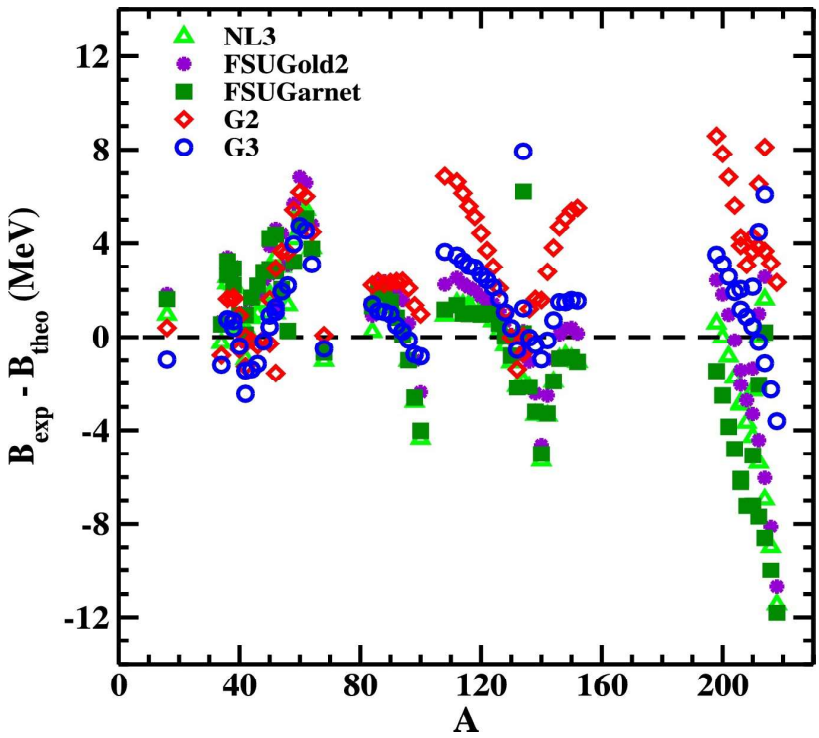

Figure 6.1: Difference between experimental and theoretical binding energies as a function of mass numbers for NL3 [29], FSUGold2 [194], FSUGarnet [231], G2 [17] and G3 parameter sets.

triangles, stars, squares, diamonds and circles are the results for the NL3, FSUGold2 , FSUGarnet, G2 and G3 parameterizations, respectively. The above results affirm that G3 set reproduces the experimental data better. The rms deviations for the binding energy as displayed in Fig. 6.1 are 2.977, 3.062, 3.696, 3.827 and 2.308 MeV for NL3, FSUGold2, FSUGarnet, G2 and G3 respectively. The rms error on the binding energy for G3 parameter set is smaller in comparison to other parameter sets.

In Fig. 6.2, the isotopic shift Δr_c^2 for Pb nucleus is shown. The isotopic shift is defined as $\Delta r_c^2 = R_c^2(A) - R_c^2(208)$ (fm^2), where $R_c^2(208)$ and $R_c^2(A)$ are the mean square radius of ^{208}Pb and Pb isotopes having mass number A. From the figure, one can see that Δr_c^2 increases with mass number monotonously till A=208 ($\Delta r_c^2 = 0$ for ^{208}Pb) and then gives a sudden kink. It was first pointed by Sharma et al [28], that the non-relativistic parameterization fails to show this effect. However, this effect is

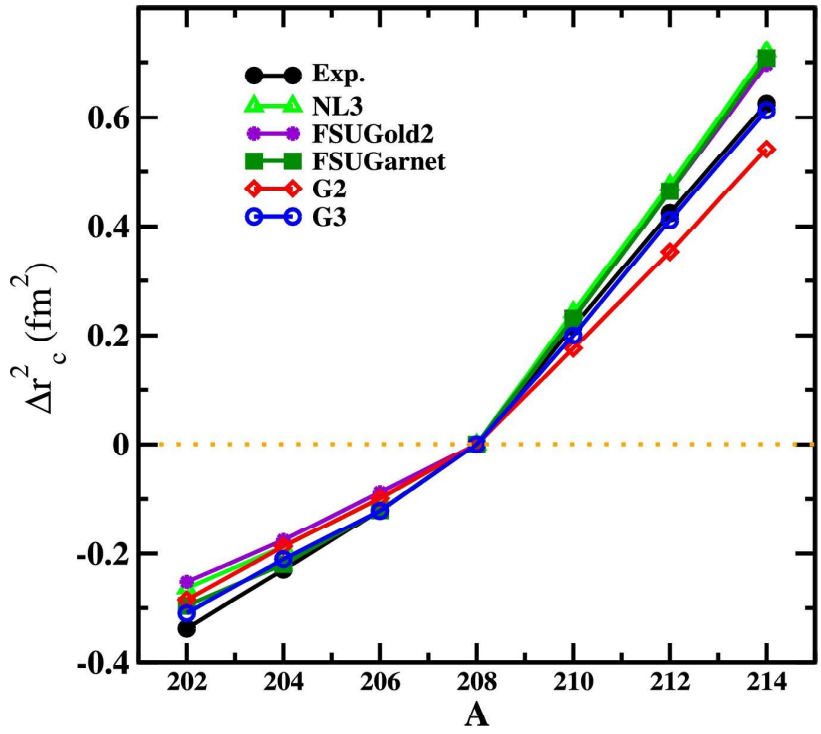

Figure 6.2: The isotopic shift $\Delta r_c{}^2 = R_c^2(208) - R_c^2(A)$ (fm^2) of Pb isotopes taking R_c of ^{208}Pb as the standard value. Calculations with the NL3 [29], FSUGold2 [194], FSUGarnet [231], G2 [17] and G3 parameter sets are compared.

well explained when a relativistic set like NL-SH [28] is used. The NL3, FSUGold2 , FSUGarnet, G2 and G3 sets also appropriately predict this shift in Pb isotopes, but the agreement with experimental data of the present parameter set G3 is marginally better.

The excess of neutrons gives rise to a neutron-skin thickness. The neutron-skin thickness Δr_{np} is defined as

$$\Delta r_{np} = \langle r^2 \rangle_n^{1/2} - \langle r^2 \rangle_p^{1/2} = R_n - R_p, \tag{6.4}$$

with R_n and R_p being the rms radii for the neutron and proton distributions, respectively. The Δr_{np}, strongly correlated with the slope of the symmetry energy [235–237], can probe the isovector part of the nuclear interaction. However, there is a large uncertainty in the experimental measurement of the neutron distribution radius of the finite nuclei. The current values of neutron radius and neutron-skin thickness of ^{208}Pb are $5.78^{+0.16}_{-0.18}$ and $0.33^{+0.16}_{-0.18}$ fm, respectively [238]. This error bar is too large to provide significant constraints on the density-dependent symmetry energy. It is expected that

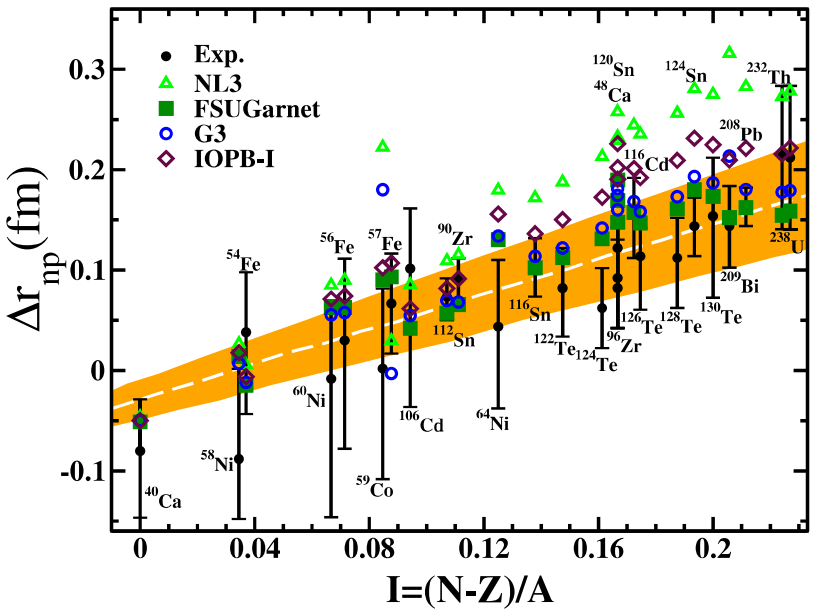

Figure 6.3: The neutron-skin thickness as a function of the asymmetry parameter. Results obtained with the parameter sets G3, and IOPB-I are compared with those of the sets NL3 [29], FSUGarnet [231], and experimental values [234]. The shaded region is calculated using Eq. (6.5).

PREX-II result will give us the neutron radius of ^{208}Pb within 1% accuracy. The inclusion of some isovector-dependent terms in the Lagrangian density is needed, which would provide the freedom to refit the coupling constants within the experimental data without compromising the quality of fit. The addition of ω-ρ cross-coupling into the Lagrangian density controls the neutron-skin thickness of ^{208}Pb as well as that of other nuclei. In Fig. 6.3, we show the neutron-skin thickness Δr_{np} for ^{40}Ca to ^{238}U nuclei as a function of proton-neutron asymmetry $I = (N - Z)/A$. The calculated results of Δr_{np} for NL3, FSUGarnet, G3, and IOPB-I parameter sets are compared with the corresponding experimental data [234]. Experiments have been done with antiprotons at CERN and the Δr_{np} are extracted for 26 stable nuclei ranging from ^{40}Ca to ^{238}U as displayed in the figure along with the error bars. The trend of the data points shows approximately linear dependence of neutron-skin thickness on the relative neutron excess I of nucleus that can be fitted by [234, 239]:

$$\Delta r_{np} = (0.90 \pm 0.15)I + (-0.03 \pm 0.02)\ fm. \tag{6.5}$$

The values of Δr_{np} obtained with IOPB-I for some of the nuclei slightly deviate from the shaded region, as can be seen from Fig. 6.3. This is because IOPB-I has a smaller strength of ω-ρ cross-coupling as compared to the FSUGarnet, and G3 sets. Recently, Fattoyev *et. al.* constrained the upper limit of $\Delta r_{np} \lesssim 0.25$ fm for the ^{208}Pb nucleus with the help of GW170817 observation data [240]. The calculated values of neutron-skin thickness for the ^{208}Pb nucleus are 0.283, 0.162, 0.180, and 0.221 fm for the NL3, FSUGarnet, G3, and IOPB-I parameter sets respectively. The proton elastic scattering experiment recently measured neutron-skin thickness $\Delta r_{np} = 0.211^{+0.054}_{-0.063}$ fm for ^{208}Pb [241]. Thus values of $\Delta r_{np} = 0.221$ for IOPB-I are consistent with the recent prediction of neutron-skin thickness.

(ii) Two-neutron separation energy $S_{2n}(Z, N)$

The large shell gap in single-particle energy levels is an indication of the magic number. This is responsible for the extra stability for the magic nuclei. The extra stability for a particular nucleon number can be understood from the sudden fall in the two-neutron separation energy S_{2n}. The S_{2n} can be estimated by the difference in ground

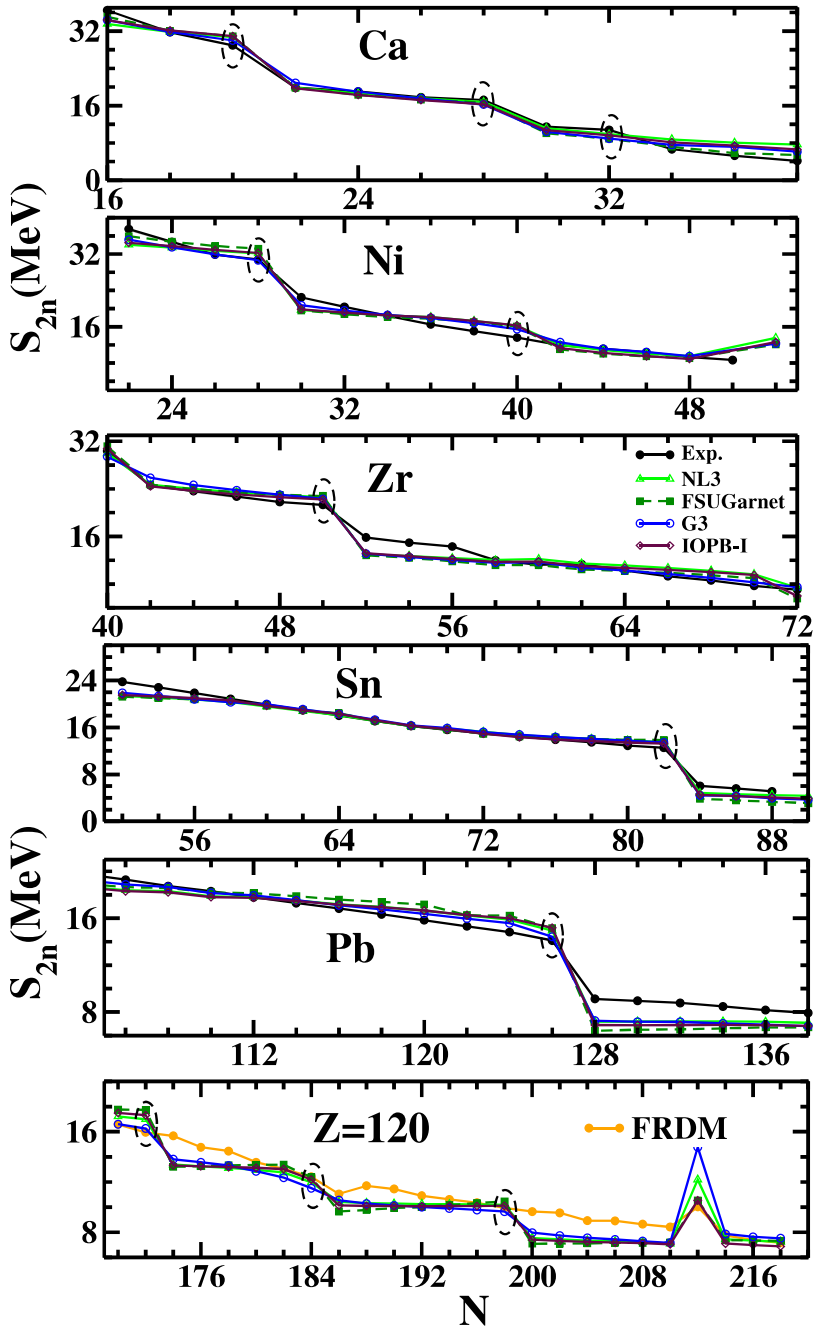

Figure 6.4: The two-neutron separation energy as a function of neutron number for the isotopic series of Ca, Ni, Zr, Sn, and Pb nuclei with NL3 [29], FSUGarnet [231], FRDM [242], and experimental data [144] whenever available. The dotted circle represents the magicity of the nuclei.

state binding energies of two isotopes, i.e.,

$$S_{2n}(Z,N) = BE(Z,N) - BE(Z,N-2). \tag{6.6}$$

In Fig. 6.4, we display results for the S_{2n} as a function of neutron numbers for Ca, Ni, Zr, Sn, Pb, and Z=120 isotopic chains. The calculated results are compared with the finite range droplet model (FRDM) [242] and most recent experimental data [144]. From the figure, it is clear that there is an evolution of magicity as one moves from the valley of stability to the drip line. In all cases, the S_{2n} values decrease gradually with increase in neutron number. The experimental manifestation of large shell gaps at neutron numbers N = 20, 28(Ca), 28(Ni), 50(Zr), 82(Sn), and 126(Pb) are reasonably well reproduced by the four relativistic sets. Figure 6.4 shows that the experimental S_{2n} of $^{50-52}$Ca are in good agreement with the prediction of the NL3 set. It is interesting to note that all sets predict the subshell closure at N=40 for Ni isotopes. Furthermore, the two-neutron separation energy for the isotopic chain of nuclei with Z=120 is also displayed in Fig. 6.4. For the isotopic chain of Z=120, no experimental information exits. The only comparison can be made with theoretical models such as the FRDM [144]. At N=172, 184 and 198 sharp falls in separation energy is seen for all forces, which have been predicted by various theoretical models in the superheavy mass region [243–246]. It is to be noted that the isotopes with Z=120 are shown to be spherical in their ground state [246]. In a detailed calculation, Bhuyan and Patra using both RMF and Skyrme-Hartree-Fock formalisms, predicted that Z=120 could be the next magic number after Z=82 in the superheavy region [250]. Thus, the deformation effects may not affect the results for Z=120. Therefore, a future mass measurement of ^{292,304,318}120 would confirm a key test for the theory, as well as direct information about the closed-shell behavior at N=172, 184, and 198.

6.3.2 Infinite Nuclear Matter

The nuclear incompressibility K determines the extent to which the nuclear matter can be compressed. This plays an important role in the nuclear EoS. Currently, the accepted value of $K = 240 \pm 20$ MeV was determined from isoscalar giant monopole resonance (ISGMR) for ^{90}Zr and ^{208}Pb nuclei [251,252]. For our parameter set IOPB-I,

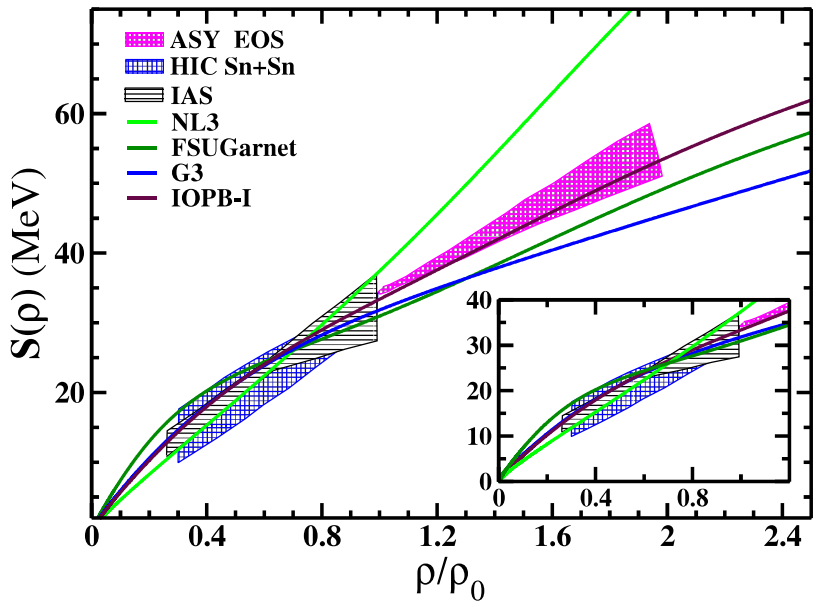

Figure 6.5: Density-dependent symmetry energy from Eq. (2.42) with different ERMF parameter sets along with G3, and IOPB-I parametrizations. The shaded region is the symmetry energy from IAS [247], HIC Sn+Sn [248] and ASY-EoS experimental data [249]. The zoomed pattern of the symmetry energy at low densities is shown in the inset.

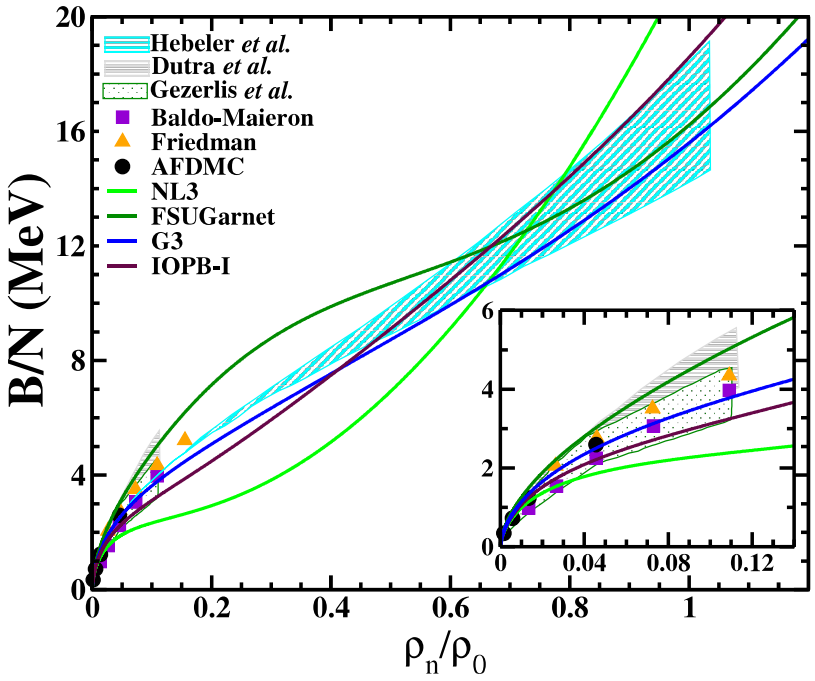

Figure 6.6: The energy per neutron as a function of neutron density with NL3 [29], FSUGarnet [231], G3, and IOPB-I parameter sets. Other curves and shaded regions represent the results for various microscopic approaches such as Baldo-Maieron [203], Friedman [253], auxiliary-field diffusion Monte Carlo [254], Dutra [89], Gezerlis [255] and Hebeler [256] methods.

we get $K = 222.65$ MeV. The density-dependent symmetry energy $S(\rho)$ is determined from Eq. (2.42) using IOPB-I along with three adopted models. The calculated results of the symmetry energy coefficient (J), the slope of symmetry energy (L), and other saturation properties are listed in Table 6.4. We find that in case of IOPB-I, $J = 33.3$ MeV and $L = 63.6$ MeV. These values are compatible with $J = 31.6 \pm 2.66$ MeV and $L = 58.9 \pm 16$ MeV obtained by various terrestrial experimental information and astrophysical observations [95].

Another important constraint K_τ has been suggested which lies in the range of -840 MeV to -350 MeV [257–259] by various experimental data on isoscalar giant monopole resonance, which we can calculate from Eq. (2.46). It is to be noticed that the calculated values of K_τ are -703.23, -250.41, -307.65, and -389.46 MeV for NL3, FSUGarnet, G3, and IOPB-I parameter sets, respectively. The ISGMR measurement

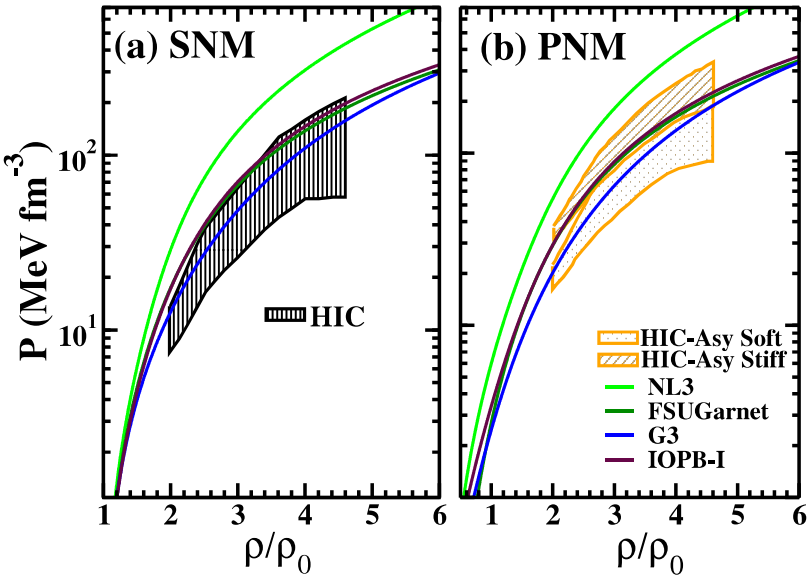

Figure 6.7: Pressure as a function of baryon density for the G3, and IOPB-I forces. The results with NL3 [29], and FSUGarnet [231] are compared with the EoS extracted from the analysis [260] for the (a) symmetric nuclear matter (SNM) and (b) pure neutron matter (PNM).

was investigated in a series of $^{112-124}$Sn isotopes, which extracted the value of $K_\tau = -395 \pm 40$ MeV [261]. It is found that $K_\tau = -389.46$ MeV for the IOPB-I set is consistent with GMR measurement [261]. In the absence of cross-coupling, $S(\rho)$ of NL3 is stiffer at low and high density regimes as displayed in Fig. 6.5. Alternatively, the presence of cross-coupling of ρ mesons to the ω (in the case of FSUGarnet and IOPB-I) and σ mesons (in case of G3) yields the softer symmetry energy at low density which is consistent with HIC Sn+Sn [248] and IAS [247] data as shown in the figure. However, the IOPB-I set has softer $S(\rho)$ in comparison to the NL3 parameter set at higher density which lies inside the shaded region of ASY-EoS experimental data [249] .

Next, we display in Fig. 6.6 the binding energy per neutron (B/N) as a function of the neutron density. Here, special attention is needed to build a nucleon-nucleon interaction to fit the data at subsaturation density. For example, the EoS of pure neutron matter (PNM) at low density is obtained within the variational method, which is obtained with a Urbana $v14$ interaction [253]. In this regard, the effective

mean-field models also fulfill this demand to some extent [38, 231, 262]. The cross-coupling ω-ρ plays an important role at low density of the PNM. The low density (zoomed pattern) nature of the FSUGarnet, G3 and IOPB-I sets are in harmony with the results obtained by microscopic calculations [89, 203, 253–255], while the results for NL3 deviate from the shaded region at low as well as high density regions. We also find a very good agreement for FSUGarnet, G3, and IOPB-I at higher densities, which have been obtained with chiral two-nucleon (NN) and three-nucleon (3N) interactions [256].

In Fig. 6.7, we show the calculated pressure P for the SNM and PNM with the baryon density for the four ERMF models, which then are compared with the experimental flow data [260]. It is seen from Fig. 6.7(a) that the SNM EoS for the G3 parameter set is in excellent agreement with the flow data for the entire density range. The SNM EoS for the FSUGarnet and IOPB-I parameter sets are also compatible with the experimental HIC data but they are stiffer relative to the EoS for the G3 parametrization. In Fig. 6.7(b), the bounds on the PNM EoS are divided into two categories (i) the upper one corresponds to a strong density dependence of symmetry energy $S(\rho)$ (HIC-Asy Stiff) and (ii) the lower one corresponds to the weakest $S(\rho)$ (HIC-Asy Soft) [260,263]. Our parameter set IOPB-I along with the G3 and FSUGarnet sets are reasonably in good agreement with experimental flow data. The PNM EoS for the IOPB-I model is quite stiffer than that of G3 at high densities.

6.4 Neutron Stars

(i) Predicted equation of states

We have solved Eqs. (2.30) and (2.31) for the energy density and pressure of the β-equilibrated charge neutral neutron star matter. Figure 6.8 displays the pressure as a function of energy density for the G3, and IOPB-I sets along with the NL3, and FSUGarnet sets. The solid circles are the central pressure and energy density corresponding to the maximum mass of the neutron star obtained from the above equations of state. The shaded region of the EoS can be divided into two parts as follows:

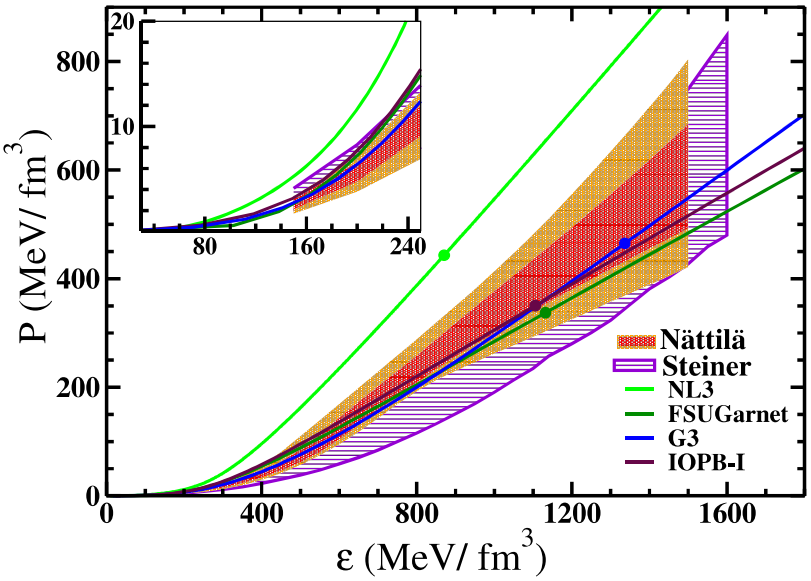

Figure 6.8: The equations of state with NL3, FSUGarnet, G3, and IOPB-I sets for nuclear matter under charge neutrality as well as the β-equilibrium condition. The shaded region (violet) represents the observational constraint at $r_{ph} = R$ with uncertainty of 2σ [59]. Here, R and r_{ph} are the neutron star radius and the photospheric radius, respectively. The other shaded region (red and orange) represents the QMC+Model A equation of state of cold dense matter with 95% confidence limit [264]. The region zoomed near the origin is shown in the inset.

(i) Nättliä *et. al.* applied the Bayesian cooling tail method to constraint (1σ and 2σ confidence limit) the EoS of cold dense matter inside the neutron stars [264].
(ii) Steiner *et. al.* determined an empirical dense matter EoS with a 95% confidence limit from a heterogeneous data set containing PRE bursts and quiescent thermal emission from x-ray transients [59].

From Fig. 6.8, it is clear that IOPB-I and FSUGarnet EoSs are similar at high density but they differ remarkably at low densities as shown in the zoomed area of the inset. The NL3 set yields the stiffer EoS. Moreover, the IOPB-I set shows the stiffest EoS up to energy densities $\mathcal{E}\lesssim$700 MeV fm^{-3}. It can be seen that the results of IOPB-I at very high densities $\mathcal{E} \sim 400 - 1600$ MeV fm^{-3} are consistent with the EoS obtained by Nättilä and Steiner *et al.* [59,264]. However, the FSUGarnet set has a softer EoS at low energy densities $\mathcal{E}\lesssim$200 MeV fm^{-3} and stiffer EoS at intermediate energy densities as compared to that for the G3 set. One can conclude from Table 6.4 that the symmetry energy elements L and K_{sym} are smaller in the G3 model compared to the IOPB-I, FSUGarnet, and NL3 sets. Hence, it yields the symmetry energy that is softer at higher density.

(ii) Mass-radius and tidal deformability of neutron star

After fixing the equation of state for the various parameter sets, we extended our study to calculate the mass, radius, and tidal deformability of a nonrotating neutron star.

In Fig. 6.9, the horizontal bars in cyan and magenta include the results from the precisely measured neutron stars masses, such as PSR J1614-2230 with mass $M = 1.97 \pm 0.04 M_\odot$ [57] and PSR J0348+0432 with $M = 2.01 \pm 0.04 M_\odot$ [58]. These observations imply that the maximum mass predicted by any theoretical model should reach the limit $\sim 2.0 M_\odot$. We also depict the 1σ and 2σ empirical mass-radius constraints for the cold densed matter inside the NS which were obtained from a Bayesian analysis of type-I x-ray burst observations [264]. A similar approach was applied by Steiner *et al.*, but they obtained the mass-radius from six sources, i.e., three from transient low-mass x-ray binaries and three from type-I x-ray bursters with photospheric radius [59].

The NL3 model of RMF theory suggests a larger and massive NS with mass

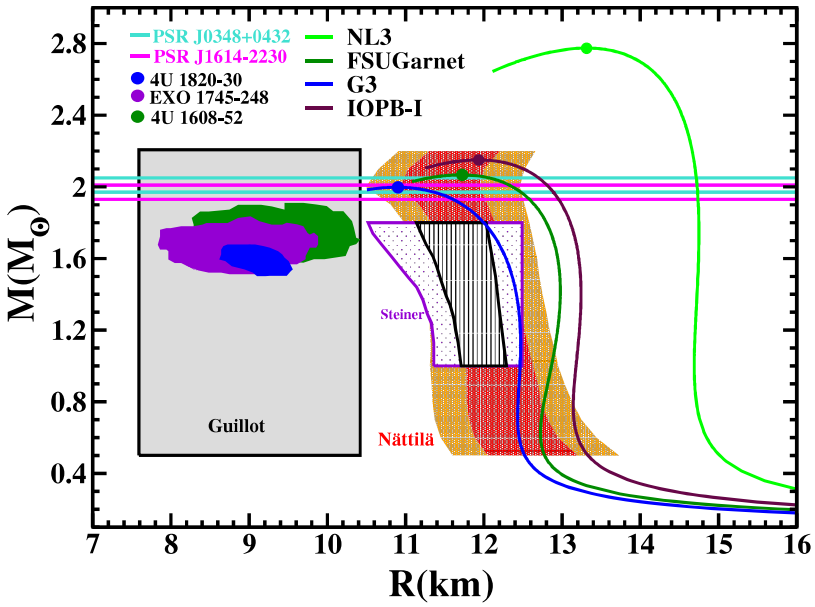

Figure 6.9: The mass-radius profile predicted by NL3, FSUGarnet, G3, and IOPB-I parameter sets. The recent observational constraints on neutron-star masses [57, 58] and radii [59, 264–266] are also shown.

$2.77M_{\odot}$ and the corresponding NS radius to be 13.314 km, which is larger than the best observational radius estimates [59, 264]. Hence it is clear that the new RMF was developed either through density-dependent couplings [84] or higher order couplings [38, 231]. These models successfully reproduce the ground-state properties of finite nuclei, nuclear matter saturation properties, and also the maximum mass of the neutron stars. Another important advantage of these models is that they are consistent with the subsaturation density of the pure neutron matter. Rezzolla *et al.* [267] combined the recent gravitational-wave observation of a merging system of binary neutron stars via the event GW170817 with quasi-universal relations between the maximum mass of rotating and non-rotating NSs. It is found that the maximum mass for nonrotating NS should be in the range $2.01 \pm 0.04 \lesssim M(M_{\odot}) \lesssim 2.16 \pm 0.03$ [267], where the lower limit is observed from massive pulsars in the binary system [58]. From the results, we find that the maximum masses for IOPB-I along with FSUGarnet and G3 EoS are consistent with the observed lower bound on the maximum NS mass. For the IOPB-I parametrization, the maximum mass of the NS is $2.15M_{\odot}$ and the radius (without including crust) of the *canonical* mass is 13.242 km, which is relatively

larger as compared to the current x-ray observation radii of range 10.5–12.8 km by Nättilä *et. al.* [264] and 11–12 km by Steiner *et. al.* [59]. Similarly, FSUGarnet fails to qualify radius constraint. However, recently Annala et al. suggested that the radius of a $1.4M_{\odot}$ star should be in the range $11.1 \leq R_{1.4M_{\odot}} \leq 13.4$ km [268], which is consistent with the IOPB-I and FSUGarnet sets. Furthermore, the G3 EoS is relatively softer at energy density $\mathcal{E} \gtrsim 200$ MeV fm^{-3} (see in Fig. 6.8), which is able to reproduce the recent observational maximum mass of $2.0M_{\odot}$ as well as the radius of the *canonical* neutron star mass of 12.416 km.

Now we move to results for the tidal deformability of the single neutron star as well as binary neutron stars (BNSs), which was recently discussed for GW170817 [16]. Figure 6.10 shows the tidal deformability as a function of NS mass. In particular, λ takes a wide range of values $\lambda \sim (1 - -8) \times 10^{36}$ g cm^2 s^2 as shown in Fig. 6.10. For the G3 parameter set, the tidal deformability λ is very low in the mass region $0.5 - -2.0M_{\odot}$ in comparison with other sets. This is because the star exerts high central pressure and energy density, resulting in the formation of a compact star which is shown as solid dots in Fig. 6.8. However, for the NL3 EoS case, it turns out that, because of the stiffness of the EoS, the λ value is increasing. The tidal deformabilities of the canonical NS ($1.4M_{\odot}$) of IOPB-I along with FSUGarnet and G3 EoSs are found to be 3.191×10^{36}, 3.552×10^{36}, and 2.613×10^{36} g cm^2 s^2, respectively as shown in Tables 6.5 and 6.6, which are consistent with the results obtained by Steiner *et al.* [211].

Next, we discuss the weighted dimensionless tidal deformability of the BNS of mass m_1 and m_2 which is defined as [16, 188, 213]

$$\tilde{\Lambda} = \frac{8}{13}\Bigg[(1+7\eta-31\eta^2)(\Lambda_1 + \Lambda_2) + \sqrt{1-4\eta}(1+9\eta-11\eta^2)(\Lambda_1-\Lambda_2)\Bigg], \tag{6.7}$$

with tidal correction

$$\delta\tilde{\Lambda} = \frac{1}{2}\Bigg[\sqrt{1-4\eta}\left(1-\frac{13272}{1319}\eta+\frac{8944}{1319}\eta^2\right)(\Lambda_1+\Lambda_2) + \left(1-\frac{15910}{1319}\eta+\frac{32850}{1319}\eta^2+\frac{3380}{1319}\eta^3\right)(\Lambda_1-\Lambda_2)\Bigg]. \tag{6.8}$$

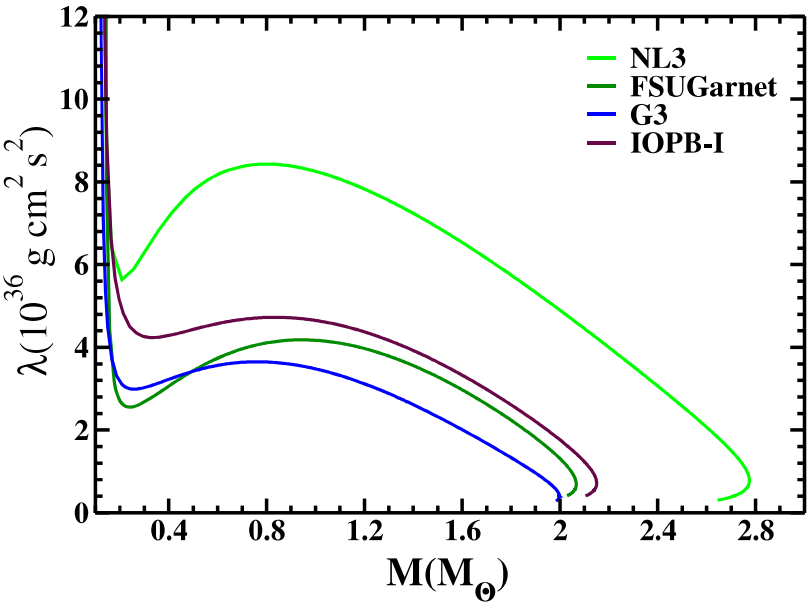

Figure 6.10: The tidal deformability λ as a function of neutron star mass with different EoS.

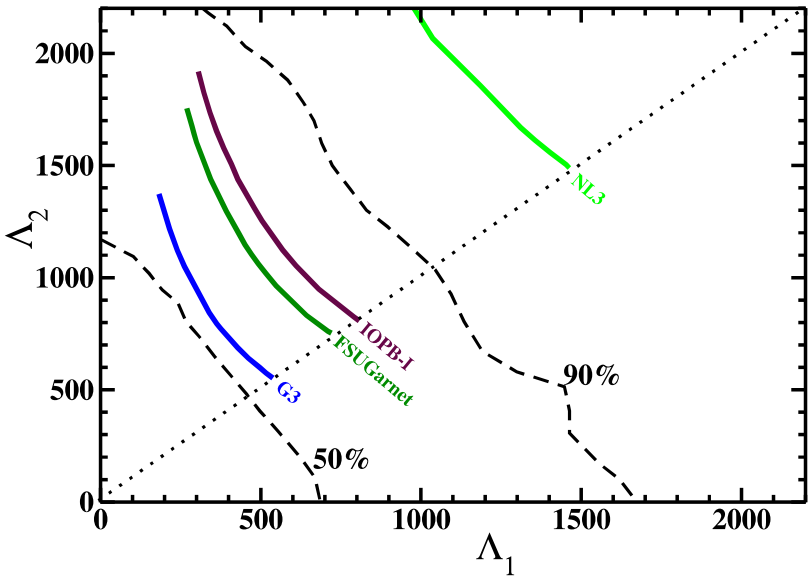

Figure 6.11: Different values of Λ generated by using G3, and IOPB-I along with NL3, and FSUGarnet EoS are compared with the 90% and 50% probability contour in the case of low spin, $|\chi| \leq 0.05$, as given in Fig. 5 of GW170817 [16].

Here, $\eta = m_1 m_2/M^2$ is the symmetric mass ratio, m_1 and m_2 are the binary masses, $M = m_1 + m_2$ is the total mass, and Λ_1 and Λ_2 are the dimensionless tidal deformabilities of the BNS, for the case $m_1 \geq m_2$. Also, we have taken equal and unequal masses (m_1 and m_2) BNS for the system as it has been done in Refs. [269, 270]. The calculated results for the Λ_1, Λ_2, and weighted tidal deformability $\tilde{\Lambda}$ of the present EoS are displayed in Tables 6.5 and 6.6. In Fig. 6.11, we display the different dimensionless tidal deformabilities corresponding to progenitor masses of the NS. It can be seen that the IOPB-I set along with FSUGarnet and G3 sets are in good agreement with the 90% and 50% probability contour of GW170817 [16]. Recently, aLIGO and VIRGO detectors measured a value of $\tilde{\Lambda}$ whose results are more precise than the results found by considering the individual values of Λ_1 and Λ_2 of the BNS [16]. It is noticed that the values of $\tilde{\Lambda} \leq 800$ in the low-spin case and $\tilde{\Lambda} \leq 700$ in the high-spin case are within the 90% credible intervals which are consistent with the 680.79, 622.06, and 461.03 of the $1.4 M_\odot$ NS binary for the IOPB-I, FSUGarnet, and G3 parameter sets, respectively (see Tables 6.5 and 6.6). We also find a reasonably good agreement in the $\tilde{\Lambda}$ value equal to 582.26 for $1.35 M_\odot$ in the G3 EoS, which is obtained using a Markov chain Monte Carlo simulation of a BNS with $\tilde{\Lambda} \approx 600$ at a signal-to-noise ratio of 30 in a single aLIGO detector [188, 213]. Finally, we close this section with the discussion on chirp mass $\mathcal{M}_c$ and chirp radius $\mathcal{R}_c$ of the BNS system which are defined as

$$\mathcal{M}_c = (m_1 m_2)^{3/5} (m_1 + m_2)^{-1/5}, \tag{6.9}$$

$$\mathcal{R}_c = 2 \mathcal{M}_c \, \tilde{\Lambda}^{1/5}. \tag{6.10}$$

The precise mass measurements of the NSs were reported in Refs. [57, 58]. However, until now no observation has been confirmed regarding the radius of the most massive NS. Recently, aLIGO and VIRGO measured a chirp mass of $1.188^{+0.004}_{-0.002} M_\odot$ with very good precision. With the help of this, we can easily calculate the chirp radius $\mathcal{R}_c$ of the BNS system and we find that the chirp radius is in the range $7.867 \leq \mathcal{R}_c \leq 10.350$ km for equal and unequal-mass BNS systems as shown in Tables 6.5 and 6.6.

6.5 Summary and Conclusions

We have built two new relativistic effective interaction for finite nuclei, infinite nuclear matter, and neutron stars. The optimization was done using experimental data for eight spherical nuclei such as binding energy and charge radius. The prediction of observables such as binding energies and radii with the new G3, and IOPB-I sets for finite nuclei are quite good. The rms error on the total binding energy calculated with G3 set is noticeably smaller than the commonly used parameter sets NL3, FSUGold2, FSUGarnet, and G2. The Z=120 isotopic chain shows that the magicity appears at neutron numbers N=172, 184, and 198. Furthermore, we find that the IOPB-I set yields slightly larger values for the neutron-skin thickness. This is due to the small strength of the ω-ρ cross-coupling. However, the Δ_{np} for G3 parameterization calculated for nuclei over a wide range of masses are in harmony with the available experimental data. For infinite nuclear matter at subsaturation and suprasaturation densities, the results of our calculations agree well with the known experimental data. The nuclear matter properties obtained by this new parameter set IOPB-I are: nuclear incompressibility $K = 222.65$ MeV, symmetry energy coefficient $J = 33.30$ MeV, symmetry energy slope $L = 63.6$ MeV, and the asymmetry term of nuclear incompressibility $K_\tau = 389.46$ MeV, at saturation density $\rho_0 = 0.149$ fm^{-3}. In general, all these values are consistent with current empirical data. The IOPB-I model satisfies the density dependence of the symmetry energy which is obtained from the different sets of experimental data. It also yields the NS maximum mass to be $2.15 M_\odot$, which is consistent with the current GW170817 observational constraint [267]. The radius of the canonical neutron star is 13.24 km, compatible with the theoretical results in Ref. [268]. Similarly, the predicted values of dimensionless tidal deformabilities are in accordance with the GW170817 observational probability contour [16].

Table 6.2: The obtained new parameter sets G3, and IOPB-I along with NL3 [29], FSUGold2 [194], FSUGarnet [231] and G2 [17] sets are listed. The nucleon mass M is 939.0 MeV. All the coupling constants are dimensionless, except k_3 which is in fm^{-1}.

	NL3	FSUGold2	FSUGarnet	G2	G3	IOPB-I
m_s/M	0.541	0.530	0.529	0.554	0.559	0.533
m_ω/M	0.833	0.833	0.833	0.832	0.832	0.833
m_ρ/M	0.812	0.812	0.812	0.820	0.820	0.812
m_δ/M	0.0	0.0	0.0	0.0	1.043	0.0
$g_s/4\pi$	0.813	0.827	0.837	0.835	0.782	0.827
$g_\omega/4\pi$	1.024	1.079	1.091	1.016	0.923	1.062
$g_\rho/4\pi$	0.712	0.714	1.105	0.755	0.962	0.885
$g_\delta/4\pi$	0.0	0.0	0.0	0.0	0.160	0.0
k_3	1.465	1.231	1.368	3.247	2.606	1.496
k_4	-5.688	-0.205	-1.397	0.632	1.694	-2.932
ζ_0	0.0	4.705	4.410	2.642	1.010	3.103
η_1	0.0	0.0	0.0	0.650	0.424	0.0
η_2	0.0	0.0	0.0	0.110	0.114	0.0
η_ρ	0.0	0.0	0.0	0.390	0.645	0.0
Λ_ω	0.0	0.000823	0.04337	0.0	0.038	0.024
α_1	0.0	0.0	0.0	1.723	2.000	0.0
α_2	0.0	0.0	0.0	-1.580	-1.468	0.0
$f_\omega/4$	0.0	0.0	0.0	0.173	0.220	0.0
$f_\rho/4$	0.0	0.0	0.0	0.962	1.239	0.0
β_σ	0.0	0.0	0.0	-0.093	-0.087	0.0
β_ω	0.0	0.0	0.0	-0.460	-0.484	0.0

Table 6.3: The binding energy per nucleon B/A(MeV), charge radius R_c (fm) and neutron skin thickness R_n-R_p (fm) for some close shell nuclei compared with the NL3, FSUGold2, FSUGarnet, and G2 with experimental data [112, 144].

Nucleus	Obs.	Expt.	NL3	FSUGold2	FSUGarnet	G2	G3	IOPB-I
^{16}O	B/A	7.976	7.917	7.862	7.876	7.952	8.037	7.977
	R_c	2.699	2.714	2.694	2.690	2.718	2.707	2.705
	R_n-R_p	-	-0.026	-0.026	-0.028	-0.028	-0.028	-0.027
^{40}Ca	B/A	8.551	8.540	8.527	8.528	8.529	8.561	8.577
	R_c	3.478	3.466	3.444	3.438	3.453	3.459	3.458
	R_n-R_p	-	-0.046	-0.047	-0.051	-0.049	-0.049	-0.049
^{48}Ca	B/A	8.666	8.636	8.616	8.609	8.668	8.671	8.638
	R_c	3.477	3.443	3.420	3.426	3.439	3.466	3.446
	R_n-R_p	-	0.229	0.235	0.169	0.213	0.174	0.202
^{68}Ni	B/A	8.682	8.698	8.690	8.692	8.682	8.690	8.707
	R_c	-	3.870	3.846	3.861	3.861	3.892	3.873
	R_n-R_p	-	0.262	0.268	0.184	0.240	0.190	0.223
^{90}Zr	B/A	8.709	8.695	8.685	8.693	8.684	8.699	8.691
	R_c	4.269	4.253	4.230	4.231	4.240	4.276	4.253
	R_n-R_p	-	0.115	0.118	0.065	0.102	0.068	0.091
^{100}Sn	B/A	8.258	8.301	8.282	8.298	8.248	8.266	8.284
	R_c	-	4.469	4.453	4.426	4.470	4.497	4.464
	R_n-R_p	-	-0.073	-0.075	-0.078	-0.079	-0.079	-0.077
^{132}Sn	B/A	8.355	8.371	8.361	8.372	8.366	8.359	8.352
	R_c	4.709	4.697	4.679	4.687	4.690	4.732	4.706
	R_n-R_p	-	0.349	0.356	0.224	0.322	0.243	0.287
^{208}Pb	B/A	7.867	7.885	7.881	7.902	7.853	7.863	7.870
	R_c	5.501	5.509	5.491	5.496	5.498	5.541	5.521
	R_n-R_p	-	0.283	0.288	0.162	0.256	0.180	0.221

Table 6.4: The nuclear matter properties such as binding energy per nucleon, $\mathcal{E}_0$(MeV), saturation density ρ_0(fm^{-3}), incompressibility coefficient for symmetric nuclear matter K(MeV), effective mass ratio M^*/M, symmetry energy J(MeV), and linear density dependence of the symmetry energy, L(MeV), at saturation.

	NL3	FSUGarnet	G3	IOPB-I
ρ_0 (fm^{-3})	0.148	0.153	0.148	0.149
$\mathcal{E}_0$(MeV)	-16.29	-16.23	-16.02	-16.10
M^*/M	0.595	0.578	0.699	0.593
J(MeV)	37.43	30.95	31.84	33.30
L(MeV)	118.65	51.04	49.31	63.58
K_{sym}(MeV)	101.34	59.36	-106.07	-37.09
Q_{sym}(MeV)	177.90	130.93	915.47	862.70
K(MeV)	271.38	229.5	243.96	222.65
Q_0(MeV)	211.94	15.76	-466.61	-101.37
K_τ(MeV)	-703.23	-250.41	-307.65	-389.46
K_{asy}(MeV)	-610.56	-246.89	-401.97	-418.58
K_{sat2}(MeV)	-703.23	-250.41	-307.65	-389.46

Table 6.5: The binary neutron star masses $(m_1(M_\odot), m_2(M_\odot))$ and corresponding radii (R_1(km), R_2 (km)), tidal Love number ($(k_2)_1$, $(k_2)_2$), and tidal deformabilities (λ_1, λ_2) in 1×10^{36}g cm^2 s^2 and dimensionless tidal deformabilities (Λ_1, Λ_2). $\tilde{\Lambda}$, $\delta\tilde{\Lambda}$, $\mathcal{M}_c(M_\odot)$, and $\mathcal{R}_c(km)$ are the dimensionless tidal deformability, tidal correction, chirp mass, and radius of the binary neutron star, respectively.

EoS	$m_1(M_\odot)$	$m_2(M_\odot)$	R_1(km)	R_2(km)	$(k_2)_1$	$(k_2)_2$	λ_1	λ_2	Λ_1	Λ_2	$\tilde{\Lambda}$	$\delta\tilde{\Lambda}$	$\mathcal{M}_c(M_\odot)$	$\mathcal{R}_c(km)$
NL3	1.20	1.20	14.702	14.702	0.1139	0.1139	7.826	7.826	2983.15	2983.15	2983.15	0.000	1.04	10.350
	1.50	1.20	14.736	14.702	0.0991	0.1139	6.889	7.826	854.06	2983.15	1608.40	220.223	1.17	10.214
	1.25	1.25	14.708	14.708	0.1118	0.1118	7.962	7.962	2388.82	2388.82	2388.82	0.000	1.09	10.313
	1.30	1.30	14.714	14.714	0.1094	0.1094	7.546	7.546	1923.71	1923.71	1923.71	0.000	1.13	10.271
	1.35	1.35	14.720	14.720	0.1070	0.1070	7.393	7.393	1556.84	1556.84	1556.84	0.000	1.18	10.224
	1.35	1.25	14.720	14.708	0.1070	0.1118	7.393	7.962	1556.84	2388.82	1930.02	91.752	1.13	10.268
	1.37	1.25	14.722	14.708	0.1061	0.1118	7.339	7.962	1452.81	2388.82	1863.78	100.532	1.14	10.271
	1.40	1.20	14.726	14.702	0.1044	0.1139	7.231	7.826	1267.07	2983.15	1950.08	183.662	1.13	10.262
	1.40	1.40	14.726	14.726	0.1044	0.1044	7.231	7.231	1267.07	1267.07	1267.07	0.000	1.22	10.174
	1.42	1.29	14.728	14.712	0.1031	0.1099	7.147	7.572	1145.72	1994.02	1515.18	95.968	1.18	10.192
	1.44	1.39	14.730	14.724	0.1027	0.1049	7.120	7.259	1108.00	1311.00	1204.83	19.212	1.23	10.179
	1.45	1.45	14.732	14.732	0.1018	0.1018	7.064	7.064	1037.13	1037.13	1037.13	0.000	1.26	10.124
	1.54	1.26	14.740	14.708	0.0969	0.1114	6.741	7.668	729.95	2303.95	1308.91	168.202	1.21	10.179
	1.60	1.60	14.746	14.746	0.0937	0.0937	6.532	6.532	589.92	589.92	589.92	0.000	1.39	9.979
FSUGarnet	1.20	1.20	12.944	12.944	0.1090	0.1090	3.961	3.961	1469.32	1469.32	1469.32	0.000	1.04	8.983
	1.50	1.20	12.972	12.944	0.0893	0.1090	3.282	3.961	408.91	1469.32	784.09	111.643	1.17	8.847
	1.25	1.25	12.958	12.958	0.1062	0.1062	3.880	3.880	1193.78	1193.78	1193.78	0.000	1.09	8.977
	1.30	1.30	12.968	12.968	0.1030	0.1030	3.777	3.777	945.29	945.29	945.29	0.000	1.13	8.910
	1.35	1.35	12.974	12.974	0.0998	0.0998	3.666	3.666	761.13	761.13	761.13	0.000	1.18	8.860
	1.35	1.25	12.974	12.958	0.0998	0.1062	3.666	3.880	761.13	1193.78	955.00	49.744	1.13	8.920
	1.37	1.25	12.976	12.958	0.0986	0.1062	3.629	3.880	710.62	1193.78	922.54	53.853	1.14	8.924
	1.40	1.20	12.978	12.944	0.0965	0.1090	3.552	3.961	622.06	1469.32	959.22	90.970	1.13	8.904
	1.40	1.40	12.978	12.978	0.0965	0.0965	3.552	3.552	622.06	622.06	622.06	0.000	1.22	8.825
	1.42	1.29	12.978	12.966	0.0949	0.1038	3.495	3.803	565.47	1001.18	755.10	50.492	1.18	8.867
	1.44	1.39	12.978	12.978	0.0939	0.0973	3.456	3.582	531.54	653.60	589.65	14.148	1.23	8.823
	1.45	1.45	12.978	12.978	0.0931	0.0931	3.427	3.427	507.70	507.70	507.70	0.000	1.26	8.776
	1.54	1.26	12.964	12.960	0.0862	0.1057	3.157	3.864	343.73	1146.73	638.35	88.892	1.21	8.817
	1.60	1.60	12.944	12.944	0.0816	0.0816	2.964	2.964	266.20	266.20	266.20	0.000	1.39	8.511

Table 6.6: Table 6.5 is continued ...

EoS	$m_1(M_\odot)$	$m_2(M_\odot)$	R_1(km)	R_2(km)	$(k_2)_1$	$(k_2)_2$	λ_1	λ_2	Λ_1	Λ_2	$\tilde{\Lambda}$	$\delta\tilde{\Lambda}$	$\mathcal{M}_c(M_\odot)$	$\mathcal{R}_c(km)$
G3	1.20	1.20	12.466	12.466	0.1034	0.1034	3.114	3.114	1776.65	1776.65	1776.65	0.000	1.04	9.331
	1.50	1.20	112.360	12.466	0.0800	0.1034	2.309	3.114	284.92	1776.65	803.43	191.605	1.17	8.890
	1.25	1.25	12.460	12.460	0.1001	0.1001	3.007	3.007	939.79	939.79	939.79	0.000	1.09	8.557
	1.30	1.30	12.448	12.448	0.0962	0.0962	2.875	2.875	728.07	728.07	728.07	0.000	1.13	8.457
	1.35	1.35	12.434	12.434	0.0925	0.0925	2.750	2.750	582.26	582.26	582.26	0.000	1.18	8.398
	1.35	1.25	12.434	12.460	0.0925	0.1001	2.750	3.007	582.26	939.79	742.29	43.064	1.13	8.482
	1.37	1.25	12.428	12.460	0.0909	0.1001	2.696	3.007	530.66	939.79	709.72	49.144	1.14	8.468
	1.40	1.20	12.416	12.466	0.0859	0.1034	2.613	3.114	461.03	1776.65	976.80	183.274	1.13	8.937
	1.40	1.40	12.416	12.416	0.0859	0.0859	2.613	2.613	461.03	461.03	461.03	0.000	1.22	8.312
	1.42	1.29	12.408	12.450	0.0868	0.0972	2.553	2.905	417.96	772.17	571.87	43.226	1.18	8.387
	1.44	1.39	12.398	12.420	0.0854	0.0894	2.501	2.643	384.42	484.90	432.22	12.671	1.23	8.292
	1.45	1.45	12.932	12.392	0.0846	0.0846	2.472	2.472	367.04	367.04	367.04	0.000	1.26	8.225
	1.54	1.26	12.334	12.458	0.0769	0.0992	2.194	2.976	239.49	883.46	474.83	75.175	1.21	8.311
	1.60	1.60	12.280	12.280	0.0716	0.0716	2.000	2.000	179.63	179.63	179.63	0.000	1.39	7.867
IOPB-I	1.20	1.20	13.222	13.222	0.1081	0.1081	4.369	4.369	1654.23	1654.23	1654.23	0.000	1.04	9.199
	1.50	1.20	13.236	13.222	0.0894	0.1081	3.631	4.369	449.62	1654.23	875.35	128.596	1.17	9.044
	1.25	1.25	13.230	13.230	0.1053	0.1053	4.268	4.268	1310.64	1310.64	1310.64	0.000	1.09	9.146
	1.30	1.30	13.238	13.238	0.1024	0.1024	4.162	4.162	1053.07	1053.07	1053.07	0.000	1.13	9.105
	1.35	1.35	13.240	13.240	0.0995	0.0995	4.050	4.050	857.53	857.53	857.53	0.000	1.18	9.074
	1.35	1.25	13.240	13.230	0.0995	0.1053	4.050	4.268	857.53	1310.64	1060.81	49.565	1.13	9.110
	1.37	1.25	13.242	13.230	0.0938	0.1053	4.004	4.268	791.92	1310.64	1019.60	56.371	1.14	9.104
	1.40	1.20	13.242	13.222	0.0960	0.1081	3.911	4.369	680.79	1654.23	1067.64	107.340	1.13	9.097
	1.40	1.40	13.242	13.242	0.0960	0.0960	3.911	3.911	680.79	680.79	680.79	0.000	1.22	8.986
	1.42	1.29	13.242	13.236	0.0949	0.1030	3.864	4.184	632.31	1099.78	835.91	52.836	1.18	9.049
	1.44	1.39	13.242	13.242	0.0935	0.0969	3.806	3.946	578.47	719.80	645.73	17.094	1.23	8.985
	1.45	1.45	13.240	13.240	0.0927	0.0927	3.771	3.771	549.06	549.06	549.06	0.000	1.26	8.915
	1.54	1.26	13.230	13.232	0.0868	0.1047	3.516	4.247	384.65	1253.00	703.58	94.735	1.21	8.991
	1.60	1.60	13.212	12.212	0.0823	0.0823	3.314	3.314	296.81	296.81	296.81	0.000	1.39	8.698

Chapter 7

Summary and Conclusions

This thesis has touched several areas of active research in nuclear structure, nuclear matter, neutron star, and gravitational waves. Here, we have applied the effective field theory motivated RMF formalism which is very successful till now for studying the finite nuclei throughout the nuclear chart, infinite nuclear matter and neutron stars.

After a brief introduction on various current phenomena for finite nuclei, infinite nuclear matter in chapter 1, chapter 2 covers mostly the mathematical derivations, which have been included in our work throughout. We began with the extended-RMF Lagrangian density by adding two extra terms *i.e.*, δ meson and $\omega - \rho$ cross-coupling which contain large number of terms with all types of self- and cross-coupling interactions. With the help of Euler-Lagrange equation we have reproduced the mean-field equations for different fields such as $\phi, \sigma, \omega, \rho$, and δ, which are then solved self-consistently. The total energy of the nucleus comes from the energy contributions from nucleons and mesons. The temperature dependent BCS and Quasi-BCS pairing correlations for open-shell nuclei have been described in detail. Also, the equation of state is derived with the help of energy-momentum tensor and several expressions for the properties of the infinite nuclear matter are obtained in the RMF approximation.

In chapter 3, on the basis of RMF formalism, we have studied systematically the decay properties of recently predicted thermally fissile Th and U isotopes. The potential energy surface is determined self-consistently by employing the quadrupole constraint approach. It is found that $^{228-230}$Th and $^{228-234}$U isotopes are showing

three maxima in the PES. Then we have calculated fission barrier height of the experimentally known nuclei, which agrees well with the available data. With the empirical estimation and quantum mechanical tunneling approach, we found that the neutron-rich isotopes of these thermally fissile nuclei such as ^{254}Th and ^{256}U are predicted to be stable against α- and *cluster*-decays. Interestingly, these isotopes have shown the lower height and larger width which make the nucleus infinitely stable against spontaneous fission decay because of the decreasing penetrability. However, these nuclei are unstable against prompt neutron emission (β-decay) from the fragments at scission and has a half-life of the order of tens of seconds. These finite lifetime suggest that they could be very useful for energy production with the help of online synthesis of these nuclei by the nuclear reactor technology. Furthermore, ^{254}Th and ^{256}U are showing the close shell nature of the neutron magic number N=164. We expected that N=164 magic number may be identified by the next generation of experimental facilities such as Facility for Rare Isotope Beam (FRIB) at MSU and RIBF at RIKEN.

In chapter 4, we have extended our study to calculate the relative binary mass distribution of β-stable nuclei ^{232}Th and ^{236}U and the neutron-rich thermally fissile nuclei ^{254}Th and ^{250}U within a statistical model. The level densities, the excitation energies, and the level density parameter a are calculated from the TRMF and FRDM formalisms. The excitation energies of the fragments are obtained from ground state single-particle energies in the FRDM calculations. The TRMF model includes the thermal evolution's of the pairing gaps and deformation in a self-consistent manner while, these are ignored in the FRDM calculations. For ^{232}Th and ^{236}U, the binary fragments influence the most favorable yields at temperatures $T = 2$ and 3 MeV—whose mass distribution end up in the vicinity or exactly at the nucleon closed shell (N=82, 50 and Z = 28). However, the fragments of the neutron-rich thermally fissile nuclei ^{254}Th and ^{250}U have shown the neutron/proton close shell N=50,82, and 100 at T=2 and 3 MeV. Although, the TRMF and FRDM formalisms yield the closed shell nucleus as one of the favorable fragments, still the details of the relative binary fragmentation yields and probability of the mass distributions are quite different in these two formalisms.

In chapter 5, the derivations of Newtonian and relativistic tides for neutron stars are presented. Using these derivations, we have thoroughly discussed the various

types of Love numbers such as electric-type Love numbers k_2, k_3, k_4, magnetic-type Love number j_2, and shape Love number h_l using the four EoSs for neutron and hyperon stars. These EoSs are calculated from an effective field theory motivated with RMF formalism under the β-equilibrium condition and we have compared the results with empirical astrophysical constraint. The inclusion of hyperon in our description which softens the EoS and there by reduces the maximum mass of the NS further. We find that the tidal deformability of the canonical neutron and hyperon stars either change slightly or remain unchanged with the addition of a hyperon in the NS. The recent observation GW170817 has also confirmed the tight constraint on the tidal deformability of the NS matter. We expect that the next generation of the gravitational wave detectors may provide obstacles on the tidal deformability of the hyperon star. Further, our calculations suggested that the higher order Love numbers k_3 and k_4 are very important for the detection of gravitational waves.

In chapter 6, we improve the existing parameterizations of the ERMF model which includes couplings of the meson field gradients to the nucleons and the tensor couplings of the mesons to the nucleons in addition to the several self and cross-coupling terms. The nuclear matter incompressibility coefficient and/or symmetry energy coefficient associated with earlier parameterizations of such ERMF model were a bit too large which has been taken care of in our new parameter set G3. The rms error on the total binding energy calculated from our parameter set is smaller than the commonly used parameter sets NL3, FSUGold2, FSUGarnet, and G2. The neutron-skin thickness Δr_{np} for G3 set calculated for nuclei over a wide range of masses are in harmony with the available experimental data. However, IOPB-I gives slightly larger value of Δr_{np}, due to the small strength of the $\omega - \rho$ cross-coupling. The neutron matter EoS at subsaturation densities for G3, and IOPB-I parameter sets show reasonable improvement over other parameter sets considered. Also, the maximum mass for the neutron star for G3 set $\sim 2.0 M_\odot$, and $2.15 M_\odot$ for IOPB-I set are compatible with the pulsar measurements, and GW170817 data. The radius of the neutron star with the canonical mass agree quite well with the two independent analyses of gravitational waves from the GW170817 neutron star merger [240, 268]. The smallness of $R_{1.4}$ for G3 parameter set in comparison to those for the earlier parametrization of the RMF models, which are compatible with the observational constraint of $2M_\odot$, is a desirable

feature. Motivated by recent astrophysical GW170817 observation of the tight constraint on the dimensionless tidal deformability, we found that the predictions of G3, and IOPB-I models to be in fairly good agreement with the GW170817 probability contour in the low spin prior as given in Fig. 5 of Ref. [16].

Future Prospects: In my thesis work, I have tried to conjoint two major branches of physics viz., (i) nuclear structure physics and (ii) astrophysics and have tried to apply ERMF theory. Having worked in the ERMF theory and the newest calculations in nuclear structure and astrophysics, I can further apply the model to various applications on nuclear fission, neutron star and gravitational waves. A brief outline of my future work is as follows:

- As we have already discussed in the thesis that the neutron-rich thermally fissile nuclei may be used in the nuclear reactor so that we can make nuclear power. But we need more work in this direction. As we have pointed out that β-stable thermally fissile isotopes are found in the mass range A=230-240. Fortunately India has rich thorium deposits constituting roughly 25% of the global reserves. As thorium isotopes too fall in the mass range A=230-240, so many tests can be done in this regard to find out other thermally fissile nuclei and our theoretical predictions can give input to the experimental findings.

- In our upcoming work, we will perform a detailed covariance analysis for the G3, and IOPB-I models used in the present thesis and access the uncertainties associated with the various parameters of the Lagrangian density. An appropriate covariance analysis of our model requires a set of fitting data which include large variety of nuclear and neutron star observables.

- The GW170817 observation has opened up a new era of gravitational astronomy as well as nuclear physics. Still a lot of work is to be done in these fields and several more events are expected to come up in near future for extraction of NS properties such as the stars mass, spin, size, and shape, which will finally lead to tighter constraints on the neutron star equation of state. With the help of GW observations, we can connect the nuclear matter properties, in particular, the slope of the symmetry energy (L) with the structure properties of neutron

star—which is an important task for the nuclear physics community.

Appendix A

Derivation of the TOV equation

Consider the general static, spherically symmetric metric [175, 271]

$$ds^2 = -e^{2\nu(r)}dt^2 + e^{2\lambda(r)}dr^2 + r^2d\theta^2 + r^2sin^2\theta d\phi^2 \tag{A.1}$$

Let's now take this metric and use Einstein's equation to solve the function $\nu(r)$ and $\lambda(r)$.

We are looking for non-vacuum solutions, so we turn to the full Einstein equation,

$$G_{\mu\nu} = R_{\mu\nu} - \frac{1}{2}Rg_{\mu\nu} = 8\pi T_{\mu\nu} \tag{A.2}$$

where $R_{\mu\nu}$ and R are the Ricci tensor and Ricci scalar, respectively. $g_{\mu\nu}$ is the metric

$$g_{\mu\nu} = \begin{bmatrix} g_{tt} & g_{tr} & g_{t\theta} & g_{t\phi} \\ g_{rt} & g_{rr} & g_{r\theta} & g_{r\phi} \\ g_{\theta t} & g_{\theta r} & g_{\theta\theta} & g_{\theta\phi} \\ g_{\phi t} & g_{\phi r} & g_{\phi\theta} & g_{\phi\phi} \end{bmatrix} = \begin{bmatrix} -e^{2\nu(r)} & 0 & 0 & 0 \\ 0 & e^{2\lambda(r)} & 0 & 0 \\ 0 & 0 & r^2 & 0 \\ 0 & 0 & 0 & r^2sin^2\theta \end{bmatrix}$$

We begin by evaluating the christoffel (or affine connection or Levi-Civita or Riemann connection) symbols. If we use labels (t, r, θ, ϕ).

$$\Gamma^{\lambda}_{\mu\nu} = \frac{1}{2}g^{\lambda\sigma}(\partial_\mu g_{\sigma\nu} + \partial_\nu g_{\mu\sigma} - \partial_\sigma g_{\mu\nu}) \tag{A.3}$$

$$\begin{aligned}
\Gamma^t_{tr} &= \frac{1}{2}g^{t\sigma}(\partial_t g_{\sigma r} + \partial_r g_{t\sigma} - \partial_\sigma g_{tr}) \\
&= \frac{1}{2}g^{t\sigma}(0 + \partial_r g_{t\sigma} - 0)) \\
&= \frac{1}{2}g^{tt}(\partial_r g_{tt}) \\
&= \frac{1}{2}(-e^{-2\nu(r)})(\partial_r(-e^{2\nu(r)})) \\
&= \frac{1}{2}(-e^{-2\nu(r)})(-2e^{2\nu(r)}\partial_r\nu) \\
&= \partial_r\nu
\end{aligned} \tag{A.4}$$

$$\begin{aligned}
\Gamma^r_{tt} &= \frac{1}{2}g^{r\sigma}(\partial_t g_{\sigma t} + \partial_t g_{t\sigma} - \partial_\sigma g_{tt}) \\
&= \frac{1}{2}g^{rr}(\partial_t g_{rt} + \partial_t g_{tr} - \partial_r g_{tt}) \\
&= \frac{1}{2}(e^{-2\lambda(r)})(0 + 0 - \partial_r(-e^{2\nu(r)})) \\
&= \frac{1}{2}(e^{-2\lambda(r)})(2e^{2\nu(r)})\partial_r\nu \\
&= e^{2(\nu(r)-\lambda(r))}\partial_r\nu
\end{aligned} \tag{A.5}$$

$$\begin{aligned}
\Gamma^r_{rr} &= \frac{1}{2}g^{r\sigma}(\partial_r g_{\sigma r} + \partial_r g_{r\sigma} - \partial_\sigma g_{rr}) \\
&= \frac{1}{2}g^{rr}(\partial_r g_{rr} + \partial_r g_{rr} - \partial_r g_{rr}) \\
&= \frac{1}{2}g^{rr}(\partial_r g_{rr}) \\
&= \frac{1}{2}(e^{-2\lambda(r)})\partial_r(e^{2\lambda(r)}) \\
&= \frac{1}{2}(e^{-2\lambda(r)})(2)e^{2\lambda(r)}\partial_r\lambda \\
&= \partial_r\lambda
\end{aligned} \tag{A.6}$$

$$\begin{aligned}
\Gamma^{\theta}_{r\theta} &= \frac{1}{2}g^{\theta\sigma}(\partial_r g_{\sigma\theta} + \partial_\theta g_{r\sigma} - \partial_\sigma g_{r\theta}) \\
&= \frac{1}{2}g^{\theta\theta}(\partial_r g_{\theta\theta} + \partial_\theta g_{r\theta} - \partial_\theta g_{r\theta}) \\
&= \frac{1}{2}(r^{-2})\partial_r(r^2) = \frac{1}{2}(r^{-2})(2r) \\
\Gamma^{\theta}_{r\theta} &= \frac{1}{r} \qquad \text{(A.7)}
\end{aligned}$$

$$\begin{aligned}
\Gamma^{r}_{\theta\theta} &= \frac{1}{2}g^{r\sigma}(\partial_\theta g_{\sigma\theta} + \partial_\theta g_{\theta\sigma} - \partial_\sigma g_{\theta\theta}) \\
&= \frac{1}{2}g^{rr}(\partial_\theta g_{r\theta} + \partial_\theta g_{\theta r} - \partial_r g_{\theta\theta}) \\
&= \frac{1}{2}g^{rr}(0 + 0 - \partial_r g_{\theta\theta}) = \frac{1}{2}g^{rr}(-\partial_r g_{\theta\theta}) \\
&= \frac{1}{2}(e^{-2\lambda(r)})(-\partial_r r^2) = -\frac{1}{2}(e^{-2\lambda(r)})(2r) \\
&= -re^{-2\lambda(r)} \qquad \text{(A.8)}
\end{aligned}$$

$$\begin{aligned}
\Gamma^{\phi}_{r\phi} &= \frac{1}{2}g^{\phi\sigma}(\partial_r g_{\sigma\phi} + \partial_\phi g_{r\sigma} - \partial_\sigma g_{r\phi}) \\
&= \frac{1}{2}g^{\phi\phi}(\partial_r g_{\phi\phi} + \partial_\phi g_{r\phi} - \partial_\phi g_{r\phi}) \\
&= \frac{1}{2}g^{\phi\phi}(\partial_r g_{\phi\phi} + 0 - 0) = \frac{1}{2}g^{\phi\phi}(\partial_r g_{\phi\phi}) \\
&= \frac{1}{2}(r^2 sin^2\theta)^{-1}\partial_r(r^2 sin^2\theta) \\
&= \frac{1}{2}(r^2 sin^2\theta)^{-1}(2r sin^2\theta) = \frac{1}{r} \qquad \text{(A.9)}
\end{aligned}$$

$$\begin{aligned}
\Gamma^{r}_{\phi\phi} &= \frac{1}{2}g^{r\sigma}(\partial_\phi g_{\sigma\phi} + \partial_\phi g_{\phi\sigma} - \partial_\sigma g_{\phi\phi}) \\
&= \frac{1}{2}g^{rr}(\partial_\phi g_{r\phi} + \partial_\phi g_{\phi r} - \partial_r g_{\phi\phi}) \\
&= \frac{1}{2}g^{rr}(0 + 0 - \partial_r g_{\phi\phi}) = \frac{1}{2}g^{rr}(\partial_r g_{\phi\phi}) \\
&= \frac{1}{2}(e^{-2\lambda(r)})(-\partial_r(r^2 sin^2\theta)) \\
&= \frac{1}{2}(e^{-2\lambda(r)})(-2r sin^2\theta) \\
&= -r sin^2\theta e^{-2\lambda(r)} \qquad \text{(A.10)}
\end{aligned}$$

$$\begin{aligned}
\Gamma^{\theta}_{\phi\phi} &= \frac{1}{2}g^{\theta\sigma}(\partial_{\phi}g_{\sigma\phi} + \partial_{\phi}g_{\phi\sigma} - \partial_{\sigma}g_{\phi\phi}) \\
&= \frac{1}{2}g^{\theta\theta}(\partial_{\phi}g_{\theta\phi} + \partial_{\phi}g_{\phi\theta} - \partial_{\theta}g_{\phi\phi}) \\
&= \frac{1}{2}g^{\theta\theta}(0 + 0 - \partial_{\theta}g_{\phi\phi}) \\
&= \frac{1}{2}(r^2)^{-1}(-\partial_{\theta}(r^2 sin^2\theta)) \\
&= -sin\theta cos\theta \qquad \text{(A.11)}
\end{aligned}$$

$$\begin{aligned}
\Gamma^{\phi}_{\theta\phi} &= \frac{1}{2}g^{\phi\sigma}(\partial_{\theta}g_{\sigma\phi} + \partial_{\phi}g_{\theta\sigma} - \partial_{\sigma}g_{\theta\phi}) \\
&= \frac{1}{2}g^{\phi\phi}(\partial_{\theta}g_{\phi\phi} + \partial_{\phi}g_{\theta\phi} - \partial_{\phi}g_{\theta\phi}) \\
&= \frac{1}{2}g^{\phi\phi}(\partial_{\theta}g_{\phi\phi} + 0 - 0) \\
&= \frac{1}{2}(r^2 sin^2\theta)^{-1}\partial_{\theta}(r^2 sin^2\theta) \\
&= \frac{1}{2}(r^2 sin^2\theta)^{-1}(2r^2 sin\theta cos\theta) \\
&= \frac{cos\theta}{sin\theta} \qquad \text{(A.12)}
\end{aligned}$$

We know that Riemann tensor

$$R^{\rho}_{\sigma\mu\nu} = \partial_{\mu}\Gamma^{\rho}_{\nu\sigma} - \partial_{\nu}\Gamma^{\rho}_{\mu\sigma} + \Gamma^{\rho}_{\mu\lambda}\Gamma^{\lambda}_{\nu\sigma} - \Gamma^{\rho}_{\nu\lambda}\Gamma^{\lambda}_{\mu\sigma} \qquad \text{(A.13)}$$

Now, We calculate Ricci tensor

$$\begin{aligned}
R_{\mu\nu} &= R^{\lambda}_{\mu\lambda\nu} \\
R_{tt} &= R^{\lambda}_{t\lambda t} = R^{r}_{trt} + R^{\theta}_{t\theta t} + R^{\phi}_{t\phi t} \qquad \text{(A.14)}
\end{aligned}$$

$$\begin{aligned}
R^{r}_{trt} &= \partial_{r}\Gamma^{r}_{tt} - \partial_{t}\Gamma^{r}_{rt} + \Gamma^{r}_{r\lambda}\Gamma^{\lambda}_{tt} - \Gamma^{r}_{t\lambda}\Gamma^{\lambda}_{rt} \\
&= \partial_{r}\Gamma^{r}_{tt} - 0 + \Gamma^{r}_{rr}\Gamma^{r}_{tt} + \Gamma^{r}_{r\theta}\Gamma^{\theta}_{tt} + \Gamma^{r}_{r\phi}\Gamma^{\phi}_{tt} - \Gamma^{r}_{tt}\Gamma^{t}_{rt} - \Gamma^{r}_{tr}\Gamma^{r}_{rt} - \Gamma^{r}_{t\theta}\Gamma^{\theta}_{rt} - \Gamma^{r}_{t\phi}\Gamma^{\phi}_{rt} \\
&= \partial_{r}(e^{2(\nu-\lambda)}\partial_{r}\nu) + \partial_{r}\lambda e^{2(\nu-\lambda)}\partial_{r}\nu + 0 + 0 - e^{2(\nu-\lambda)}\partial_{r}\nu\partial_{r}\nu - 0 - 0 - 0 \\
&= \partial^2_{r}\nu e^{2(\nu-\lambda)} + \partial_{r}\nu\partial_{r}(e^{2(\nu-\lambda)}) + \partial_{r}\nu\partial_{r}\lambda e^{2(\nu-\lambda)} - e^{2(\nu-\lambda)}(\partial_{r}\nu)^2 \\
&= \partial^2_{r}\nu e^{2(\nu-\lambda)} + (2e^{2(\nu-\lambda)}\partial_{r}\nu - 2e^{2(\nu-\lambda)}\partial_{r}\lambda)\partial_{r}\nu + \partial_{r}\nu\partial_{r}\lambda e^{2(\nu-\lambda)} - e^{2(\nu-\lambda)}(\partial_{r}\nu)^2 \\
&= e^{2(\nu-\lambda)}[\partial^2_{r}\nu + 2(\partial_{r}\nu)^2 - 2\partial_{r}\nu\partial_{r}\lambda + \partial_{r}\nu\partial_{r}\lambda - (\partial_{r}\nu)^2] \\
&= e^{2(\nu-\lambda)}[\partial^2_{r}\nu + (\partial_{r}\nu)^2 - \partial_{r}\nu\partial_{r}\lambda] \qquad \text{(A.15)}
\end{aligned}$$

$$
\begin{aligned}
R^{\theta}_{t\theta t} &= \partial_\theta \Gamma^{\theta}_{tt} - \partial_t \Gamma^{\theta}_{\theta t} + \Gamma^{\theta}_{\theta\lambda}\Gamma^{\lambda}_{tt} - \Gamma^{\theta}_{t\lambda}\Gamma^{\lambda}_{\theta t} \\
&= 0 + 0 + \Gamma^{\theta}_{\theta t}\Gamma^{t}_{tt} + \Gamma^{\theta}_{\theta r}\Gamma^{r}_{tt} + \Gamma^{\theta}_{\theta\theta}\Gamma^{\theta}_{tt} + \Gamma^{\theta}_{\theta\phi}\Gamma^{\phi}_{tt} - \Gamma^{\theta}_{tt}\Gamma^{t}_{\theta t} - \Gamma^{\theta}_{tr}\Gamma^{r}_{\theta t} - \Gamma^{\theta}_{t\theta}\Gamma^{\theta}_{\theta t} - \Gamma^{\theta}_{t\phi}\Gamma^{\phi}_{\theta t} \\
&= 0 + 0 + 0 + \Gamma^{\theta}_{\theta r}\Gamma^{r}_{tt} + 0 + 0 - 0 - 0 - 0 - 0 \\
&= \frac{1}{r} e^{2(\nu-\lambda)} \partial_r \nu \qquad \text{(A.16)}
\end{aligned}
$$

$$
\begin{aligned}
R^{\phi}_{t\phi t} &= \partial_\phi \Gamma^{\phi}_{tt} - \partial_t \Gamma^{\phi}_{\phi t} + \Gamma^{\phi}_{\phi\lambda}\Gamma^{\lambda}_{tt} - \Gamma^{\phi}_{t\lambda}\Gamma^{\lambda}_{\phi t} \\
&= 0 + 0 + \Gamma^{\phi}_{\phi\lambda}\Gamma^{\lambda}_{tt} - \Gamma^{\phi}_{t\lambda}\Gamma^{\lambda}_{\phi t} \\
&= \Gamma^{\phi}_{\phi t}\Gamma^{t}_{tt} + \Gamma^{\phi}_{\phi r}\Gamma^{r}_{tt} + \Gamma^{\phi}_{\phi\theta}\Gamma^{\theta}_{tt} + \Gamma^{\phi}_{\phi\phi}\Gamma^{\phi}_{tt} - \Gamma^{\phi}_{tt}\Gamma^{t}_{\phi t} - \Gamma^{\phi}_{tr}\Gamma^{r}_{\phi t} - \Gamma^{\phi}_{t\theta}\Gamma^{\theta}_{\phi t} - \Gamma^{\phi}_{t\phi}\Gamma^{\phi}_{\phi t} \\
&= 0 + \Gamma^{\phi}_{\phi r}\Gamma^{r}_{tt} + 0 + 0 - 0 - 0 - 0 - 0 \\
&= \frac{1}{r} e^{2(\nu-\lambda)} \partial_r \nu \qquad \text{(A.17)}
\end{aligned}
$$

From eq.(A.15) can be written as:

$$
\begin{aligned}
R_{tt} &= R^{\lambda}_{t\lambda t} = R^{r}_{trt} + R^{\theta}_{t\theta t} + R^{\phi}_{t\phi t} \\
&= e^{2(\nu-\lambda)}[\partial_r^2 \nu + (\partial_r \nu)^2 - \partial_r \nu \partial_r \lambda] + \frac{2}{r} e^{2(\nu-\lambda)} \partial_r \nu \\
&= e^{2(\nu-\lambda)}[\partial_r^2 \nu + (\partial_r \nu)^2 - \partial_r \nu \partial_r \lambda + \frac{2}{r} \partial_r \nu] \qquad \text{(A.18)}
\end{aligned}
$$

$$
R_{rr} = R^{\lambda}_{r\lambda r} = R^{t}_{rtr} + R^{\theta}_{r\theta r} + R^{\phi}_{r\phi r}
$$

$$
\begin{aligned}
R^{t}_{rtr} &= \partial_t \Gamma^{t}_{rr} - \partial_r \Gamma^{t}_{tr} + \Gamma^{t}_{t\lambda}\Gamma^{\lambda}_{rr} - \Gamma^{t}_{r\lambda}\Gamma^{\lambda}_{tr} \\
&= 0 - \partial_r \Gamma^{t}_{tr} + \Gamma^{t}_{tt}\Gamma^{t}_{rr} + \Gamma^{t}_{tr}\Gamma^{r}_{rr} + \Gamma^{t}_{t\theta}\Gamma^{\theta}_{rr} + \Gamma^{t}_{t\phi}\Gamma^{\phi}_{rr} - \Gamma^{t}_{rt}\Gamma^{t}_{tr} - \Gamma^{t}_{rr}\Gamma^{r}_{tr} - \Gamma^{t}_{r\theta}\Gamma^{\theta}_{tr} - \Gamma^{t}_{r\phi}\Gamma^{\phi}_{tr} \\
&= -\partial_r(\partial_r \nu) + 0 + \partial_r \nu \partial_r \lambda + 0 + 0 - \partial_r \nu \partial_r \nu - 0 - 0 - 0 \\
&= \partial_r \nu \partial_r \lambda - \partial_r^2 \nu - (\partial_r \nu)^2 \qquad \text{(A.19)}
\end{aligned}
$$

$$
\begin{aligned}
R^{\theta}_{r\theta r} &= \partial_\theta \Gamma^{\theta}_{rr} - \partial_r \Gamma^{\theta}_{\theta r} + \Gamma^{\theta}_{\theta\lambda}\Gamma^{\lambda}_{rr} - \Gamma^{\theta}_{r\lambda}\Gamma^{\lambda}_{\theta r} \\
&= 0 - \partial_r(\frac{1}{r}) + \Gamma^{\theta}_{\theta t}\Gamma^{t}_{rr} + \Gamma^{\theta}_{\theta r}\Gamma^{r}_{rr} + \Gamma^{\theta}_{\theta\theta}\Gamma^{\theta}_{rr} + \Gamma^{\theta}_{\theta\phi}\Gamma^{\phi}_{rr} - \Gamma^{\theta}_{rt}\Gamma^{t}_{\theta r} - \Gamma^{\theta}_{rr}\Gamma^{r}_{\theta r} - \Gamma^{\theta}_{r\theta}\Gamma^{\theta}_{\theta r} - \Gamma^{\theta}_{r\phi}\Gamma^{\phi}_{\theta r} \\
&= \frac{1}{r^2} + 0 + \frac{1}{r}\partial_r\lambda + 0 - \frac{1}{r}\frac{1}{r} - 0 - 0 - 0 \\
&= \frac{1}{r}\partial_r\lambda \qquad \text{(A.20)}
\end{aligned}
$$

$$
\begin{aligned}
R^{\phi}_{r\phi r} &= \partial_\phi \Gamma^{\phi}_{rr} - \partial_r \Gamma^{\phi}_{\phi r} + \Gamma^{\phi}_{\phi\lambda}\Gamma^{\lambda}_{rr} - \Gamma^{\phi}_{r\lambda}\Gamma^{\lambda}_{\phi r} \\
&= 0 - \partial_r(\frac{1}{r}) + \Gamma^{\phi}_{\phi t}\Gamma^{t}_{rr} + \Gamma^{\phi}_{\phi r}\Gamma^{r}_{rr} + \Gamma^{\phi}_{\phi\theta}\Gamma^{\theta}_{rr} + \Gamma^{\phi}_{\phi\phi}\Gamma^{\phi}_{rr} - \Gamma^{\phi}_{rt}\Gamma^{t}_{\phi r} - \Gamma^{\phi}_{rr}\Gamma^{r}_{\phi r} - \Gamma^{\phi}_{r\theta}\Gamma^{\theta}_{\phi r} - \Gamma^{\phi}_{r\phi}\Gamma^{\phi}_{\phi r} \\
&= \frac{1}{r^2} + 0 + \frac{1}{r}\partial_r\lambda + 0 - 0 - 0 - 0 - \frac{1}{r}\frac{1}{r} \\
&= \frac{1}{r}\partial_r\lambda \qquad \text{(A.21)}
\end{aligned}
$$

$$
\begin{aligned}
R_{rr} &= \partial_r\nu\partial_r\lambda - \partial_r^2\nu - (\partial_r\nu)^2 + \frac{1}{r}\partial_r\lambda + \frac{1}{r}\partial_r\lambda \\
&= \partial_r\nu\partial_r\lambda - \partial_r^2\nu - (\partial_r\nu)^2 + \frac{2}{r}\partial_r\lambda \qquad \text{(A.22)}
\end{aligned}
$$

$$
R_{\theta\theta} = R^{\lambda}_{\theta\lambda\theta} = R^{t}_{\theta t\theta} + R^{r}_{\theta r\theta} + R^{\phi}_{\theta\phi\theta}
$$

$$
\begin{aligned}
R^{t}_{\theta t\theta} &= \partial_t \Gamma^{t}_{\theta\theta} - \partial_\theta \Gamma^{t}_{t\theta} + \Gamma^{t}_{t\lambda}\Gamma^{\lambda}_{\theta\theta} - \Gamma^{t}_{\theta\lambda}\Gamma^{\lambda}_{t\theta} \\
&= 0 - 0 + \Gamma^{t}_{tt}\Gamma^{t}_{\theta\theta} + \Gamma^{t}_{tr}\Gamma^{r}_{\theta\theta} + \Gamma^{t}_{t\theta}\Gamma^{\theta}_{\theta\theta} + \Gamma^{t}_{t\phi}\Gamma^{\phi}_{\theta\theta} - \Gamma^{t}_{\theta t}\Gamma^{t}_{t\theta} - \Gamma^{t}_{\theta r}\Gamma^{r}_{t\theta} - \Gamma^{t}_{\theta\theta}\Gamma^{\theta}_{t\theta} - \Gamma^{t}_{\theta\phi}\Gamma^{\phi}_{t\theta} \\
&= 0 + \partial_r\nu(-re^{-2\lambda}) + 0 + 0 - 0 - 0 - 0 - 0 \\
&= -re^{-2\lambda}\partial_r\nu \qquad \text{(A.23)}
\end{aligned}
$$

$$
\begin{aligned}
R^{r}_{\theta r\theta} &= \partial_r \Gamma^{r}_{\theta\theta} - \partial_\theta \Gamma^{r}_{r\theta} + \Gamma^{r}_{r\lambda}\Gamma^{\lambda}_{\theta\theta} - \Gamma^{r}_{\theta\lambda}\Gamma^{\lambda}_{r\theta} \\
&= \partial_r(-re^{-2\lambda}) - 0 + \Gamma^{r}_{rt}\Gamma^{t}_{\theta\theta} + \Gamma^{r}_{rr}\Gamma^{r}_{\theta\theta} + \Gamma^{r}_{r\theta}\Gamma^{\theta}_{\theta\theta} + \Gamma^{r}_{r\phi}\Gamma^{\phi}_{\theta\theta} - \Gamma^{r}_{\theta t}\Gamma^{t}_{r\theta} - \Gamma^{r}_{\theta r}\Gamma^{r}_{r\theta} - \Gamma^{r}_{\theta\theta}\Gamma^{\theta}_{r\theta} - \Gamma^{r}_{\theta\phi}\Gamma^{\phi}_{r\theta} \\
&= 2re^{-2\lambda}\partial_r\lambda - e^{-2\lambda} + 0 + \partial_r\lambda(-re^{-2\lambda}) + 0 + 0 - 0 - 0 - (-re^{-2\lambda})\frac{1}{r} - 0 \\
&= 2re^{-2\lambda}\partial_r\lambda - e^{-2\lambda} + \partial_r\lambda(-re^{-2\lambda}) + e^{-2\lambda} \\
&= re^{-2\lambda}\partial_r\lambda \qquad \text{(A.24)}
\end{aligned}
$$

$$
\begin{aligned}
R^{\phi}_{\theta\phi\theta} &= \partial_{\phi}\Gamma^{\phi}_{\theta\theta} - \partial_{\theta}\Gamma^{\phi}_{\phi\theta} + \Gamma^{\phi}_{\phi\lambda}\Gamma^{\lambda}_{\theta\theta} - \Gamma^{\phi}_{\theta\lambda}\Gamma^{\lambda}_{\phi\theta} \\
&= 0 - \partial_{\theta}\Gamma^{\phi}_{\phi\theta} + \Gamma^{\phi}_{\phi t}\Gamma^{t}_{\theta\theta} + \Gamma^{\phi}_{\phi r}\Gamma^{r}_{\theta\theta} + \Gamma^{\phi}_{\phi\theta}\Gamma^{\theta}_{\theta\theta} + \Gamma^{\phi}_{\phi\phi}\Gamma^{\phi}_{\theta\theta} - \Gamma^{\phi}_{\theta t}\Gamma^{t}_{\phi\theta} - \Gamma^{\phi}_{\theta r}\Gamma^{r}_{\phi\theta} - \Gamma^{\phi}_{\theta\theta}\Gamma^{\theta}_{\phi\theta} - \Gamma^{\phi}_{\theta\phi}\Gamma^{\phi}_{\phi\theta} \\
&= -\partial_{\theta}(cot\theta) + 0 + \frac{1}{r}(-re^{-2\lambda}) + 0 - 0 - 0 - 0 - cot^{2}\theta \\
&= (1 - e^{-2\lambda}) \qquad \text{(A.25)}
\end{aligned}
$$

$$
\begin{aligned}
R_{\theta\theta} &= -re^{-2\lambda}\partial_{r}\nu + re^{-2\lambda}\partial_{r}\lambda + (1 - e^{-2\lambda}) \\
&= e^{-2\lambda}[r(\partial_{r}\lambda - \partial_{r}\nu) - 1] + 1 \qquad \text{(A.26)}
\end{aligned}
$$

$$
\begin{aligned}
R_{\phi\phi} &= R^{\lambda}_{\phi\lambda\phi} = R^{t}_{\phi t\phi} + R^{r}_{\phi r\phi} + R^{\theta}_{\phi\theta\phi} \\
&= -re^{-2\lambda}sin^{2}\theta\partial_{r}\nu + re^{-2\lambda}sin^{2}\theta\partial_{r}\lambda + (1 - e^{-2\lambda})sin^{2}\theta \\
&= \{e^{-2\lambda}[r(\partial_{r}\lambda - \partial_{r}\nu) - 1] + 1\}sin^{2}\theta \\
&= sin^{2}\theta R_{\theta\theta} \qquad \text{(A.27)}
\end{aligned}
$$

Note: $\partial_r^2\nu = \nu'', \partial_r\nu = \nu', \partial_r\lambda = \lambda'$

Curvature scalar or Ricci scalar is

$$
\begin{aligned}
R &= g^{\mu\nu}R_{\mu\nu} = g^{tt}R_{tt} + g^{rr}R_{rr} + g^{\theta\theta}R_{\theta\theta} + g^{\phi\phi}R_{\phi\phi} \\
&= -e^{-2\nu}e^{2(\nu-\lambda)}[\nu'' - \nu'^{2} - \nu'\lambda' + \frac{2}{r}\nu'] + e^{-2\lambda}[-\nu'' - \nu'^{2} + \nu'\lambda' + \frac{2}{r}\lambda'] + \\
&\quad \frac{1}{r^{2}}\{e^{-2\lambda}[r(\lambda' - \nu') - 1] + 1\} + \frac{1}{r^{2}sin^{2}\theta}\{e^{-2\lambda}[r(\lambda' - \nu') - 1] + 1\}sin^{2}\theta \\
&= e^{-2\lambda}[-\nu'' - \nu'^{2} + \nu'\lambda' - \frac{2}{r}\nu' - \nu'' - \nu'^{2} + \nu'\lambda' + \frac{2}{r}\lambda'] \\
&\quad + \frac{2}{r^{2}}\{e^{-2\lambda}[r(\lambda' - \nu') - 1] + 1\} \\
&= 2e^{-2\lambda}[-\nu'' - \nu'^{2} + \nu'\lambda' - \frac{1}{r}(\nu' - \lambda')] + 2e^{-2\lambda}[\frac{1}{r}(\lambda' - \nu') - \frac{1}{r^{2}}] + \frac{2}{r^{2}} \\
&= 2e^{-2\lambda}[-\nu'' - \nu'^{2} + \nu'\lambda' - \frac{2}{r}(\nu' - \lambda') - \frac{1}{r^{2}}] + \frac{2}{r^{2}} \\
&= -2e^{-2\lambda}[\nu'' + \nu'^{2} - \nu'\lambda' + \frac{2}{r}(\nu' - \lambda') + \frac{1}{r^{2}}(1 - e^{2\lambda})] \\
&= -2e^{-2\lambda}[\nu'' + \nu'^{2} - \nu'\lambda' + \frac{2}{r}(\nu' - \lambda') + \frac{1}{r^{2}}(1 - e^{2\lambda})] \qquad \text{(A.28)}
\end{aligned}
$$

Now, calculate full Einstein's equation

$$G_{\mu\nu} = R_{\mu\nu} - \frac{1}{2}g_{\mu\nu}R \tag{A.29}$$

tt-component:

$$\begin{aligned}
G_{tt} &= R_{tt} - \frac{1}{2}g_{tt}R \\
&= e^{2(\nu-\lambda)}[\nu'' + \nu'^2 - \nu'\lambda' + \frac{2}{r}\nu'] - \frac{1}{2}(-e^{2\nu})(-2e^{-2\lambda})[\nu'' + \nu' \\
&\quad -\nu'\lambda' + \frac{2}{r}(\nu' - \lambda') + \frac{1}{r^2}(1 - e^{2\lambda}] \\
&= e^{2(\nu-\lambda)}[\nu'' + \nu'^2 - \nu'\lambda' + \frac{2}{r}\nu' - \nu'' - \nu'^2 + \nu'\lambda' \\
&\quad -\frac{2}{r}(\nu' - \lambda') - \frac{1}{r^2}(1 - e^{2\lambda})] \\
&= e^{2(\nu-\lambda)}[\frac{2}{r}\lambda' - \frac{1}{r^2}(1 - e^{2\lambda})] \\
&= \frac{1}{r^2}e^{2(\nu-\lambda)}[2\lambda' r - (1 - e^{2\lambda})] \\
&= \frac{1}{r^2}e^{2(\nu-\lambda)}[2r\lambda' - 1 + e^{2\lambda}]
\end{aligned} \tag{A.30}$$

rr-component:

$$\begin{aligned}
G_{rr} &= R_{rr} - \frac{1}{2}g_{rr}R \\
&= -\nu'' - \nu'^2 + \nu'\lambda' + \frac{2}{r}\lambda' - \frac{1}{2}e^{2\lambda}(-2e^{-2\lambda})[\nu'' + \nu'^2 \\
&\quad -\nu'\lambda' + \frac{2}{r}(\nu' - \lambda') + \frac{1}{r^2}(1 - e^{2\lambda})] \\
&= \frac{2}{r}\nu' + \frac{1}{r^2}(1 - e^{2\lambda}) \\
&= \frac{1}{r^2}[2r\nu' + 1 - e^{2\lambda}]
\end{aligned} \tag{A.31}$$

$$\begin{aligned}
G_{\theta\theta} &= R_{\theta\theta} - \frac{1}{2}g_{\theta\theta}R \\
&= e^{-2\lambda}[r(\lambda' - \nu') - 1] + 1 - \frac{1}{r^2}(-2e^{-2\lambda})[\nu'' + \nu'^2 \\
&\quad -\nu'\lambda' + \frac{2}{r}(\nu' - \lambda') + \frac{1}{r^2}(1 - e^{2\lambda})] \\
&= r^2e^{-2\lambda}[\nu'' + \nu'^2 - \nu'\lambda' + \frac{1}{r}(\nu' - \lambda')]
\end{aligned} \tag{A.32}$$

$$
\begin{aligned}
G_{\phi\phi} &= R_{\phi\phi} - \frac{1}{2} g_{\phi\phi} R \\
&= sin^2\theta\{e^{-2\lambda}[r(\lambda' - \nu') - 1] + 1\} - \frac{1}{2} r^2 sin^2\theta(-2e^{-2\lambda})[\nu'' + \nu'^2 \\
&\quad -\nu'\lambda' + \frac{2}{r}(\nu' - \lambda') + \frac{1}{r^2}(1 - e^{2\lambda}] \\
&= e^{-2\lambda} sin^2\theta[r(\lambda' - \nu') - 1 + e^{2\lambda}] + r^2 sin^2\theta e^{-2\lambda}[\nu'' + \nu'^2 \\
&\quad -\nu'\lambda' + \frac{2}{r}(\nu' - \lambda') + \frac{1}{r^2}(1 - e^{2\lambda})] \\
&= e^{-2\lambda} sin^2\theta[r\lambda' - r\nu' - 1 + e^{2\lambda} + r^2\nu'' + r^2\nu'^2 \\
&\quad -r^2\nu'\lambda' + 2r\nu' - 2r\lambda' + 1 - e^{2\lambda}] \\
&= e^{-2\lambda} sin^2\theta[r\nu' - r\lambda' + r^2\nu'' + r^2\nu'^2 - r^2\nu'\lambda'] \\
&= sin^2\theta G_{\theta\theta} \qquad \text{(A.33)}
\end{aligned}
$$

The energy-momentum tensor of the star itself as a perfect fluid is given by

$$T_{\mu\nu} = (\mathcal{E} + P)u_\mu u_\nu + P g_{\mu\nu} \qquad \text{(A.34)}$$

Here, the energy density ($\mathcal{E}$) and pressure density (P) is a function of r alone. Since, the fluid is static, there are no other contributions to the fluid velocity except time-like components (μ_0). The velocity is normalized so that $u_\mu u^\mu = -1$. Then, it becomes

$$u_\mu = (e^\nu, 0, 0, 0) \qquad \text{(A.35)}$$

So, the component of energy momentum tensor will be

$$T = \begin{bmatrix} -e^{2\nu(r)}\mathcal{E} & 0 & 0 & 0 \\ 0 & e^{2\lambda(r)}P & 0 & 0 \\ 0 & 0 & r^2 P & 0 \\ 0 & 0 & 0 & r^2 P sin^2\theta \end{bmatrix}$$

Einstein tensor:

$$G_{\mu\nu} = R_{\mu\nu} - \frac{1}{2} g_{\mu\nu} R = 8\pi T_{\mu\nu} \qquad \text{(A.36)}$$

Using all previous results we can find that the components of the Einstein tensor are: The tt-component:

$$
\begin{aligned}
\frac{1}{r^2} e^{2(\nu-\lambda)}(2r\lambda' - 1 + e^{2\lambda}) &= 8\pi e^{2\nu}\mathcal{E} \\
\frac{1}{r^2} e^{-2\lambda}(2r\lambda' - 1 + e^{2\lambda}) &= 8\pi\mathcal{E} \qquad \text{(A.37)}
\end{aligned}
$$

The rr-component:

$$\begin{aligned} \frac{1}{r^2}(2r\nu' + 1 - e^{2\lambda}) &= 8\pi e^{2\lambda} P \\ \frac{1}{r^2} e^{-2\lambda}(2r\nu' + 1 - e^{2\lambda}) &= 8\pi P \end{aligned} \tag{A.38}$$

The $\theta\theta$-component:

$$\begin{aligned} r^2 e^{-2\lambda}[\nu'' + \nu'^2 - \nu'\lambda' + \frac{1}{r}(\nu' - \lambda')] &= 8\pi r^2 P \\ e^{-2\lambda}[\nu'' + \nu'^2 - \nu'\lambda' + \frac{1}{r}(\nu' - \lambda')] &= 8\pi P \end{aligned} \tag{A.39}$$

The $\phi\phi$-component is proportional to the $\theta\theta$-equation, so there is no need to consider separately. So, the tt-component of the Einstein equation gives:

$$\begin{aligned} \frac{1}{r^2} e^{-2\lambda}(2r\lambda' - 1 + e^{2\lambda}) &= 8\pi\mathcal{E} \\ e^{-2\lambda}(2r\lambda' - 1) + 1 &= 8\pi\mathcal{E} r^2 \\ -\frac{d}{dr}\{r(e^{-2\lambda} - 1)\} &= 8\pi\mathcal{E} r^2 \\ \frac{d}{dr}\{r(e^{-2\lambda} - 1)\} &= -k\mathcal{E} r^2 \\ d\{r(e^{-2\lambda} - 1)\} &= -k\mathcal{E} r^2 dr \end{aligned} \tag{A.40}$$

Where, $k = -8\pi$ and previous equation can be integrated

$$e^{-2\lambda} = 1 + \frac{k}{r}\int_0^R \mathcal{E}(r) r^2 dr \tag{A.41}$$

Let us define

$$\begin{aligned} m(r) &= 4\pi \int_0^R \mathcal{E}(r) r^2 dr \\ e^{-2\lambda} &= 1 - \frac{8\pi G}{4\pi r} m(r) \\ e^{-2\lambda} &= \Big(1 - \frac{2Gm(r)}{r}\Big) \\ e^{2\lambda} &= \Big(1 - \frac{2Gm(r)}{r}\Big)^{-1} \end{aligned} \tag{A.42}$$

So that, the metric will be

$$ds^2 = -e^{2\nu(r)} dt^2 + \Big(1 - \frac{2Gm(r)}{r}\Big)^{-1} dr^2 + r^2 d\theta^2 + r^2 sin^2\theta d\phi^2 \tag{A.43}$$

The gravitational mass of the neutron stars is given by

$$\begin{aligned} M_B &= 4\pi \int_0^R \rho_B(r) r^2 e^{2\lambda} dr \\ M_B &= 4\pi \int_0^R \frac{\rho_B(r) r^2}{(1-\frac{2Gm(r)}{r})} dr \end{aligned} \tag{A.44}$$

The binding energy due to the internal gravitational attraction of the fluid elements in the star, which is given by

$$E_B = M - M_B < 0 \tag{A.45}$$

The binding energy is the amount of energy that would be required to disperse the matter in the star to be infinity. The rr-component can be written as

$$\begin{aligned} \frac{1}{r^2} e^{-2\lambda}(2r\frac{d\nu}{dr} + 1 - e^{-2\lambda}) &= 8\pi p \\ 2r\frac{d\nu}{dr} + 1 - e^{2\lambda} &= 8\pi P r^2 e^{2\lambda} \\ 2r\frac{d\nu}{dr} &= 8\pi P r^2 e^{2\lambda} + e^{2\lambda} - 1 \\ &= \frac{(8\pi P r^2 + 1)}{(1-\frac{2m(r)}{r})} - 1 \\ &= \frac{(8\pi P r^3 + r)}{(r - 2m(r))} - 1 \\ &= \frac{8\pi P r^3 + r - r + 2m(r)}{(r-2m(r))} \\ &= \frac{8\pi P r^3 + 2m(r)}{(r-2m(r))} \\ \frac{d\nu}{dr} &= \frac{(4\pi P r^3 + m(r))}{r(r-2m(r))} \end{aligned} \tag{A.46}$$

Now, we have to calculate $\frac{dP}{dr} = ?$. Again, solve the tt-component equation

$$\begin{aligned} (2r\lambda' - 1 + e^{2\lambda}) &= 8\pi \epsilon r^2 e^{2\lambda} \\ 2r\lambda' &= (8\pi \mathcal{E} r^2 e^{2\lambda} - 1)e^{2\lambda} + 1 \end{aligned} \tag{A.47}$$

$$\begin{aligned} (2r\nu' + 1 - e^{2\lambda}) &= 8\pi P r^2 e^{2\lambda} \\ 2r\nu' &= (1 + 8\pi P r^2 e^{2\lambda})e^{2\lambda} - 1 \end{aligned} \tag{A.48}$$

Take the derivative of the equation (A.48) then

$$\begin{aligned} 2\nu' + 2r\nu'' &= (8\pi P' r^2 + 16\pi P r)e^{2\lambda} + 2\lambda'(1 + 8\pi P r^2)e^{2\lambda} \\ 2r\nu' + 2r^2\nu'' &= [2r\lambda'(1 + 8\pi r^2 P) + (16\pi r^2 P + 8\pi r^3 P')]e^{2\lambda} \\ 2r^2\nu'' &= [2r\lambda'(1 + 8\pi r^2 P) + (16\pi r^2 P + 8\pi r^3 P')]e^{2\lambda} - 2r\nu' \end{aligned} \quad (A.49)$$

Put the values of $2r\nu'$ and $2r\lambda'$ from eqs.(A.47) and (A.48), then

$$2r^2\nu'' = 1 + (16\pi r^2 P + 8\pi r^3 P')e^{2\lambda} - (1 + 8\pi r^2 P)(1 - 8\pi r^2 \mathcal{E})e^{4\lambda} \quad (A.50)$$

Square eq.(A.50) to obtain the result

$$2r^2\nu'^2 = \frac{1}{2}(1 + 8\pi r^2 P)^2 e^{4\lambda} - (1 + 8\pi r^2 P)e^{2\lambda} - \frac{1}{2} \quad (A.51)$$

Now, we have the expressions for ν', ν'', ν'^2, and λ' in terms of $P, P', \mathcal{E}$, and $e^{2\lambda}$. Hence, equation (A.51) can be written as:

$$\begin{aligned} (\mathcal{E} + P)\frac{d\nu}{dr} &= -\frac{dP}{dr} \\ \frac{dP}{dr} &= -\frac{(\mathcal{E} + P)(m(r) + 4\pi r^3 P)}{r(r - 2m(r))} \end{aligned} \quad (A.52)$$

Summary: the TOV equations is written as [195]

$$\frac{dP}{dr} = -\frac{(\mathcal{E} + P)(m(r) + 4\pi r^3 P)}{r(r - 2m(r))} \quad (A.53)$$

$$\frac{dm}{dr} = 4\pi r^2 \mathcal{E} \quad (A.54)$$

REFERENCES

[1] L. D. Landau, "On the theory of stars", Phys. Z. Sowjetunion **1**, 285 (1932).

[2] J. Chadwick, "Possible existence of a neutron", Nature **129**, 312 (1932).

[3] H. Yukawa, "On the interaction of elementary particles", Proc. Phys. Math. Soc. Japan **17**, 48(1935).

[4] http://pdg.lbl.gov/

[5] L. Meitner and O. R. Frisch, "Products of the fission of the uranium nucleus", Nature **143**, 239 (1939).

[6] N. Bohr and J. A. Wheeler, "The mechanism of nuclear fission", Phys. Rev. **56**, 426 (1939).

[7] The DOE/NSF Nuclear Science Advisory Committee, The Frontiers of Nuclear Science (2007).

[8] J. W. Xia *et al.*, The heavy ion cooler-storage-ring project (HIRFL-CSR) at Lanzhou, Nucl. Instr. and Meth. A **488**, 11 (2002).

[9] J. W. Xia, W. L. Zhan, B. W. Wei, and CSR group, Cooler storage ring at china institute of modern physics, Proc. PAC **05**, 271 (2005).

[10] An International Accelerator Facility for Beams of Ions and Antiprotons, GSI report 2006. http://www.gsi.de/GSI-Future/cdr/.

[11] H. Simon, in Proceedings of the International Workshop XXXII on Gross Properties of Nuclei and Nuclear Excitations, Hirschegg (Austria), 2004,

edited by M. Buballa, J. Knoll, W. Norenberg, B.-J. Schaefer, and J. Wambach (GSI, Darmstad, 2004) 290.

[12] M.-G. Saint-Laurent et al. Final report SPIRAL PHASE-II (2001) in: http://pro.ganilspiral2.eu/spiral2/origin-of-spiral2/ spiral-phase-iieuropean-rtt-final-report/view.

[13] T. Suda, K. Maruyama, and I. Tanihata, RIKEN Accel. Prog. Rep. **34**, 49 (2001).

[14] Facility for Rare Isotope Beams at Michigan State University, http://www.frib.msu.edu/about/msu-frib-proposal.

[15] http://www.nndc.bnl.gov/nudat2/

[16] P. B. Abbott *et al.*, "GW170817: Observation of gravitational waves from a binary neutron star inspiral", Phys. Rev. Lett. **119**, 161101 (2017).

[17] R. J. Furnstahl, B. D. Serot and H. B. Tang, "Analysis of chiral mean-field models for nuclei", Nucl. Phys. A **598**, 539 (1996); R. J. Furnstahl, B. D. Serot and H. B. Tang, "A chiral effective lagrangian for nuclei", Nucl. Phys. A **615**, 441 (1997).

[18] P. Arumugam, B. K. Sharma, P. K. Sahu, S. K. Patra, Tapas Sil, M. Centelles, and X. Viñas, "Versatility of field theory motivated nuclear effective Lagrangian approach", Phys. Lett. B **601**, 51 (2004).

[19] M. Del Estal, M. Centelles, X. Viñas and S. K. Patra, "Effects of new nonlinear couplings in relativistic effective field theory", Phys. Rev. C **63**, 024314 (2001).

[20] E. Chabanat, P. Bonche, P. Haensel, J. Meyer, and R. Schaeffer, "A Skyrme parametrization from subnuclear to neutron star densities Part II. nuclei far from stabilities", Nucl. Phys. A **635**, 231 (1998).

[21] N. Sandulescu, Nguyen Van Giai, and R. J. Liotta, "Resonant continuum in the Hartree-Fock+BCS approximation", Phys. Rev. C **61**, 061301(R) (2000).

[22] J. Dobaczewski, H. Flocard, and J. Treiner, "Hartree-Fock-Bogolyubov description of nuclei near the neutron-drip line", Nucl. Phys. A **422**, 103 (1984).

[23] J. Dobaczewski, W. Nazarewicz, T. R. Werner, J. F. Berger, R. C. Chin, and J. Dechargé, "Mean-field description of ground-state properties of drip-line nuclei: Pairing and continuum effects", Phys. Rev. C **53**, 2809 (1996).

[24] J. Dechargé and D. Gogny, "Hartree-Fock-Bogolyubov calculations with the D1 effective interaction on spherical nuclei", Phys. Rev. C **21**, 1568 (1980).

[25] J. D. Walecka, "A theory of highly condensed matter", Ann. Phys. (N. Y.) **83**, 491 (1974).

[26] J. Boguta and A. R. Bodmer, "Relativistic calculation of nuclear matter and the nuclear surface", Nucl. Phys. A **292**, 413 (1977).

[27] P. -G. Reinhard, "The Relativistic Mean Field Description of Nuclei and Nuclear Dynamics", Rep. Prog. Phys. **52**, 439 (1989).

[28] M. M. Sharma, G. A. Lalazissis and P. Ring, "Anomaly in the charge radii of Pb isotopes", Phys. Lett. B **317**, 9 (1993).

[29] G. A. Lalazissis, J. König and P. Ring, "New parametrization for the Lagrangian density of relativistic mean field theory", Phys. Rev. C **55**, 540 (1997).

[30] G. A. Lalazissis, S. Karatzikos, R. Fossion, D. Pena Arteaga, A. V. Afanasjev and P. Ring, "The effective force NL3 revisited", Phys. Lett. B **671**, 36 (2009).

[31] A. R. Bodmer, "Relativistic mean field theory of nuclei with a vector meson self-interaction", Nucl. Phys. A **526**, 703 (1991)

[32] S. Gmuca, "Finite-nuclei calculations based on relativistic mean-field effective interactions", Nucl. Phys. A **547**, 447 (1992); J. K. Bunta and S. Gmuca, "Asymmetric nuclear matter in the relativistic mean-field approach with vector cross interaction", Phys. Rev. C **68**, 054318 (2003).

[33] Y. Sugahara and H. Toki, "Relativistic mean-field theory for unstable nuclei with non-linear σ and ω terms", Nucl. Phys. A **579**, 557 (1994).

[34] F. Coester, S. Cohen, B. Day, and C. M. Vincent, "Variation in nuclear-matter binding energies with phase-shift-equivalent two-body potentials", Phys. Rev. C, **1**, 769 (1970).

[35] D. Vretenar, G. A. Lalazissis and P. Ring, "Neutron density distributions for atomic parity nonconservation experiments", Phy. Rev. C **62**, 045502 (2000).

[36] B. G. Todd-Rutel and J. Piekarewicz, "Neutron-rich nuclei and neutron stars: A new accurately calibrated interaction for the study of neutron-rich matter", Phys. Rev. Lett **95**, 122501 (2005); C. J. Horowitz and J. Piekarewicz, "Neutron star structure and the neutron radius of ^{208}Pb", Phys. Rev. Lett. **86**, 5647 (2001).

[37] S. Kubis and M. Kutschera, "Nuclear matter in relativistic mean-field theory with isovector scalar meson", Phys. Lett. B **399**, 191 (1997).

[38] Bharat Kumar, S. K. Singh, B. K. Agrawal, S. K. Patra, "New parameterization of the effective field theory motivated relativistic mean-field model", Nucl. Phys. A **966**, 197 (2017).

[39] G. Ferini, M. Colonna, T. Gaitanos and M. Di Toro, "Aspects of particle production in isospin-asymmetric matter", Nucl. Phys. A **762**, 147 (2005).

[40] H. Chiu and E. E. Salpeter, "Surface X-ray emission from neutron stars", Phys. Rev. Lett. **12**, 413 (1964).

[41] J. N. Bahcall and R. A. Wolf, "Neutron stars", Phys. Rev. Lett. **14**, 343 (1965).

[42] J. M. Lattimer, C. J. Pethic, M. Prakash and P. Haensel, "Direct URCA process in neutron stars", Phys. Rev. Lett. **66**, 2701 (1991).

[43] C. J. Horowitz, S. J. Pollock, P. A. Souder and R. Michaels, "Parity violating measurements of neutron densities", Phys. Rev. C **63**, 025501 (2001).

[44] P. G. Reinhard, M. Rufa, J. Maruhn, W. Greiner and J. Friedrich, "Nuclear ground-state properties in a relativistic meson-field theory", Z. Phys. A **323**, 13 (1986).

[45] Z. Y. Zhu, H. J. Mang and P. Ring, "Vacuum polarization in a relativistic description of open shell nuclei", Phys. Lett. B **254**, 325 (1991).

[46] S. Karatzikos, A. V. Afanasjev, G. A. Lalazissis and P. Ring, "The fission barriers in Actinides and superheavy nuclei in covariant density functional theory", Phys. Lett. B **689**, 72 (2010).

[47] P. Ring, "Relativistic mean-field theory in finite nuclei", Prog. Part. Nucl. Phys. **37**, 193 (1996).

[48] P. Ring and P. Schuck, "The Nuclear Many-Body Problem", Springer-Verlag, Berlin, 1980.

[49] S. K. Singh, S. K. Biswal, M. Bhuyan, S. K. Patra, "Effects of δ mesons in relativistic mean-field theory", Phys. Rev. C **89**, 044001 (2014).

[50] V. M. Strutinsky, "Shell effects in nuclear masses and deformation energies", Nucl. Phys. A **95**, 420 (1967).

[51] Ph.D. thesis by Dmitry Gorelov, "Nuclear fission studies with the IGISOL method and JYFLTRAP".

[52] P. Lichtner, D. Drechsel, J. Maruhn and W. Greiner, "Fission mass asymmetry as a dynamic process described by a collective coordinate", Phys. Lett. B **45**, 175 (1978).

[53] P. Fong, "Statistical theory of nuclear fission: Asymmetric fission", Phys. Rev. **102**, 434 (1956).

[54] M. Rajasekaran and V. Devanathan, "Nuclear level density and the mass distribution of fission fragments", Phys. Rev. C **24**, 2606 (1981).

[55] M. Balasubramaniam, C. Karthikraj, N. Arunachalam and S. Selvaraj, "Ternary-fission mass distribution of ^{252}Cf: A level-density approach", Phys. Rev. C **90**, 054611 (2014).

[56] P. Möller, J. R. Nix and K. L. Kratz, "Nuclear properties for astrophysical and radioactive-ion-beam applications", At. Data and Nucl. Data Tables **59**, 185 (1995).

[57] P. B. Demorest, T. Pennucci, S. M. Ransom, M. S. E. Roberts, and J. W. T. Hessels, "A two-solar-mass neutron star measured using Shapiro delay", Nature (London) **467**, 1081 (2010).

[58] J. Antoniadis *et al.*, "A massive pulsar in a compact relativistic binary", Science **340**, 6131 (2013).

[59] A. W. Steiner, J. M. Lattimer and E. F. Brown, "The equation of state from observed masses and radii of neutron stars", Astrophys. J. **722** , 33 (2010).

[60] J. R. Oppenheimer and G. M. Volkoff, "On Massive Neutron Cores", Phys. Rev. 55, 374 (1939); R. C. Tolman, "Static solutions of Einstein's field equations for spheres of fluid", Phys. Rev. **55**, 364 (1939).

[61] Jocelyn S. Read, Benjamin D. Lackey, Benjamin J. Owen, and John L. Friedman, "Constraints on a phenomenologically parametrized neutron-star equation of state", Phys. Rev. D **79**, 124032 (2009).

[62] R. A. Hulse and J. H. Taylor, "Discovery of a pulsar in a binary system", Astrophys. J. **195**, L51 (1975).

[63] Philippe Landry, and Eric Poisson, "Dynamical tidal response of a rotating neutron star", https://ui.adsabs.harvard.edu/#abs/2017APS..APR.E6004L/abstract.

[64] T. Hinderer, "Tidal Love numbers of neutron stars", Astrophys. J. **677**, 1216 (2008); 697964(E) (2009).

[65] $\acute{E}.\acute{E}$. Flanagan and T. Hinderer, "Constraining neutron-star tidal Love numbers with gravitational-wave detectors", Phys. Rev. D **77**, 021502 (2008).

[66] T. Hinderer, B. D. Lackey, R. N. Lang, and J. S. Read, "Tidal deformability of neutron stars with realistic equations of state and their gravitational wave signatures in binary inspiral", Phys. Rev. D **81**, 123016 (2010).

[67] T. Damour and A. Nagar, "Effective one body description of tidal effects in inspiralling compact binaries", Phys. Rev. D **81**, 084016 (2010).

[68] P. Landry and Eric Poisson, "Relativistic theory of surficial Love numbers", Phys. Rev. D **89**, 124011 (2014).

[69] H. P. D*ü*rr, "Relativistic effects in nuclear forces" Phys. Rev. **103**, 469 (1956).

[70] M. H. Johnson and E. Teller,"Classical field theory of nuclear forces", Phys. Rev. **98**, 783 (1955); H. P. D*ü*rr and E. Teller, Interaction of antiprotons with nuclear fields, Phys. Rev. **101**, 494 (1956).

[71] L. D. Miller and A. E. S. Green, "Relativistic self-consistent meson field theory of spherical nuclei", Phys. Rev. C **5**, 241 (1972).

[72] B. D. Serot and J. D. Walecka, "Recent Progress in Quantum Hadrodynamics", Int. J. Mod. Phys. E **6**, 515 (1997).

[73] H. Müller and B. D. Serot, "Relativistic mean-field theory and the high-density nuclear equation of state", Nucl. Phys. A **606**, 508 (1996).

[74] R. J. Furnstahl, C. E. Price and G. E. Walker, "Systematics of light deformed nuclei in relativistic mean-field models", Phys. Rev. C **36**, 2590 (1987).

[75] J. P. Elliott and T. H. R. Skyrme, "Centre-of-mass effects in the nuclear shell-model", Proc. Soc. (London) A **232**, 561 (1955).

[76] J. W. Negele, "Structure of finite nuclei in the local-density approximation", Phys. Rev. C **1**, 1260 (1970).

[77] M. A. Preston and R. K. Bhaduri, *Structure of Nucleus, Addison-Wesley Publishing Company*, Ch. 8, page 309 (1982).

[78] S. K. Patra, "Effects of pairing correlation in light nuclei", Phys. Rev. C **48**, 1449 (1993).

[79] Y. K. Gambhir, P. Ring and A. Thimet, "Relativistic mean-field theory for finite nuclei", Ann. of Phys. **198**, 132 (1990).

[80] D. Vautherin, "Hartree-Fock Calculations with Skyrme's Interaction. II. Axially deformed nuclei", Phys. Rev. C **7**, 296 (1973).

[81] B. D. Serot and J. D. Walecka, "The relativistic nuclear many-body problem", Adv. Nucl. Phys. **16**, 1 (1986).

[82] W. Kohn and L. J. Sham, "Self-Consistent equations including exchange and correlation effects", Phys. Rev. A **140**, 1133 (1965); C. Speicher, R. M. Dreizler, and E. Engel, "Density functional approach to Quantumhadrodynamics", Ann. Phys. N.Y. **213**, 312 (1992).

[83] T. Matsui, "Fermi-liquid properties of nuclear matter in a relativistic mean-field theory", Nucl. Phys. A **370**, 365 (1981).

[84] X. Roca-Maza, X. Viñas, M. Centelles, P. Ring and P. Schuck, "Relativistic mean-field interaction with density-dependent meson-nucleon vertices based on microscopical calculations", Phys. Rev. C **84**, 054309 (2011).

[85] S. K. Singh, M. Bhuyan, P. K. Panda and S. K. Patra, "The effect of isoscalar-isovector coupling in infinite nuclear matter", J. Phys. G: Nucl. Part. Phys. **40**, 085104 (2013).

[86] C. J. Horowitz and J. Pickarewicz, "Neutron radii of ^{208}Pb and neutron stars", Phys. Rev. C **64**, 062802 (R) (2001).

[87] L. -W. Lattimer, B. -J. Cai, C. M. Ko, B. -A. Li, C. Shen and J. Xu, "Higher-order effects on the incompressibility of isospin asymmetric nuclear matter", Phys. Rev. C **80**, 014322 (2009).

[88] M. B. Tsang *et al.*, "Constraints on the symmetry energy and neutron skins from experiments and theory", Phys. Rev. C **86**, 015803 (2012).

[89] M. Dutra *et al.*, "Skyrme interaction and nuclear matter constraints", Phy. Rev. C **85**, 035201 (2012).

[90] C. Xu, B.-A. Li and L.-W. Chen, "Symmetry energy, its density slope, and neutron-proton effective mass splitting at normal density extracted from global nucleon optical potentials", Phys. Rev. C **82**, 054607 (2010).

[91] W. G. Newton, M. Gearheart and B.-A. Li, "A survey of the parameter space of the compressible liquid drop model as applied to the neutron star inner crust", Astrophys. J. **204**, 9 (2013).

[92] A. W. Steiner and S. Gandolfi, "Connecting neutron star observations to three-body forces in neutron matter and to the nuclear symmetry energy", Phys. Rev. Lett. **108**, 081102 (2012).

[93] F. J. Fattoyev, W. G. Newton, J. Xu and B.-A. Li, "Generic constraints on the relativistic mean-field and Skyrme-Hartree-Fock models from the pure neutron matter equation of state", Phys. Rev. C **86**, 025804 (2012).

[94] M. Centelles, X. Roca-Maza, X. Viñas and M. Warda, "Nuclear symmetry energy probed by neutron-skin thickness of nuclei", Phys. Rev. Lett. **102**, 122502 (2009).

[95] B. A. Li and X. Han, "Constraining the neutronâĂŞproton effective mass splitting using empirical constraints on the density dependence of nuclear symmetry energy around normal density", Phys. Lett. B **727**, 276 (2013).

[96] L. Satpathy, S. K. Patra and R. K. Choudhury, "Fission decay properties of ultra neutron-rich uranium isotopes", Pramana J. Phys. **70**, 87 (2008).

[97] P. Arumugam, B. K. Sharma, S. K. Patra and R. K. Gupta, "Relativistic mean-field study of clustering in light nuclei", Phys. Rev. C **71**, 064308 (2005).

[98] BirBikram Singh, B. B. Sahu and S. K. Patra, "α-decay and fusion phenomena in heavy ion collisions using nucleon-nucleon interactions derived from relativistic mean-field theory", Phys. Rev. C **83**, 064601 (2011).

[99] S. K. Patra, Raj. K. Gupta, B. K. Sharma, P. D. Stevenson and W. Greiner, "Exotic clustering in heavy and superheavy nuclei within the relativistic and non-relativistic mean field formalisms", J. Phys. G. **34**, 2073 (2007).

[100] B. K. Sharma, P. Arumugam, S. K. Patra, P. D. Stevenson, R. K. Gupta and W. Greiner, "Clustering in superheavy nuclei within the relativistic mean-field approach", J. Phys. G. **32**, L1 (2006).

[101] G. R. Satchler and W. G. Love, "Folding model potentials from realistic interactions for heavy-ion scattering", Phys. Rep. **55**, 183 (1979).

[102] BirBikram Singh, M. Bhuyan, S. K. Patra and Raj. K. Gupta, "Optical potential obtained from relativistic-mean-field theory-based microscopic nucleon-nucleon interaction: applied to cluster radioactive decays", J. Phys. G. **39**, 025101 (2012).

[103] B. B. Sahu, S. K. Singh, M. Bhuyan, S. K. Biswal and S. K. Patra, "Importance of nonlinearity in the NN potential", Phys. Rev. C **89**, 034614 (2014).

[104] S. K. Patra and C. R. Praharaj, "Relativistic mean field study of light medium nuclei away from beta stability", Phys. Rev. C **44**, 2552 (1991).

[105] C. J. Horowitz and B. D. Serot, "Self-consistent hartree description of finite nuclei in a relativistic quantum field theory", Nucl. Phys. A **368**, 503 (1981).

[106] J. Boguta and A. R. Bodmer, "Relativistic calculation of nuclear matter and the nuclear surface", Nucl. Phys. A **292**, 413 (1977).

[107] C. E. Price and G. E. Walker, "Self-consistent Hartree description of deformed nuclei in a relativistic quantum field theory", Phys. Rev. C **36**, 354 (1987).

[108] J. R. Stone and P. G. Reinhard, "The Skyrme Interaction in finite nuclei and nuclear matter", Prog. Part. Nucl. Phys. **58**, 587 (2007).

[109] F. Tondeur, S. Goriely, J. M. Pearson, and M. Onsi, "Towards a Hartree-Fock mass formula", Phys. Rev. C **62**, 024308 (2000).

[110] U. Hofmann and P. Ring, "A new method to calculate magnetic moments in relativistic mean field theories", Phys. Lett. B **214**, 307 (1988).

[111] G. A. Lalazissis, D. Vretenar, and P. Ring, "Ground-state properties of deformed proton emitters in the relativistic Hartree-Bogoliubov model", Nucl. Phys. A **650**, 133 (1999).

[112] I. Angeli, K. P. Marinova, "Ground-state properties of deformed proton emitters in the relativistic Hartree-Bogoliubov model", At. Data and Nucl. Data Tables **99**, 69 (2013).

[113] P. Möller, J. R. Nix, W. D. Myers and W. J. Swiatecki, "Nuclear properties for astrophysical and radioactive-ion-beam appications", At. Data and Nucl. Data Tables **66**, 131 (1997).

[114] Zhongzhou Ren and Hiroshi Toki, "Superdeformation in the newly discovered superheavy elements", Nucl. Phys. A **689**, 691 (2001).

[115] Zhongzhou Ren, Ding-Han Chen, Fei Tai, H. Y. Zhang, and W. Q. Shen, "Ground state properties of odd-Z superheavy nuclei", Phys. Rev. C **67**, 064302 (2003).

[116] Z. Patyk and A. Sobiczewski, "Ground-state properties of the heaviest nuclei analyzed in a multidimensional deformation space", Nucl. Phys. A **533**, 132 (1991).

[117] S. Bjϕrnholm and J. E. Lynn, "The double-humped fission barrier", Rev. Mod. Phys. **52**, 725 (1980).

[118] S. K. Patra, F. H. Bhat, R. N. Panda, P. Arumugam and R. K. Gupta, "Isomeric state in ^{53}Co:A mean-field analysis", Phys. Rev. C **79**, 044303 (2009).

[119] H. Flocard, P. Quentin and D. Vautherin, "Self-consistent calculation of the ground state properties of some rare-earth nuclei", Phys. Lett. B **46**, 304 (1973).

[120] W. Koepf and P. Ring, "Has the nucleus ^{24}Mg a triaxial shape? a relativistic investigation", Phys. Lett. B **212**, 397 (1988).

[121] J. Fink, V. Blum, P. G. Reinhard, J. A. Maruhn and W. Greiner, "Systematic study of potential energy surfaces of light nuclei in relativistic Hartree calculations", Phys. Lett. B **218**, 277 (1989).

[122] D. Hirata, H. Toki, I. Tanihata and P. Ring, "Systematic study of Sr isotopes in the relativistic mean-field theory", Phys. Lett. B **314**, 168 (1993).

[123] J. Meng, H. Toki, S. G. Zhou, S. Q. Zhang, W. H. Long and L. S. Geng, "Relativistic Continuum Hartree Bogoliubov theory for ground state properties of exotic nuclei", Prog. Part. Nucl. Phys. **57**, 470 (2006).

[124] Bing-Nan Lu, En-Guang Zhao and Shan-Gui Zhou, "Potential energy surfaces of actinide nuclei from a multidimensional constrained covariant density functional theory: Barrier heights and saddle point shapes", Phys. Rev. C **85**, 011301(R) (2012).

[125] Bing-Nan Lu, Jie Zhao, En-Guang Zhao and Shan-Gui Zhou, "Multidimensionally-constrained relativistic mean-field models and potential-energy surfaces of actinide nuclei", Phys. Rev. C **89**, 014323 (2014).

[126] Jie Zhao, Bing-Nan Lu, Dario Vretenar, En-Guang Zhao and Shan-Gui Zhou, "Multidimensionally constrained relativistic mean-field study of triple-humped barriers in actinides", Phys. Rev. C **91**, 014321 (2015).

[127] B. B. Back, H. C. Britt, J. D. Garrett, and O. Hansen, "Subbarrier Fission Resonances in Th Isotopes", Phys. Rev. Lett. **28**, 1707 (1972); J. Blons, C. Mazur, D. Paya, M. Ribrag, and H. Weigmann, "Rotational bands in asymmetrically deformed ^{231}Th", Phys. Rev. Lett. **41**, 1282 (1978).

[128] D. M. Brink and A. Weiguny, "The generator-coordinate method and the random phase approximation", Phys. Lett. B **26**, 497 (1968).

[129] Myers and W. D. Swiatecki, "Nuclear masses and deformations", Nucl. Phys. **81**, 1 (1966).

[130] Bharat Kumar, S. K. Singh and S. K. Patra, "Shape coexistence and parity doublet in Zr isotopes", Int. J. Mod. Phys. **24**, 1550017 (2015).

[131] P. G. Thirolf and D. Habs, "Spectroscopy in the second and third minimum of actinide nuclei", Prog. Part. Nucl. Phys. **49**, 325 (2002).

[132] S. K. Patra and C. R. Praharaj, "Q-values for α-decays in the chain", J. Phys. G **23**, 939 (1997).

[133] S. B. Duarte, O. A. P. Tavares, F. Guzman and A. Dimarco, "Half-lives for proton emission, alpha decay, cluster radioactivity, and cold fission processes calculated in a unified theortical framework", At. Data and and Nucl. Data Table **80**, 235 (2009).

[134] V. E. Viola Jr. and G. T. Seaborg, "Nuclear systematics of the heavy elements-II Lifetimes for alpha, beta and spontaneous fission decay", J. Inorg. Nucl. Chem. **28**, 741 (1966).

[135] A. Sobiczewski, Z. Patyk and S. C. Cwiok, "Refelection-asymmetric shapes in transitional odd-A isotopes Th isotopes", Phys. Lett. **224**, 1 (1989).

[136] A. M. Kobos, B. A. Brown, R. Lindsay and G. R. Satchler, "Folding-model analysis of elastic and inelastic α-particle scattering using a density-dependent force", Nucl. Phys. A **425**, 205 (1984).

[137] Dao T. Khoa, W. von Oertzen and H. G. Bohlen, "Double-folding model for heavy-ion optical potential: Revised and applied to study ^{12}C and ^{16}O elastic scattering", Phys. Rev. C **49**, 1652 (1994).

[138] D. N. Basu, "Folding model analysis of alpha radioactivity", J. Phys. G. **29**, 2079 (2003).

[139] E. O. Fiset and J. R. Nix, "Calculation of half-lives for superheavy nuclei", Nucl. Phys. A **193**, 647 (1972).

[140] R. C. Nayak and L. Satpathy, "Mass predictions in the infinite nuclear model", At. Data and Nucl. Data Tables **73**, 213 (1999).

[141] D. Vautherin and D. M. Brink, "Hartree-Fock calculations with Skyrme's interaction", Phys. Lett. B **32**, 149 (1970); "Hartree-Fock calculations with Skyrme's interaction. I. Spherical nuclei", Phys. Rev. C **5**, 626 (1972).

[142] M. K. Pal and A. P. Stamp, "Pairing effects in nuclei described by the Hartree-Fock theory", Nucl. Phys. A **99**, 228 (1967).

[143] S. K. Patra, R. K. Choudhury and L. Satpathy, "Anatomy of neck configuration in fission decay", J. Phys. G. **37**, 085103 (2010).

[144] M. Wang, G. Audi, A. H. Wapstra, F. G. Kondev, M. MacCromick, X. Xu and B. Pfeiffer, "The Ame2012 atomic mass evaluation", Chin. Phys. C **36**, 1603 (2012).

[145] B. K. Sharma, P. Arumugam, S. K. Patra, P. D. Stevenson, R. K. Gupta and W. Greiner, "Clustering in superheavy nuclei within the relativistic mean-field approach", J. Phys. G. **32**, L1 (2006).

[146] S. K. Patra, Raj. K. Gupta, B. K. Sharma, P. D. Stevenson and W. Greiner, "Exotic clustering in heavy and superheavy nuclei within the relativistic and non-relativistic mean-field formalisms", J. Phys. G. **34**, 2073 (2007).

[147] Raj. K. Gupta, S. K. Patra, P. D. Stevenson, C. Beck, and W. Greiner, "Fission of hyper-hyperdeformed ^{56}Ni: a clustering analysis within mean-field approaches", J. Phys. G. **35**, 075106 (2008).

[148] K. Rutz, J. A. Maruhn, P.-G. Reinhard and W. Greiner, "Fission of hyper-hyperdeformed ^{56}Ni: a clustering analysis within mean-field approaches", Nucl. Phys. A **590**, 680 (1995).

[149] D. W. Bergen and R. R. Fullwood," Neutron-induced fission cross-section of ^{242}Pu", Nucl. Phys. A **163**, 577 (1971).

[150] A. J. Cole, in *"Fundamental and Applied Nuclear Physics Series - Statistical models for nuclear decay from evaporation to vaporization"*, edited by R. R. Betts and W. Greiner, Institute of Physics Publsihing, Bristol and Philadelphia, 2000.

[151] J. R. Huizenga and L. G. Moretto, "Nuclear level densities", Annu. Rev. Nucl. Sci. **22**, 427 (1972).

[152] H. Bethe, "Nuclear Dynamics, Theoretical", Rev. Mod. Phys. **9**, 69 (1937).

[153] M.T. Senthil Kannan and M. Balasubramaniam, "Charge distribution in the ternary fragmentation of ^{252}Cf", Eur. Phys. J. A **53**, 164 (2017).

[154] M.T. Senthil kannan, Bharat Kumar, M. Balasubramaniam, B. K. Agrawal, S. K. Patra, "Relative fragmentation in ternary systems within the temperature-dependent relativistic mean-field approach", Phys. Rev. C **95**, 064613 (2017).

[155] Bharat Kumar, M.T. Senthil kannan, M. Balasubramaniam, B. K. Agrawal and S. K. Patra, "Structure effects on fission yields", arXiv:1701.00731.

[156] Bharat Kumar, S. K. Biswal, S. K.Singh and S. K. Patra, "Examining the stability of thermally fissile Th and U isotopes", Phys. Rev. C **92**, 054314 (2015).

[157] F. Y. Niu, Z. H. Linag and J. Meng, "Stability of Strutinsky shell correction energy in relativistic mean-field theory", Chin. Phys. Lett. **26**, 032103 (2009).

[158] B. K. Agrawal, Tapas Sil, J. N. De and S. K. Samaddar, "Nuclear shape transition at finite temperature in a relativistic mean field approach", Phys. Rev. C **62**, 044307 (2000); "Shape transition in some rare-earth nuclei in relativistic mean-field theory", Phys. Rev. C **63**, 024002 (2001).

[159] B. K. Agrawal, S. K. Samaddar, J. N. De, and S. Shlomo, "Large-model-space calculation of the nuclear level density parameter at finite temperature", Phys. Rev. C **58**, 3004 (1998).

[160] https://www-nds.iaea.org/RIPL-3/.

[161] B. Nerlo-Pomorska, K. Pomorski, J. Bartel and K. Dietrich, "Nuclear level densities within the relativistic mean-field theory", Phys. Rev. C **66**, 051302(R) (2002).

[162] J. M. Blatt and V. F. Weisskopf *"Theoretical Nuclear Physics", Courier Corporation, 1991.*

[163] L. Satpathy and S. K. Patra, "Shell overcomes repulsive nuclear force instability", J. Phys. G. **30**, 771 (2004).

[164] Z. Patel *et al.*, "Isomer decay spectroscopy of ^{164}Sm and ^{166}Gd:Midshell collectivity around N=100", Phys. Rev. Lett. **113**, 262502 (2014).

[165] A. Chaudhuri *et al.*, "Direct evidence of "washing out" of nuclear shell effects", Phys. Rev. C **91**, 044620 (2015).

[166] H. Pasca, A. V. Andreev, G. G. Adamian, and N. V. Antonenko, "Unexpected asymmetry of the charge distribution in the fission of ^{222,224}Th at high excitation energies", Phys. Rev. C **94**, 064614 (2016).

[167] E. F. Jones *et al.*, "Identification of levels in ^{162,164}Gd and decrease in moment of inertia between N = 98-100", J. Phys. G **30**, L43 (2004).

[168] E. Poisson, and C. M. Will, "Gravity: Newtonian, Post-Newtonian Relativistic", Cambridge University Press (2014).

[169] *É*. Racine, and *É.É*. Flanagan, "Post-1-Newtonian equations of motion for systems of arbitrarily structured bodies", Phys. Rev. D **71**, 044010 (2005).

[170] J. Vines, *É.É*. Flanagan, and T. Hinderer, "Post-1-Newtonian tidal effects in the gravitational waveform from binary inspirals", Phys. Rev. D **83**, 084051 (2011).

[171] J. E. Vines and *É.É*. Flanagan, "First-post-Newtonian quadrupole tidal interactions in binary systems", Phys. Rev. D **88**, 024046 (2013).

[172] Series of lectures given by Tanja Hinderer at ICTS-TIFR, Bangalore, https://www.icts.res.in/program/gws2017.

[173] Kip S. Thorne, "Gravitational-wave research: Current status and future prospects", Rev Mod Phys. **52**, 285 (1980).

[174] Kip S. Thorne, "Tidal stabilization of rigidly rotating, fully relativistic neutron stars", Phys. Rev. D, **58**, 124031 (1998).

[175] C. W. Misner, Kip S. Thorne, and J. A. Wheeler, 1973, Gravitation (San Francisco:W. H. Freeman and Co.).

[176] T. Regge, and J. A. Wheeler, "Stability of a Schwarzschild singularity", Phys. Rev., **108**, 1063 (1957).

[177] Kip S. Thorne, and A. Campolattaro, "Non-radial pulsation of general-relativistic stellar models. I. analytic analysis for $L \geq 2$", Astrophys. J. **149**, 591 (1967).

[178] B. P. Abbott *et al.*, "Observation of Gravitational waves from a binary black hole merger", Phys. Rev. Lett. **116**, 061102 (2016).

[179] "VIRGO," www.virgo.infn.it.

[180] "Kagra," http://gwcenter.icrr.u-tokyo.ac.jp/en/.

[181] L. Baiotti, T. Damour, B. Giacomazzo, A. Nagar, and L. Rezzolla, "Analytic modeling of tidal effects in the relativistic inspiral of binary neutron stars", Phys. Rev. Lett. **105**, 261101 (2010).

[182] L. Baiotti, T. Damour, B. Giacomazzo, A. Nagar, and L. Rezzolla, "Accurate numerical simulations of inspiralling binary neutron stars and their comparison with effective-one-body analytical models", Phys. Rev. D **84**, 024017 (2011).

[183] F. Pannarale, L. Rezzolla, F. Ohme, and J. S. Read, "Will black hole-neutron star binary inspirals tell us about the neutron star equation of state?", Phys. Rev. D **84**, 104017 (2011).

[184] B. D. Lackey, K. Kyutoku, M. Shibata, P. R. Brady, and J. L. Friedman, "Extracting equation of state parameters from black hole-neutron star mergers: Nonspinning black holes", Phys. Rev. D **85**, 044061 (2012).

[185] T. Damour, A. Nagar and L. Villain, "Measurability of the tidal polarizability of neutron stars in late-inspiral gravitational-wave signals", Phys. Rev. D **85**, 123007 (2012).

[186] J. S. Read *et al.*, "Matter effects on binary neutron star waveforms", Phys. Rev. D **88**, 044042 (2013).

[187] B. D. Lackey, K. Kyutoku, M. Shibata, P. R. Brady, and J. L. Friedman, "Extracting equation of state parameters from black hole-neutron star mergers: Aligned-spin black holes and a preliminary waveform model", Phys. Rev. D **89**, 043009 (2014).

[188] M. Favata, "Systematic parameter errors in inspiraling neutron star binaries", Phys. Rev. Lett. **112**, 101101 (2014).

[189] A. E. H. Love, "Some Problems of Geodynamics (Cornell University Library, Ithaca, NY, 1911)".

[190] T. Binnington and E. Poisson, "Relativistic theory of tidal Love numbers", Phys. Rev. D **80**, 084018 (2009).

[191] R. J. Furnstahl, B. D. Serot and H. B. Tang, "Analysis of chiral mean-field models for nuclei", Nucl. Phys. A **598**, 539 (1996).

[192] R. J. Furnstahl, B. D. Serot , H. B. Tang, "A chiral effective Lagrangian for nuclei", Nucl. Phys. A **615**, 441 (1997).

[193] B. G. Todd-Rutel and J. Piekarewicz, "Neutron-rich nuclei and neutron stars: A new accurately calibrated interaction for the study of neutron-rich matter", Phys. Rev. Lett. **95**, 122501 (2005).

[194] Wei-Chai Chen and J. Piekarewicz, "Building relativistic mean-field models for finite nuclei and neutron stars", Phys. Rev. C **90**, 044305 (2014).

[195] N. K. Glendenning, *Compact Stars*, Springer, New York -Second Edition (2000).

[196] B. K. Sharma, P. K. Panda and S. K. Patra, "Phase transition and properties of a compact star", Phys. Rev. C **75**, 035808 (2007).

[197] P. G. Reinhard, M. Rufa, J. Maruhn, W. Greiner, and J. Friedrich, "Nuclear ground-state properties in a relativistic Meson-Field theory", Z. Phys. A **323**, 13 (1986).

[198] P. G. Reinhard, "The Nonlinearity of the scalar field in a relativistic mean-field theory of the nucleus", Z. Phys. A **329**, 257 (1988).

[199] M. Oka, K. Shimizu, and K. Yazaki, "Hyperon-nucleon and hyperon-hyperon interaction in a quark model", Nucl. Phys. A **464**, 700 (1987).

[200] C. Nakamoto, Y. Suzuki, and Y. Fujiwara, "Central Force of the Hyperon-Nucleon Interaction in the SU6 Quark Model", Prog. Theor. Phys. **94**, 65 (1995).

[201] C. Nakamoto, Y. Suzuki, and Y. Fujiwara, "Central Force of Baryon-Baryon Interactions with S=-2 in the SU6 Quark Model", Prog. Theor. Phys. **97**, 761 (1997).

[202] C. Nakamoto, and Y. Suzuki, "Quark-Pauli effects in three octet-baryons", Phys. Rev. C **94**, 035803 (2016).

[203] M. Baldo, G. F. Burgio, and H. J. Schulze, "Hyperon stars in the Brueckner-Bethe-Goldstone theory", Phys. Rev. C **61**, 55801 (2000).

[204] A. L. Espíndola and D. P. Menezes, "Relativistic equations of state in a Thomas-Fermi approach for neutron stars", Phys. Rev. C **65**, 045803 (2002).

[205] S. Weissenborn, D. Chatterjee, J. Schaffner-Bielich, "Hyperons and massive neutron stars: The role of hyperon potentials", Nucl. Phys. A **881**, 62 (2012); S. Weissenborn, D. Chatterjee, J. Schaffner-Bielich, "Hyperons and massive neutron stars: Vector repulsion and SU(3) symmetry", Phys. Rev. C **85**, 065802 (2012).

[206] L. L. Lopes and D. P. Menezes, "Hypernuclear matter in a complete SU(3) symmetry group", Phys. Rev. C **89**, 025805 (2014).

[207] R. Rutledge, L. Bildsten, E. Brown, G. Paplov, and V. Zavlin, , "Variable Thermal Emission from Aquila X-1 in Quiescence", Astrophys. J. **577**, 346 (2002); "A possible transient neutron star in quiescence in the globular cluster NGC 5139", Astrophys. J. **578** , 405 (2002).

[208] B. Gendre, D. Barret, and N. A. Webb, "Testing general relativity with present and future astrophysical observations", Astron. Astrophys. **400** , 521 (2003).

[209] J. Cottam, F. Paerels, and M. Mendez, "Gravitationally redshifted absorption lines in the X-ray burst spectra of a neutron star", Nature (London) **420**, 51 (2002).

[210] T. Damour and A. Nagar, "Relativistic tidal properties of neutron stars", Phys. Rev. D **80**, 084035 (2009).

[211] A. W. Steiner, S. Gandolfi, F. J. Fattoyev, and W. G. Newton, "Using neutron star observations to determine crust thicknesses, moments of inertia, and tidal deformabilities", Phys. Rev. C **91**, 015804 (2015).

[212] F. J. Fattoyev, J. Carvajal, W. G. Newton, and B. A. Li, "Constraining the high-density behavior of the nuclear symmetry energy with the tidal polarizability of neutron stars", Phys. Rev. C **87**, 015806 (2013).

[213] Leslie Wade *et al.*, "Systematic and statistical errors in a Bayesian approach to the estimation of the neutron-star equation of state using advanced gravitational wave detectors", Phys. Rev. D **89**, 103012 (2014).

[214] LSC Algorithm Llibrary, http://www.lsc-group.phys.uwm.edu/lal.

[215] J. Piekarewicz *et al.*, "Electric dipole polarizability and the neutron skin", Phys. Rev. C **85**, 041302(R) (2012).

[216] B. K. Agrawal, A. Sulaksono, P. -G. Reinhard, "Optimization of relativistic mean field model for finite nuclei to neutron star matter", Nucl. Phys. A **882**, 1 (2012).

[217] D. Patel *et al.*, "Giant monopole resonance in even-A Cd isotopes, the asymmetry term in nuclear incompressibility, and the "softness" of Sn and Cd nuclei", Phys. Lett. B **718**, 447 (2012).

[218] X. Roca-Maza *et al.*, "Neutron skin thickness from the measured electric dipole polarizability in ^{68}Ni, ^{120}Sn, and ^{208}Pb", Phys. Rev. C **92**, 064304 (2015).

[219] J. M. Lattimer and M. Prakash, "Neutron star observations: Prognosis for equation of state constraints", Phys. Rept. **442**, 109 (2007).

[220] Bharat Kumar, S. K. Biswal and S. K. Patra, "Tidal deformability of neutron and hyperon stars within relativistic mean-field equations of state", Phys. Rev. C **95**, 015801 (2017).

[221] B. K. Agrawal, Shashi K. Dhiman and Raj Kumar, "Exploring the extended density-dependent Skyrme effective forces for normal and isospin-rich nuclei to neutron stars", Phys. Rev. C **73**, 034319 (2006).

[222] B. K. Agrawal, S. Shlomo and V. K. Au, "Determination of the parameters of a Skyrme type effective interaction using the simulated annealing approach", Phys. Rev. C **72**, 014310 (2005).

[223] Raj Kumar, B. K. Agrawal and Shashi K. Dhiman, "Effects of ω meson self-coupling on the properties of finite nuclei and neutron stars", Phys. Rev. C **74**, 034323 (2006).

[224] S. Kirkpatrick, C. D. Gelatt and M. P. Vecchi, "Optimization by Simulated Annealing", Science **220**, 671 (1983).

[225] W. H. Press, S. A. Teukolsky, W. T. Vetterling and B. P. Flannery, "Numerical Recipes in Fortran, (*Cambridge University Press, New York*, 1992)".

[226] S. Kirkpatrick, "Optimization by simulated annealing: Quantitative studies", J. Stat. Phys. **34**, 975 (1984).

[227] L. Ingber, "Very fast simulated re-annealing", Math. Comput. Model. **12**, 967 (1989).

[228] B. Cohen, Master's thesis, Tel-Aviv University, 1994.

[229] J. Dobaczewski, W. Nazarewicz and P. -G. Reinhard, "Error estimates of theoretical models: a guide", J. Phys. G **41**,074001 (2014).

[230] P. Klüpfel, P. -G. Reinhard, T. J. Bürvenich, and J. A. Maruhn, "Variations on a theme by Skyrme: A systematic study of adjustments of model parameters", Phys. Rev. C **79**, 034310 (2009).

[231] Wei-Chai Chen and J. Piekarewicz, "Searching for isovector signatures in the neutron-rich oxygen and calcium isotopes", Phys. Lett. B **748**, 284 (2015).

[232] S. K. Patra, "Structure of light nuclei in relativistic mean-field theory", Int. J. Mod. Phys. E **2**, 471 (1993).

[233] R. F. Garcia Ruiz *et al.*, "Unexpectedly large charge radii of neutron-rich calcium isotopes", Nature Phys. **12**, 594 (2016).

[234] A. Trzcińska *et al.*, "Neutron density distributions deduced from antiprotonic atoms", Phys. Rev. Lett. **87**, 082501 (2001); J. Jastrzębski *et al.*, "Neutron density distributions from antiprotonic atoms compared with hadron scattering data", Int. J. Mod. Phys. E **13**, 343 (2004).

[235] P. -G. Reinhard and W. Nazarewicz, "Information content of a new observable: The case of the nuclear neutron skin", Phys. Rev. C **81**, 051303 (R) (2010).

[236] X. Roca-Maza, M.Centelles, X. Viñas, and M. Warda, "Neutron-skin of ^{208}Pb, nuclear symmetry energy, and the parity radius experiment", Phys. Rev. Lett. **106**, 252501 (2011).

[237] B. A. Brown, "Neutron radii in nuclei and the neutron equation of state", Phy. Rev. Lett. **85**, 5296 (2000).

[238] S. Abrahamyan *et al.*, "Measurement of the neutron radius of ^{208}Pb through parity violation in electron scattering", Phys. Rev. Lett. **108**,112502 (2012).

[239] X. Viñas, M. Centelles, X. Roca-Maza and M. Warda, "Density dependence of the symmetry energy from neutron skin thickness in finite nuclei", Eur. Phys. J. A **50** (2014) 27.

[240] F. J. Fattoyev, J. Piekarewicz and C. J. Horowitz, "Neutron-skins and neutron stars in the multimessenger era", Phys. Rev. Lett. **120**, 172702 (2018).

[241] J. Zenihiro *et. al.*, "Neutron density distributions of ^{204,206,208}Pb deduced via proton elastic scattering at $E_p = 295$ MeV", Phys. Rev. C **82**, 044611 (2010).

[242] P. Möller, A. J. Sierk, T. Ichikawa, and H. Sagawa, "Nuclear ground-state masses and deformations: FRDM(2012)", At. Data Nucl. Data Tables **109**, 1 (2016).

[243] K. Rutz *et al.*, "Superheavy nuclei in self-consistent nuclear calculations", Phys. Rev. C **56**, 238 (1997).

[244] R. K. Gupta, S. K. Patra and W. Greiner, "Structure of ^{294,302}120 nuclei using the relativistic mean-field method", Mod. Phys. Lett. A **12**, 1727 (1997).

[245] S. K. Patra, C. -L. Wu, C. R. Praharaj and R. K. Gupta, "A systematic study of superheavy nuclei for Z = 114 and beyond using the relativistic mean-field approach", Nucl. Phys. A **651**, 117 (1999).

[246] M. S. Mehta, Harvinder Kaur, Bharat Kumar, and S. K. Patra, "Properties of superheavy nuclei with Z=124", Phys. Rev. C **92**, 054305 (2015).

[247] P. Danielewicz and J. Lee, "Symmetry energy II: Isobaric analog states", Nucl. Phys. A **922**, 1 (2014).

[248] M. B. Tsang *et al.*, "Constraints on the density dependence of the symmetry energy", Phys. Rev. Lett. **102**, 122701 (2009); "Constraints on the density dependence of the symmetry energy", Int. J. Mod. Phys. E **19**, 1631 (2010).

[249] P. Russotto *et al.*, "Results of the ASY-EOS experiment at GSI: The symmetry energy at suprasaturation density", Phys. Rev. C **94**, 034608 (2016).

[250] M. Bhuyan and S. K. Patra, "Magic nuclei in superheavy valley", Mod. Phys. Lett. A **27**, 1250173 (2012).

[251] G. Coló, U. Garg, and H. Sagawa, "Symmetry energy from the nuclear collective motion: constraints from dipole, quadrupole, monopole and spin-dipole resonances", Eur. Phys. J. A **50**, 26 (2014).

[252] J. Piekarewicz, "Symmetry energy constraints from giant resonances: A relativistic mean-field theory overview", Eur. Phys. J. A **50**, 25 (2014).

[253] B. Friedman and V. R. Pandharipande, "Hot and cold, nuclear and neutron matter", Nucl. Phys. A **361**, 502 (1981).

[254] S. Gandolfi *et al.*, "Equation of state of superfluid neutron matter and the calculation of the $^1S_0$ pairing gap", Phys. Rev. Lett. **101**, 132501 (2008).

[255] A. Gezerlis and J. Carlson, "Low-density neutron matter", Phys. Rev. C **81**, 025803 (2010).

[256] K. Hebeler, J. M. Lattimer, C. J. Pethick and A. Schwenk, "Equation of state and neutron star properties constrained by nuclear physics and observation", Astrophys. J. **773**, 11 (2013).

[257] J. R. Stone, N. J. Stone, and S. A. Moszkowski, "Incompressibility in finite nuclei and nuclear matter", Phys. Rev. C **89**, 044316 (2014).

[258] J. M. Pearson, N. Chamel, and S. Goriely, "Breathing-mode measurements in Sn isotopes and isospin dependence of nuclear incompressibility", Phys. Rev. C **82**, 037301 (2010).

[259] T. Li *et al.*, "Isoscalar giant resonances in the Sn nuclei and implications for the asymmetry term in the nuclear-matter incompressibility", Phys. Rev. C **81**, 034309 (2010).

[260] P. Danielewicz, R. Lacey, and W. G. Lynch, "Determination of the equation of state of dense matter", Science **298**, 1592 (2002).

[261] U. Garg *et al.*, "The Giant monopole resonance in the Sn isotopes: Why is Tin so "Fluffy"? "Nucl. Phys. A **788**, 36 (2007).

[262] C. Mondal, B. K. Agrawal, J. N. De, and S. K. Samaddar, "Sensitivity of elements of the symmetry energy of nuclear matter to the properties of neutron-rich systems", Phys. Rev. C **93**, 044328 (2016).

[263] M. Praksh, T. L. Ainsworth and J. M. Lattimer, "Equation of state and the maximum mass of neutron stars", Phys. Rev. Lett. **61**, 2518 (1988).

[264] J. Nättilä, A. W. Steiner, J. J. E. Kajava, V. F. Suleimanov and J. Poutanen, "Equation of state constraints for the cold dense matter inside neutron stars using the cooling tail method", A. & A. **591**, 25 (2016).

[265] F. Ozel, G. Baym and T. Guver, "Astrophysical measurement of the equation of state of neutron star matter", Phys. Rev. D **82**, 101301 (2010).

[266] V. Suleimanov, J. Poutanen, M. Revnivtsev and K. Werner, "A neutron star stiff equation of state derived from cooling phases of the X-ray burster 4U 1724-307", Astrophys. J. **742**, 122 (2011).

[267] L. Rezzolla, Elias R. Most and Lukas R. Weth, "Using gravitational-wave observations and Quasi-universal relations to constrain the maximum mass of neutron stars", Astrophys. J. Lett. **852**, L25 (2018).

[268] Eemeli Annala, Tyler Gorda, Aleksi Kurkela and Aleksi Vuorinen, "Gravitational-wave constraints on the neutron-star-matter equation of state", Phys. Rev. Lett. **120**, 172703 (2018).

[269] P. B. Abbott *et al.*, "On the progenitor of binary neutron star merger GW170817", Astrophys. J. **851**, L16 (2017).

[270] D. Radice, A. Perego and F. Zappa, "GW170817: Joint constraint on the neutron star equation of state from multimessenger observations", arXiv:1711.03647v1.

[271] Sean M. Carroll, "Spacetime and Geometry, An introduction to general relativity".